UNIVERSITÀ
DEGLI STUDI
DI PADOVA

Head Office: Università degli Studi di Padova

Department of Chemical Sciences

Ph.D. COURSE IN: MOLECULAR SCIENCES
CURRICULUM: CHEMICAL SCIENCES
SERIES: THIRTY-FIRST CYCLE

RESPONSIVE SELF-ASSEMBLY AS A TOOL FOR CONTROLLING CHEMICAL REACTIVITY

Thesis written with the financial contribution of the European Union Horizon 2020 research and innovation programme under the Marie-Sklodowska-Curie grant agreement Nº 642793

Coordinator: Prof. Leonard J. Prins
Supervisor: Prof. Leonard J. Prins

Ph.D. student: Maria Cardona

With special dedication to my parents,

who have allowed me to be who I am

And to my friends,

whether near or far

who walked with me along the way

Table of Contents

List of Abbreviations

a.u.	arbitrary units
AAP	Arylazopyrazole
AAP-CB	carboxylate-functionalised arylazopyrazole
Ad	Adamantane
Ad2-CB	carboxylate-functionalised adamantane
AMP	adenosine 5'-monophosphate
ATP	adenosine triphosphate
ATP_f	2-aminopurine riboside-5'-o-triphosphate
Boc	*tert*-butyloxycarbonyl
Boc-ON	2-(Boc-oxyimino)-2-phenylacetonitrile
Cac	critical aggregation concentration
CD	cyclodextrin
CDV	cyclodextrin vesicles
cGDDD	coumarin343-Gly-Asp-Asp
Con A	concavalin A
Ddwater	doubly deionised water
DPA	Dipicolylethylenediamine
DPH	1,6-Diphenyl-1,3,5-hexatriene
F.I.	fluorescence intensity
GDP	guanosine diphosphate
GP	general polarisation
GTP	guanosine triphosphate
HED	Hydroxyethylcellulose
HEPES	(4-(2-hydroxyethyl)-1-piperazineethanesulfonic acid)
His	Histidine
HPNPP	2-hydroxypropyl-4-nitrophenylphosphate

ITC	Isothermal Calorimetry
LED	longitudinal-eddy-current delay
MPC	monolayer-protected clusters
NMR	nuclear magnetic resonance
OD	optical density
Pi	inorganic phosphate
PSS	photostationary state
RNA	ribonucleic acid
R_t	retention time
Ser	Serine
S_N2	nucleophilic aromatic substitution
SPR	surface plasmon resonance
SSC	surface saturation concentration
TACN	1,4,7-triazacyclononane
TEA	Triethylamine
TEM	Transmission Electron Microscopy
TFA	trifluoroacetic acid
TGA	thermogravimetric analysis
TOABr	tetraoctylammonium bromide
Trp	Trypthophan
UCNP	upconversion cyclodextrin nanoparticles
UV	Ultraviolet
Vis	Visible

Chapter 1

Introduction

Scientists have always looked to nature as a source of inspiration. Nature is capable of performing highly selective chemical reactions[1] at unprecedented rates,[2,3] to stabilise reactive chemical species[4] and to synthesize complex molecules,[5] all of this in a seemingly effortless manner. Nature achieves this by taking advantage of well-defined reaction environments in confined spaces, which vary from nanometer-sized spaces, such as the active sites of enzymes,[6] to micrometer-sized compartments and assemblies with a highly complex architecture, such as the cell.[7,8]

This has provided a stimulus for chemists to develop structures and assemblies with confined spaces, which have the potential of displaying properties similar to those of natural systems. Although the synthesis of covalent reactors has been attempted, this approach has met rather limited success. This mainly originates from the multistep synthesis required for their formation, which creates a major drawback for practical applications. In order to develop synthetically more accessible structures, a more natural approach was required. Self-assembly emerged as a suitable strategy to achieve this.[9]

Self-assembly lies at the core of supramolecular chemistry.[10,11] Self-assembly can be defined as the spontaneous association of molecules under equilibrium conditions to form stable aggregates joined together by noncovalent bonds.[12] The central importance of self-assembly is dictated by life itself. Indeed, the philosopher Kant has described life as a self-organised process through which function emerges.[8] While self-assembly is a simple process which involves the collection and aggregation of separate components into a confined entity, self-organisation is the spontaneous generation of well-defined functional supramolecules as a result of self-assembly from the individual components.[11,13,14] The process uses molecular information inherent in the individual components without external control.[13] Self-assembly is therefore the means to achieve organised systems and move towards progressive complexity in synthetic systems. The instructions to generate well-

defined functional structures are programmed within the individual components. Therefore, comprehension, induction and direction of self-assembly processes is key to moving towards constructing complex synthetic structures capable of performing advanced functions[15] and to observe emergent properties and adaptation in complex matter.[13]

1.1 Self-assembly in nature and synthetic systems

Nature provides us with a myriad of examples of self-assembled structures which are essential to life. Self-assembly is involved in protein folding, in structuring nucleic acids, in the formation of lipid membranes, in protein aggregation and in the formation of vessels such as the iron storage vessel ferretin, to mention just a few.[7,16] Protein folding represents a canonical example of natural self-assembly. In proteins, long, linear chains of amino acids fold in a three-dimensional structure to give a protein whose functions emerge as a result of the interactions of the individal amino-acid sub-units (Figure 1.1a).[14]

The phospholipid cell membrane represents another impressive example of self-assembly where an interplay of hydrophobic and hydrophilic forces entail the arrangement of the polar phospholipid head groups on the outside of the membrane and the hydrophobic tails clustered in the apolar region of the membrane.[17] The plasma membrane delimits the boundary of the cell and segregates the intracellular organelles from the outer environment. Apart from these morphological functions, the cell membrane exerts selective control over what goes in and out of the cell through membrane ion channels and incorporates mechanisms to take in and secrete large particles (endo- and exocytosis, respectively) (Figure 1.1b).[18]

Chemists have recognised in natural self-assembly a process to be mimicked in synthetic systems. This has le d to the design of structures which nowadays approach the size and complexity of natural systems. Using self-assembly as a new synthetic strategy, it has become possible to design structures with dimensions of 1 to 100 nanometers, which were previously inaccessible through conventional synthesis.[20,21] Exploiting the principles of coordination chemistry and using metals as templates, it has been possible to construct supramolecular cages,[22-26] macrocyles,[27,28] grids,[29] racks,[30] ladders,[31] clusters[32] and even helices.[33] New chemical structures have been developed using self-assembly as a tool to promote the formation of mechanical bonds, inluding catenanes,[34] rotaxanes[35,36] and interwoven cages.[37,38] The reversible nature of self-assembly has allowed the construction

of even more impressive structures including molecular switches,[39,40] molecular motors[41] and molecular machines[42,43] as well as structures which are adaptive[44] and autopoietic[45] in nature. Figure 1.2 illustrates a few of these examples.

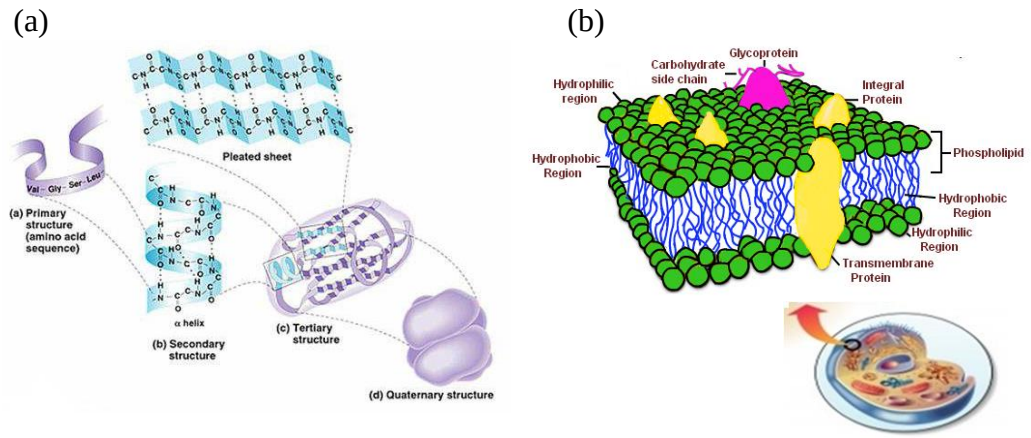

Figure 1.1: Examples of self-assembled structures in natural systems. (a) Folding of linear chains of amino acids giving rise to the structure of the protein and (b) phospholipid bilayer which carried out numerous functions including compartmentalisation.[19]

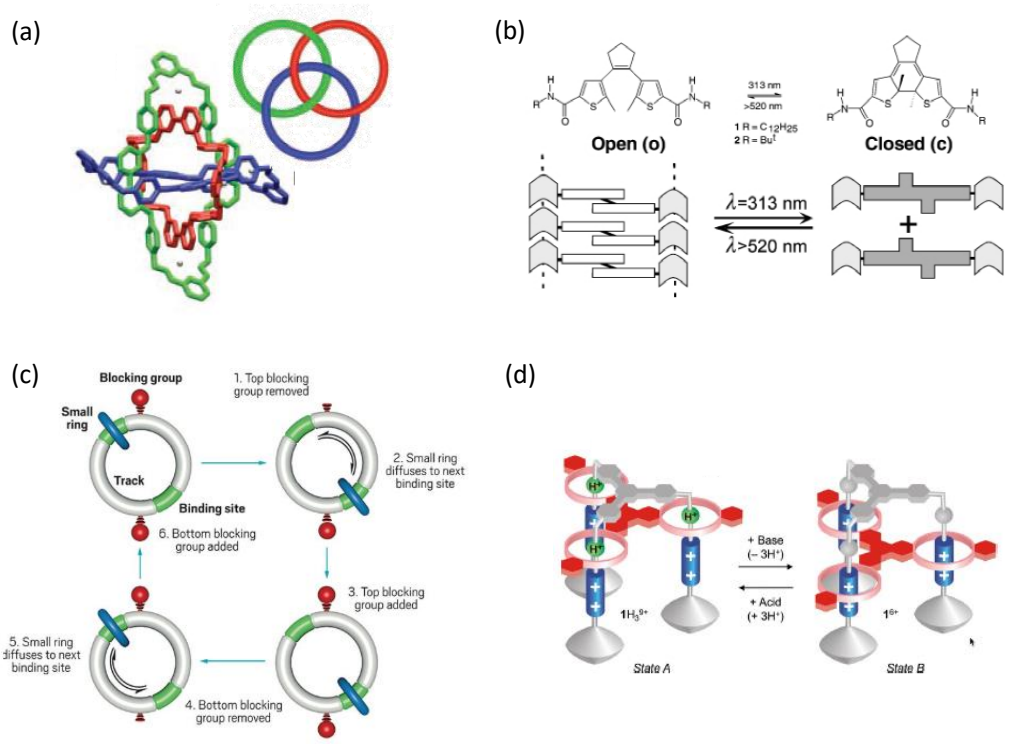

Figure 1.2: Examples of synthetic self-assembled structures: (a) Molecular Borromean ring[37] (b) photochemical switch[46] (c) a molecular rotor[47] and (d) a molecular elevator.[48]

1.2 Self-assembled nanoreactors

The potential of such self-assembled structures and systems goes beyond their aesthetic value. Self-assembly results in the formation of ordered - yet dynamic - structures under thermodynamic control. The reversibility of the interaction permits error-correction, and structures typically form with a quantitative yield. The equilibrium structures are also sensitive to external stimuli which can affect the position of the equilibrium.[49] This enables a wide variety of applications, ranging from optoelectronics to drug delivery systems. One valuable asset of self-assembled structures is the ability to create micro- and nano-sized cavities, which can be exploited for chemical synthesis and catalysis. In such nanospaces, it is possible to alter not only the reaction pathways but the size and morphology of the products as well. Several self-assembled nanoreactors have been developed, ranging from small organic molecular containers to large compartment-containing assemblies.[9,50]

1.2.1 Molecular capsules

Large synthetic efforts has been spent to construct molecular capsules and boxes, in an attempt to mimic the high reactivity and selectivity of enzymes' active sites.[51] Capsules are able to work as catalysts because they are capable of stabilising the transition state. Molecular capsules can be divided into covalent capsules or non-covalent (supramolecular) capsules. Cycloaddition reactions have frequently been studied in covalent capsules. Figure 1.3 shows an example of a cucurbit[6]uril molecular cage, **1**, which is capable of encapsulating reagents **2** and **3**. These reagents react to give the Diels-Alder products **4A** and **4B**.[52] A number of other hosts, especially cyclodextrins,[53] have also been used as catalysts for this class of reactions. It was possible to achieve catalytic turn-over by carefully designing the binding sites of the capsule such that the products bind weaker than the reactants, or by making sure that the reaction products have a weaker affinity to the host.[54]

Non-covalent capsules enable the construction of highly elaborate structures with relatively less effort (time, cost etc.) compared to to the construction of covalent capsules.[9] Self-assembled capsules contain enclosed cavities formed between two complementary subunits held together by non-covalent bonds such as hydrogen-bonding or metal-ligand interactions.[26,51,55] An example of a hydrogen-bonded structure is the "molecular softball" developed by the group of Rebek.[51] In this capsule, glycoluril moieties are connected

through seven fused rings. The monomer **5** dimerised to form $\mathbf{5}_2$ on account of an ethylene bridge in the central ring, which provided the extra curvature needed to form a hydrogen-bonded dimer. The result was a capsule held together by 12 hydrogen bonds (Figure 1.4a).

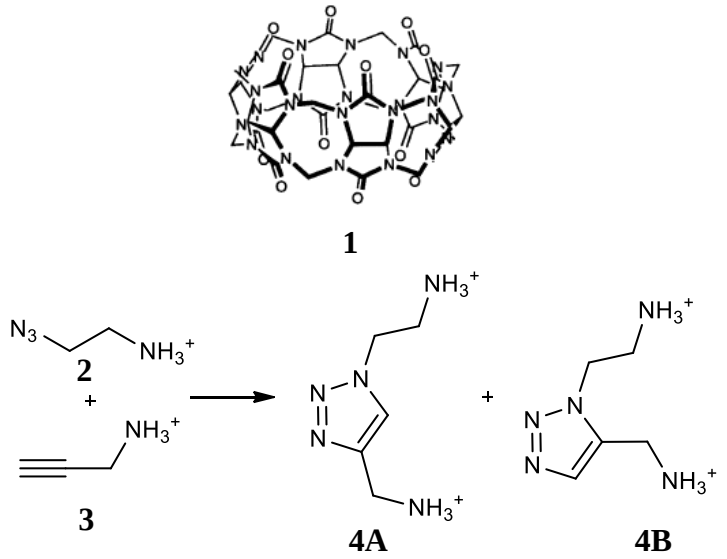

Figure 1.3: Figure showing a cucurbit[6]uril cage **1** in which the 1, 3-dipolar cycloaddition reaction between propargylammonium **2** and azidoethylammonium **3** could occur with enhanced yield.[52]

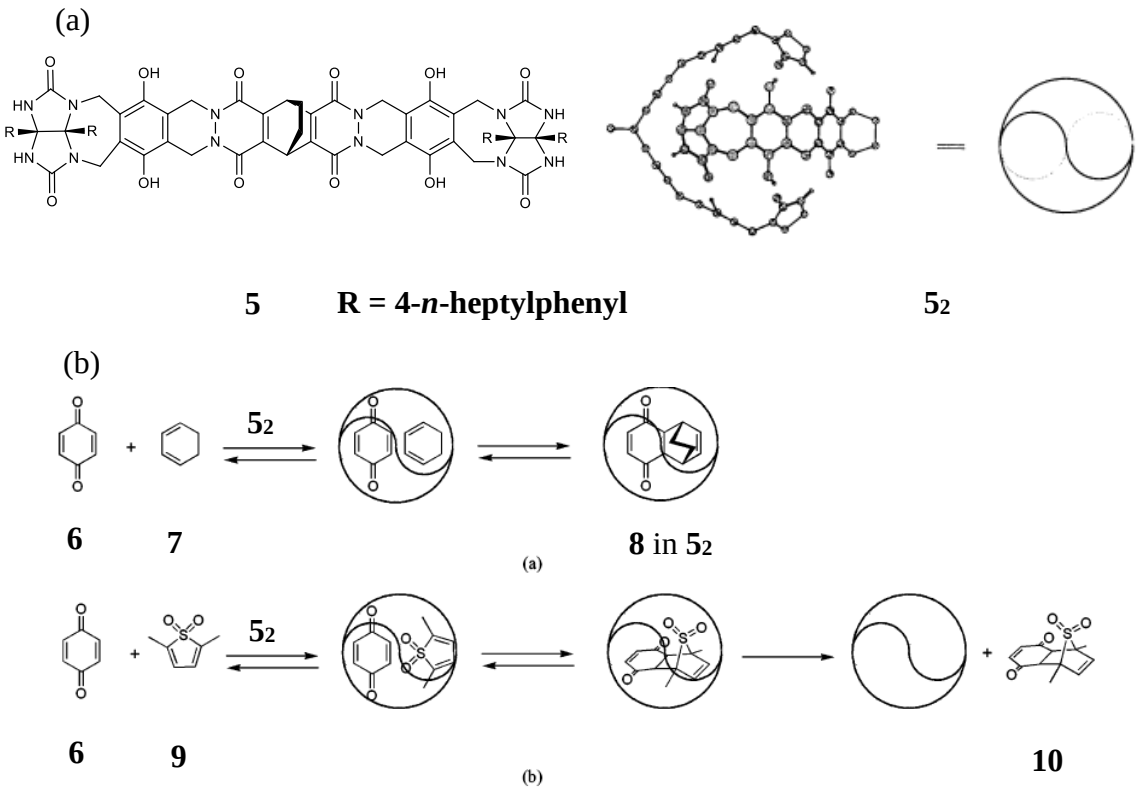

Figure 1.4: (a): Glycoluril-based capsule $\mathbf{5}_2$ which is self-assembled by hydrogen-bonds and the formation of dimers from monomer **5.** (b) The Diels-Alder reaction between *p*-benzoquinone, **6,** and cyclohexadiene, **7**, to form **8** in microreactor $\mathbf{5}_2$. Product is required in stoichiometric quantities because of product inhibition. (c) The Diels-Alder reaction between *p*-benzoquinone, **6**, and 2,5-dimethylthiophene dioxide, **9**, to give the product **10** catalyzed by the microreactor $\mathbf{5}_2$; in this case, product release makes $\mathbf{5}_2$ available for catalyzing further reactions.

The cage could encapsulate *p*-benzoquinone, **6** and cyclohexadiene **7**, which reacted to form the Diels-Alder product **8** 200 times faster than the non-encapsulated reaction in xylene.[56,57] The space restriction in the capsule favoured the exclusive formation of the *endo* isomer, but catalytic turn-over was difficult since the product fit perfectly in the cavity. On the other hand, by using 2,5-dimethylthiophene dioxide **9** as the diene, it was possible to obtain catalytic turnover, since the capsule did not have a high affinity for the product **10**. New reactants could be encapsulated due to the dynamic nature of the assembly.

Figure 1.5 represents an example of a cage, **11**, held together coordination bonds. It was constructed from the spontaneous self-assembly of four *tris* (4-pyridinyl) triazine ligands and six palladium complexes, generating an inner compartment with a volume of approximately 500 Å.[22] This enabled the rate enhancement of the Wacker oxidation of styrene, **12**, to acetophenone, **13**, in aqueous conditions and the product yield increased from 4 % to 82 % in the presence of a catalytic amount of the cage.[58] Molecular capsules have also been used to slow down reactions. Thus, Nitschke synthesized molecular cage **14** consisting of twelve sulfonate groups at the exterior of the cage for water solubility. Aromatic rings at the edges of the cage defined the hydrophobic interior (Figure 1.6). The encapsulation of furan, **15**, into the cage prevented the Diels-Alder reaction with maleimide, **16**. Addition of benzene, **17**, as a competitor released **15** from the cage and initiated the reaction to form **18**.[59]

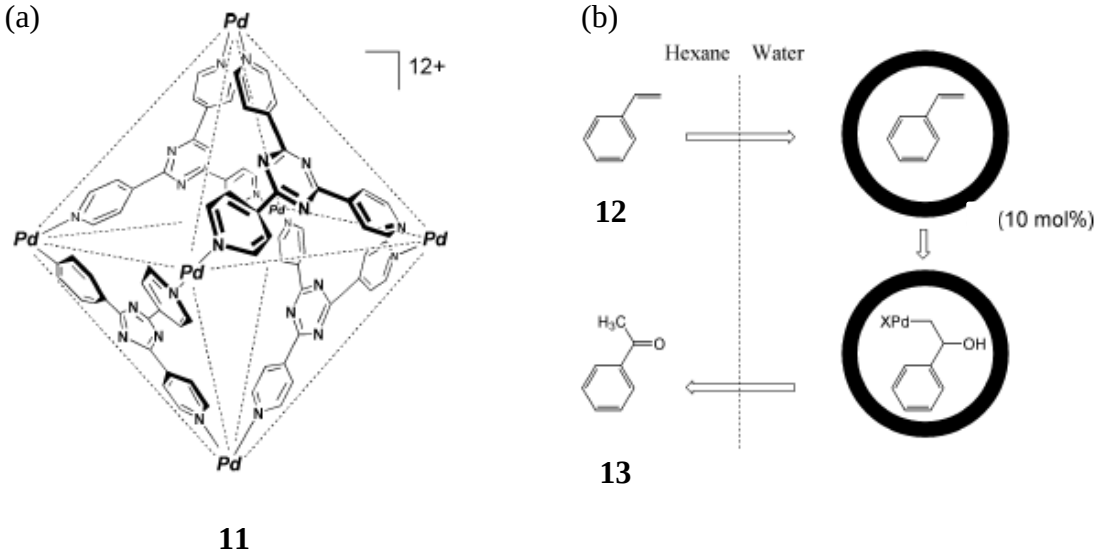

Figure 1.5: Capsule **11** which acted as a phase-transfer catalyst for the Wacker oxidation of styrene, **12**, to give acetophenone, **13**, in a two-phase system.[22]

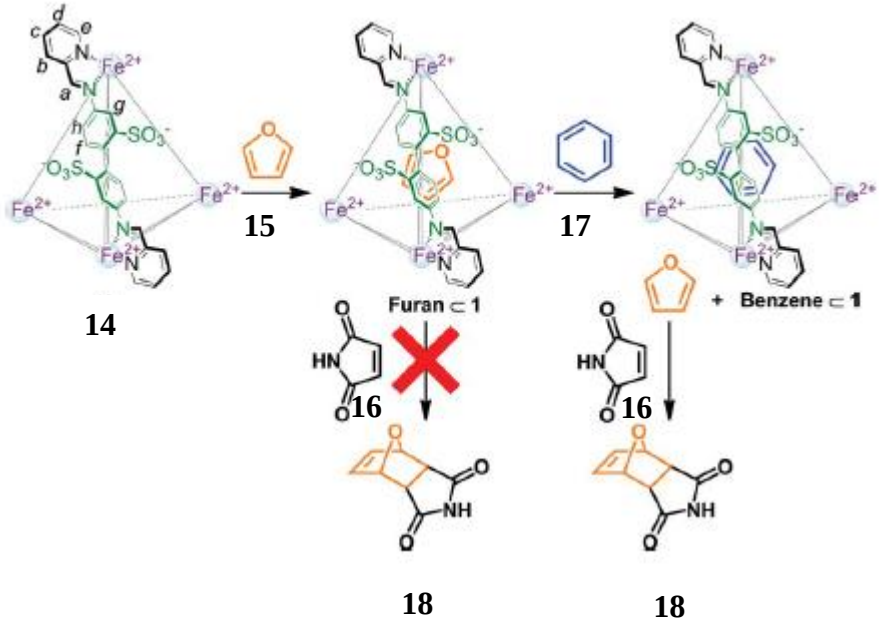

Figure 1.6: Schematic representation of Diels-Alder reaction inhibited by capsule **14.** Furan **15** is encapsulated in **14** and inhibited from reacting with **16**. Addition of benzene **17** as a competing guest releases **15** and the Diels-Alder reaction to produce **18** could be initiated.[59]

In these and other similar examples, the capsules act as catalysts. In some cases, reactive species are concentrated inside the cavity. In other cases, they act as phase transfer catalysts, shuttling the guests from one solvent phase to another. In yet other cases, they can stabilise reactive intermediates within the confined space or enable conversion of substrates with improved selectivity or activity.[9]

1.2.2 Micelles and vesicles

Micelles and vesicles constitute the next most important synthetic nanoreactors. These are man-made structures which are closest to the cell membrane. The simplest cell is capable of performing much better than the best fabricated reactors, in terms of efficiency, yield and so on, and is capable of performing cascade reactions providing chemical processes occurring within a cell.[9] It is therefore not surprising that tremendous effort has been invested in attempting to mimic cell-like structures and behaviour. Micelles and vesicles form because of the hydrophobic effect, which drives the aggregation of apolar molecules in aqueous solution.[60] The bilayer of vesicles and the interior of micelles constitute an apolar pseudophase possessing different solvating properties compared to the surrounding bulk water. Indeed the hydrophobic core is generally considered to be a small volume of

liquid hydrocarbon due to the highly disordered hydrophobic chains. It therefore affords a different microenvironment from the surrounding medium.[49] Indeed, hydrophobic substrates partition favourably in the lipophilic interior of micelles and vesicles, realizing a high concentration of substrate in a small volume. This permits large rate enhancements due to the enhanced local concentration of reagents.[61] It also becomes possible to retard the rate of chemical reactions if, for example, only one reagent partitions inside the aggregate, thus reducing the possibilities of encounter required for reaction to occur.[60]

1.2.2.1 Micelles

The enhanced reaction rate in micelles has been termed micellar catalysis, and has been a field of intensive research.[61-67] Micellar catalyis is attributed to a number of phenomena, often occuring simultaneously. Most intuitively, the increase in the local concentration of reactants in the interior or at the surface of the micelle is responsible for an improved reactivity. Interaction with the surfactant molecules can also stabilise a transition state. Enhanced reactivity can also arise from the medium effect, which is a combined effect of the polarity, microviscosity and charge inside the micelle.[9] Though the number of reactions promoted by micellar catalysis is large, they can roughly be categorised into three kinds; polar, charged molecules reacting in assemblies of nonfunctional, ionic surfactants, lipophilic reagents reacting in aggregates of nonfunctional surfactants and reactions where the reactant is the functional surfactant.[60]

One particularly exciting example of micellar catalysis is demonstrated by self-replicating micelles. The pioneer in this area is Luisi, who has pinned the term “autopoiesis” to describe the formation of an organized unit, such as a micelle, which is capable of self-maintenance and self-reproduction (Figure 1.7).[68] This places micellar catalysis in a good position to speculate on the origin of life and evolution,[45,69-75] but it also evidences the impressive increase in reaction rates upon the spontaneous aggregation of surfactants.[60]

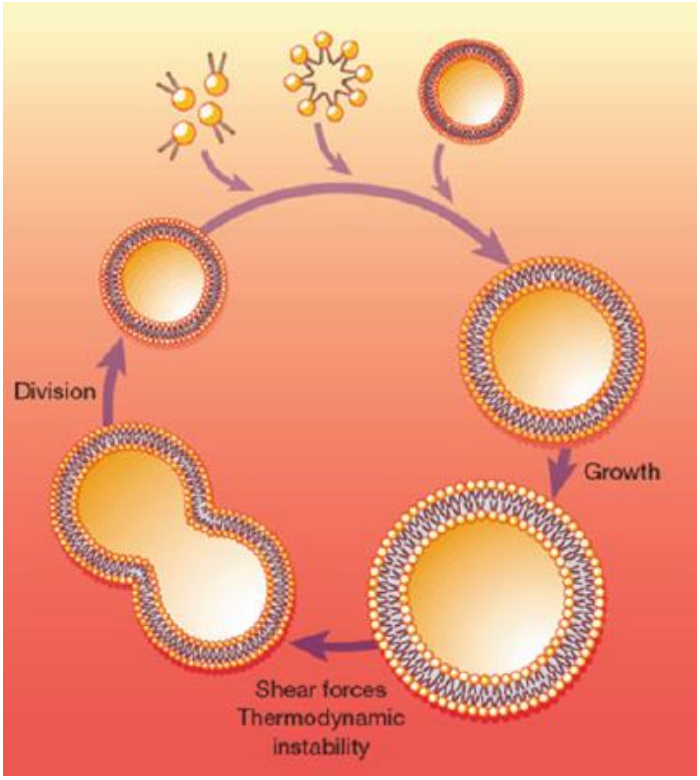

Figure 1.7: Schematic representation of autopoeisis showing vesicle growth and division as a function of increasing concentration of surfactants.

One recent example of self-replicating micelles was developed by Giuseppone *et al.*, [76] who used reversible imine formation between hydrophilic aliphatic, benzylic, aromatic and hydroxyl amines **19-26** and hydrophobic benzaldehyde **A** to construct dynamic amphiphilic molecules, which were termed dynablocks (Figure 1.8a). The amines reacted with the aldehyde **A**, and the resulting imines self-assembled into micelles (Figure 1.8b). Progressive evolution from cylindrical to spherical micelles was observed for some of the imines. The micelles could grow by encapsulating the free **A** in their core, which was a vital step necessary for observing self-replicating behaviour. Whereas imine **19A** did not form micelles in water, imine **25A** showed exponential growth in water (Figure 1.9a). Thus, mixing **19**, **25** and **A** together in acetonitrile led to the preferential formation of imine **19A**. However, changing the solvent to water resulted in a completely different evolution of the system to favour imine **25A** (Figure 1.9b).

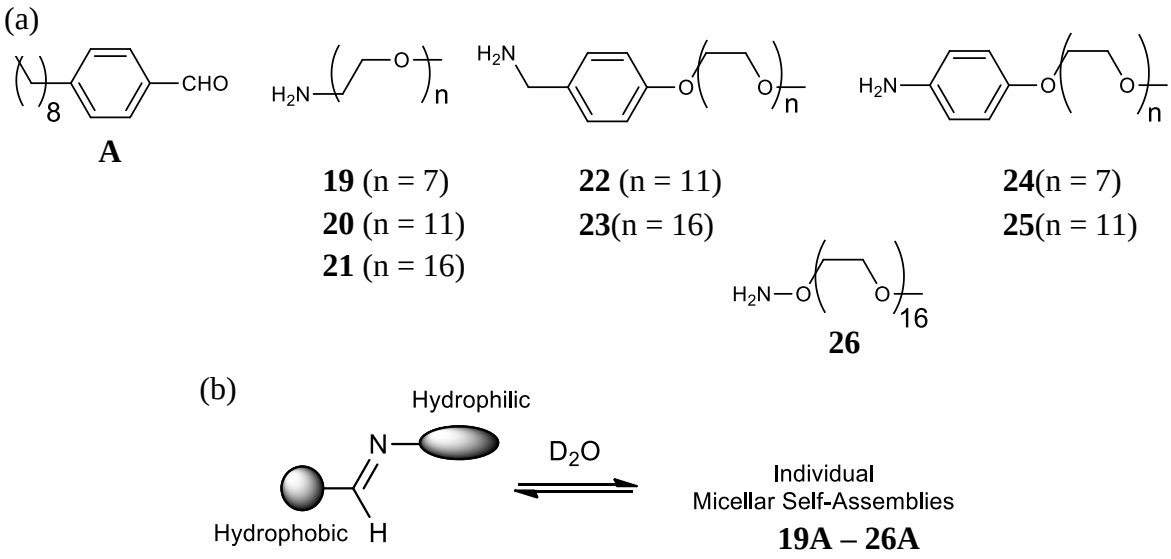

Figure 1.8: (a). The structure of aldehyde **A** and amines **19-26**. (b). Representative figure showing the structure of imines **19A-26A**.[76]

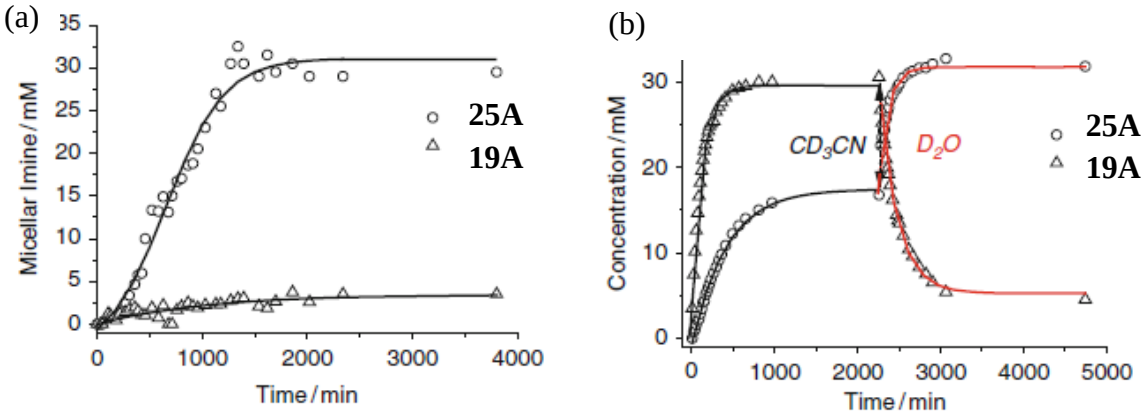

Figure 1.9: (a) A graph showing the concentration of imines **19A** and **25A** against time for an equimolar mixture of **19**, **25** and **A** in D_2O (concentration = 50 mM each). (b) A graph showing the concentration of imines **19A** and **25A** against time starting from a 50 mM mixtures of **19**, **25** and **A** in acetonitrile and, after reaching the thermodynamic equilibrium, by changing the solvent to pure D_2O.

1.2.2.2 Vesicles

Vesicles constitute a synthetic self-assembled structure with greater resemblance to natural cells. Vesicles are involved in numerous processes inside the cell. Some examples of natural vesicles include endosomes, which internalise molecules and particles in eukaryotic cells, lysosomes, which are responsible for enzymatic degradation of macromolecules, vesicles, which transport molecules within eukaryotic cells, secretory vesicles, which bring molecules out of the cells and extracellular vesicles, which are responsible for the exchange of molecules between cells. Vesicles within the cell allow the possibility of having diverse microenvironments in the cell. Thus, endosomes present an oxidising internal space inside the reducing cytoplasm of eukaryotic cells, whilst exosomes offer a reducing interior inside an oxidising extracellular medium.[77] Synthetic vesicles are formed by self-assembly as a consequence of the structure of the amphiphile and due to the experimental conditions such as concentration, temperature and the composition of the aqueous solution.

Vesicle surfaces are better organised than micelle surfaces and have the same excellent solvating properties.[9] A variety of reactions have been performed in vesicles, including both unimolecular and bimolecular reactions. Thus, the decarboxylation of 6-nitrobenzisaoxazole-3-carboxylate **27** to give **28** in positively charged vesicles formed from dialkylammonium bromide at pH 9.1 is an example of a unimolecular reaction catalysed by the localisation of the reagents on the surface of positively charged vesicles (Figure 1.10a).[78-80] The deprotonation of 5-nitrobenzisaxole **29** as a result of a Kemp elimination of water to give **30** is an example of a bimolecular reaction accelerated by cationic vesicles (Figure 1.10b).[81] This was attributed to (a) the increased local concentration of the reacting species, (b) the lower dielectric constant on the surface of the vesicles, (c) the lower micropolarity and (d) the fluidity of the membrane. The latter insight emerged from the observation that higher rates were obtained above the chain melting temperature which cause higher membrane fluidity.

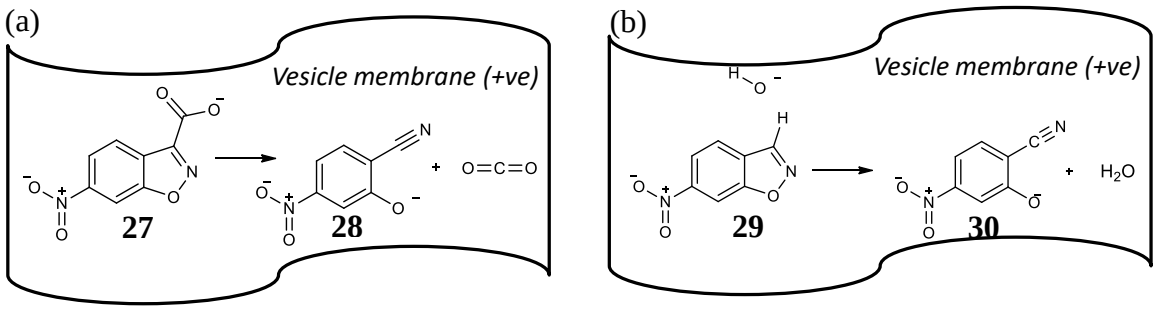

Figure 1.10: Schematic representation of (a) the decarboxylation of 6-nitrobenzisoxazole-3-carboxylate, **27** resulting in **28** occurring in the membrane of positively charged vesicles and (b) the deprotonation of 5-nitrobenzisoxazole, **29** (Kemp elimination) to give **30** in the vesicle membrane of positively charged vesicles.

Catalysts, both organic[77] and inorganic,[82-84] have also been enclosed within vesicles. The catalytic activity could be modified within vesicles because of co-localisation within or on the surface of the vesicle membrane or due to a different polarity on the surface membrane.[77] One example of a reaction catalysed by a membrane-embedded catalyst is the enhanced hydrolysis of *p*-nitrophenyl *N*-dodecanoyl-phenylalaninate **31** to give **32** and **33** (Figure 1.11). This was catalysed by short peptides confined in the membranes as a result of their hydrophobic His residues, such as **35**, and resulted in the preferential formation of the L-enantiomer.[85,86]

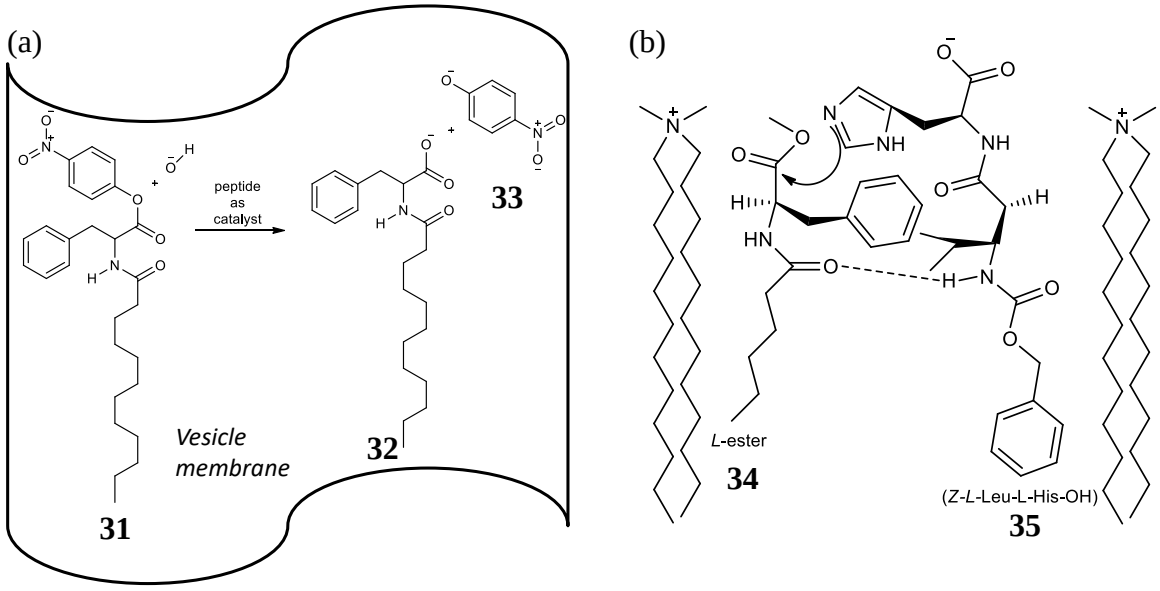

Figure 1.11: (a). Schematic representation of a racemic mixture of *p*-nitrophenyl *N*-dodecanoyl-phenyl-alaninate, **31** (amino acid ester) being hydrolysed within the walls of positive vesicles at slightly alkaline pH. (b) The reaction is catalysed by membrane-embedded catalysts. The observed reactivity can be explained by the close proximity of the L-enantiomer of the amino acid ester and the peptide catalyst (Z-L-Leu-L-His-OH), **35**. This was demonstrated with a methyl ester derivative containing a hexanoyl chain protecting group, **34**, which is less reactive.

Membrane-assisted reactions inside vesicles are mostly oxidative and hydrolytic reactions of small molecules and decarboxylations leading to the degradation or small modifications of molecules. The products diffuse away after the reaction takes place. Reports of membrane-promoted or -controlled reactions which lead to the synthesis of larger molecules from smaller ones are much less common.

Engberts *et al.* used metallo-vesicles to enhance the rate of formation of a Diels-Alder reaction between **36/37** and **38** using vesicles consisting of a phosphate surfactant and Cu(II) as counterion (Figure 1.12).[87] The product, **39**/**40**, was formed 1×10^6 faster in the vesicles relative to the uncatalysed reaction in acetonitrile. Smaller vesicles were more efficient at catalysing the reaction than larger ones, probably because of more efficient binding of the substrate to smaller vesicles.

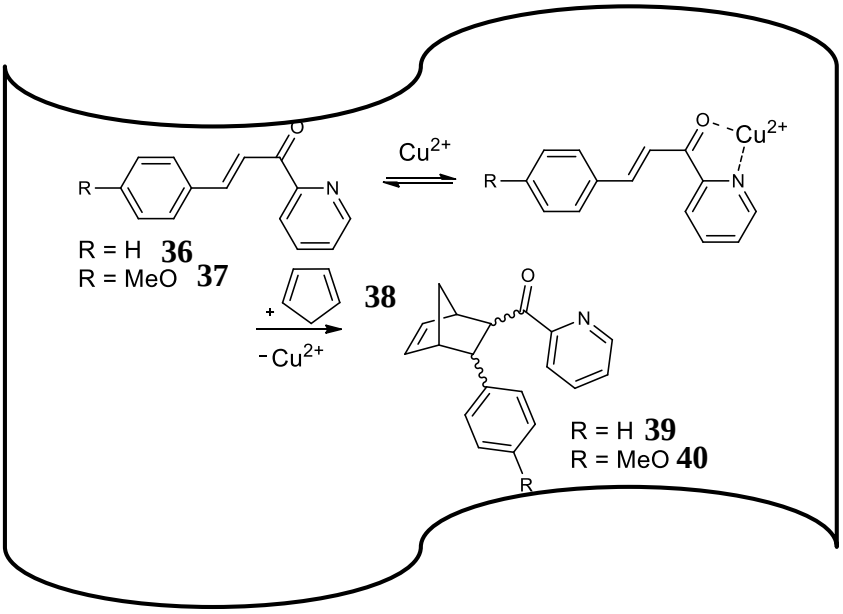

Figure 1.12: Diels-Alder reaction between **36**/**37** and **38** catalysed by metallo-vesicles composed of a phosphate surfactant and copper (II) as the counterion.

In another study by Murakami *et al.* trypthophan, **43**, was synthesized by a β-replacement reaction of serine, **41**, and indole, **42**, using the catalytic effect of a functionalised bilayer membrane consisting of a cationic peptide lipid containing an L-histidyl residue, **44**, copper (II) ions and a hydrophobic pyridoxal derivative, **45**, (Figure 1.13).[88,89] This provided a preference for the formation of the D-isomer. The vesicles thus function as an artifical trypthophan synthase. The bilayer offerred a hydrophobic environment (evaluated to be equivalent to propanol) which eliminated water, significantly favouring the formation of

intermediates. The surfactant used for the formation of the vesicles was a peptide lipid with an imidazolyl group, which offered general acid-base catalysis. The copper(II) ions afforded a coordination effect.

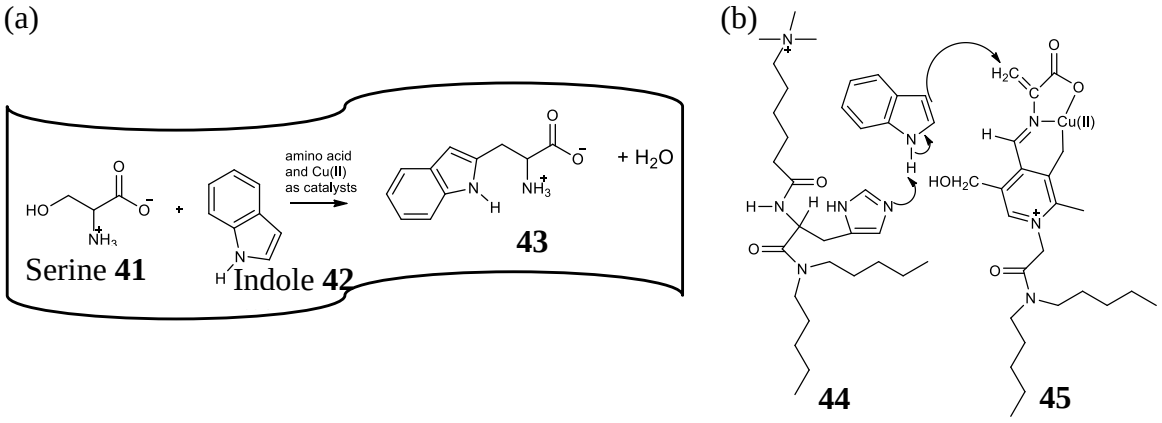

Figure 1.13: (a) The formation of trypthophan (Trp), **43**, from serine, **41**, and indole, **42**, in the presence of cationic vesicles and Cu(ii). (b) Key steps of a possible activation mechanism for the reaction occurring in the vesicle membranes.

1.2.3 Other self-assembled nanoreactors

The examples highlighted above are examples of molecular nanoreactors. However, self-assembly has been a fundamental tool for the construction of a wider variety of nanoreactors. Macromolecular nanoreactors utilise polymers for the construction of aggregates and these include polymerosomes (aggregates assembled from block copolymers)[90] and polymer micelles (micelles formed from amphiphilic block copolymers)[91,92] as nanoreactors. It has also been possible to isolate biological self-assembled structures and use these as nanoreactors. These include ferretin[93] and other protein cages[94] together with viruses.[95] All of these contain cavities and have been exploited for carrying out chemical reactions.[96] Figure 1.14 illustrates examples of some of these nanoreactors.

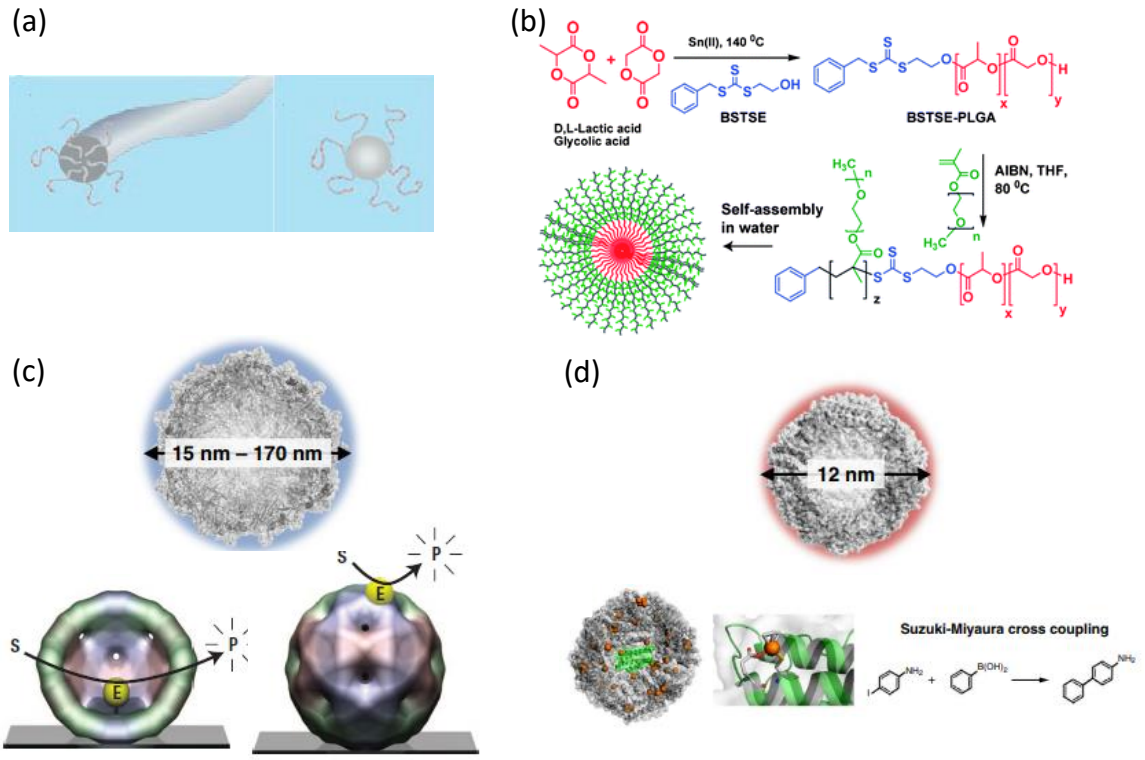

Figure 1.14: Examples of macronanoreactors. (a). Worm-like micelle and spherical micelle formed from block copolymers and related amphiphiles.[90] (b). Self-assembly of a polymer micelle.[97] (c). Schematic representation of a virus cavity. Encapsulation of an enzyme inside the viral cavity resulted in the enhanced formation of product when the substrate diffused in the cavity. Adsorption of the enzyme on the surface did not affect product formation.[94] (d). Schematic representation of a ferritin cavity and one example of a reaction carried out inside a ferritin cavity.[98]

1.3 Temporal control in self-assembled nanoreactors

In Nature, reactions in confined spaces are closely geared such that the product of one chemical reaction functions as the catalyst or the substrate for the next one.[9] For strict regulation, not only do the reactions need to be controlled in space, but they also need to be precisely timed. Thus, for example bacterial cell division involves molecular recognition between several proteins in conjunction with transport phenomena occuring along concentration gradients. Through complex control, cell division occurs in the middle of the cell with high precision, but most importantly, it occurs at the right time.[99]

Traditionally, the aim of chemistry has been the synthesis of organic molecules. However, in order to come closer to natural systems, it is becoming increasingly important to control where and when chemical reactions occur in complex systems. Designing reactions with high temporal and spatial resolution would be the next phase towards the design of reaction networks.[100] The control of chemical reactions in self-assembled nanoreactors is a first

step towards controlling reactions in time and space. This, however, is still far from the eloquent complexity present in natural systems. Recently, a number of innovative approaches are being proposed which involve temporal control over self-assembly processes. This brings self-assembly closer to Nature whilst promising to permit a more creative manipulation of chemical reactivity, producing results previously unattainable using classical self-assembly processes.

1.3.1 Light as a means of controlling self-assembly processes

In biological systems the emergence of function is related to triggers induced by biological cofactors.[101] Coupling a self-assembly process to a cofactor could be a potential means of exerting control over the process. A change can be induced in the cofactor which translates into a consequent modification of the properties and/or functions of the self-assembly. Light is a very commonly used source of energy to modulate processes.[100] It is a non-invasive, easy to use technique and can be delivered instantaneously to a precisely determined location.[102] Control via optical methods therefore holds promise to deliver innovative materials with a variety of applications in sensing, optics and delivery systems.[103]

The visual phototransduction mechanism is an example of a complex chemical network controlled by light.[104] Photons trigger the *cis-trans* isomerisation of retinal, a key cofactor involved in vision. This activates a cascade of reactions leading to the generation of an electrical signal to be processed by the nervous system. Inspired by this system, light was used to regulate the catalytic activity of gold nanoparticles passivated with a monolayer of C-9 thiols terminated with a 1,4,7-triazacyclononane (TACN)•Zn^{2+} headgroup, **46** (Figure 1.15). These nanoparticles are an example of a self-assembled system which uses the gold core as an inorganic support for the assembly of the thiols. The close distance between the TACN•Zn^{2+} allows them to act cooperatively to catalyse the transphosphorylation of 2-hydroxypropyl-4-nitrophenylphosphate (HPNPP), **47** a model for RNA hydrolysis.[105,106] The reaction can be monitored spectroscopically by the formation of the highly coloured PNP, **48.**

The catalytic activity of the nanoparticles **46** could be regulated by the light sensitive 4-(phenylazo)-benzoic acid, **49**. The *trans*- isomer of the azobenzene **49** presented a much higher affinity to the gold nanoparticle **46** than the *cis*- isomer (~2.2 times more). This was

attributed to an increase in the polarity of **49** upon *trans-cis* isomerisation, which decreases the hydrophobic interactions with the apolar part of the monolayer. This fundamental property meant that **49** could act as a photoresponsive cofactor for the regulation of the catalytic reaction by the nanoparticles **46**.[107] In the presence of the *trans*- isomer of **49**, the nanoparticle **46** was less capable of exerting its catalytic influence because **49** was bound within its hydrophobic domain, preventing contact with the subsrate **47**. Upon *cis-trans* isomerisation induced by UV-Vis light, the affinity of the nanoparticle **46** for azobenzene **49** was greatly reduced. Consequently, it was released from **46** and enabled the nanoparticle **46** to exert its catalytic function. The experiment was started with **49** in the *cis*-state. Irradiation with visible light transformed the *cis*- to the *trans*- form of **49** and caused a resultant downregulation in the catalytic activity when compared with the *cis*- isomer. This system worked in a similar manner to the natural visual transduction pathway. Irradiation by light led to a structural change in a cofactor which in turn influenced its affinity for the catalytic site.

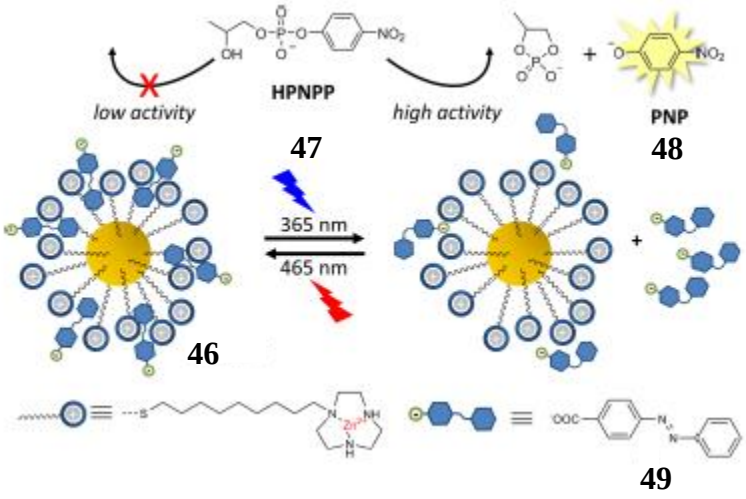

Figure 1.15: The *trans*- form of the azobenzene **49** has a high affinity for nanoparticle **46** while the *cis*- form loses its binding affinity for **46**. Irradiation with visible/UV-Vis light is thus used to modulate the affinity of **49** for **46**, affecting the transphosphorylation rate of HPNPP, **47**, and thus the rate of formation of the coloured product **48**.

1.3.2 Self-assembly far-from-equilibrium

Mastering the key principles of self-assembly has granted scientists the possibility to construct complex nanostructures for the regulation of chemical reactions. In traditional uses of self-assembly, the self-assembled structure is static and thermodynamically or kinetically stable (Figure 1.16a and b). In equilibrium assemblies, the assembly is driven by the fact that the self-assembled structure is more stable than the separate components.[12]

In kinetically stable assemblies, the systems are trapped in a local minimum of energy, and need time or activation energy to be converted to a more stable energy state.[108] Such static self-assembly is used by Nature[109] for example in the formation of DNA[110] or in the assembly of the majority of folded, globular proteins.[111] The construction of some of these assemblies frequently involves energy. However, the resulting structure is then stable.

More precise control in natural systems arises when the self-assembled structure demands the continuous input of energy in order to be maintained (Figure 1.16a and c). Self-assembly processes which operate far-from-equilibrium on account of their requirement for energy are termed dissipative self-assembly processes.[112,113] Such systems need energy in order to be assembled, but have an in-built mechanism which dissipates the energy, reverting the system back to the unassembled state unless additional energy is provided. This enables Nature to attain temporal control over the duration of the assembled state and therefore over any associated function. The function is therefore transient in nature and dependent upon the source of energy.[114-116] In contrast with synthetic systems, dissipative self-assembly is the predominant method used by natural systems and gives rise to capacities such as signal processing, self-healing, motility and self-replication, processes which are of critical importance to life.[117]

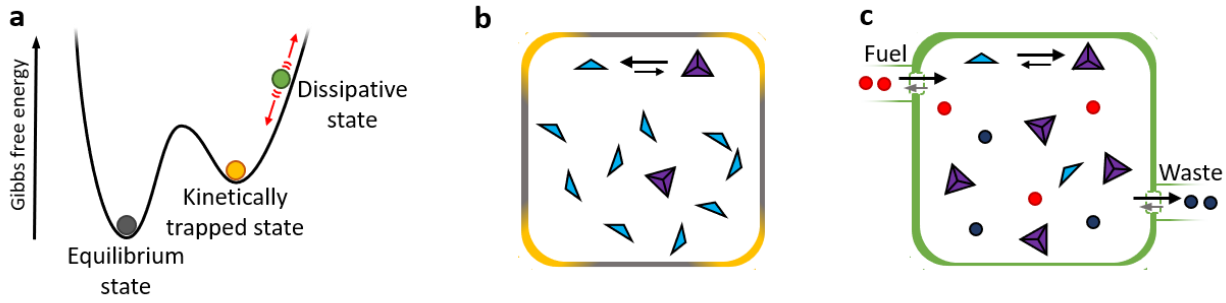

Figure 1.16: Self-assembly at equilibrium and out-of-equilibrium. (a). Representation of the Gibbs free energy landscape for a generic system as a whole (*i.e.* the sum of the energy of every component), on which different situations are represented: the equilibrium state (grey circle), a kinetically trapped state (orange circle) and a dissipative state (green circle). (b). Cartoon representation of a self-assembling system at equilibrium or in a kinetically trapped state (c). Cartoon representation of the same system, but now in the presence of a chemical energy flux, which drives the equilibrium towards the aggregated state.[118]

A number of external energy sources have been used to drive systems away from equilibrium.[119] Electromagnetic fields[120,121] and light[102,122,123] provide excellent control since the assembly can be regulated by switching the energy source on or off. In one

particular example, it has been possible to devise a reaction "nanoflask", a confined space where a chemical reaction could occur for a definite period of time using light to control the lifetime of a self-assembly (Figure 1.17).[124]

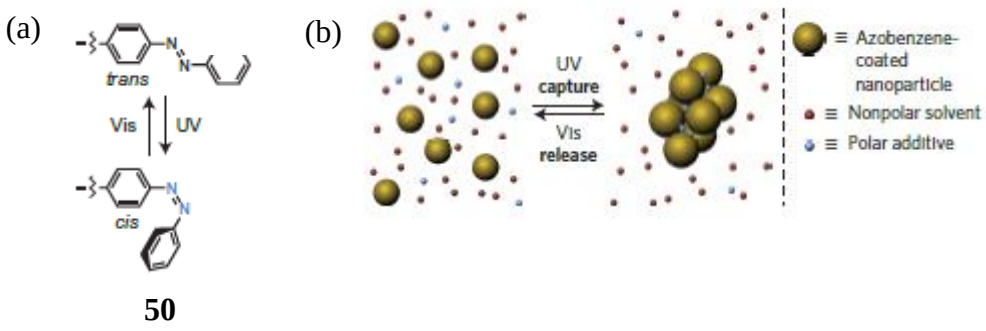

50

Figure 1.17: (a). *Cis-trans* isomerisation of azobenzene **50**. The azobenzene was attached to an appropriate functional group depending on the nanoparticle used. (b). Reversible trapping of polar molecules upon self-assembly induced by UV irradiation of photoresponsive nanoparticles.

The assembly was constructed using a variety of nanoparticle cores (gold, magnetite and silica) of different sizes functionalised with azobenzene, **50** (Figure 1.17a). The nanoparticles functionalised with the *trans*- form of **50** were stable in toluene. Upon irradiation with UV-Vis light however, the resulting *cis*- form resulted in aggregation of the nanoparticles (Figure 1.17b). This was attributed to two main factors; the polar nature of the *cis*- azobenzenes, leading to poor solvation by toluene[125] and attractive dipole-dipole interactions between *cis*-azobenzene mioieties on adjacent nanoparticles.[102] The assemblies disaggregated again upon irradiation with visible light. Cavities were formed when nanoparticles functionalised with the *cis*- azobenzenes aggregated, and these acted as a nanospace which could entrap polar molecules such as water and methanol. Back isomerisation of the azobenzenes to the *trans*- form generated an explosion as the interactions of the polar molecules with the hydrophobic *trans*- azobenzenes destabilised the assembly (Figure 1.18). Further investigations determined that the cavities could entrap aromatic compounds and hydrogen bond donors (e.g. alcohols, primary amines) but did not trap hydrogen bond acceptors (e.g. tertiary amines, ethers, ketones).

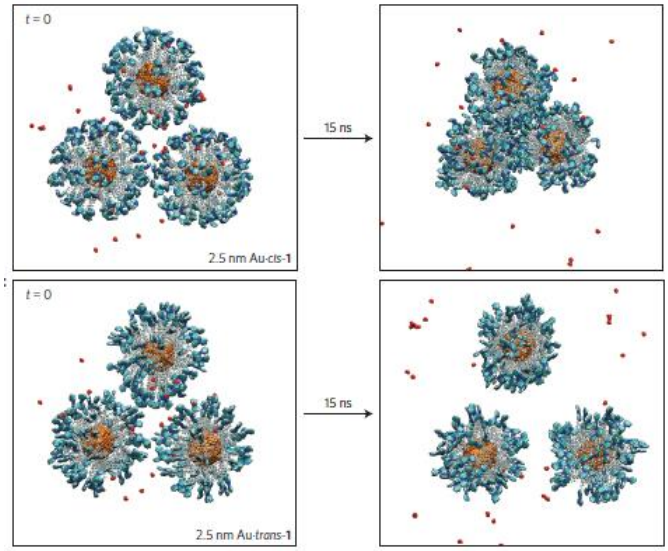

Figure 1.18: Atomistic simulations of gold nanoparticles functionalised with *cis*-**50** and *trans*-**50** in toluene saturated with water (red balls). Gold nanoparticle aggregation and trapping of water occurs only with *cis*-**50**.

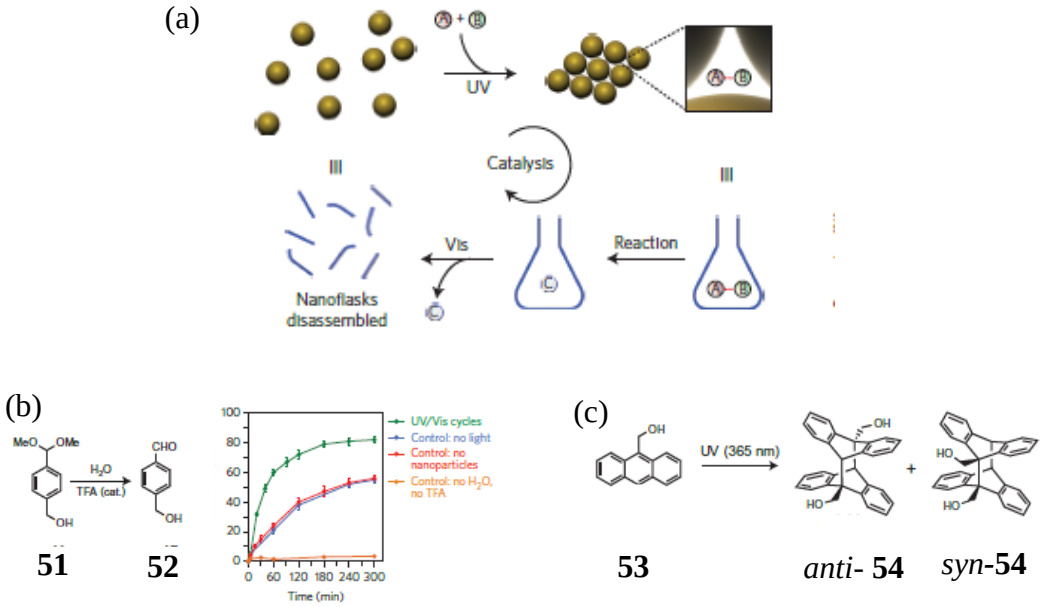

Figure 1.19: (a). Schematic representation of reversible formation of confined spaces and how they can be utilised to accelerate a chemical reaction. (b) Hydrolysis of acetal **51** to **52** accelerated in the cavities. (c) UV-Vis induced dimerisation of anthracene **53** to give **54**.[124]

The trapping of polar molecules could be utilised to promote a chemical reaction inside the cavities, the duration of which could be controlled simply by irradation with visible light to revert the *cis*-azobenzene to the *trans*-azobenzene. This would result in disaggregation of the assembly, and the consequent release of product (Figure 1.19a). The acid catalysed hydrolysis of acetal **51** to **52** as well as the dimerisation of anthracene **53** to **54** were found

to occur markedly faster in the presence of the *trans*- azobenzene-functionalised nanoparticles (Figure 1.19b). Not only were the so called "nanoflasks" capable of promoting a chemical reaction, but the different environment also altered the chemical reactivity. Indeed, the dimerization of **53** could be carried out in non-deoxygenated solvents since encapsulation rendered **53** inert to the outcompeting oxidative degradation to anthraquinone. Encapsulation also resulted in a preferential formation of the unstable *syn*-isomer of **54** which contrasts to the preferred formation of the *anti*-product when the reaction is carried out in the absence of nanoparticles. The advantage of this approach lies in its generality, as it can be applied to all systems where control of chemical reactivity is dependent on the dimensions and surface chemistry of the reaction vessel.[6]

1.3.3 Chemical-fuel controlled self-assembly processes

Biological systems however, use kinetically stable, high energy molecule as fuels to maintain an energy-consuming assembled state.[126] The fuel acts as the currency to keep the aggregate assembled, and without it the assembly decays.[127] Such chemically-driven dissipative self-assembly processes require a means by which to dissipate the energy and return the system to its initial basal state.

An extensively studied example of dissipative self-assembly in Nature is the formation and disassembly of actin filaments. Here, ATP is used as a chemical fuel to assemble actin filaments in a well-defined structure.[115] Polymerization of F-actin with ATP gives globular actin (G actin)-ATP as a complex, which subsequently undergoes a conformational change that causes the hydrolysis of ATP in ADP and inorganic phosphate P_i. The resulting complex is unstable and depolymerises spontaneously to G actin-ADP.[128] ADP is replaced with ATP and the cycle can be repeated once again.

Currently, there is a strong interest to implement the principle of dissipative self-assembly in synthetic systems for the design of materials which would be difficult to obtain by other means. These include transiently formed hydrogels, membranes with transient conductivity as well as vesicular nanoreactors.[129-131] These systems are making it possible to achieve innovative materials and processes, but in most of the systems developed there is a fundamental difference in the way the energy is dissipated when compared to natural systems. In natural dissipative self-assembled systems such as the polymerisation and depolymerisation of actin filaments, the fuel to waste conversion is mediated by the same

building block which was initially assembled. On the other hand, in most synthetic systems developed, the fuel to waste conversion necessitates an external agent, with no influence from the building block. This has been termed self-assembly under dissipative conditions.[118] Dissipative self-assembly will be treated in more depth in Chapter 2.

Using the principles of self-assembly under dissipative conditions enables self-assembled compartments to communicate with the outside environment and between themselves.[117] Indeed, recently, the transient formation of vesicles was demonstrated using the principles of self-assembly under dissipative conditions. This has been applied for the temporal control of a chemical reaction.[132] Below the *cac* (100 μM), the surfactant $C_{16}TACN{\bullet}Zn^{2+}$, **55**, was capable of forming vesicles with dimensions in the order of 50-70 nm in diameter upon addition of ATP as a chemical fuel. The aggregates consisted of a hydrophobic bilayer enclosing an inner aqueous phase. To establish an out-of-equilibrium system, the enzyme potato apyrase was included in the system. Hydrolysis of ATP by the apyrase *in-situ* removed the stabilisation factor and reverted the system back to the dissociated state since the waste products AMP and Pi were not capable of stabilising the aggregate. A new addition of ATP induced a second cycle of transient vesicle formation (Figure 1.20).

The vesicles could function as a chemical nanoreactor for the nucleophilic aromatic substitution reaction between 1-octanethiol, **56**, and NBD-Cl, **57**, to give **58**. This reaction did not spontaneously occur in the buffer or the free surfactant, but could proceed with yields of up to 20% in the presence of the ATP (the vesicles). It was rationalised that the localisation of the reactants inside the hydrophobic bilayer promotes the reaction. It was found that product formation was dependent on the lifetime of the vesicles. At a fixed concentration of ATP, increasing enzyme concentration led to a lower quantity of product. This proved to be the first example where the outcome of a chemical reaction was determined by the lifetime of the vesicle.

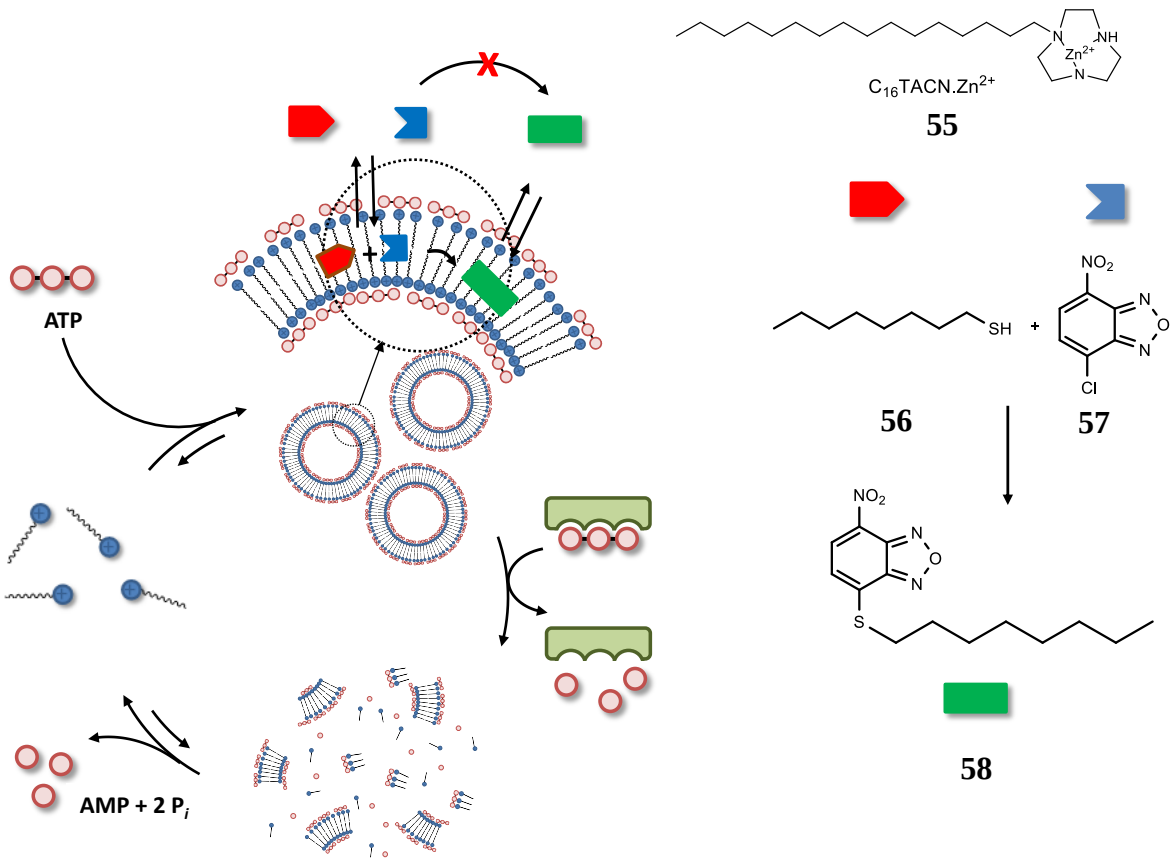

Figure 1.20 Schematic representation of the self-assembly of the surfactant C_{16}TACN•Zn^{2+}, **55** upon addition of ATP under dissipative conditions. The reaction between 1-octanethiol, **56** and NBD-Cl, **57** is also depicted. The reaction could only occur once the vesicles were present.

In summary, in far-from-equilibrium systems the functions arise from continuous transitioning between different structures and from the fact that an energy source is used. This contrasts the case of equilibrium and kinetically controlled systems, where the functions correspond to the stable state. Far-from-equilibrium, especially chemically driven dissipative self-assembly represents the realm which enables the richest harnessing of the system's potential.[108] Carrying out reactions in the assembled state ties reactivity to the lifetime of the assembly, and concedes complex control over the chemical reactivity.

Self-assembly is a fundamental process to achieve self-organisation and the generation of higher order matter.[133] As highlighted above, it is possible to tune the properties of self-assembly processes to achieve complicated regulation of chemical reactivity and autonomous behaviour. Intricate regulation of the self-assembly process allows the development of increasingly complex systems. As the complexity increases, the properties of the system become distinct and unpredictable from those of the individual components.

This provides for the possibility to observe emergent properties, properties which are not implicit in those of the individual constituents.[14,108]

1.4 Concept of the thesis

The examples illustrated above show that the importance of self-assembly goes beyond the formation of beautiful structures. It is possible to install a function to the self-assembly process by coupling it to processes one wishes to control, such as chemical reactions. Coupling self-assembly processes with chemical reactivity provides for the attainment of innovative control over chemical reactions which might be hard to achieve through other means. Self-assembly in this case assumes the role of a control element, and can, eventually, be incorporated into larger, networked systems providing direction to a sequence of chemical reactions. Compartmentalisation allows for the emergence of new functions and could even provide a means of connecting chemically incompatible reactions in a reaction network.[134] It might be envisaged that by further developments in the field, it could be possible to use self-assembly to design non-equilibrium "assembly lines" serving to channel and process matter in programmed manners, further contributing to novel emergent behaviour.[135] Different tasks might be programmed depending on the external controls provided, much like a coffee-machine which can be programmed to prepare an espresso, a cappuccino or a macchiato depending on which button one pushes. In other words, reactions within nanocontainers could be developed as miniature chemical factories, performing synthesis which are currently unattainable or which necessitise harsh environments.[117] Such nanoscale systems can be integrated to develop the next generation of smart and intelligent materials, with the potential of being interfaced with living systems, such as for example to be incorporated as components of biocompatible electronics or optofluidics.[136]

In this thesis, the aim is to develop self-assembling structures in which the lifetime of the self-assembly is dependent upon external means of control. Such self-assemblies are then utilised to exert control over chemical reactions in novel ways.

In Chapter 2, the dissipative self-assembly of vesicles is described.

In Chapter 3, this system is used to promote a hydrazone bond formation reaction. It is shown that the controlled formation of assemblies using chemical fuels can be used to control the selectivity in a minimal reaction network.

In Chapter 4, the ATP hydrolysis by potato apyrase, a mechanism which is used in reported dissipative self-assembled processes, is investigated by ^{31}P NMR spectroscopy. The capacity of nanoparticles passivated with a monolayer of C-9 thiols terminating with a 1,4,7-triazacyclononane•Zn^{2+} head group to enhance enzymatic ATP-cleavage is studied.

In Chapter 5, a different self-assembled system is developed using nanoparticles and β-cyclodextrin vesicles. Temporal control over the self-assembly is imparted by using chemical fuels and light as sources of energy. It is shown that the confined spaces arising from the aggregation process change the rate of a chemical reaction.

1.5 References

(1) Hong, Y. J.; Tantillo, D. J. *J. Am. Chem. Soc.* **2009**, *131*, 7999.

(2) Tripp, B. C.; Smith, K.; Ferry, J. G. *J. Biol. Chem.* **2001**, *276*, 48615.

(3) Forman, H. J.; Fridovich, I. *Arch. Biochem. Biophys.* **1973**, *158*, 396.

(4) Poole, L. B.; Karplus, P. A.; Claiborne, A. *Annu. Rev. Pharmacol. Toxicol.* **2004**, *44*, 325.

(5) Yasumoto, T.; Murata, M. *Chem. Rev.* **1993**, *93*, 1897.

(6) Hecht, S. *Nat. Nanotech.* **2015**, *11*, 6.

(7) Bruce Alberts, A. J., Julian Lewis, Martin Raff, Keith Roberts, Peter Walter *Molecular Biology of the Cell*; 5 ed.; Garland: New York, 2007.

(8) Karsenti, E. *Nat. Rev. Mol. Cell Biol.* **2008**, *9*, 255.

(9) Vriezema, D. M.; Comellas Aragonès, M.; Elemans, J. A. A. W.; Cornelissen, J. J. L. M.; Rowan, A. E.; Nolte, R. J. M. *Chem. Rev.* **2005**, *105*, 1445.

(10) Philp, D.; Stoddart, J. F. *Angew. Chem., Int. Ed.* **1996**, *35*, 1154.

(11) Lehn, J.-M. *Angew. Chem., Int. Ed.* **1990**, *29*, 1304.

(12) Whitesides, G. M.; Grzybowski, B. *Science* **2002**, *295*, 2418.

(13) Lehn, J.-M. *Eur. Rev.* **2009**, *17*, 263.

(14) Newth, D.; Finnigan, J. *Aust. J. Chem.* **2006**, *59*, 841.

(15) Grzybowski, B. A.; Wilmer, C. E.; Kim, J.; Browne, K. P.; Bishop, K. J. M. *Soft Matter* **2009**, *5*, 1110.

(16) Proulx-Curry, P. M.; Chasteen, N. D. *Coord. Chem. Rev.* **1995**, *144*, 347.

(17) Singer, S. J.; Nicolson, G. L. *Science* **1972**, *175*, 720.

(18) In *Integrated Molecular and Cellular Biophysics*; Raicu, V., Popescu, A., Eds.; Springer Netherlands: Dordrecht, 2008, p 73.

(19) Carl Ivar Branden, J. T. *Introduction to Protein Structure*; 2nd Edition ed.; Garland Science, 1999

(20) Whitesides, G.; Mathias, J.; Seto, C. *Science* **1991**, *254*, 1312.

(21) Whitesides, G. M.; Simanek, E. E.; Mathias, J. P.; Seto, C. T.; Chin, D.; Mammen, M.; Gordon, D. M. *Acc. Chem. Res.* **1995**, *28*, 37.

(22) Fujita, M.; Oguro, D.; Miyazawa, M.; Oka, H.; Yamaguchi, K.; Ogura, K. *Nature* **1995**, *378*, 469.

(23) Marquis-Rigault, A.; Dupont-Gervais, A.; Baxter, P. N. W.; Van Dorsselaer, A.; Lehn, J.-M. *Inorg. Chem.* **1996**, *35*, 2307.

(24) Fujita, D.; Suzuki, K.; Sato, S.; Yagi-Utsumi, M.; Yamaguchi, Y.; Mizuno, N.; Kumasaka, T.; Takata, M.; Noda, M.; Uchiyama, S.; Kato, K.; Fujita, M. *Nat. Commun.* **2012**, *3*, 1093.

(25) Garenne, D.; Beven, L.; Navailles, L.; Nallet, F.; Dufourc, E. J.; Douliez, J. P. *Angew. Chem., Int. Ed.* **2016**, *55*, 13475.

(26) Fujita, M. *Chem. Soc. Rev.* **1998**, *27*, 417.

(27) Fujita, M.; Sasaki, O.; Mitsuhashi, T.; Fujita, T.; Yazaki, J.; Yamaguchi, K.; Ogura, K. *Chem. Commun.* **1996**, 1535.

(28) Whiteford, J. A.; Lu, C. V.; Stang, P. J. *J. Am. Chem. Soc.* **1997**, *119*, 2524.

(29) Baxter, P. N. W.; Lehn, J.-M.; Fischer, J.; Youinou, M.-T. *Angew. Chem., Int. Ed.* **1994**, *33*, 2284.

(30) Hanan, G. S.; Arana, C. R.; Lehn, J.-M.; Baum, G.; Fenske, D. *Chem.–Eur. J.* **1996**, *2*, 1292.

(31) Baxter, P. N. W.; Hanan, G. S.; Lehn, J.-M. *Chem. Commun.* **1996**, 2019.

(32) Beissel, T.; Powers, R. E.; Raymond, K. N. *Angew. Chem., Int. Ed.* **1996**, *35*, 1084.
(33) Funeriu, D. P.; Lehn, J.-M.; Baum, G.; Fenske, D. *Chem.–Eur. J.* **1997**, *3*, 99.
(34) Amabilino, D. B.; Ashton, P. R.; Reder, A. S.; Spencer, N.; Stoddart, J. F. *Angew. Chem., Int. Ed.* **1994**, *33*, 433.
(35) Cantrill, S. J.; Rowan, S. J.; Stoddart, J. F. *Org. Lett.* **1999**, *1*, 1363.
(36) Rowan, S. J.; Stoddart, J. F. *Org. Lett.* **1999**, *1*, 1913.
(37) Chichak, K. S.; Cantrill, S. J.; Pease, A. R.; Chiu, S.-H.; Cave, G. W.; Atwood, J. L.; Stoddart, J. F. *Science* **2004**, *304*, 1308.
(38) Ashton, P. R.; Collins, A. N.; Fyfe, M. C. T.; Glink, P. T.; Menzer, S.; Stoddart, J. F.; Williams, D. J. *Angew. Chem., Int. Ed.* **1997**, *36*, 59.
(39) *Molecular Switches*; Second Edition ed.; Wiley-VCH Verlag GmbH & Co. KGaA.
(40) Harris, J. D.; Moran, M. J.; Aprahamian, I. *Proc. Natl. Acad. Sci.* **2018**.
(41) Roke, D.; Wezenberg, S. J.; Feringa, B. L. *Proc. Natl. Acad. Sci.* **2018**.
(42) Pezzato, C.; Cheng, C.; Stoddart, J. F.; Astumian, R. D. *Chem. Soc. Rev.* **2017**.
(43) Baroncini, M.; Casimiro, L.; de Vet, C.; Groppi, J.; Silvi, S.; Credi, A. *ChemistryOpen* **2018**, *7*, 169.
(44) Rybtchinski, B. *ACS Nano* **2011**, *5*, 6791.
(45) Bachmann, P. A.; Luisi, P. L.; Lang, J. *Nature* **1992**, *357*, 57.
(46) Lucas, L. N.; van Esch, J.; Kellogg, R. M.; Feringa, B. L. *Chem. Commun.* **2001**, 759.
(47) Wilson, M. R.; Solà, J.; Carlone, A.; Goldup, S. M.; Lebrasseur, N.; Leigh, D. A. *Nature* **2016**, *534*, 235.
(48) Badjić, J. D.; Balzani, V.; Credi, A.; Silvi, S.; Stoddart, J. F. *Science* **2004**, *303*, 1845.
(49) Moulin, E.; Giuseppone, N. *Supramolecular Chemistry: From Molecules to Nanomaterials* **2012**.
(50) Hof, F.; Rebek, J. *Proc. Natl. Acad. Sci.* **2002**, *99*, 4775.
(51) Hof, F.; Craig, S. L.; Nuckolls, C.; Rebek, J. J. *Angew. Chem., Int. Ed.* **2002**, *41*, 1488.
(52) Kim, S. P.; Leach, A. G.; Houk, K. N. *J. Org. Chem.* **2002**, *67*, 4250.
(53) Schneider, H.-J.; Sangwan, N. K. *J. Chem. Soc., Chem. Commun.* **1986**, 1787.
(54) Yoshizawa, M.; Tamura, M.; Fujita, M. *Science* **2006**, *312*, 251.
(55) Wang, L.; Vysotsky, M. O.; Bogdan, A.; Bolte, M.; Böhmer, V. *Science* **2004**, *304*, 1312.
(56) Kang, J.; Rebek Jr, J. *Nature* **1997**, *385*, 50.
(57) Kang, J.; Santamaría, J.; Hilmersson, G.; Rebek, J. *J. Am. Chem. Soc.* **1998**, *120*, 7389.
(58) Hu Yi-Zhen, T. S., Shinkai Seiji, Oishi Shigero, Durr Heinz, Hamachi Itaru *Chem. Lett.* **2000**, *22*.
(59) Smulders, M. M. J.; Nitschke, J. R. *Chem. Sci.* **2012**, *3*, 785.
(60) Scrimin, P. *Supramolecular Control of Structure and Reactivity* **1996**, 101.
(61) Bunton, C. A.; Savelli, G. *Adv. Phys. Org. Chem.* **1986**, *22*, 213.
(62) Dwars, T.; Paetzold, E.; Oehme, G. *Angew. Chem., Int. Ed.* **2005**, *44*, 7174.

(63) Kunitake, T.; Shinkai, S. *Adv. Phys. Org. Chem.* **1980**, *17*, 435.
(64) Cordes, E. *Pure Appl. Chem.* **1978**, *50*, 617.
(65) Menger, F. M.; Portnoy, C. E. *J. Am. Chem. Soc.* **1967**, *89*, 4698.
(66) Ta§cioğlu, S. *Tetrahedron* **1996**, *52*, 11113.
(67) Lindström, U. M. *Chem. Rev.* **2002**, *102*, 2751.
(68) Bachmann, P. A.; Walde, P.; Luisi, P. L.; Lang, J. *J. Am. Chem. Soc.* **1991**, *113*, 8204.
(69) Sadownik, J. W.; Mattia, E.; Nowak, P.; Otto, S. *Nat. Chem.* **2016**.
(70) Moulin, E.; Giuseppone, N. In *Constitutional Dynamic Chemistry*; Springer: 2011, p 87.
(71) Paul, N.; Joyce, G. F. *Curr. Opin. Chem. Biol.* **2004**, *8*, 634.
(72) Morrow, S. M.; Bissette, A. J.; Fletcher, S. P. *Tetrahedron* **2017**, *73*, 5005.
(73) Tjivikua, T.; Ballester, P.; Rebek, J. *J. Am. Chem. Soc.* **1990**, *112*, 1249.
(74) Duim, H.; Otto, S. *Beilstein J. Org. Chem.* **2017**, *13*, 1189.
(75) Szostak, J. W.; Bartel, D. P.; Luisi, P. L. *Nature* **2001**, *409*, 387.
(76) Nguyen, R.; Allouche, L.; Buhler, E.; Giuseppone, N. *Angew. Chem., Int. Ed.* **2009**, *48*, 1093.
(77) Walde, P.; Umakoshi, H.; Stano, P.; Mavelli, F. *Chem. Commun.* **2014**, *50*, 10177.
(78) Kunitake, T.; Okahata, Y.; Ando, R.; Shinkai, S.; Hirakawa, S. *J. Am. Chem. Soc.* **1980**, *102*, 7877.
(79) Kunitake, T.; Shinkai, S. In *Adv. Phys. Org. Chem.*; Gold, V., Bethell, D., Eds.; Academic Press: 1980; Vol. 17, p 435.
(80) Bunton, C. A.; Minch, M. J. *Tetrahedron Lett.* **1970**, *11*, 3881.
(81) Pérez-Juste, J.; Hollfelder, F.; Kirby, A. J.; Engberts, J. B. F. N. *Org. Lett.* **2000**, *2*, 127.
(82) Scrimin, P.; Tecilla, P.; Tonellato, U. *J. Am. Chem. Soc.* **1992**, *114*, 5086.
(83) Cleij, M. C.; Scrimin, P.; Tecilla, P.; Tonellato, U. *Langmuir* **1996**, *12*, 2956.
(84) Mancin, F.; Scrimin, P.; Tecilla, P.; Tonellato, U. *Coord. Chem. Rev.* **2009**, *253*, 2150.
(85) Kikuchi, J.-i.; Zhang, Z.-Y.; Murakami, Y. *J. Am. Chem. Soc.* **1995**, *117*, 5383.
(86) Blackmond, D. G. *Proc. Natl. Acad. Sci. U. S. A.* **2004**, *101*, 5732.
(87) Rispens, T.; Engberts, J. B. F. N. *Org. Lett.* **2001**, *3*, 941.
(88) Yukito, M.; Yoshio, H.; Koichiro, N.; Jun-ichi, K. *Chem. Lett.* **1990**, *19*, 1765.
(89) Yukito, M.; Jun-ichi, K.; Yoshio, H.; Koichiro, N.; Tomoyuki, K.; Hidenori, K. *Bull. Chem. Soc. Jpn.* **1990**, *63*, 2339.
(90) Discher, D. E.; Eisenberg, A. *Science* **2002**, *297*, 967.
(91) Kästle, G.; Boyen, H.-G.; Weigl, F.; Lengl, G.; Herzog, T.; Ziemann, P.; Riethmüller, S.; Mayer, O.; Hartmann, C.; Spatz, J. P.; Möller, M.; Ozawa, M.; Banhart, F.; Garnier, M. G.; Oelhafen, P. *Adv. Funct. Mater.* **2003**, *13*, 853.
(92) Croy, S. R.; Kwon, G. S. *Current Pharmaceutical Design* **2006**, *12*, 4669.
(93) Pulsipher, K. W.; Dmochowski, I. J. *Isr. J. Chem.* **2016**, *56*, 660.
(94) Niemeyer, C. M. *Angew. Chem., Int. Ed.* **2001**, *40*, 4128.
(95) Comellas-Aragonès, M.; Engelkamp, H.; Claessen, V. I.; Sommerdijk, N. A. J. M.; Rowan, A. E.; Christianen, P. C. M.; Maan, J. C.; Verduin, B. J. M.; Cornelissen, J. J. L. M.; Nolte, R. J. M. *Nat. Nanotech.* **2007**, *2*, 635.

(96) de la Escosura, A.; Nolte, R. J. M.; Cornelissen, J. J. L. M. *J. Mater. Chem.* **2009**, *19*, 2274.
(97) Saeed, A. O.; Dey, S.; Howdle, S. M.; Thurecht, K. J.; Alexander, C. *J. Mater. Chem.* **2009**, *19*, 4529.
(98) Maity, B.; Fujita, K.; Ueno, T. *Curr. Opin. Chem. Biol.* **2015**, *25*, 88.
(99) Lutkenhaus, J. *Annu. Rev. Biochem.* **2007**, *76*, 539.
(100) Göstl, R.; Hecht, S. *Angew. Chem., Int. Ed.* **2014**, *53*, 8784.
(101) Zwaag, D. v. d.; Meijer, E. W. *Science* **2015**, *349*, 1056.
(102) Klajn, R.; Bishop, K. J. M.; Grzybowski, B. A. *Proc. Natl. Acad. Sci.* **2007**, *104*, 10305.
(103) Astumian, R. D. *Faraday Discuss.* **2016**, *195*, 583.
(104) Chabre, M.; Deterre, P. In *EJB Reviews 1989*; Springer Berlin Heidelberg: Berlin, Heidelberg, 1989, p 1.
(105) Manea, F.; Houillon, F. B.; Pasquato, L.; Scrimin, P. *Angew. Chem., Int. Ed.* **2004**, *43*, 6165.
(106) Zaupa, G.; Mora, C.; Bonomi, R.; Prins, L. J.; Scrimin, P. *Chem.–Eur. J.* **2011**, *17*, 4879.
(107) Neri, S.; Garcia Martin, S.; Pezzato, C.; Prins, L. J. *J. Am. Chem. Soc.* **2017**, *139*, 1794.
(108) Mattia, E.; Otto, S. *Nat. Nanotech.* **2015**, *10*, 111.
(109) Kushner, D. J. *Bacteriological Reviews* **1969**, *33*, 302.
(110) Maginn, S. J. *J. Appl. Crystallogr.* **1991**, *24*, 265.
(111) Rose, G. D. *Biophys. J.* **1980**, *32*, 419.
(112) Fialkowski, M.; Bishop, K. J. M.; Klajn, R.; Smoukov, S. K.; Campbell, C. J.; Grzybowski, B. A. *J. Phys. Chem. B* **2006**, *110*, 2482.
(113) England, J. L. *Nat. Nanotech.* **2015**, *10*, 919.
(114) Perelson, A. S. *Q Rev Biol* **1978**, *53*, 362.
(115) Desai, A.; Mitchison, T. J. *Annual review of cell and developmental biology* **1997**, *13*, 83.
(116) Saibil, H. *Nat. Rev. Mol. Cell Biol.* **2013**, *14*, 630.
(117) Grzybowski, B. A.; Huck, W. T. *Nat. Nanotech.* **2016**, *11*, 585.
(118) Ragazzon, G.; Prins, L. J. *Nat. Nanotech.* **2018**.
(119) Heinen, L.; Walther, A. *Soft Matter* **2015**, *11*, 7857.
(120) Timonen, J. V. I.; Latikka, M.; Leibler, L.; Ras, R. H. A.; Ikkala, O. *Science* **2013**, *341*, 253.
(121) Grzybowski, B. A.; Stone, H. A.; Whitesides, G. M. *Nature* **2000**, *405*, 1033.
(122) Klajn, R.; Wesson, P. J.; Bishop, K. J. M.; Grzybowski, B. A. *Angew. Chem., Int. Ed.* **2009**, *48*, 7035.
(123) Kathan, M.; Hecht, S. *Chem. Soc. Rev.* **2017**, *46*, 5536.
(124) Zhao, H.; Sen, S.; Udayabhaskararao, T.; Sawczyk, M.; Kučanda, K.; Manna, D.; Kundu, P. K.; Lee, J.-W.; Král, P.; Klajn, R. *Nat. Nanotech.* **2015**, *11*, 82.
(125) Manna, A.; Chen, P.-L.; Akiyama, H.; Wei, T.-X.; Tamada, K.; Knoll, W. *Chem. Mat.* **2003**, *15*, 20.
(126) Walsh, C. T.; Tu, B. P.; Tang, Y. *Chem. Rev.* **2018**, *118*, 1460.
(127) Mishra, A.; Korlepara, D. B.; Kumar, M.; Jain, A.; Jonnalagadda, N.; Bejagam, K. K.; Balasubramanian, S.; George, S. J. *Nat. Commun.* **2018**, *9*, 1295.
(128) Pfaendtner, J.; Lyman, E.; Pollard, T. D.; Voth, G. A. *J. Mol. Biol.* **2010**, *396*, 252.

(129) della Sala, F.; Neri, S.; Maiti, S.; Chen, J. L.; Prins, L. J. *Curr. Opin. Biotechnol.* **2017**, *46*, 27.

(130) De, S.; Klajn, R. *Adv. Mater.* **2018**, *0*, 1706750.

(131) van Rossum, S. A. P.; Tena-Solsona, M.; van Esch, J. H.; Eelkema, R.; Boekhoven, J. *Chem. Soc. Rev.* **2017**.

(132) Maiti, S.; Fortunati, I.; Ferrante, C.; Scrimin, P.; Prins, L. J. *Nat. Chem.* **2016**.

(133) Lehn, J.-M. *Chem. Soc. Rev.* **2007**, *36*, 151.

(134) Grzybowski, B. A.; Fitzner, K.; Paczesny, J.; Granick, S. *Chem. Soc. Rev.* **2017**.

(135) Nitschke, J. R. *Nature* **2009**, *462*, 736.

(136) Jeong, J.-W.; McCall, Jordan G.; Shin, G.; Zhang, Y.; Al-Hasani, R.; Kim, M.; Li, S.; Sim, Joo Y.; Jang, K.-I.; Shi, Y.; Hong, Daniel Y.; Liu, Y.; Schmitz, Gavin P.; Xia, L.; He, Z.; Gamble, P.; Ray, Wilson Z.; Huang, Y.; Bruchas, Michael R.; Rogers, John A. *Cell* **2015**, *162*, 662.

Chapter 2

Vesicular Nanoreactors Based on Metallosurfactants for Hydrazone Bond Formation Reactions

The cell constitutes the basic unit of life, a spatially enclosed self-generated and self-maintained complex system.[1] It is a central hub of activity, a complex nanofactory capable of performing a myriad of functions at the nano- and microscales through molecular interactions and chemical reactions.[2] Look for example at the delicate work of the ribosome in protein synthesis or the intricate mechanism by which actin and myosin trigger muscular contraction, or the way movement is induced by mictubule formation and destruction. The viral structure compels marvel at its simplicity while the cellular membrane impels awe at its complexity and the variety of functions it can execute. Indeed the cell has proved to be the ultimate source of inspiration for chemists. Supramolecular chemistry has adopted a "bottom-up" approach towards self-assembling nanomaterials, providing material which can be applied in fields as diverse as diagnosis and catalysis and which is propelling advances in nanotechnology and materials chemistry.[3]

A distinguishing and ubiquitous feature of the way Nature works is the requirement for energy in order to maintain a functional assembly. Nature uses dissipative self-assembly as a self-regulating feature in order to control the time over which a particular function occurs. Dissipative self-assembled structures are metastable, far-from-equilibrium, steady-state structures which require continual input of energy due to an inherent urge to dissipate energy to the environment in order to restore a thermodynamic minimum.[4] This, together with precise control over the timing of events, allows natural systems to communicate, coordinate, synchronise and dephase as required.[5]

A most impressive example of dissipative self-assembly in Nature is the cytoskeleton, a network of dynamic structures which is involved in sorting out chromosomes during the process of cell division and in the provision of tracks for the transport of large cellular components. This involves three main out of equilibrium supramolecular assemblies,

namely microtubules, actin filaments and intermediate filaments, which are in a process of continual polymerisation and depolymerisation (Figure 2.1). The building block for microtubule formation is α/β-tubulin, which polymerises upon binding to GTP in an energy-consuming step. The energy uptake destabilises the GTP-tubulin building block, and these become metastable, spontaneously hydrolysing into GDP-tubulin in an energy-dissipating step. This puts the dimer in a high-energy state, as the stabilizing factor –GTP- is no longer present. The polymeric structure is maintained as long as terminating GTP-containing dimers are present. Hydrolysis of GTP in the caps leads to a catastrophic collapse of the microtubules.[6] Thus, energy dissipation results in dynamic instability. A distinguishing feature of this system is the fact that the structures are dependent upon the presence of the chemical fuel and once all the GTP is consumed, the system undergoes total decay.

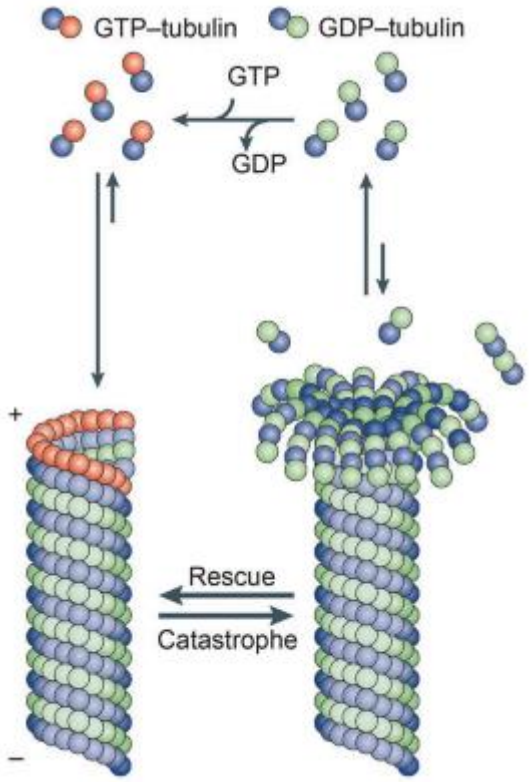

Figure 2.1: Schematic representation of microtubule self-assembly and dynamics.[6]

The formation and destruction of actin filaments in the cytoskeleton follows a similar pattern using ATP as the chemical fuel. In this case the polymerisation and depolymerisation steps are slower, since their use is different. Polymerisation of actin filaments provides steady unidirectional growth allowing deformation in the cell membrane. They are involved, for example, in the extrusion of filopodia to enable the cell to crawl and spread. They are also involved in mitotic cell division. In this case, dissipative self-assembly allows complex functions such as quick spatial search and autonomous reconfiguration.[6,7] It is interesting to note that the cell controls the concentration of fuel and this ultimately determines the function of the assembly.[8] By attempting to understand the principles of dissipative self-assembly, synthetic chemists can start to achieve highly complex, emergent functions with adaptive and regenerative properties.[9]

In order to instill a time domain to self-assembly, two antagonistic triggers are required: a positive stimulus needs to activate the formation of the self-assembly, while a delayed negative stimulus deactivates and disassembles the structure. For autonomous behaviour, the activation and deactivation steps need to be decoupled so that they take independent or interdependent pathways.[5] The energy uptake step needs to be faster than than the dissipation step. The duration of the energy supply determines the lifetime of the transient structure.[5] Synthetic systems using the principles of dissipative self-assembly utilise a number of external energy sources, including light[10] and electromagnetic fields[11] but chemically-fuelled dissipative self-assembly[12] enables a higher level of autonomy and brings the systems closer to natural dissipative systems.

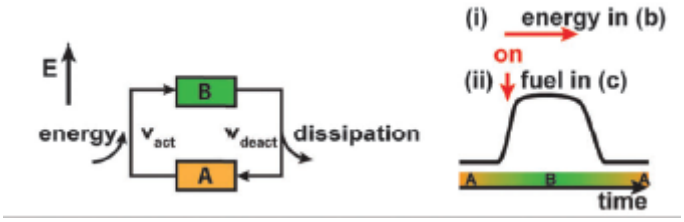

Figure 2.2: Transient self-assembly via energy dissipation requires faster energy uptake than dissipation. The lifetime of the self-assembly is dependent upon the time the energy is supplied (i) or the amount of chemical fuel (ii) as well as the rate of dissipation.[5]

The pioneers in the development of synthetic self-assembled structures were the group of Jan H. van Esch, who realised the potential of developing an out-of-equilibrium system using the pH responsive hydrogelator dibenzoyl-L-cysteine (DBC, **1**) (Figure 2.3).[13] Electrostatic repulsion between the carboxylate groups prevents the gelation of **1** above its pK_a. However, below the pK_a, the carboxylic acid groups are protonated and the neutralised structure is capable of assembling into long, hydrogen bonded fibers. The hydrogelator **1** could be esterified with methyl iodide (the chemical fuel) to form an ester, **2**. This could form a gel at all pHs. The diester spontaneously hydrolysed, dissipating the energy and reverting back to **1**. The cycle could be repeated until all the fuel was consumed. The fact that the rate of formation of the gel was higher than the rate of ester hydrolysis satisfied one precondition for the design of dissipative self-assembled systems. This was of critical importance for the assembly process. It is important to realise that in this example, the properties of the system are determined by the kinetics of the reaction and on the fuel levels. This is different from traditional chemistry, where the properties and functions of a system are dependant on the thermodynamics.[14]

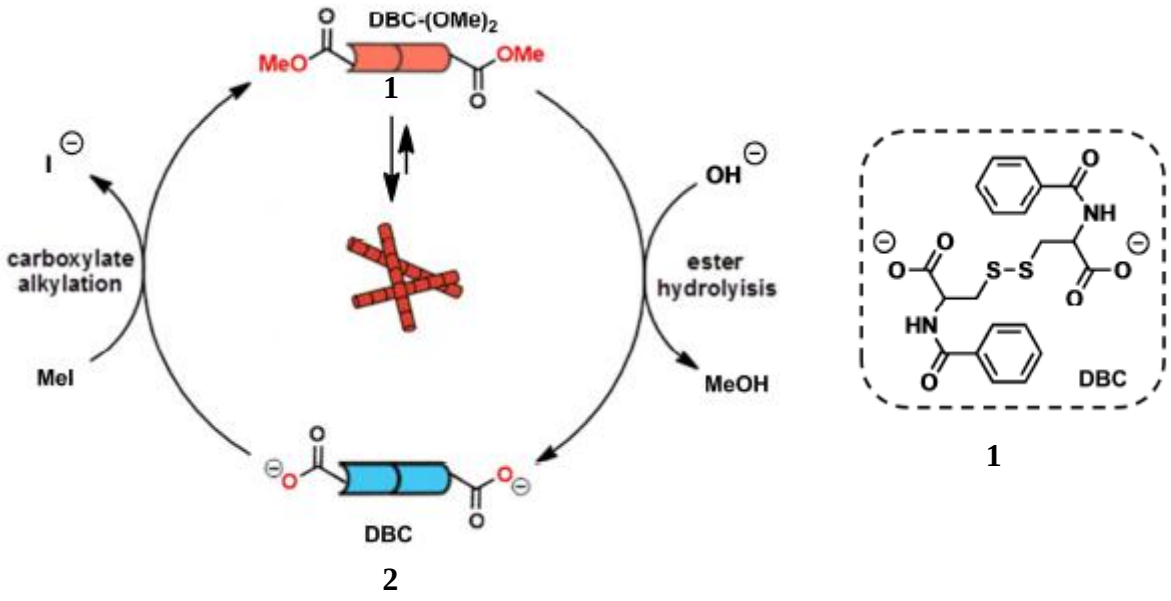

Figure 2.3: Reaction cycle in a dissipative self-assembled system. DBC, **1** reacts with MeI (fuel) to give the dieste (OMe)$_2$, **2**. This spontaneously hydrolyses to give the free dicarboxylate, **1**. The cycle can be repeated upon fresh a of chemical fuel.

This contribution represented a milestone in supramolecular chemistry, enabling chemists to step into new territory where the composition of self-assembly is determined by the capability to populate high energy states.[15] The beauty of this system is that it is also intrinsically dissipative, that is the assembled state plays a key role in the dissipation of energy. This makes it analogous to what occurs in natural systems such as in microtubule formation. Since then, a number of systems have been developed using the principles of dissipative self-assembly.[12,16] In most of the reported examples, however, an external additive is added in order to dissipate the energy. This is a point of divergence from natural, inherently dissipating system and such assemblies have been termed self-assembly under dissipative conditions, in order to provide a point of distinction.[15]

Self-assembly under dissipative conditions can be illustrated by the ATP-fueled supramolecular polymerisation of a phosphate-receptor functionalised monomer, **3** (Figure 2.4).[8] The monomer, a derivative of π-conjugated oligo(*p*-phenylenevinylene) functionalised with a dipicolylethylenediamine-zinc (DPA-Zn) complex (a phosphate acceptor) on either ends does not spontaneously self-assemble (i). Allosteric binding of ATP converts the dormant state into an active form capable of self-assembly (ii). The initial stacking is achiral (iii), but beyond a critical stack length, the assembly acquires left-handed helicity (iv). This cooperative polymerisation was selective to ATP. Other phosphates were unable to induce the same effect. The stacks acted as seeds on which further polymerisation could occur upon re-addition of ATP and the monomer (v). Transiency was introduced by incorporating the enzyme potato apyrase in the system. The ATP-hydrolysing enzyme degraded the ATP and destabilised the assembly (vi), resulting in a return to the inital monomeric unit (i). The behaviour was reminiscent of the growth characteristics observed in microtubules, but an external enzyme was required in order to induce ATP hydrolysis.

In such cases, the properties of the assembly depend upon the availability of the fuel to maintain a high energy state. Systems developed using dissipative self-assembly as a principle[17] have resulted in the transient formation of gels,[18] molecular cages,[19] vesicles[20] and even transient signal generation[21] and catalysis.[22]

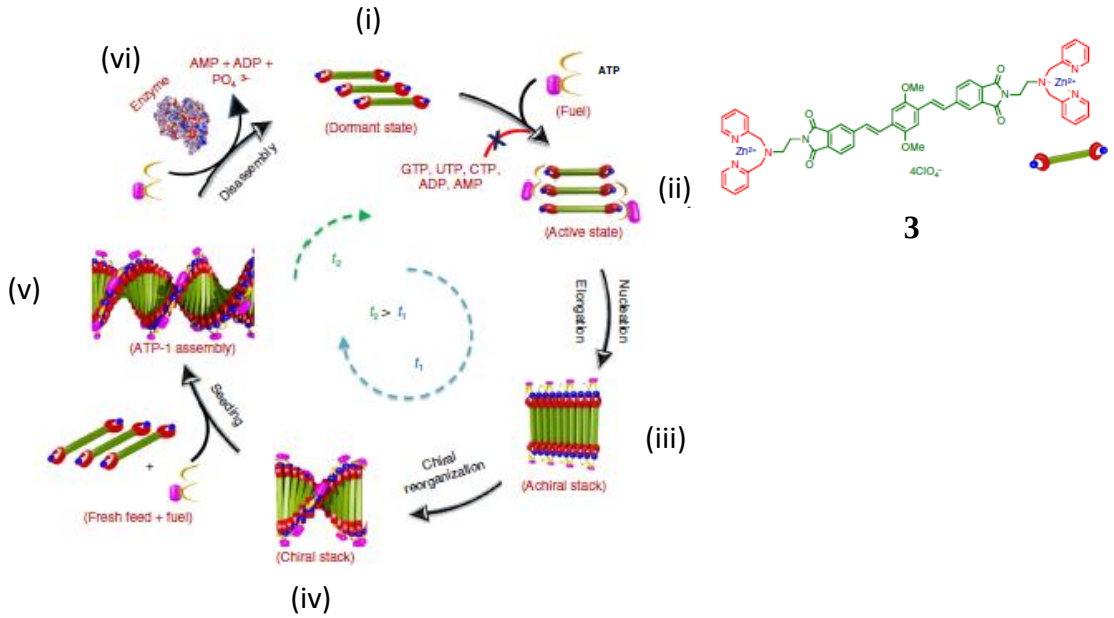

Figure 2.4: Schematic representation of the ATP-driven assembly. Addition of ATP converts the dormant monomer (i) into the active one (ii) capable of polymerisation. The stack was initially achiral (iii) but upon further elongation it re-organised itself into a chiral, left-handed polymer (iv). Further seeding resulted in elongation of the stack (v). ATP hydrolysis induced by the enzyme potato apyrase disassembled the polymer (vi), resorting back to the dormant monomer (i), ready to be re-assembled.

In dissipative self-assembled systems, the function associated with the system is temporally regulated by controlling the assembled state.[5] In Chapter 1, vesicles which could only self-assemble upon addition of ATP to the amphiphilic C_{16}TACN•Zn^{2+}, **4** were presented (Scheme 2.1a).[23] In this example, dissipative self-assembly was used to modulate the reactivity of the nucleophilic aromatic substitution reaction between 1-octanethiol, **5** and NBD-Cl, **6** to give the hydrazone **7**. This proved to be the first example where the outcome of a chemical reaction was determined by the lifetime of the vesicle. Such a system offers huge potential for the development of responsive and adaptive systems,[24] and this provided motivation to further expand this work.

In this Chapter we develop a nanoreactor suitable for the promotion and regulation of an imine/hydrazone bond-formation reaction. We initially attempt to expand the scope of the transient C_{16}TACN•Zn^{2+} nanoreactors for imine/hydrazone bond-formation reaction. We then develop and study another self-assembling system operating under dissipative conditions based on the surfactant C_{12}TACN•Zn^{2+}. This system is better suited to study the characteristics of the systems chosen.

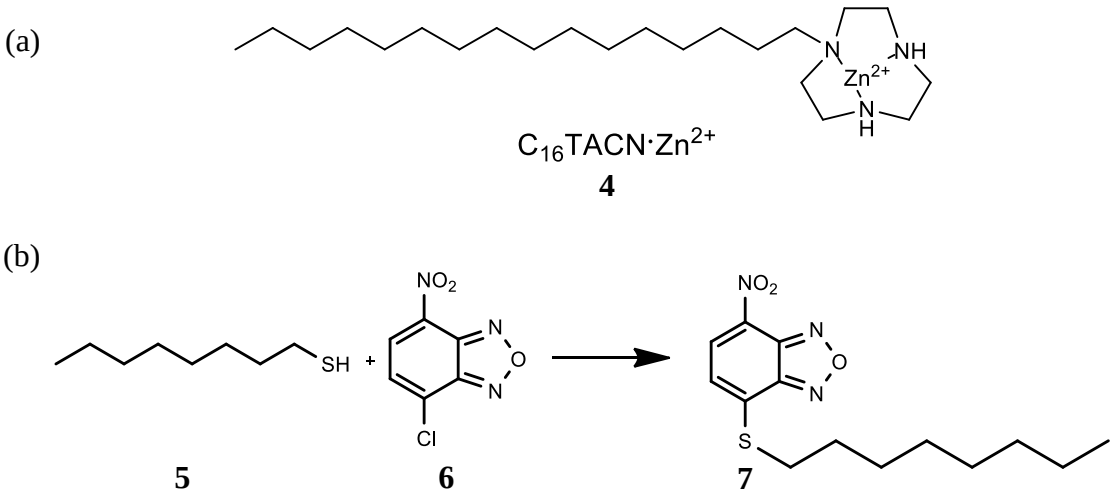

Scheme 2.1: (a). Structure of $C_{16}TACN•Zn^{2+}$, **4** used as the building block for the assembly of transient vesicles with ATP. (b). Reaction scheme showing the reaction between octanethiol, **5**, and NBD-Cl, **6**, to form hydrazone **7**. The reaction was promoted by vesicles formed from **4** in the presence of ATP as a chemical fuel.

2.1 Exploring the $C_{16}TACN•Zn^{2+}$ system as a nanoreactor for imine/hydrazone formation

The equilibrium between imine **10** and its precursors amine, **8** and aldehyde, **9** lies strongly to the side of the starting materials in aqueous conditions (Scheme 2.2). The equilibrium can be influenced by a number of factors, including pH, temperature, concentration and solvent.[25] Vesicles provide a hydrophobic environment which precludes water. Therefore it was hypothesized that inside the vesicles the environment would be more conducive to reaction, permitting the observation of some imine. Initial tests were carried out using the system assembled from the monomeric $C_{16}TACN•Zn^{2+}$, **4**, in the presence of ATP, as described in Maiti *et al.*[23] The surfactant **4** was synthesized and characterised using the protocol reported in literature.[23]

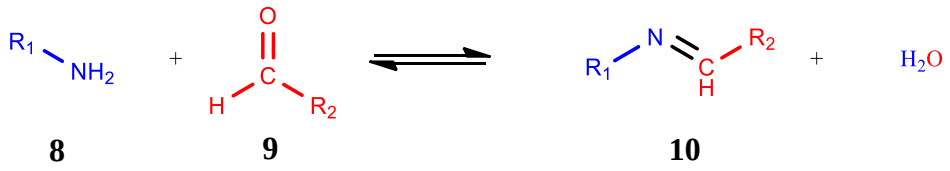

Scheme 2.2: General scheme for the imine bond formation reaction between an amine (**8**) and an aldehyde (**9**) resulting in the formation of an imine (**10**) and water. A hydrazone bond formation reaction is analogous to imine bond formation but involves the reaction of a hydrazine instead of an amine and results in the formation of a hydrazone.[25]

2.1.1 ATP-templated $C_{16}TACN \bullet Zn^{2+}$-based vesicles as a chemical nanoreactor for imines/hydrazones

Initially an imine equilibrium reaction between 4-carboxybenzaldehdye, **11**, and *p*-toluidine, **12**, was chosen for investigation, since the reagents and the product, **13**, could be distinguished by UV-Vis spectroscopy (Scheme 2.3). As expected the imine was unstable in aqueous buffer (HEPES (5 mM), pH 7.0), and the imine peak at 324 nm was observed to decrease over a period of five minutes (Figure 2.5). However, as the concentration of the surfactant **4** increased, the rate of degradation decreased sharply up to the *cac* of the surfactant (100 µM). At concentrations higher than the *cac*, the rate of hydrolysis remained relatively constant (Figure 2.6). However, at all surfactant concentrations, a complete disappearance of the imine was observed, indicating that the equilibrium composition of the reaction was not affected.

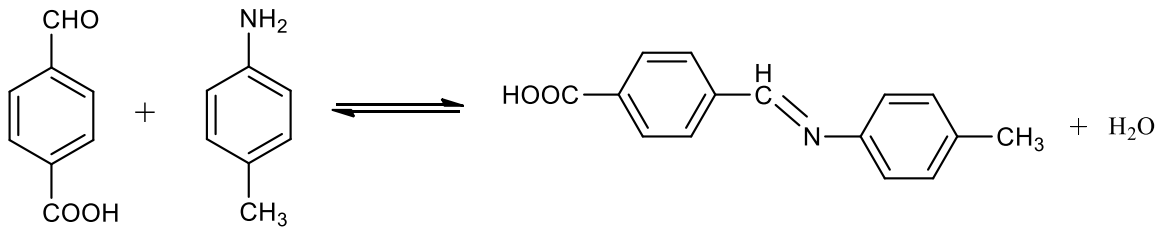

11 **12** **13**

λ_{max} = 259 nm λ_{max} = 240 nm λ_{max} = 342 nm

Scheme 2.3: Scheme for the reaction between 4-carboxybenzaldehyde, **11**, and *p*-toluidine, **12**, to form imine **13**. The absorption at λ_{max} of each of the components in methanol is also included.

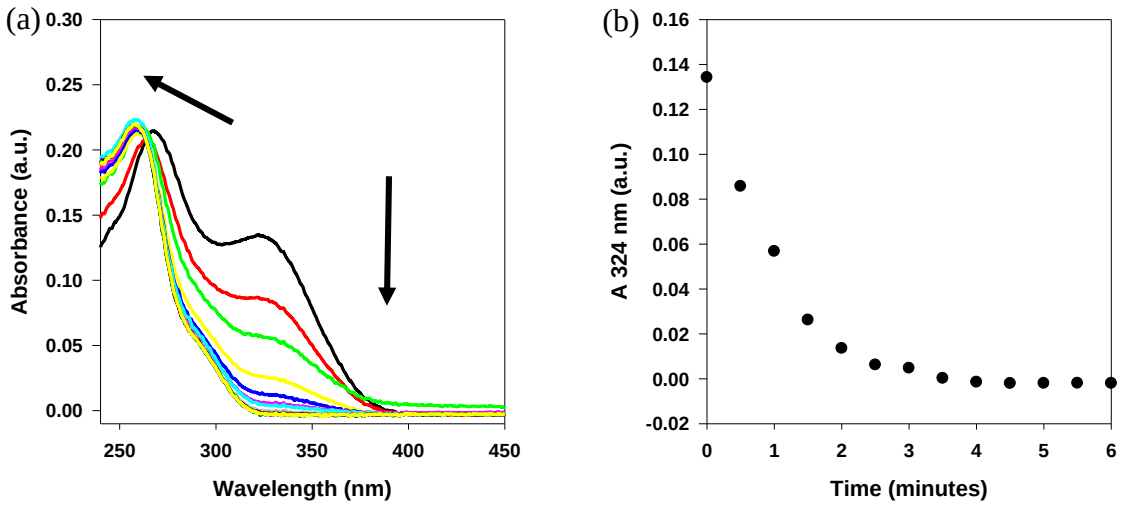

Figure 2.5: (a) Changes in the UV-Vis absorption spectrum of 10 µM imine **13** over time (minutes) in aqueous buffer. (b) Changes in the absorption peak of imine **13** at 324 nm over time. [HEPES] = 5 mM, pH 7.0, [**13**] = 10 µM.

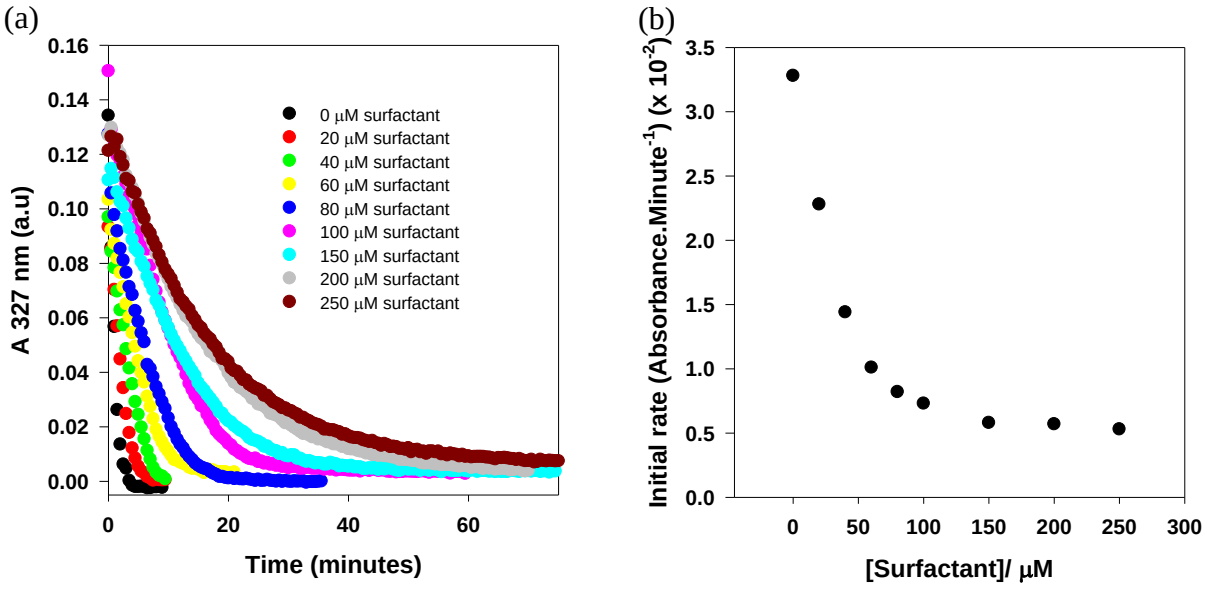

Figure 2.6: (a) Change in the A (327 nm) of imine **13** against time in the presence of increasing surfactant **4** concentration up to 250 μM. (b) Changes in the rate of degradation of **13** as the surfactant **4** concentration increases. The individual points were obtained by plotting the slope of the linear portion of the A (327 nm) against surfactant **4** concentration. [HEPES] = 5 mM, pH 7.0 [**13**] = 10 μM.

Next, attention was shifted to reaction in ATP-templated vesicles. Surfactant **4** has a *cac* of 100 μM and thus vesicle formation was carried out using a surfactant concentration of 30 μM, i.e. below the *cac*. An ATP concentration of 5 μM ATP was used. These concentrations were consistent with the concentrations used in Maiti's work.[23] However, the molar extinction coefficient of **13** was not high enough to clearly distinguish product formation from absorbance changes caused by turbidity.

In order to surmount these challenges, it was decided to use UPLC as a detection method. The focus was shifted to hydrazones due to their higher stability, which enables hydrazones to be analysed by chromatographic means.[25-27] Studies with hydrazones are sometimes limited by their slow kinetics of formation at neutral pH.[25,28] Notwithstanding this, it has been reported that electron-deficient aldehydes react with a high rate at physiological pH.[28] Indeed, when 2-pyridinecarboxaldehyde, **14**, having an electron-withdrawing nitrogen, was reacted with 4-chlorophenylhydrazine, **15**, the reaction proceeded with a good rate in aqueous buffer (HEPES (5 mM), pH 7.0) giving hydrazone **16** which showed a prominent peak at 353 nm in the UV-Vis spectrum (Scheme 2.4). Lower concentrations were used for the reactions in vesicles, but the reaction was improved by increasing the hydrazide: aldehyde ratio from 1:1 to 1:5 and 1:10. Initial tests with UV-Vis were quite promising

despite the occurrence of turbidity. When 10 µM of aldehyde **14** was reacted with 2 µM of hydrazine **15** barely any reaction occurred overnight in aqueous buffer (HEPES (5 mM), pH 7.0) (black). Only some reaction occurred in surfactant **4** (red). However, a significant increase in the amount of product was noticed with surfactant **4** and ATP (green), even after subtracting the increase in absorbance originating from the turbidity (blue) (Figure 2.7).

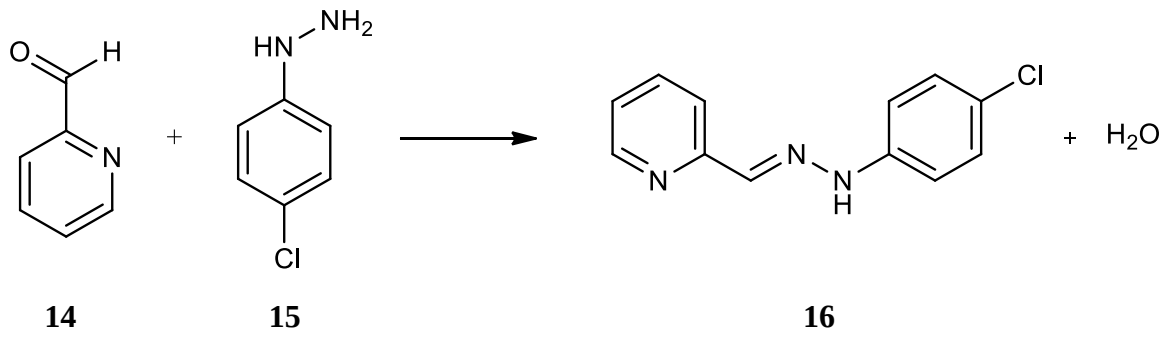

Scheme 2.4: Scheme for the reaction between 2-pyridinecarboxylaldehyde, **14**, and chlorophenylhydrazine, **15**, to form hydrazone **16**.

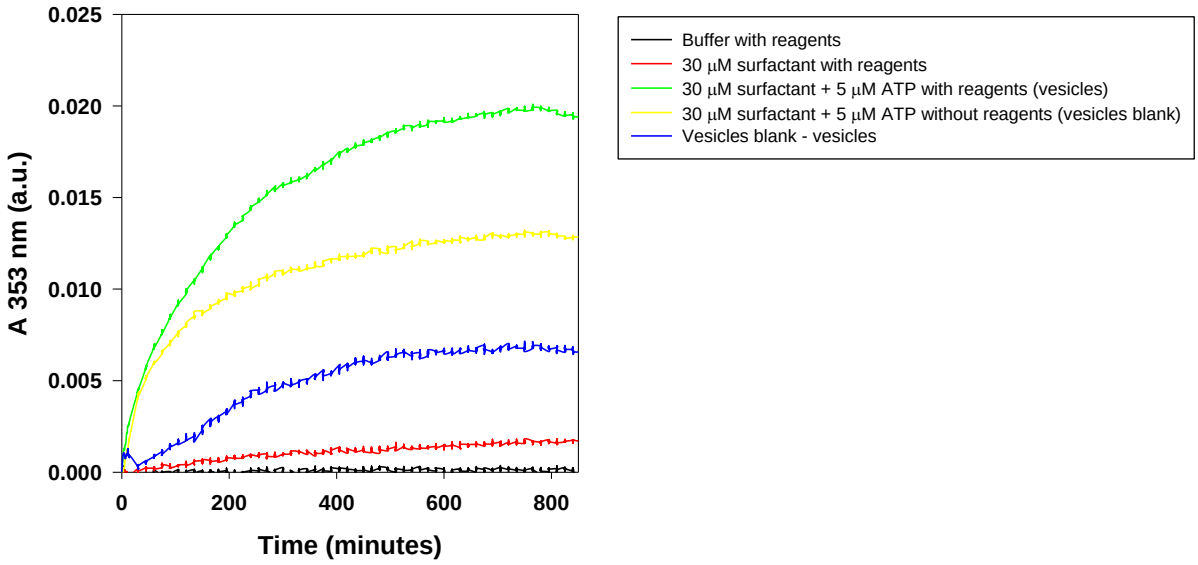

Figure 2.7: Figure showing representative UV-Vis results from the reaction between 2-pyridinecarboxylaldehdye, **14** and 4-chlorophenylhydrazine, **15** in aqueous buffer, 30 µM surfactant and vesicles. The vesicles blank was prepared in the same manner as for the sample for the vesicles but with the addition of acetonitrile instead of the reactants. [HEPES] = 5 mM, pH 7.0, [Surfactant **4**] = 30 µM, [ATP] = 5 µM, [**14**] = 10 µM, [**15**] = 2 µM.

The results were verified using UPLC. Hydrazone **16** gave a peak with a retention time of 2.98 minutes when observed at 353 nm (Figure 2.8). After monitoring the reaction overnight, a very small amount of **16** was obtained both in the aqueous buffer (black) and in 30 μM surfactant (red). When the reaction was carried out in 30 μM surfactant and 5 μM ATP, the area of the hydrazone peak was higher (green), suggesting that the reaction was indeed faster in vesicles compared to buffer and surfactant alone. An ideal reaction to investigate would be one in which product formation occurs exclusively, or in much higher quantities in the vesicles when compared to the aqueous solution. However, in this particular reaction, product formation also occured in buffer. Thus, the amount of product was not enhanced much upon addition of ATP. It was also necessary to use one of the reagents in excess in order to observe a difference between the amount of product formed in the vesicles and in the unaggregated **4**. Ambiguous results were also obtained when the ratio of the reagents was changed. Nevertheless, by using UPLC as a detection method and by improving the conditions of the experiment, it was possible to obtain a first insight that hydrazone bond formation reactions can preferentially occur in the aggregated state when compared to the unaggregated state. Yet, it was difficult to obtain reliable data for quantification of the effect. This prompted us to first improve the design of the system.

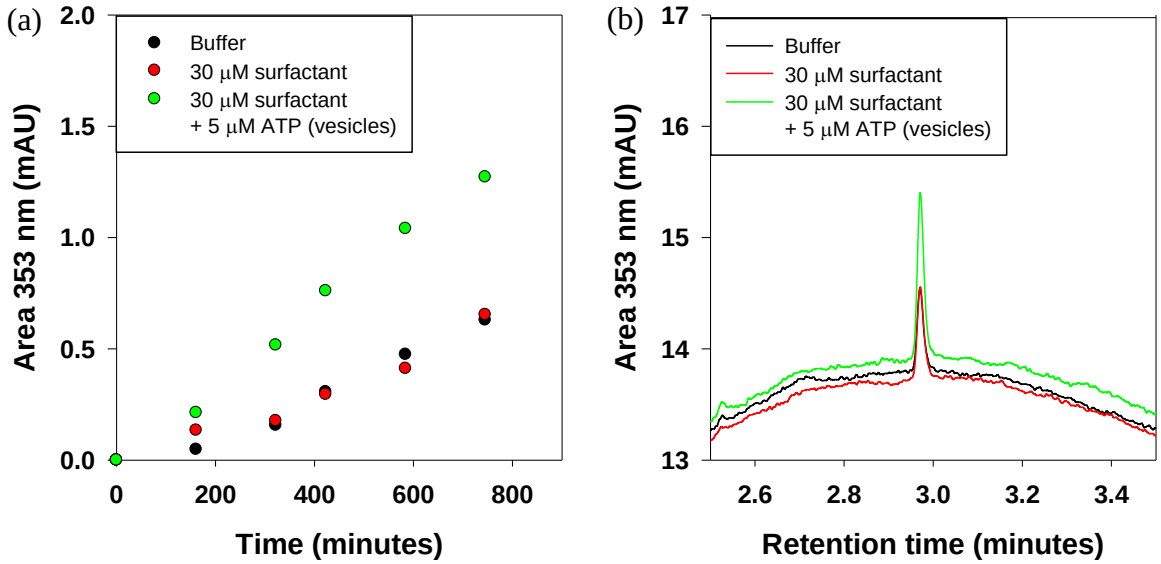

Figure 2.8: (a). Figure showing the area for the absorbance at 353 nm for the reaction between 4-chlorophenylhydrazine, **15**, and 2-pyridinecarboxaldehyde, **14**, in aqueous buffer, surfactant and vesicles. Reaction was monitored by UPLC. (b). Overlaid UPLC chromatograms for the peak of the product obtained overnight for the different conditions. [HEPES] = 5 mM, pH 7.0, [Surfactant **4**] = 30 μM, [ATP] = 5 μM, [**14**] = 5 μM, [**15**] = 1 μM.

It was hypothesized that the reaction could be improved by choosing more hydrophobic reagents, but also by increasing the concentration of the surfactant used for vesicle formation. It was aspired that reagents with a higher degree of hydrophobicity would preferentially migrate to the hydrophobic bilayer. Their entrapment should lead to an enhanced reaction due to a higher local concentration of reactants in an environment more conducive to reaction.[29] The studies were limited by the molar extinction coefficient of the products, since the low concentration of reagents used for the experiments limited the detection of the product. It was therefore desirable to increase the reagent concentration for further studies. This implied the need to use a higher concentration of surfactant, in order to improve the volume of the hydrophobic environment available for reaction. The surfactant **4** was limited by its *cac* of 100 μM. It was therefore decided to synthesize another surfactant with a shorter alkyl chain which could assemble into a similar vesicular system upon addition of ATP, but only at higher concentrations.[30,31] The choice fell on a surfactant with a shorter C_{12} alkyl chain, **17** (Figure 2.9).

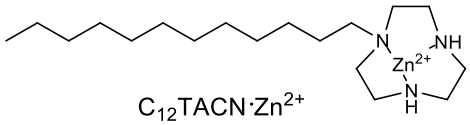

17

Figure 2.9: Structure of C_{12}TACN•Zn^{2+}, **17**, used as the building block for the assembly of transient vesicles with ATP.

2.2 Development of a vesicular chemical nanoreactor based on self-assembly under dissipative conditions of C_{12}TACN•Zn^{2+}

2.2.1 Comparison of the aggregation behaviour of C_{12}TACN•Zn^{2+} with other reported TACN-based surfactants in the absence of ATP

The surfactant C_{12}TACN•Zn^{2+}, **17**, was synthesized using a similar protocol as the one used for **4**.[23] The critical aggregation concentration or the *cac* of a surfactant can be experimentally determined by monitoring the change in physiochemical properties of the surfactant solution as the amphiphile concentration is altered. The onset of aggregate formation is typically marked by a change in the slope of a graph describing the change in

a physiochemical property of the substrate against the log of the concentration of the amphiphile.[32]

The aggregation behaviour of C_{12}TACN•Zn^{2+}, **17**, alone was studied by titrating increasing amount of **17** to an aqueous solution buffered at pH 7.0 containing the fluorescent apolar probe DPH, **18** (1,6-diphenyl-1,3,5-hexatriene (2.5 μM, λ_{ex} = 355 nm, λ_{em} = 428 nm)). This probe is a rigid, linear and rod-like fluorophore and contains no polar groups. It is insoluble in aqueous solution, but its spontaneous partitioning inside apolar compartments of aggregates results in an increase in fluorescence intensity.[33] Therefore, an increase in fluorescence intensity of **18** is an indication that the *cac* is reached. Using this method, **17** did not have a perceivable *cac*, because the fluorescence of the probe continued to increase linearly as the concentration of **17** increased up to 8 mM. This suggested that **17** did not spontaneously aggregate at these concentrations. This contrasts with the behaviour of the C_{16}TACN•Zn^{2+} system, where **4** started to aggregate at around 100 μM (Figure 2.10a). This result was important as it suggested that a higher concentration regime of surfactant **17** could be used in the ATP-templation studies.

The result was confirmed using surface tension measurements on the two surfactants (Figure 2.10b). Surfactants in solution can either adsorb at the air-water interface or form aggregates. Below the *cac*, surfactants are adsorbed at the air-water interface and decrease the surface tension of the solution. Once the *cac* is reached, additional surfactants are incorporated in water-soluble aggregates. There is, therefore, no further change in the surface tension of the solution upon increasing addition of surfactant. This is evident by a sudden change in the slope of a plot showing the change in surface tension against logarithm of the surfactant concentration.[34,35] Surface tension analysis of equilibrated solutions of surfactant **4** at different concentrations in aqueous HEPES buffer at pH 7.0 (5 mM) revealed the formation of aggregates at a *cac* of around 100 μM, in accordance with the fluorescence measurements. The same analysis on the amphiphile **17**, however revealed no clear *cac* and the surface tension continued to decrease unabated even at a concentration of 2.8 mM surfactant **17**, confirming the result obtained by fluorescence spectroscopy.

Lack of aggregation was also confirmed by UV-Vis spectroscopy. DPH, **18**, is insoluble in aqueous solution and therefore does not show any absorbance in the UV-Vis spectrum. Formation of aggregates solubilises **18**, and a characteristic absorbance is observed at 377 nm. In the case of the surfactant **17**, no such absorbance was observed upon increasing

concentration of **17** (Figure 2.10c). This again confirms the lack of aggregate formation for the concentrations used. Figure 2.10d shows the same experiment for the surfactant **4** as reported by Maiti for comparison. In this case, below the *cac*, **17** shows very little absorbance at 377 nm. However, above the *cac* a distinctive absorption peak is observed at 377 nm which increases in intensity as the concentration of **4** increases.[23] DLS (Dynamic Light Scattering) measurements on surfactant **17** at various concentrations suggested polydisperse samples with no organised structure at all concentrations analysed (200 µM, 500 µM, 1000 µM), giving further evidence for the lack of aggregate formation by the free surfactant.

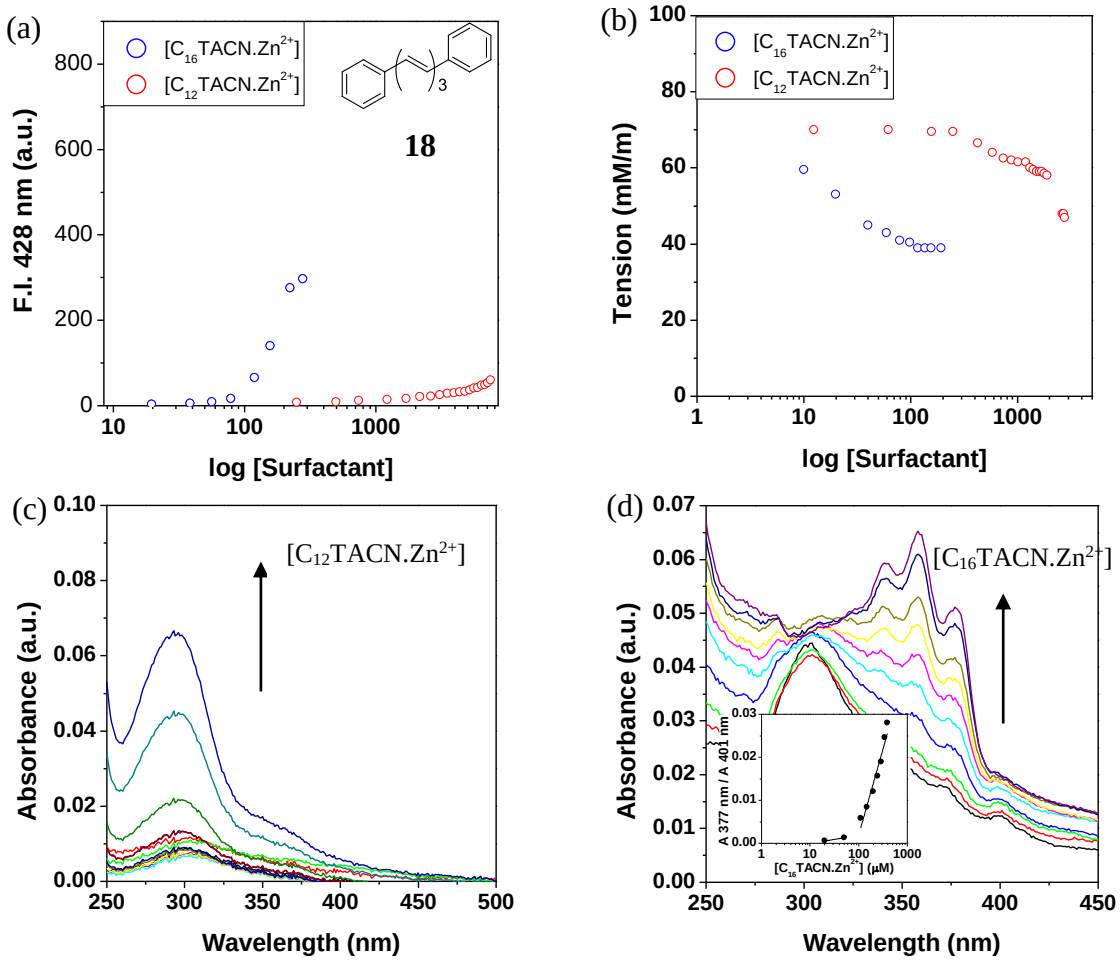

Figure 2.10: (a). The fluorescence intensity of **18** as a function of the log of the surfactant concentration for (i) $C_{16}TACN{\bullet}Zn^{2+}$ **4**, (ii) $C_{12}TACN{\bullet}Zn^{2+}$ **17**. A sharp change in the slope is obtained at around 100 µM $C_{16}TACN{\bullet}Zn^{2+}$ (the *cac*) but no sharp change in slope was observable for $C_{12}TACN{\bullet}Zn^{2+}$. [DPH] = 2.5 µM, HEPES = 5 mM, pH 7.0, λ_{ex} / λ_{em} = 355/ 428 nm, Slits = 5/5 nm (ex/em), T = 25 °C. (b). Determination of *cac* using tensiometry. The tension for $C_{16}TACN{\bullet}Zn^{2+}$, **4** stops decreasing at a surfactant concentration of around 100 µM, marking the *cac*, while for $C_{12}TAC{\bullet}Zn^{2+}$, **17** no clear decrease in the tension is observed up to a concentration of 2.8 mM. (c). In UV-Vis spectroscopy, the absorbance of DPH, **18** at 377 nm is absent at all concentrations, suggesting it is not solubilised. The spectra obtained in the $C_{16}TACN{\bullet}Zn^{2+}$ **4** system obtained by Maiti are included for comparison in (d). Graph adapted from 23.

2.2.2 The effect of ATP on the aggregation behaviour of C_{12}TACN•Zn^{2+}

Addition of ATP to the previously used C_{16}TACN•Zn^{2+}-amphiphile induced vesicle formation, with a reported *cac* of around 10 μM for all concentrations of ATP used.[23] It was therefore of interest to study the behaviour of the surfactant **17** in the presence of ATP. Increasing concentrations of **17** were titrated to a fixed concentrations of ATP (20 – 200 μM) in the presence of 2.5 μM DPH, **18**, in buffered solution (pH 7.0) and the fluorescence emission intensity of **18** was monitored (Figure 2.11). In contrast to the situation without ATP, the fluorescence intensity started to increase at low surfactant concentrations (*cac* ≈ 30 μM), suggesting that aggregates with higher stability are formed in the presence of ATP. This value is slightly higher than that obtained by Maiti *et al.* with the C_{16}TACN•Zn^{2+} system, indicating that the surfactant has a lower propensity to aggregate also in the presence of ATP.[30,31]

In the C_{12}TACN•Zn^{2+} system, the fluorescence intensity in the presence of ATP continues to increase until a maximum is reached, after which further addition of surfactant results in a decrease in the fluorescence intensity (Figure 2.11). The maximum was reached at a well-defined ratio of ATP:surfactant of 1:5 for surfactant concentrations up to 100 μM. In the case of 200 μM surfactant, the maximum was reached at a ratio of ATP:surfactant of 1:1.5. Above this ratio, it is probable that the concentration of surfactant was too high to be stabilised by the ATP present in solution. Consequently, the aggregates fall apart resulting in a decrease in the fluorescence intensity. However, similar profiles were recently reported for a C_{20}TACN•Zn^{2+} surfactant. In this study, the decrease in the fluorescence following a maximum was attributed to a change in the bilayer structure which affected the fluorescence of **18**.[36]

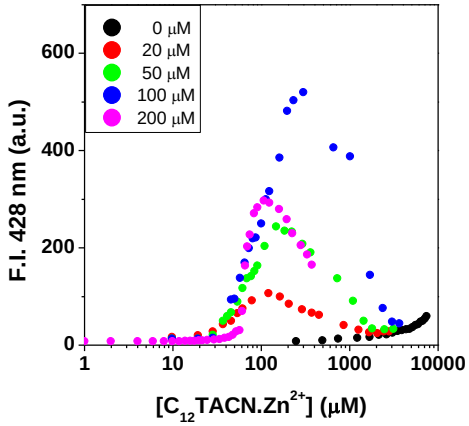

Figure 2.11: Determining the *cac* of **17** in the absence and in the presence of increasing concentrations of ATP. No *cac* could be clearly determined in the absence of ATP at the concentrations used. [DPH] = 2.5 μM, [HEPES] = 5 mM, pH 7.0, $\lambda_{ex}/\lambda_{em}$ = 355/428 nm, Slits = 5/5 nm (ex/em) T = 25 °C.

Next, the experiment was carried out in the opposite way, that is by adding ATP to a solution with a constant concentration of surfactant **17**. It was observed that the fluorescence intensity continued to increase rapidly until a plateau was reached at a molar ratio of ATP: surfactant of approximately 1:3, in a similar manner to what was reported for the surfactant **4**.[23] Similar results have also been reported for a related C_{20}TACN•Zn^{2+} surfactant.[36] Further addition of ATP resulted in a slight decrease in fluorescence intensity (Figure 2.12). The presence of vesicles at higher concentration of ATP was confirmed by TEM (*vide infra*). This experiment was carried out both in the presence and in the absence of Zn^{2+}. It was observed that the experiment in the absence of Zn^{2+} showed the same pattern, but the fluorescence intensity was much lower. This highlights the importance of Zn^{2+} in the assembly of the vesicles, as was shown in previous work using nanoparticles.[37]

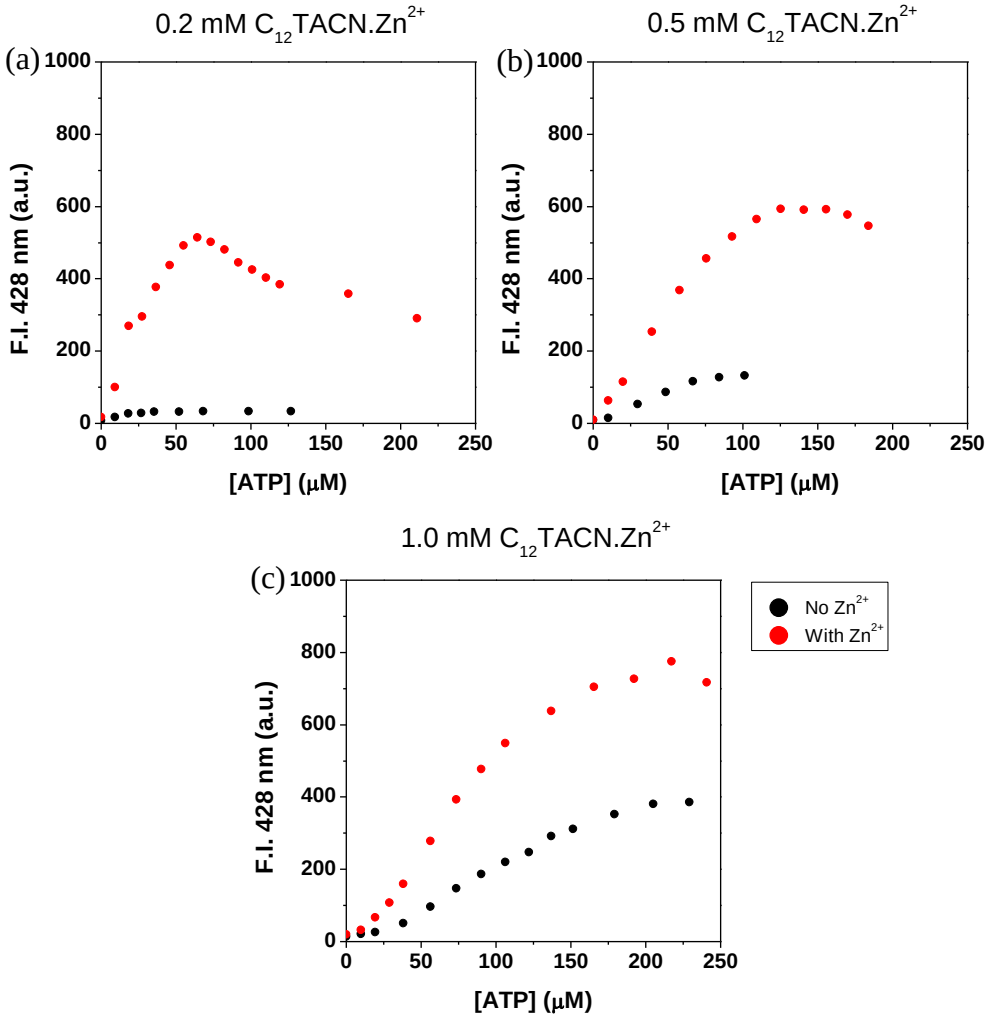

Figure 2.12: Addition of ATP to a constant concentration ((a) = 0.2 mM, (b) = 0.5 mM and (c) = 1 mM) of surfactant **17** in the absence and presence of Zn^{2+}. In all cases, the F.I. increases to a maximum and then drop slightly. [DPH] = 2.5 μM, [HEPES] = 5 mM, pH 7.0, $\lambda_{ex}/\lambda_{em}$ = 355/428 nm, Slits = 5/5 nm (ex/em) T = 25 °C.

2.2.3 Study of the stability of the aggregates by fluorescence spectroscopy

The stability of ATP-templated vesicles was initially studied by fluorescence spectroscopy by monitoring the DPH-fluorescence as a function of time. Fluorescence experiments using vesicles formed from 100 μM surfactant **17** and increasing amount of ATP (50, 100 and 200 μM ATP) showed that the fluorescence intensity of **18** decreased over time, especially for the lower concentrations of ATP (Figure 2.13a). In the case of the addition of 200 μM ATP to 100 μM surfactant **17**, the fluorescence intensity was stable for longer than 900 minutes, following an initial stabilisation period. The decrease in the fluorescence intensity over time could perhaps be due to the formation of turbidity in the solution as a result of aggregation.[38] Slow aggregation over time with different ATP concentration was reported with surfactant **4** as well,[23] and was also evident in the preliminary reactivity experiments reported in Section 2.1.1. Turbidity in the solution was monitored by UV-Vis spectroscopy where the absorbance at a fixed wavelength (450 nm) for a surfactant **17** solution (80 μM) in the presence of ATP (20 μM) was observed to increase in the absence of any absorbing species (Figure 2.13b). Similar profiles were obtained with other compositions of surfactant **17** and ATP. This formation of turbidity in the solution called for caution since it suggested that the vesicles could only be used for a certain period of time and could also pose limitations on which techniques of analysis could be useful to analyse product formation. From the fluorescence experiments, it can safely be said that the vesicles are stable overnight (approximately 900 minutes).

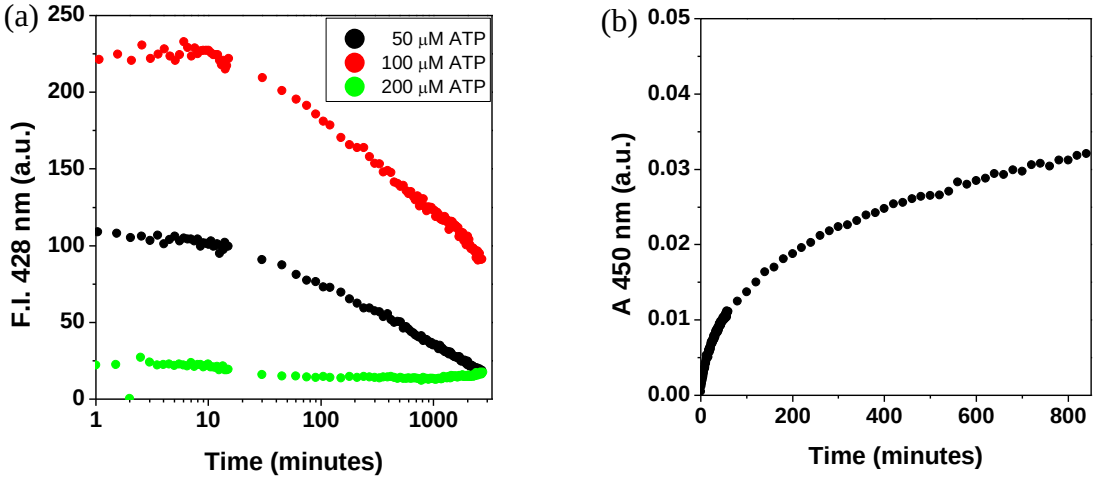

Figure 2.13: (a). The fluorescence intensity of DPH, **18**, over time in vesicles formed from 100 μM surfactant **17** and increasing amount of ATP (50 – 200 μM). (b). Increase in the baseline (Absorbance at 450 nm) for vesicles composed of 80 μM surfactant **17** and 20 μM ATP in the absence of any absorbing species.

Further insight into the structure of the vesicles was gained using laurdan dye, **19**, which is a very common fluorophore used in membrane studies (Figure 2.14).[39,40] Similarly to **18**, **19** is barely soluble in water and its quantum yield of fluorescence is much higher in membranes compared to aqueous environments, resulting in a turn-on of the fluorescence intensity when the dye partitions into hydrophobic membranes. Its popularity arises from the fact that its fluorescence excitation and emission spectra are very sensitive to the polarity and the dipolar dynamics of the environment, displaying large emission shifts as the polarity of the solvent changes. This solvent relaxation effect originates from the reorientation of the solvent dipoles with respect to the excited fluorophore molecules. Consequently, **19** can distinguish between a membrane in a gel or a liquid crystalline phase state, and undergoes red shifts of up to 50 nm upon shifting from gel (more ordered) to liquid crystalline (more disordered) states. [41] This change can be monitored using the general polarisation (GP),[42] which can be defined as:

$$GP = \frac{I_{440} - I_{490}}{I_{440} + I_{490}}$$

Where GP is the general polarisation

I_{440} is the fluorescence emission intensity for laurdan at 440 nm

I_{490} is the fluorescence emission intensity for laurdan at 490 nm

When **19** intercalates into a more disordered part of the membrane, its emission spectrum is red shifted, decreasing the general polarization (GP). A study with **19** in vesicles (100 µM surfactant **17**, 200 µM ATP) suggests that over time the intensity of the fluorescence goes down and is shifted to the blue, indicating a slight change in the environment (Figure 2.14a). The GP value increases over time, suggesting that there is increased order as time goes by (Figure 2.14b). This implies that the vesicles become more tightly packed over time. This shows the complexity of the vesicle forming process, suggesting that the system studied is quite dynamic.

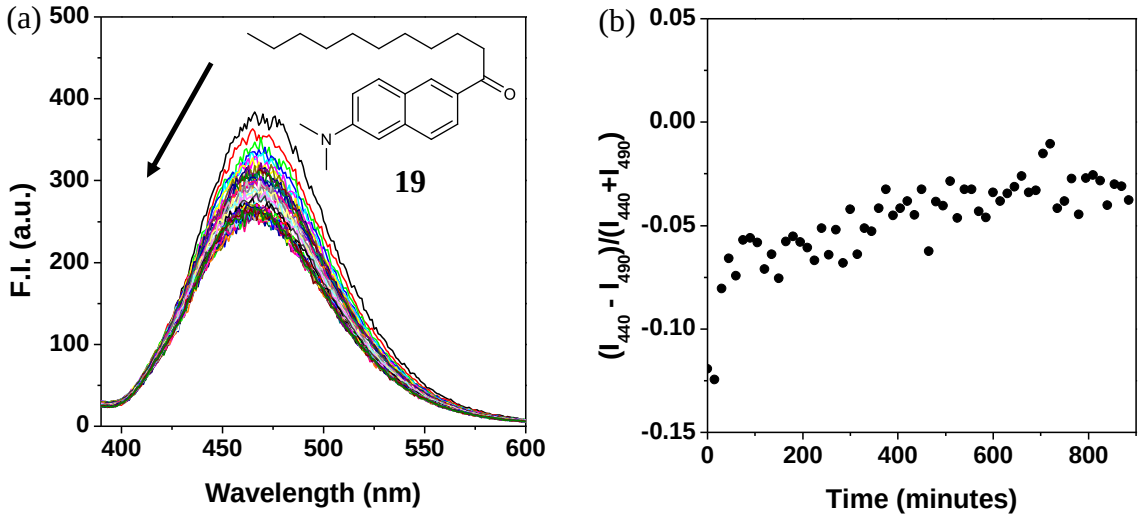

Figure 2.14: (a). The fluorescence intensity of laurdan dye in vesicles formed from 100 µM surfactant **17** and 200 µM ATP over a period of time. The peak maximum undergoes a decrease in fluorescence intensity and a slight blue shift, suggesting an alteration in the structure of the composite. The structure of laurdan is included in the figure. (b). Change in the GP index over time for vesicles formed from 100 µM surfactant **17**, 200 µM ATP. [Laurdan] = 2 µM, λ_{ex} = 370 nm, Slits = 5/10 nm (ex/em), 25 °C, [HEPES] = 5 mM, pH 7.0.

The stability of ATP-templated vesicles formed from 100 µM C_{12}TACN•Zn^{2+} and 200 µM ATP was also assessed by monitoring the fluorescence of **19** inside such vesicles at different pHs from 5.5 to 7. The fluorescence intensity of the dye was pH dependent, but in all cases, the fluorescence intensity was stable overnight (600 minutes) (Figure 2.15). The fact that a significantly different fluorescence intensity is obtained at different pHs suggests that perhaps there is a pH effect from the dye under these conditions. This calls for caution when it comes to interpreting fluorescence data involving dyes.

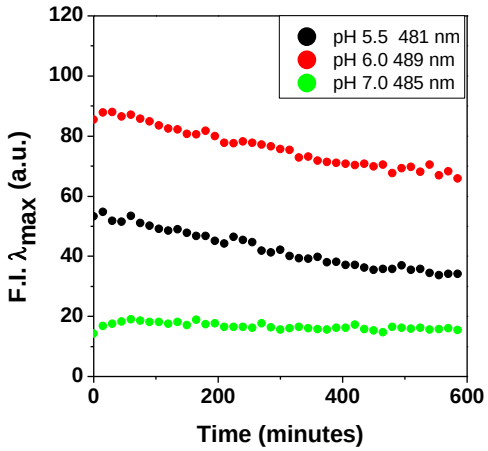

Figure 2.15: The fluorescence intensity of laurdan, **19** over time in vesicles formed from 100 µM surfactant **17** and 200 µM ATP. [Laurdan] = 2 µM, λ_{ex} = 370 nm, Slits = 5/10 nm (ex/em), 25 °C, [HEPES] = 5 mM, pH 7.0.

2.2.4 Study of aggregate formation by DLS

The formation of large aggregates of various sizes was also demonstrated by Dynamic Light Scattering (DLS) measurements. The surfactant **17** alone was not perceived to form stable aggregates for all the concentrations studied. The size of the aggregate was dependent on the concentration of **17** and ATP. When the ATP concentration was kept constant at 200 μM and the concentration of **17** was increased from 100 μM to 200 μM, the aggregates formed were larger in size. Thus, aggregates from 100 μM $C_{12}TACN{\bullet}Zn^{2+}$ and 200 μM ATP showed a hydrodynamic diameter of 100 ± 50 nm while those formed from 200 μM $C_{12}TACN{\bullet}Zn^{2+}$ and 200 μM ATP were larger with a hydrodynamic diameter of 200 ± 80 nm (Figure 2.16 and Table 2.1).

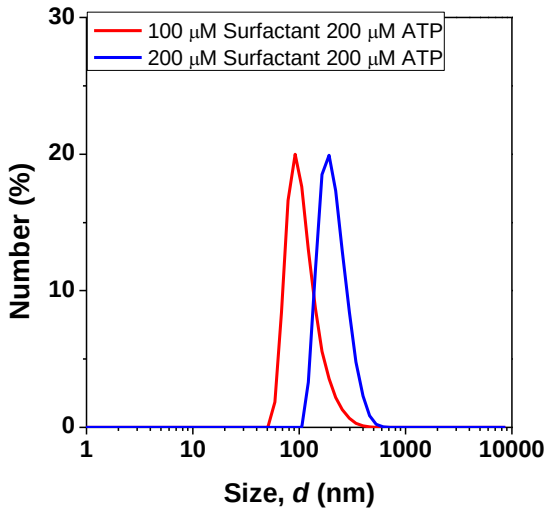

Figure 2.16: The hydrodianamic diameter of the aggregates formed from (a) 100 μM surfactant **17** and 200 μM ATP and (b) 200 μM surfactant **17** and 200 μM ATP over time. [HEPES] = 5 mM, pH 7.0, 25 ^{0}C**.**

The same trend was observed when the concentration of surfactant **17** was kept constant at 500 μM and the ATP concentration was increased. No stable aggregates were observed for surfactant **17** on its own. Assemblies were also not detected upon mixing the surfactant **17** with just 10 μM ATP. Higher ATP concentration resulted in the formation of aggregates, which became bigger in size with increasing ATP concentration (Figure 2.17, Table 2.1). Thus, aggregates with 25 μM ATP were 50 nm while those formed with 50 μM and 75 μM were approximately 100 nm. Larger sizes of 200 nm were obtained with 100 μM ATP. Similar plots were obtained with 1000 μM **17** at increasing ATP concentrations (Table 2.2). No stable aggregates could be detected in 1000 μM surfactant solution alone or in the presence of 10 μM ATP, but increasing the ATP concentration up to a 100 μM resulted in

the formation of assemblies. Vesicles in the order of 50 nm were obtained with ATP concentrations of 20 and 50 μM while larger vesicles in the order of 100 nm were obtained with 100 μM ATP.

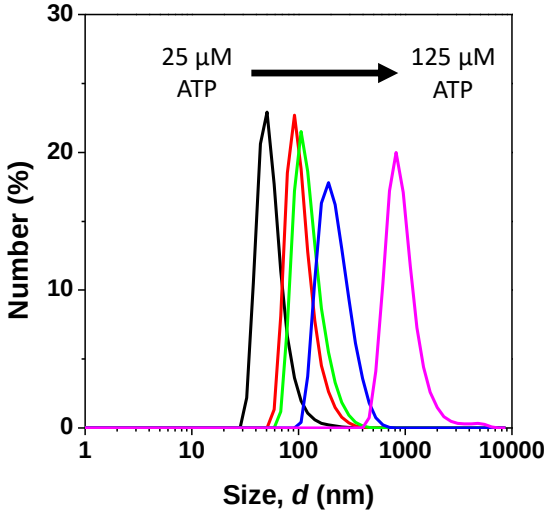

Figure 2.17: Figure showing the DLS of vesicles formed from 500 μM surfactant **17** and increasing concentrations of ATP from 25 to 150 μM (No structures were visible at 0 and 10 μM ATP upon mixing). [HEPES] = 5 mM, pH 7.0, 25 ^{0}C.

The aggregates persisted over time and the aggregate size slightly increased as time went by (Table 2.1 and Table 2.2). Thus, for a surfactant **17** concentration of 500 μM, the aggregates increased in size by about 30 nm in the presence of 25 μM and 75 μM ATP, by 10 nm in the presence of 50 μM ATP and by 110 nm in the presence of 100 μM ATP. With a surfactant **17** concentration of 1000 μM, the aggregate increased in size by about 20 nm in the presence of 20 μM and 50 μM ATP and by 40 nm in the presence of 100 μM ATP. Over time, addition of 10 μM ATP to the surfactant **17** resulted in the formation of stable aggregates of around 40 nm. The size of aggregates formed from 100 μM **17** and 200 μM ATP was monitored over time and the vesicles were shown to be stable overnight (Figure 2.18). DLS data complimented fluorescence data and showed that some compositions of vesicles are stable over time while others are not.

Time (minutes)	Size (nm) at different ATP concentrations over time (500 µM C_{12}TACN•Zn^{2+})						
	0 µM ATP	**10 µM ATP**	**25 µM ATP**	**50 µM ATP**	**75 µM ATP**	**100 µM ATP**	**150 µM ATP**
0	N/A	N/A	50 ± 20	100 ± 40	130 ± 40	240 ± 80	1000 ± 500
180	N/A	40 ± 20	70 ± 30	100 ± 40	140± 50	340 ± 100	N/A
900	N/A	60 ± 20	80 ± 30	100 ± 40	160 ± 50	350 ± 80	N/A

Table 2.1: Table showing the size of aggregates formed from 500 µM C_{12}TACN•Zn^{2+} and increasing concentrations of ATP over time. N/A signifies that the data obtained was not reliable enough to confirm the presence of aggregates. [HEPES] = 5 mM, pH 7.0, 25 ^{0}C

Time (minutes)	Size (nm) at different ATP concentrations over time (500 µM C_{12}TACN•Zn^{2+})						
	0 µM ATP	**10 µM ATP**	**25 µM ATP**	**50 µM ATP**	**75 µM ATP**	**100 µM ATP**	**150 µM ATP**
0	N/A	N/A	50 ± 20	100 ± 40	130 ± 40	240 ± 80	1000 ± 500
180	N/A	40 ± 20	70 ± 30	100 ± 40	140± 50	340 ± 100	N/A
900	N/A	60 ± 20	80 ± 30	100 ± 40	160 ± 50	350 ± 80	N/A

Table 2.2: Table showing the size of aggregates formed from 1000 µM C_{12}TACN•Zn^{2+} and increasing concentrations of ATP over time. [HEPES] = 5 mM, pH 7.0, 25 ^{0}C.

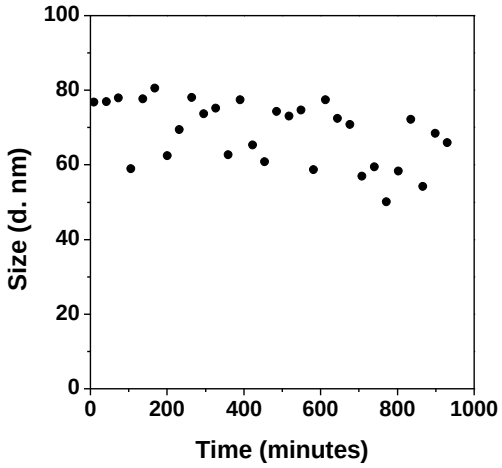

Figure 2.18: Hydrodynamic diameter of vesicles formed from 100 µM surfactant **17**, 200 µM ATP over time. [HEPES] = 5 mM, pH 7.0, 25 ^{0}C**.**

2.2.5 Visualisation of the assemblies by Transmission Electron Microscopy

The formation of vesicles was confirmed by Transmission Electron Microscopy (TEM). The vesicles were visualised by staining with uranyl acetate. TEM images of a 100 μM solution of **17** did not reveal explicit structures (Figure 2.19). However, images of solutions containing also ATP (50, 100 and 200 μM) showed distinct structures of larger dimensions with sizes ranging between 25 and 100 nm. A contrasting outer shell could be delineated, which was attributable to the Zn^{2+} in the outer layer. This was sometimes hard to demarcate unambiguously due to the staining applied. The vesicles could sometimes be observed as aggregates forming a complex network. The images were analysed by manually measuring the diameter of the particles in a select number of images. The average diameter for the vesicles formed from 100 μM surfactant **17** and 200 μM ATP estimated by TEM, 50 ± 30 nm (Figure 2.20), was somewhat lower than that estimated by DLS (90 ± 50 nm). This can be attributed to the properties of the different techniques. DLS measures the hydrodynamic radius, which also includes the sphere of solvent interacting with the individual vesicles. Therefore, a larger diameter can be expected with DLS measurements.

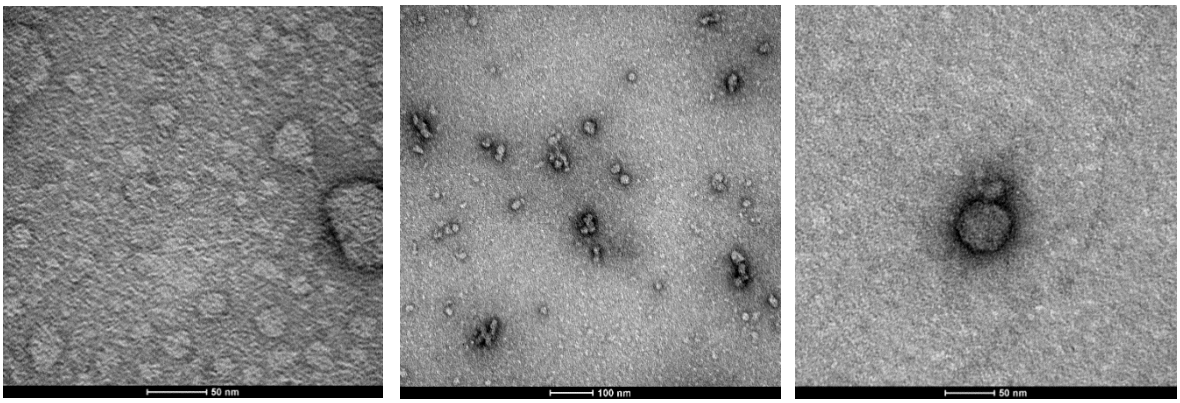

Figure 2.19: TEM of structures formed from (a) 100 μM surfactant **17**, (b) 100 μM surfactant **17** and 50 μM ATP in 5 mM HEPES buffer pH 7, (c) 100 μM surfactant **17** and 200 μM ATP in 5 mM HEPES buffer pH 7.

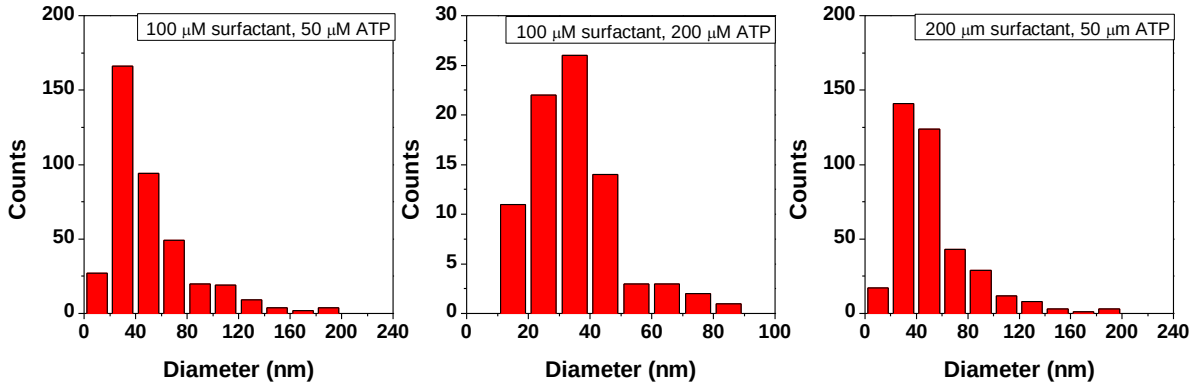

Figure 2.20: Size distribution of a representative batches of vesicles formed from different compositions of surfactant **17** and ATP. [HEPES] = 5 mM, pH 7.0.

2.2.6 Investigation of ATP hydrolysis by potato apyrase in the presence of C_{12}TACN•Zn^{2+}

Self-assembly under dissipative conditions requires the introduction of an additional process to release the chemical energy stored in ATP and eliminate the stabilising interactions between ATP and surfactant **17**.[23] The enzyme potato apyrase has been demonstrated in previous work to be an efficient enzyme for the hydrolysis of ATP into AMP and inorganic phosphates, P_i.[21,23,43] Direct evidence for the cleavage of ATP by the potato apyrase was obtained by ^{31}P NMR. Solutions containing ATP (2 mM), surfactant **17** (0.1 mM) and potato apyrase (0.4 U) were analysed by ^{31}P NMR studies (Figure 2.21, see also Section 2.7.7 in the Appendix). ATP in a solution of surfactant **17** (0.1 mM) shows three peaks corresponding to the three phosphorus atoms: two doublets at -10.93 ppm and -11.73 ppm, corresponding to the α and γ phosphorus atoms, respectively, and a triplet at -23.30 ppm, corresponding to the β phosphorus. Recording spectra at regular time intervals after the addition of the enzyme led to the observation that the ATP signals decreased in intensity. This could be particularly well observed for the peak at -23.30 ppm (β-phosphorus atom), because the doublet at -10.93 ppm overlapped partly with a new peak appearing at -11.19 ppm. This arose from the formation of ADP. The ATP and ADP peaks eventually disappeared and new peaks at -0.09 ppm and -0.38 ppm corresponding to AMP and Pi, continued to increase in intensity (Figure 2.21). The identity of the peaks was checked against reference standards. The conversion of ATP into ADP and Pi and eventually AMP and Pi could be clearly observed by plotting the integral of the respective peaks against time (Figure 2.22a).

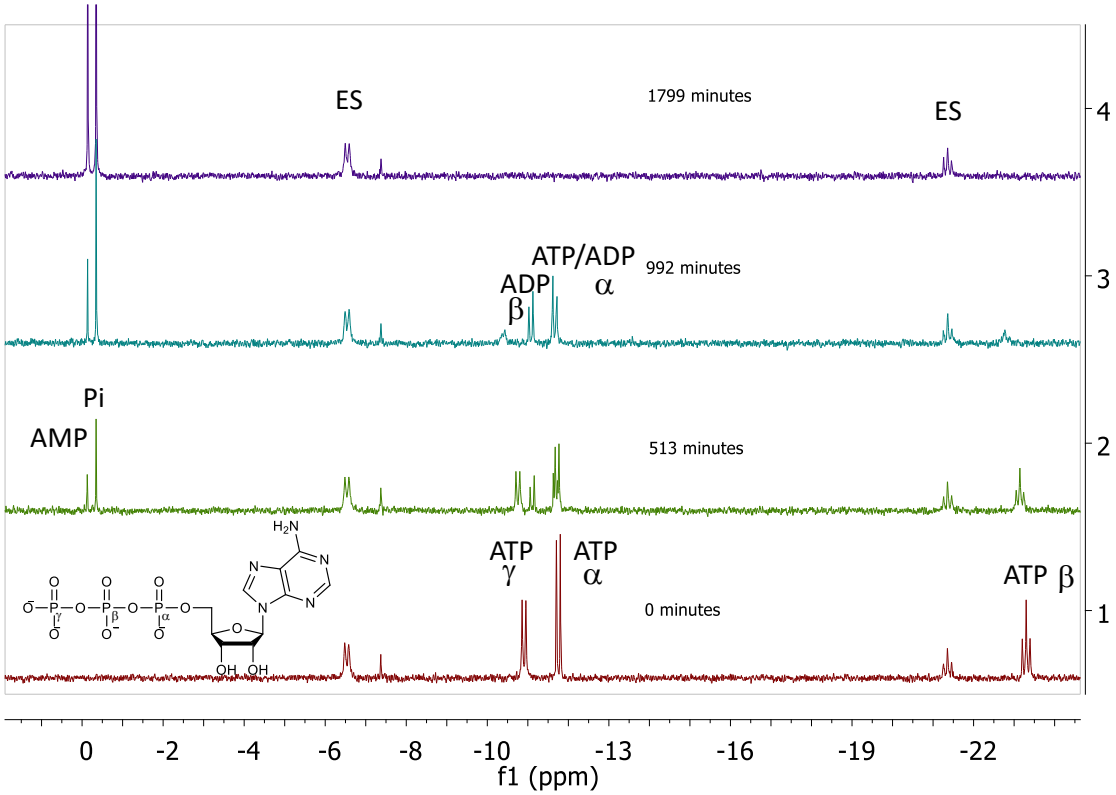

Figure 2.21: Selected ^{31}P NMR spectra of 2 mM ATP in the presence of 0.1 mM surfactant **17** and 0.4 U potato apyrase over time, showing the conversion of ATP to ADP and Pi and eventually to AMP and Pi. ES = internal standard. More spectra are found in the appendix. (10% D_2O, 202 MHz, 300 K) [HEPES] = 5 mM, pH 7.0.

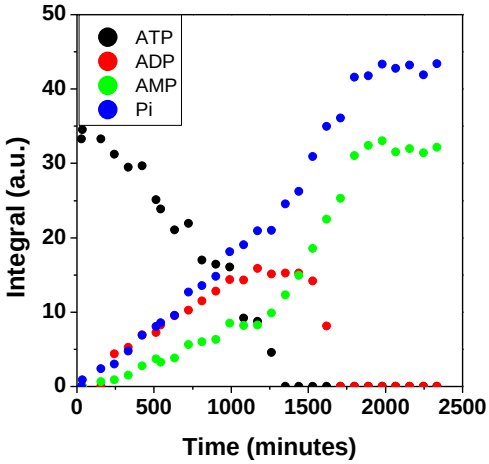

Figure 2.22: Kinetic profile showing the change in the integral of ATP, ADP, AMP and Pi when 2 M ATP is allowed to stand in the presence of 100 µM surfactant **17** and 0.4 U potato apyrase. [HEPES] = 5 mM, pH 7.0.

These concentrations of ATP are much higher than those used in the fluorescence experiments but they show nonetheless that the enzyme is able to cleave ATP in the presence of surfactant **17** even at higher concentrations of ATP. It has to be noted that enzyme studies with surfactant **17** were carried out in the absence of metal salts, such as $CaSO_4$ and $MgSO_4$. These are usually needed to activate the enzyme.[44] When ATP (2 mM) was allowed to stand in aqueous buffer (HEPES (5 mM), pH 7.0) (without metal salts and without surfactant) in the presence of 0.4 U apyrase, there was little change in the spectrum of ATP (Figure 2.23a, see also Section 2.7.8 in the Appendix). This is very interesting since it suggests that the enzyme on its own is not capable of appreciably cleaving ATP without activation by metal ions. (A small peak corresponding to a phosphate was observed at -0.33 ppm suggesting that there is a very small activity by the unactivated apyrase.) Even more interesting is that fact that the C_{12}TACN.Zn^{2+} complex is potentially activating the enzyme for hydrolysis. Nevertheless, the surfactant **17** on its own does not have an intrinsic capacity to cleave the ATP. A study of 2 mM ATP in the presence of the analogous surfactant C_{16}TACN•Zn^{2+} (**4**) in the absence of potato apyrase was not found to cleave ATP at the concentrations used (Figure 2.23b, see also Section 2.7.9 in the Appendix). ATP cleavage in the presence of related TACN•Zn^{2+}-based complexes is the subject of study of Chapter 4.

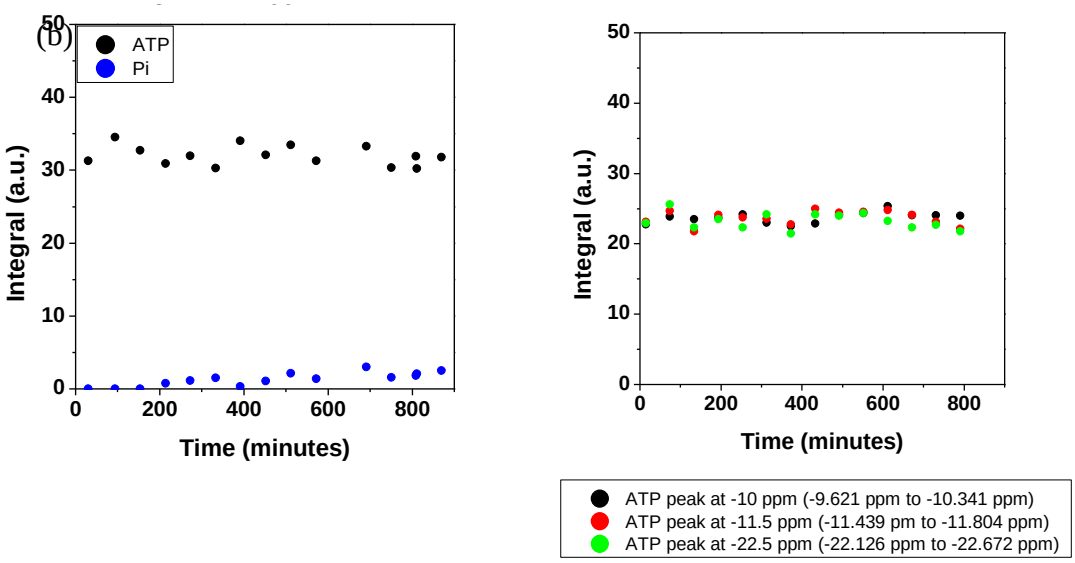

Figure 2.23: (a) Kinetic profile showing the change in the intergral of ATP and Pi when 2 M ATP is allowed to stand in buffer and in the presence of 0.4 U potato apyrase. (b) Kinetic profile showing the change in the intergral of ATP when 2 M ATP is allowed to stand in the presence of buffered 0.6 mM C_{16}TACN•Zn^{2+} without potato apyrase. [HEPES] = 5 mM, pH 7.0.

2.2.7 Effects of waste products of ATP hydrolysis on aggregate-formation

One condition for the observation of transient vesicle formation is that waste products of ATP hydrolysis have a lower capacity to stabilize the vesicles.[23] This was assessed by titrating increasing amounts of ATP and its products of hydrolysis (ADP and Pi in a 1:1 ratio and AMP and Pi in a 1:2 ratio) to a constant amount of surfactant **17** (either 100 μM or 200 μM) in the presence of 2.5 μM DPH, **18** (Figure 2.24). The F.I. of **18** started to increase immediately upon addition of increasing ATP concentration, as expected from the excellent affinity of ATP to stabilise aggregates of free surfactants. In the presence of (ADP+Pi) and (AMP+ 2Pi), the fluorescence intensity of **18** increased more gradually. These results suggests that the waste products are capable of stabilising aggregate formation as well albeit at higher concentrations. The decrease in fluorescence intensity at higher ATP concentrations has been discussed previously. This experiment suggests that careful consideration needs to be given to the concentration of ATP used for inducing transient stability. Results indicate that it would be wise to limit ATP concentrations to between 25-50 μM to ascertain that aggregates are only stabilised to a minimal extent, if any, in the presence of waste products.

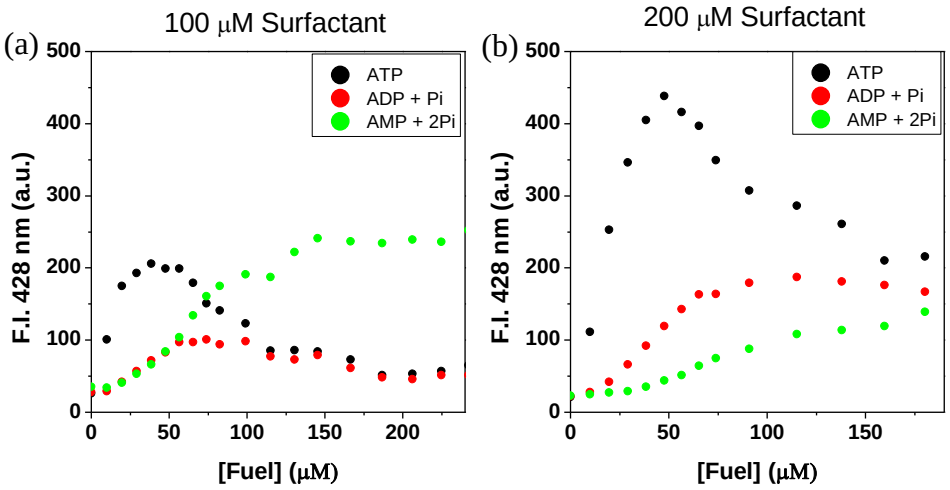

Figure 2.24: Addition of ATP, ADP + P_1 and AMP + $2P_i$ to a (a) 100 μM and (b) 200 μM solution of surfactant **17**. [DPH] = 2.5 μM, [HEPES] = 5 mM, pH 7.0, $\lambda_{ex}/\lambda_{em}$ = 355/428 nm, Slits = 5/5 nm (ex/em) T = 25 °C.

Fluorescence experiments with laurdan dye suggested that the aggregates formed with the waste products of ATP hydrolysis might have different properties compared to the aggregates templated by ATP (Figure 2.25). Laurdan dye did not show any fluorescence in

the presence of 100 μM surfactant **17**, as expected since it is not solubilised in the absence of any aggregate. Addition of 200 μM ATP led to a turn-on of the fluorescence with a λ_{em} of 472 nm (*vide sopra*). Likewise, the same amount of **17** with 200 μM ADP and P_i resulted in a turn-on of the fluorescence but the intensity was lower and the wavelength of emission was slightly blue-shifted to 469 nm. The fluorescence intensity of laurdan was even less in the presence of 100 μM **17**, 200 μM AMP and 400 μM P_i, and the λ_{em} was further shifted to the blue (463 nm). The GP factor increased from 0.66 in the presence of ATP to 0.75 in the presence of ADP and Pi to 0.96 in the presence of AMP and Pi. This data suggests that aggregates stabilised by waste products form more rigid structures with higher order than those formed with ATP.

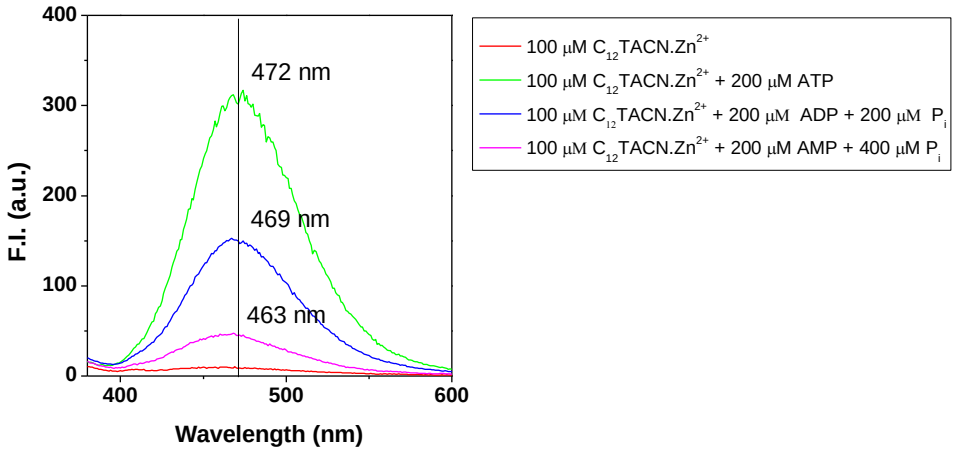

Figure 2.25: The fluorescence spectrum of laurdan in the presence of the various components of vesicles. [Laurdan] = 2 μM, λ_{ex} = 370 nm, Slits = 5/10 nm (ex/em), 25 ºC, [HEPES] = 5 mM , pH 7.0.

Further insight into the properties of aggregates formed upon ATP hydrolysis was obtained by monitoring the fluorescence of laurdan in vesicles formed from 100 μM surfactant **17** and 200 μM ATP both in the absence and in the presence of 0.1 U potato apyrase (Figure 2.26). Under these conditions, the dye DPH, **18**, did not show a decrease in the fluorescence intensity over time in the presence of apyrase. This is expected since the concentration of waste products is high enough for them to stabilise the aggregate (Figure 2.26b). In both cases, the fluorescence intensity of laurdan diminished over time and this was accompanied by a slight blue-shift in the peak. However, the decrease was larger in the presence of the enzyme and the GP value increased more over time in the presence of 0.1 U apyrase.

Carrying out the experiment with increasing apyrase concentration suggested a progressive increase in the GP factor over time as a function enzyme concentration (Figure 2.27). This again supports the idea that the waste products of hydrolysis might form different structures compared to those formed with ATP.

.

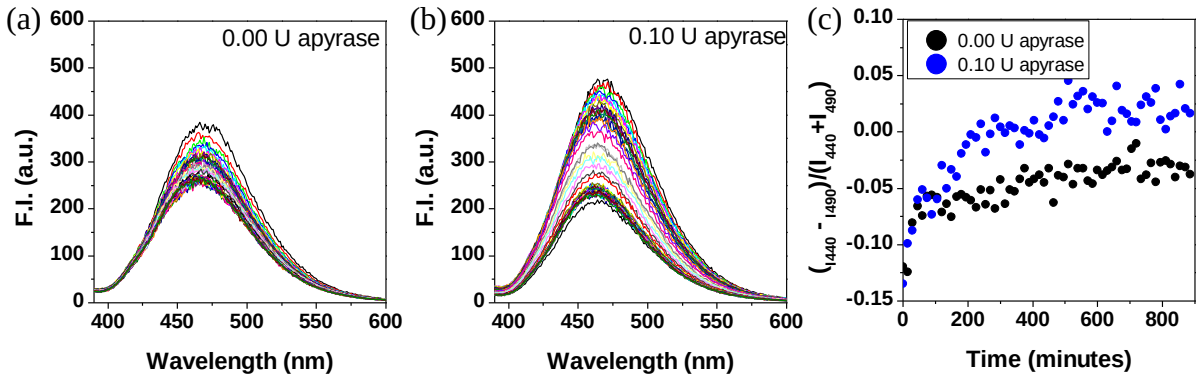

Figure 2.26: The fluorescence intensity of laurdan in the presence of vesicles formed from 100 µM surfactant, 200 µM ATP and (a) 0.0 U and (b) 0.1 U potato apyrase. (c) The GP ratio for the case of vesicles in the presence of 0.0 U apyrase and 0.1 U apyrase. [Laurdan] = 2 µM, λ_{ex} = 370 nm, Slits = 5/10 nm (ex/em), 25 °C, [HEPES] = 5 mM , pH 7.0.

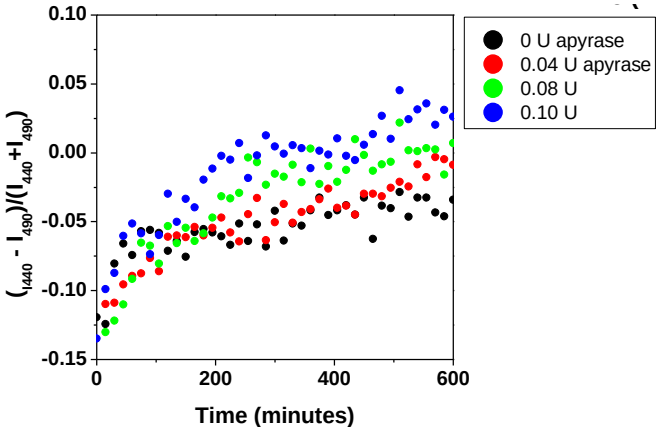

Figure 2.27: The GP ratio for the case of vesicles in the presence of increasing concentrations of enzyme over time. [Laurdan] = 2 µM, λ_{ex} = 370 nm, Slits = 5/10 nm (ex/em), 25 °C, [HEPES] = 5 mM , pH 7.0.

2.3 Self-assembly under dissipative conditions

For efficient dissipation, it was decided to reduce the amount of ATP to minimise aggregation effects from the waste products. A concentration of 50 μM ATP was added to a solution of 100 μM surfactant **17** in a solution containing 2.5 μM laurdan and increasing concentrations of enzyme between 0.0 and 2.0 U. The fluorescence intensity of laurdan was monitored over time. The process could not be monitored well when using the enzyme potato apyrase, possibly because the waste products AMP and Pi provided sufficient stabilisation of aggregate formation. However, better results were obtained with the enzyme alkaline phosphatase. Alkaline phosphatase cleaves nucleotides into nucleosides and inorganic phosphate, Pi.[45]

Laurdan, **19** was not fluorescent in the presence of 100 μM surfactant **17**. Addition of ATP resulted in an increase in the fluorescence intensity signal in all cases. Over time, the fluorescent signal decreased in intensity in the samples containing the enzyme. The rate of decrease was higher with increasing enzyme concentration (Figure 2.28a). This suggested that the system was assembling and disassembling as expected for self-assembly under dissipative conditions. Addition of the chemical fuel ATP to the free monomeric **17** resulted in the formation of vesicles (increase in the fluorescence of **19**). The enzyme alkaline phosphatase hydrolysed the ATP into Pi. Pi could not stabilise the vesicles as well as ATP and the assembly disaggregates (decrease in the fluorescence of **19**) (Figure 2.28b). The process was repeatable upon re-addition of ATP. Consecutive cycles occured with decreasing efficiency but it was possible to repeat the cycles for seven times under the conditions used (100 μM **17**, 50 μM ATP, 2 U alkaline phosphatase) before the system was saturated (Figure 2.29).

The decreasing efficiency with each consecutive cycle can probably be attributed to the accumulation of waste in the system, as reported for other systems.[23] The accumulation of waste is a general problem in the development of systems which self-assemble under dissipative conditions. A way to by-pass the problem is to carry out the assembly under continuous flow or dialysis conditions where the waste products can be removed from the system as they are produced.[46]

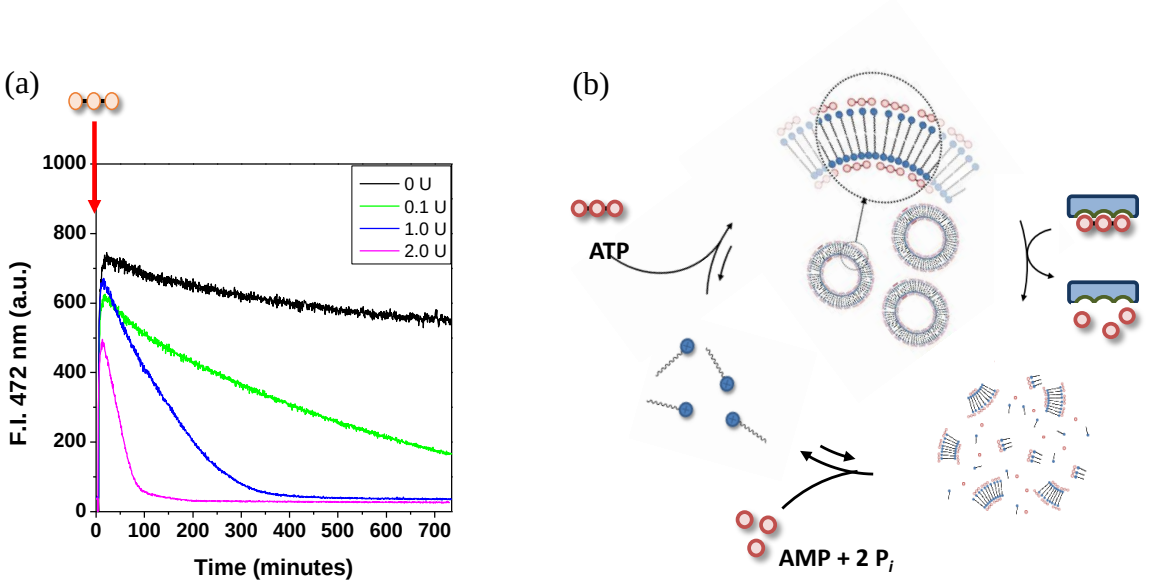

Figure 2.28: Figure showing the F.I. 472 nm for laurdan in the presence of surfactant **17** and increasing amount of alkaline phosphatase upon addition of ATP. [Laurdan] = 2 μM, λ_{ex} = 370 nm, Slits = 5/10 nm (ex/em), 25 ºC, [HEPES] = 5 mM , pH 7.0, [Surfactant **17**] = 100 μM, [ATP] = 50 μM.

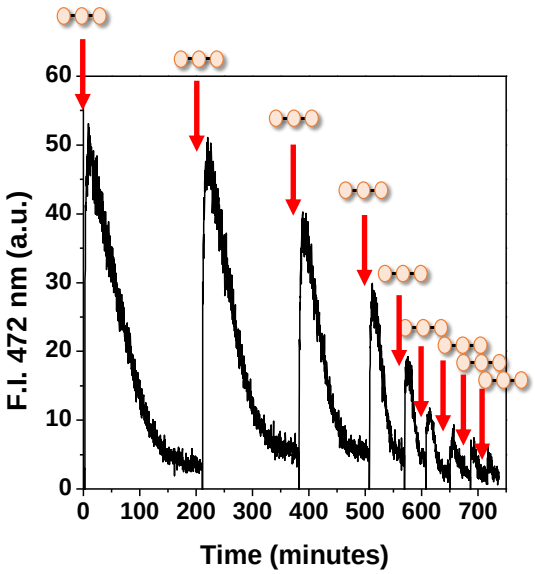

Figure 2.29: Figure showing the F.I. 472 nm for laurdan dye in the presence of surfactant and alkaline phosphatase upon repeated additions of ATP. λ_{ex} = 370 nm, Slits = 5/10 nm (ex/em), 25 ºC, [HEPES] = 5 mM , pH 7.0, [Laurdan] = 2 μM, [Surfactant **17**] = 100 μM, [ATP] = 50 μM, [alkaline phosphatase] = 2 U.

2.4 Conclusions

In this study, a surfactant with a shorter C_{12} chain attached to a TACN-macrocyle was synthesized and the resulting complex with Zn^{2+}, $C_{12}TACN{\bullet}Zn^{2+}$, **17** was used for self-assembly studies. The surfactant **17** has a lower propensity to aggregate compared to the analogous compound $C_{16}TACN{\bullet}Zn^{2+}$**4** with a C_{16} chain. This caused an increase in the *cac*. Addition of ATP to the monomer lead to the templation of vesicles well below the *cac*. Under dissipative conditions, installed by the addition of the enzyme alkaline phosphatase, transient vesicle formation was observed upon the addition of ATP. Hydrolysis of ATP into AMP and Pi lead to dissociation and the process could be repeated upon re-addition of ATP. In the next Chapter studies will be carried out to investigate the use of these transient vesicles for the promotion and regulation of a hydrazone bond formation reaction in water.

2.5 Experimental

2.5.1 Materials and methods

2.5.1.1 Instrumentation

NMR Analysis

^{1}H were recorded using a Bruker spectrometer operating at 300 MHz for ^{1}H. ^{13}C NMR (proton decoupled) and ^{31}P NMR spectra were recorded on a Bruker AV500 operating at 500 MHz for ^{1}H, at 126 MHz for ^{13}C and at 202 MHz for ^{31}P. Chemical shifts, δ are reported in ppm and were referenced against TMS (δ_H = 0.00 ppm) or the solvent residual peak (δ_H = 7.26 for $CDCl_3$, δ_H = 2.49 ppm for DMSO-d_5 residual peak, δ_H = 3.31 for CD_3OD residual peak), (δ_C = 77.16 ppm for $CDCl_3$, δ_C = 39.52 ppm for DMSO-d_5 residual peak, δ_C = 49.00 for CD_3OD residual peak).[47] A solution of $Na_5P_3O_{10}$ at pH 7 (HEPES buffer 5 mM) was used as a coaxial reference for ^{31}P NMR spectra ($Na_5P_3O_{10}$ gives a triplet centered at δ = –21.16 ppm and a doublet centered at δ = –6.42 ppm).[48] Abbreviations for multiplicity are as follows: s = singlet, br s = broad singlet, d = doublet, t = triplet, q = quartet, m = multiplet, dd = doublet of doublet, etc.).

MS Measurements

ESI-MS measurements were acquired on an Agilent Technologies 1100 Series LC/MSD Trap-SL spectrometer, equipped with an ESI source, hexapole filter and ionic trap.

pH Measurements

The pH of buffer solutions was determined at room temperature using a Metrohm-632 pH meter equipped with a Ag/AgCl/KCl reference electrode and calibrated with standard buffer solutions at pH 7.00 and pH 10.00.

UV-Vis Measurements

UV-Vis measurements were recorded on a Varian Cary50 spectrophotometer holding a thermostated multiple cuvette holder or a Varian Cary100 spectrophotometer hosted with a thermostated multiple cuvette holder. Individual spectra were acquired in Scan Mode while kinetics were followed in Scanning Kinetics Mode. The spectra were then exported and analysed using Excel and plotted using Origin. Analysis were conducted using 1 mL Quartz cuvettes.

Fluorescence Spectroscopy

Fluorescence measurements were recorded on a Varian Cary Eclipse Fluorescence spectrophotometer equipped with a thermostated cell holder hosting a maximum of 4 cuvettes. Experiments were typically conducted in 1 mL fluorescence quartz cuvettes. Fluorescence spectra were obtained in Scan mode while other experiments were determined in Kinetics Mode where the emission at a particular wavelength was monitored over time. After each addition of the respective component to the sample cuvette, the sample was allowed to equilibrate before noting the reading to ensure an accurate reading.

UPLC Analysis

The UHPLC analysis were performed on an Agilent Technologies 1290 Infinity equipped with a DAD detector and a Quadrupole LC/MS. Conditions: Flow rate: 0.6 ml/min, Gradient: 5-95%B (A: H_2O+0.1%HCOOH, B: ACN+ 0.1% HCOOH) from 0.00 to 5.00 min; 95-100 % B in 5 to 5.10 min; 100 % B from 5.10 to 8.10 min; 100-5 % B in 8.10 to 9.10 min; and finally 5% B from 9.10 to 10.00 min. Column: Agilent Zorbax SB-C3 Rapid Resolution HT 3.0 × 100 mm 1.8 micron. Early studies were carried out using a Zorbax Eclipse SB-C8 Rapid Resolution HD 2.1 × 100 mm 1.8 micron**.** Injection volume: 20 µL Column temperature: 40 ^{o}C.

DLS Analysis

DLS measurements were recorded on a Malvern Zetasizer Nano-S instrument. Samples were analysed in disposable low volume cuvettes.

TEM Analysis

TEM images were recorded on a Jeol 300 PX electron microscope. One drop of sample was placed on the sample grid for 1 minute. For staining purposes, it was then placed on a drop of uranyl acetate (2%) for 30 s. The solvent was evaporated before the stained grid was imaged. TEM images were elaborated using the software ImageJ (http:// rsb.info.nih.gov/ij/).

2.5.1.2 Materials

All fine chemicals were sourced from commercial suppliers and were used directly without purification unless mentioned. The final solutions for analysis by UV-Vis and UPLC were

prepared from stock solutions prepared in the respective solvent and diluted in MilliQ water.

ATP, ADP and AMP were obtained from Sigma Aldrich. Solutions were prepared as an approximately 10 mM solution in MilliQ water by weight and the exact concentration was calculated by UV-Vis spectroscopy using the molar extinction coefficients: ε_{259} (ATP, ADP AMP) = 15400 M^{-1} cm^{-1}.[49] Inorganic phosphate solution was prepared as a 20 mM stock solution by weight in MilliQ water.

The aldehydes 4-carboxybenzaldehyde, **11** and 2-pyridinecarboxylaldehyde, **14** the amine *p*-toluidine, **12** and the hydrazide 4-chlorophenylhydrazine, **15** were purchased from Sigma Aldrich and used without further purification. Solutions were prepared by weight in acetonitrile at the required concentration, typically 20 mM fresh before use. The concentration of **14** was further determined by UV-Vis spectroscopy using the molar extinction coefficient, ε = 5290 M^{-1} cm^{-1}.[51]

The $Zn(NO_3)_2$-stock solution was standardized using EDTA following standard procedures.

The buffer 4-(2-hydroxyethyl)-1-piperazineethanesulfonic acid (HEPES) was procured from Sigma-Aldrich and used without further purification. The buffer were prepared as 100 mM solutions in MilliQ water and adjusted to a pH of 7.0.

The fluorophores DPH, 1,6-diphenyl-1,3,5- hexatriene (**18**) and laurdan, 6-dodecanoyl-N,N-dimethyl-2-naphthylamine (**19**) were procured from Sigma-Aldrich and used without further purification.

The enzymes potato apyrase and alkaline phosphatase were obtained from Sigma Aldrich and used without further purification. The apyrase was dissolved in 1.0 mL of MilliQ water to give a concentration of 100 U/mL, divided into working aliquots of 20 µL and preserved at -20 ^{o}C. The solution was further diluted by a factor of 10 in order to obtain a stock solution of 10 U/mL when necessary. The alkaline phosphatase was diluted in 1 mL water to give a concentration of 1000 U/mL.

2.5.2 Synthesis

2.5.2.1 Synthesis of the surfactants

2.5.2.1.1 Synthesis of the surfactant C_{16}TACN

The surfactant was synthesized using a three-step pathway as described previously (Scheme 2.5).[23] Two of the nitrogen atoms on the macrocycle 1,4,7-triazacyclononane (TACN), **20** were deprotected by a Boc group,[52] a common protecting group for amines.[53] The Boc group was introduced by reacting **20** with 2-(Boc-oxyimino)-2-phenylacetonitrile (Boc-ON) in basic conditions (triethylamine (TEA)) in chloroform. The TEA functions as a proton scavenger to avoid the protonation of the amine groups. The desired di-protected macrocyle, **21**, is the major product but the mono and tri-Boc side products, together with any residual reagents are removed by a series of extractions. Washing the solution with aqueous $NaHCO_3$ and brine removes triethylamine residues and mono-Boc derivatives. Washing with aqueous citric acid protonates the amine groups of the Boc derivatives. Basification of the citric acid solution deprotonates the di-Boc TACN selectively and this is extracted into the chloroform free from other side-products. The alkyl chain is then introduced via an S_N2 nucleophilic aromatic substitution reaction with the respective bromide to give **22** under alkaline conditions in acetonitrile. The alkylated di-Boc protected macrocyle was purified by silica chromatography and acidified with 6 N HCl in order to give the pure C_{16}TACN surfactant, **23**, as the hydrochloride salt, an off-white solid. The product **23** was characterised by ^{1}H NMR, ^{13}C NMR and ESI. The solid was preserved in the fridge. The final C_{16}TACN•Zn^{2+}, **4** was obtained by mixing **23** with an equimolar solution of $Zn(NO_3)_2$.

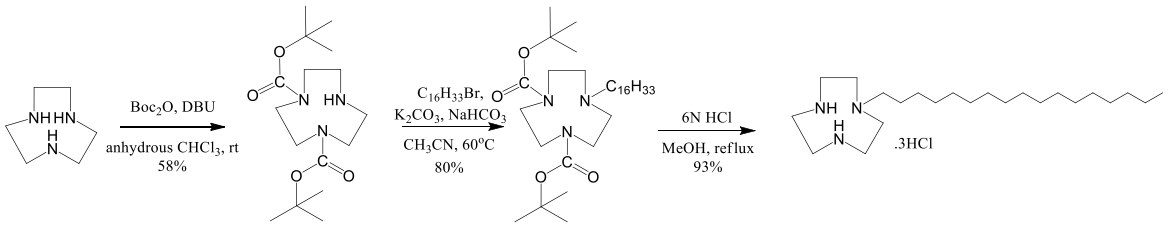

20 **21** **22** **23**

Scheme 2.5: Synthetic scheme for the synthesis of C_{16}TACN.

Synthesis of di-*tert*-Butyl 1,4,7-triazanonane-1,4-dicarboxylate (21)

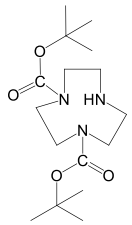

A solution of 1,4,7-triazacyclononane, **20** (506.4 mg, 3.9 mmol) was prepared in anhydrous $CHCl_3$ (40 mL) in a 250 mL round-bottomed flask equipped with a half-inch magnetic stirrer. Triethylamine (2 mL) was added dropwise to the solution. A solution of 2-(boc-oxymino)-2-phenylacetonitrile (1905 mg, 7.7 mmol) was prepared in 10 mL $CHCl_3$ and this was added dropwise under continual stirring at room temperature to the solution of **20** with a syringe pump at a rate of 1 mL/hour over a period of 20 hours. The solution was stirred for a further two hours and the solvent was evaporated under reduced pressure. The residual solid was dissolved in 50 mL of $CHCl_3$ and washed with 5% aqueous $NaHCO_3$ (3 x 10 mL), brine (2 x 20 mL) and 10% aqueous citric acid (6 x 10 mL). The acidic aqueous solution was basified with 2M NaOH to pH 11, and extracted with $CHCl_3$ (3 x 20 mL). The organic phase was dried over $MgSO_4$ and filtered. The solvent was evaporated under reduced pressure to give 733.4 mg pure **21** as a light yellow oil. The spectral data was in accordance to the literature.[54]

Yield: 57.6%

R_f = 0.31 ($CHCl_3$:MeOH 94:6)

^{1}H NMR ($CDCl_3$, 300 MHz, 300 K, ppm): δ 1.42 (s, 18 H, 6 × CH_3), 2.53 (bs, 1H, NH), 3.52 (s, 4H, 2 × CH_2N), 3.18–3.30 (m, 4H, 2 × CH_2N), 3.36–3.45 (m, 4H, 2 × CH_2N).

Synthesis of 1-Hexadecyl-4,7-bis(*tert*-butoxycarbonyl)-1,4,7-triazacyclononane (22)

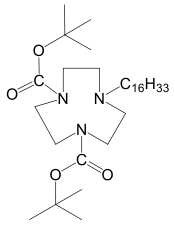

A mass of 100 mg of **21** (0.3 mmol) and 153 µl of hexadecyl bromide (152.8 mg, 5 mmol) were dissolved in 10 mL acetonitrile in a 50 mL round bottomed flask. A mass of 157.1 mg K_2CO_3 and 87.4 mg $NaHCO_3$ were added and the suspension was stirred at 60 ºC for 9 hours. The mixture was subsequently filtered under gooch and the solvent evaporated under reduced pressure. The residual solid was then purified by silica flash chromatography using a mixture of methanol and dichloromethane as an eluent (3% CH_2Cl_2:97% MeOH). Compound **22** was obtained as a pale yellow oil (107.1 mg, 82.45%). A drop of 1M NaOH was added to the proton NMR sample since the acidity in the $CDCl_3$ broadened the peaks of the product. Basification of the solution yielded the desired spectrum.

R_f = 0.1 (CH_2Cl_2: MeOH 97:3)

^{1}H NMR ($CDCl_3$, 400 MHz, 300 K, ppm): δ 0.81 (t, *J*= 6.9 Hz, 3H, CH3), 1.19 (s, 26 H, 13 × CH_2), 1.40 (m, 18H, 6 × CH_3), 2.10 (s, 2H, CH_2), 2.39 (m, 2H, CH_2N), 2.55 (m, 4H,2 × CH_2N), 3.17 (m, 4H, 2 × CH_2N), 3.38 (m, 4H, 2 × CH_2N).

Synthesis of 1-Hexadecyl-1,4,7-triazacyclononane (23)

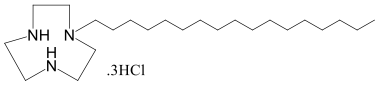

Compound **22** obtained previously (107.1 mg) were dissolved in 7 mL MeOH in a 25 mL round-bottomed flask. A volume of 6 N HCl was added to the solution and the mixture was stirred for two hours at 60 ºC. The solvent was evaporated under reduced pressure and the solid was collected as a pinkish-white solid in almost quantitative yield. The solid was washed with cold chloroform to remove any organic residue.

^{1}H NMR (CD_3OD, 300 MHz, 300 K, ppm): δ 0.80 (m, 3H, CH_3), 1.20 (s, 26 H, 9 × CH_2), 1.55 (m, 2H, CH_2), 2.76 (m, 2H, CH_2N), 3.01 (m, 4H,2 × CH_2N), 3.21 (s, 4H, 2 × CH_2N), 3.46 (s, 4H, 2 × CH_2N).

^{13}C NMR (CD_3OD, 125 MHz, 300 K): δ 13.16, 22.46, 24.37, 27.12, 29.19, 29.32, 29.50, 31.80, 42.29, 43.41, 55.96

ESI-MS(ESI+, H_2O:CH_3CN = 1:1). M.z calculated for $C_{18}H_{39}N_3$ [M+H]+ 298.3217, found 298.3.

2.5.2.1.2 Synthesis of the shorter chain surfactant C_{12}TACN

The surfactant with a C_{12}-chain was synthesized using the same procedure as described for the C_{16}TACN surfactant (Scheme 2.6). Protection of two of the nitrogens of TACN, **20** gave **21** in 58% yield, which was subsequently alkylated under basic conditions to afford **24** in 80% yield. This was deprotected under acidic conditions to give the surfactant C_{12}TACN, **25**, as the hydrochlorice salt (slight pink solid). The solid was subsequently washed with chloroform to remove any organic residue and characterised by ^{1}H NMR, ^{13}C NMR and ESI-MS. The solid was preserved in the fridge. Solutions of surfactant were prepared as small volume 10 mM solutions in milliQ water and preserved at room temperature to avoid aggregation and precipitation. The solutions were subsequently diluted to the required concentration prior to analysis. The Zn^{2+} was added to the surfactant in equimolar quantities during the setting up of the experiments to give the final surfactant C_{12}TACN•Zn^{2+}, **17**.

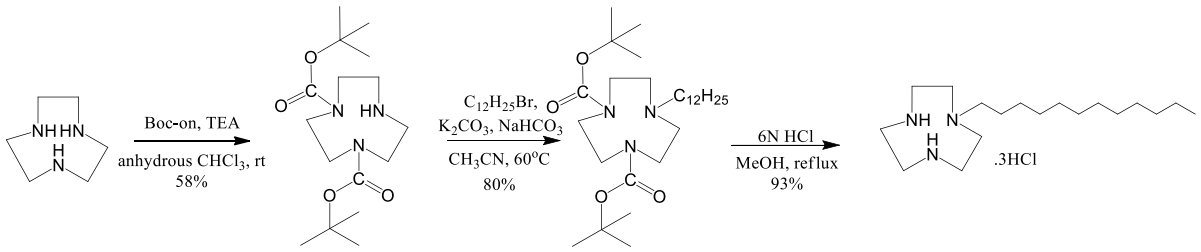

20 **21** **24** **25**

Scheme 2.6: Synthetic scheme for the synthesis of C_{12}TACN.

Synthesis of 1-Dodecyl-4,7-bis(tert-butoxycarbonyl)-1,4,7-triazcyclononane (24)

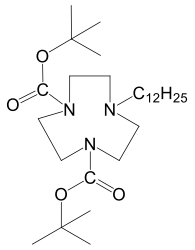

A mass of 200.5 mg of **21** (0.609 mmol) and 171 µl of dodecyl bromide (0.177 g, 0.710 mmol) were dissolved in 10 mL acetonitrile in a 50 mL round bottomed flask. A mass of 329.5 mg (1.994 mmol) $K_2CO_3.6H_2O$ and 215.8 mg (2.569 mmol) $NaHCO_3$ were added and the suspension was stirred at 60 ^oC for 9 hours. The mixture was subsequently filtered under gooch and the solvent evaporated under reduced pressure. The residual solid was then purified by silica flash chromatography using a mixture of methanol and dichloromethane as an eluent. A gradient was used, starting with 2% MeOH, which was gradually increased to 3% MeOH until the product was eluted and then increasing the gradient to 10% MEOH. Compound **24** was obtained as a pale yellow oil (216.1 mg, 71.35%).

^1H NMR ($CDCl_3$, 400 MHz, 300 K, ppm): δ 0.81 (t, *J*= 6.9 Hz, 3H, CH3), 1.19 (s, 18 H, 9 × CH_2), 1.40 (m, 18H, 6 × CH_3), 1.52 (s, 2H, CH_2), 2.39 (s, 2H, CH_2N), 2.54 (m, 4H,2 × CH_2N), 3.17 (m, 4H, 2 × CH_2N), 3.38 (m, 4H, 2 × CH_2N).

Synthesis of 1-Dodecyl-1,4,7-triazacyclononane (25)

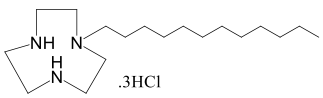

Compound **24** obtained previously (216.1 mg, 0.000435 mol) were dissolved in 7 mL MeOH in a 25 mL round-bottomed flask. A volume of 6 N HCl was added to the solution and the mixture was stirred for two hours at 60 ^oC. The solvent was evaporated under reduced pressure and the solid was collected as a pinkish-white solid in almost quantitative yield (120.2 mg, 93% yield). The solid was washed with cold chloroform to remove any organic residue.

^{1}H NMR (CD_3OD, 300 MHz, 300 K, ppm): δ 0.86 (m, 3H, CH_3), 1.20 (s, 18H, 9 × CH_2), 1.54 (s, 2H, CH_2), 2.75 (s, 2H, CH_2N), 2.99 (s, 4H,2 × CH_2N), 3.22 (s, 4H, 2 × CH_2N), 3.45 (s, 4H, 2 × CH_2N).

^{13}C NMR (CD_3OD, 125 MHz, 300 K): δ 14.48, 23.78, 25.72, 28.46, 30.52, 30.65, 30.78, 33.12, 43.67, 44.83, 57.25

ESI-MS(ESI+, H_2O:CH_3CN = 1:1). M.z calculated for $C_{18}H_{39}N_3$ [M+H]+ 298.3217, found 298.3.

2.5.2.2 General synthetic method for the synthesis of reference imine/hydrazone

The imine and hydrazones were synthesized using general literature procedures for reference purposes.[55] Approximately equimolar quantities of the respective amine/hydrazine/hydrazide and aldehyde were dissolved in the minimum quantity of ethanol in a round-bottomed flasks and the solution stirred with a magnetic stirrer. A slight excess of one of the reagents was typically used to ensure completion of the reaction. A few drops of TFA were sometimes added as a catalyst. The hydrazones precipitated out of solution as white or yellow solids, which were filtered and, if necessary, recrystallised from methanol.

Imine 13

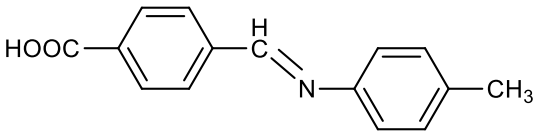

Imine **13** was synthesized from 546.7 mg (3.64 mmol) 4-carboxylbenzaldehyde, **11** and 345.6 mg (3.33 mmol) *p*-toluidine, **12** in 40 mL absolute ethanol. The product precipitated out of solution as a bright, light yellow solid, which was filtered, washed with cold absolute ethanol and recrystallised from ethanol.

R_f = 0.50 (Petroleum ether: ethyl acetate 6:4)

^{1}H NMR (DMSO-*d6*, 300 MHz, 300 K, ppm): δ 2.33 (s, 3H, CH_3), 7.24 (s, 4H, Ar-H), 8.00-8.10 (m, 4H, Ar-H), 8.72 (s, 1H, CH=N), 13.13 (s, 1H, COOH)

UV-*vis*: λ_{max} = 342 nm (methanol)

Hydrazone 16

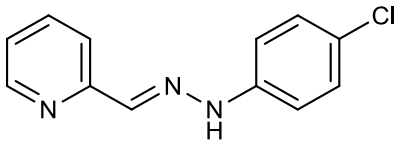

Hydrazone **16** was synthesized from 110 mg (1.03 mmol) pyridinecarboxyaldehyde, **14** and 180 mg (1.01 mmol) chlorophenylhydrazine, **15** under basic conditions (using 490 mg (59.7 mmol) sodium acetate in 30 ml of 50% aqueous ethanol solution. The reaction was refluxed for one hour and a bright yellow solid crystallised out upon cooling. This was recrystallised from ethanol to give the pure solid.

^{1}H NMR (DMSO-*d6*, 300 MHz, 300 K, ppm): δ7.11 (d, *J* = 8.2 Hz, 2H, Ar-H), 7.28 (d, *J* = 8.1 Hz, Ar-H), 7.77-7.79 (m, 2H, Ar-H), 7.89 (s, 1H, Ar-H), 7.92-7.94 (m, 1H, Ar-H), 8.51 (s, 1H, CH=N), 10.79 (s (broad), 1H, NH)

UV-*vis*: λ_{max} = 353 nm (methanol)

2.5.3 Following the reactions by UV-Vis spectroscopy

The solutions of reagents needed to follow the reactions by UV-Vis spectroscopy were prepared in 1 mL quartz cuvettes. The required volumes of the appropriate stock solutions were added to the cuvette and the solution made up with MilliQ water to give a final volume of 1 mL. The order of addition of solutions was the following (as needed): buffer, MilliQ water, surfactant, Zn^{2+}, reagents, added sequentially, ATP. The baseline was taken on individual cuvettes prior to the addition of the reagents. One of the reagents was then added and the spectrum taken. The reaction was started by the addition of the second reagent in the case of the reaction in buffer and surfactant and the addition of the second reagent followed by the addition of ATP in the case of the reaction in vesicles. The solution was shaken well after the addition of each reactant to ensure homogenous solution and to minimise immediate reaction due to local concentrations of reagents. ATP was added after the reagents in order to entrap the reagents inside the vesicles since diffusion of the reactants to the inside of the bilayer would require crossing a charged barrier, which might prove to be difficult, thus affecting the results.

Spectra were taken in Scanning Kinetics mode, taking spectra between 220 nm and 600 nm at regular intervals. Using Scanning Kinetics was more laborous than using Kinetics mode, but enabled better monitoring of the reaction with the possibility of monitoring multiple wavelengths and checking whether the reaction was proceeding as expected. The individual spectra were exported to excel where they were separated according to the different samples. From the data, the absorbance of the baseline at 600 nm was subtracted from the absorbance at the λ_{max} of the hydrazone in the corresponding solvent (buffer, surfactant, vesicles) and the corrected absorbance was converted to concentration of hydrazone by using the calibration curve of the hydrazone in the appropriate solvent.

It was necessary to correct for the baseline at 600 nm because the formation of vesicles resulted in a degree of turbidity in the solution which was evident in the UV-Vis spectrum as an increase in the baseline of the spectrum (Figure 2.30). Correction of the values for the baseline minimised the effect of this turbidity on the results obtained. The following is an example of how the baseline in the UV-*vis* spectrum changed over time during the experiments, illustrating the importance of correcting for the baseline in order to obtain reliable measurements.

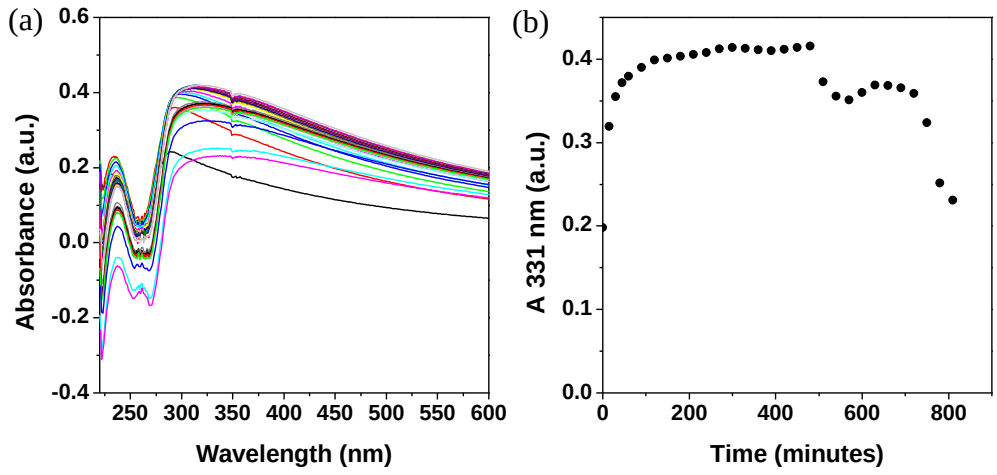

Figure 2.30: (a) Changes in the baseline of the UV-*vis* spectrum when monitoring the absorbance in the presence of 200 µM C_{12}TACN•Zn^{2+} and 200 µM ATP. (b) Changes at an absorbance of 331 nm over time.

2.5.4 Following the reactions by UPLC

In order to follow the reactions, samples were prepared in HPLC amber vials. Amber vials were used to minimise photo-oxidation of the aldehydes. As an additional precaution, the light in the UPLC sample holder was switched off during analysis. The suitability of the UPLC system in each experiment was verified by periodic injection of a solution of the hydrazide, which was known to be stable. The area of the sample was monitored regularly and ensured to be constant throughout the analysis.

The reaction solution was prepared from the appropriate stock solutions to give a final volume of 1 mL. The order of addition of solutions was the following (as needed): buffer, MilliQ water, surfactant, Zn^{2+}, reagents, added sequentially, ATP. Any other reagent which needed to be added, e.g. potato apyrase or Ca^{2+} were added just before the addition of the reactants. The last reagents to be added were introduced in the solution just before injection in order to minimise the time difference from sample preparation to sample injection. The solution was shaken well after the addition of each reactant to ensure homogenous solution and to minimise immediate reaction due to local concentrations of reagents. Samples were injected at regular intervals, allowing some washing steps with 100% ACN + 0.1% HCOOH in between analysis to ensure that the column was clean from the surfactant.

The reagents were monitored at an appropriate wavelength as determined by UV-*vis* spectroscopy. The identity of the components was verified by MS, carried out once, and when verification was necesary. The area of the component of interest was monitored over time and then converted to concentration through the use of the appropriate calibration curve constructed using the appropriate standard solutions.

2.5.4.1 Calibration curve for quantification of hydrazone, 16 formed between 2-pyridinecarboxylaldehyde, 14 and chlorophenylhydrazine, 15

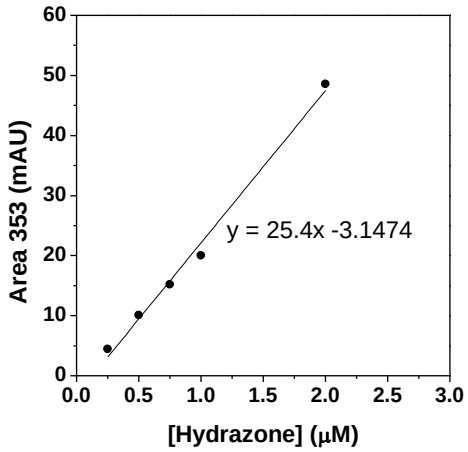

Figure 2.31: Figure showing the area at 353 nm for hydrazone **16** at various concentrations and linear regression of the points to give the equation for the straight line. [HEPES] = 5 mM, pH 7.0

2.5.5 Following the reactions by ^{31}P NMR

The study of ATP hydrolysis by ^{31}P NMR is the subject of study of Chapter 4. The reader is referred to Chapter 4 for experimental details.

2.6 References

(1) Mann, S. *Angew. Chem., Int. Ed.* **2008**, *47*, 5306.

(2) Epstein, I. R.; Xu, B. *Nat. Nanotech.* **2016**, *11*, 312.

(3) Gale, P. A., Steed, JW (EDs) In *Supramolecular Chemsitry: From Molecules to Nanomaterials*; John Wiley and Sons Ltd. : USA, 2012; Vol. 5.

(4) Grzybowski, B. A.; Wilmer, C. E.; Kim, J.; Browne, K. P.; Bishop, K. J. M. *Soft Matter* **2009**, *5*, 1110.

(5) Heinen, L.; Walther, A. *Soft Matter* **2015**, *11*, 7857.

(6) Merindol, R.; Walther, A. *Chem. Soc. Rev.* **2017**.

(7) Desai, A.; Mitchison, T. J. *Annu. Rev. Cell Dev. Biol.* **1997**, *13*, 83.

(8) Mishra, A.; Korlepara, D. B.; Kumar, M.; Jain, A.; Jonnalagadda, N.; Bejagam, K. K.; Balasubramanian, S.; George, S. J. *Nat. Commun.* **2018**, *9*, 1295.

(9) Hess, H.; Ross, J. L. *Chem. Soc. Rev.* **2017**.

(10) Klajn, R.; Bishop, K. J. M.; Grzybowski, B. A. *Proc. Natl. Acad. Sci.* **2007**, *104*, 10305.

(11) Timonen, J. V. I.; Latikka, M.; Leibler, L.; Ras, R. H. A.; Ikkala, O. *Science* **2013**, *341*, 253.

(12) De, S.; Klajn, R. *Adv. Mater.* **2018**, *0*, 1706750.

(13) Boekhoven, J.; Brizard, A. M.; Kowlgi, K. N.; Koper, G. J.; Eelkema, R.; van Esch, J. H. *Angew. Chem.* **2010**, *122*, 4935.

(14) Boekhoven, J.; Hendriksen, W. E.; Koper, G. J.; Eelkema, R.; van Esch, J. H. *Science* **2015**, *349*, 1075.

(15) Ragazzon, G.; Prins, L. J. *Nat. Nanotech.* **2018**.

(16) della Sala, F.; Neri, S.; Maiti, S.; Chen, J. L.; Prins, L. J. *Curr. Opin. Biotechnol.* **2017**, *46*, 27.

(17) Chen, J. L. Y.; Maiti, S.; Fortunati, I.; Ferrante, C.; Prins, L. J. *Chem.–Eur. J.* **2017**, *23*, 11549.

(18) Angulo-Pachón, C. A.; Miravet, J. F. *Chem. Commun.* **2016**, *52*, 5398.

(19) Wood, C. S.; Browne, C.; Wood, D. M.; Nitschke, J. R. *ACS Cent. Sci.* **2015**, *1*, 504.

(20) Dambenieks, A.; Vu, P.; Fyles, T. *Chem. Sci.* **2014**, *5*, 3396.

(21) Pezzato, C.; Prins, L. J. *Nat. Commun.* **2015**, *6*.

(22) Fanlo-Virgós, H.; Alba, A.-N. R.; Hamieh, S.; Colomb-Delsuc, M.; Otto, S. *Angew. Chem., Int. Ed.* **2014**, *53*, 11346.

(23) Maiti, S.; Fortunati, I.; Ferrante, C.; Scrimin, P.; Prins, L. J. *Nat. Chem.* **2016**.

(24) von Kiedrowski, G.; Otto, S.; Herdewijn, P. *J. Syst. Chem.* **2010**, *1*, 1.

(25) Belowich, M. E.; Stoddart, J. F. *Chem. Soc. Rev.* **2012**, *41*, 2003.

(26) Dal Molin, M.; Gasparini, G.; Scrimin, P.; Rastrelli, F.; Prins, L. J. *Chem. Commun.* **2011**, *47*, 12476.

(27) Gasparini, G.; Vitorge, B.; Scrimin, P.; Jeannerat, D.; Prins, L. J. *Chem. Commun.* **2008**, 3034.

(28) Kool, E. T.; Park, D.-H.; Crisalli, P. *J. Am. Chem. Soc.* **2013**, *135*.

(29) Walde, P.; Umakoshi, H.; Stano, P.; Mavelli, F. *Chem. Commun.* **2014**, *50*, 10177.

(30) Hoffman, H. *Ber. Bunsenges. Phys. Chem.* **1978**, *82*, 988.

(31) R.Zana In *Encyclopedia of Surface and Colloid Science*; Hubbard, A. T., Ed.; Taylor & Francis: New York, 2002.

(32) Furton, K. G.; Norelus, A. *J. Chem. Educ.* **1993**, *70*, 254.

(33) Repáková, J.; Čapková, P.; Holopainen, J. M.; Vattulainen, I. *J. Phys. Chem. B* **2004**, *108*, 13438.
(34) Bresler, M. R.; Hagen, J. P. *J. Chem. Educ.* **2008**, *85*, 269.
(35) Berberan-Santos, M. N. *J. Chem. Educ.* **2009**, *86*, 433.
(36) della Sala, F.; Verbeet, W.; Silvestrini, S.; Fortunati, I.; Ferrante, C.; Prins, L. J. *ChemNanoMat.* **2018**, *4*, 821.
(37) Pieters, G.; Pezzato, C.; Prins, L. J. *J. Am. Chem. Soc.* **2012**, *134*, 15289.
(38) Lakowicz, J., R. *Principles of Fluorescence Spectroscopy*; 3rd ed.; Springer: USA, 2006.
(39) Uppu, D. S. S. M.; Konai, M. M.; Baul, U.; Singh, P.; Siersma, T. K.; Samaddar, S.; Vemparala, S.; Hamoen, L. W.; Narayana, C.; Haldar, J. *Chem. Sci.* **2016**, *7*, 4613.
(40) Leung, S. S. W.; Brewer, J. R.; Thewalt, J.; Bagatolli, L. *Biophys. J.* **2014**, *106*, 507a.
(41) Yu, W.; So, P. T.; French, T.; Gratton, E. *Biophys. J.* **1996**, *70*, 626.
(42) Parasassi, T.; De Stasio, G.; Ravagnan, G.; Rusch, R. M.; Gratton, E. *Biophys. J.* **1991**, *60*, 179.
(43) Lee, K.-H.; Krezanoski, J. Z.; Eiler, J. J. *Proc. Soc. Exp. Biol. Med.* **1957**, *94*, 193.
(44) Kettlun, A. M.; Espinosa, V.; García, L.; Valenzuela, M. A. *Phytochemistry* **2005**, *66*, 975.
(45) Sharma, U.; Pal, D.; Prasad, R. *Indian J. Clin. Biochem.* **2014**, *29*, 269.
(46) Sorrenti, A.; Leira-Iglesias, J.; Sato, A.; Hermans, T. M. **2017**, *8*, 15899.
(47) Fulmer, G. R.; Miller, A. J. M.; Sherden, N. H.; Gottlieb, H. E.; Nudelman, A.; Stoltz, B. M.; Bercaw, J. E.; Goldberg, K. I. *Organometallics* **2010**, *29*, 2176.
(48) Jastrzębska, A.; Szłyk, E. *Chem. Pap.* **2009**, *63*, 414.
(49) Missoouri, USA; Vol. 2018.
(50) Ceppan, M.; Fiala, R.; Brezová, V.; Panák, J.; Motlíková, V. *Chem. Papers*, **1994**, *48*, 25.
(51) Nakamoto, K.; Martell, A. E. *J. Am. Chem. Soc.* **1959**, *81*, 5857.
(52) Diez-Castellnou, M.; Mancin, F.; Scrimin, P. *J. Am. Chem. Soc.* **2014**, *136*, 1158.
(53) Greene, P. G. M. W. W. *Greene's Protective Groups in Organic Synthesis*; 4 ed.; John Wiley & Sons, Inc.: USA, 2006.
(54) Pieters, G.; Cazzolaro, A.; Bonomi, R.; Prins, L. J. *Chem. Commun.* **2012**, *48*, 1916.
(55) A.I. Vogel, A. R. T., B.S. Furnis, A.J. Hannaford, P.W.G. Smith *Vogel's Textbook of Practical Organic Chemistry*; 5 ed.; John Wiley & Sons: New York, 1991.

2.7 Appendix

2.7.1 ^{1}H NMR, ^{13}C NMR, MS Spectra

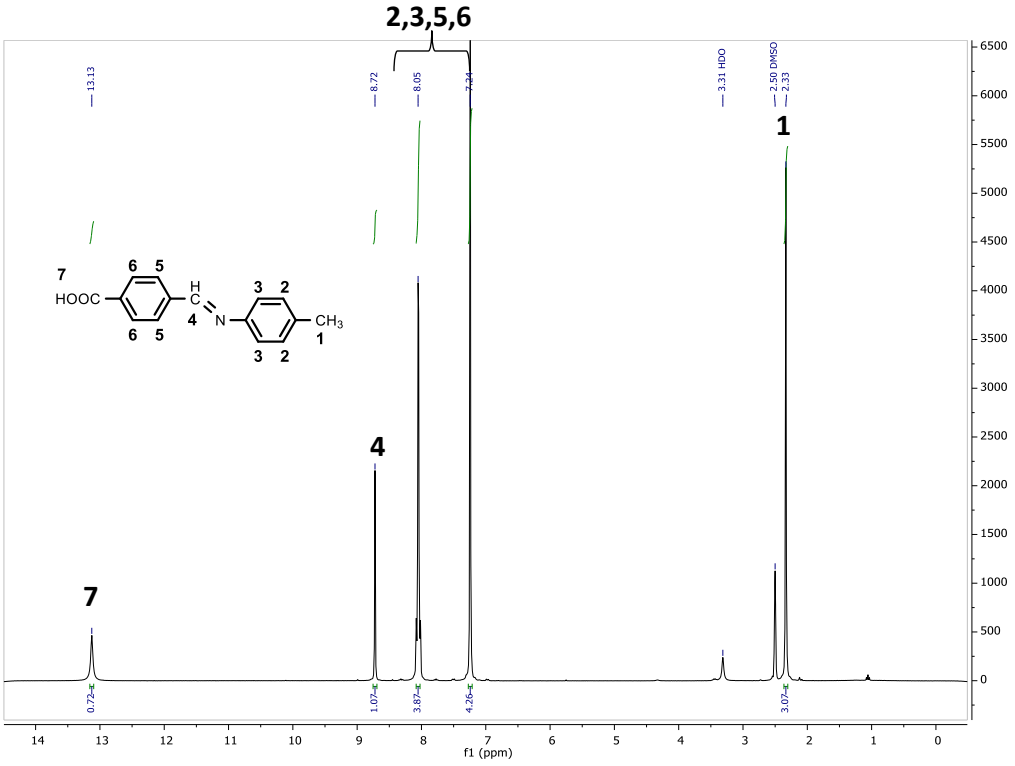

Figure 2.32: ^{1}H NMR spectrum of **13** in DMSO-*d6* (300 MHz, 300K).

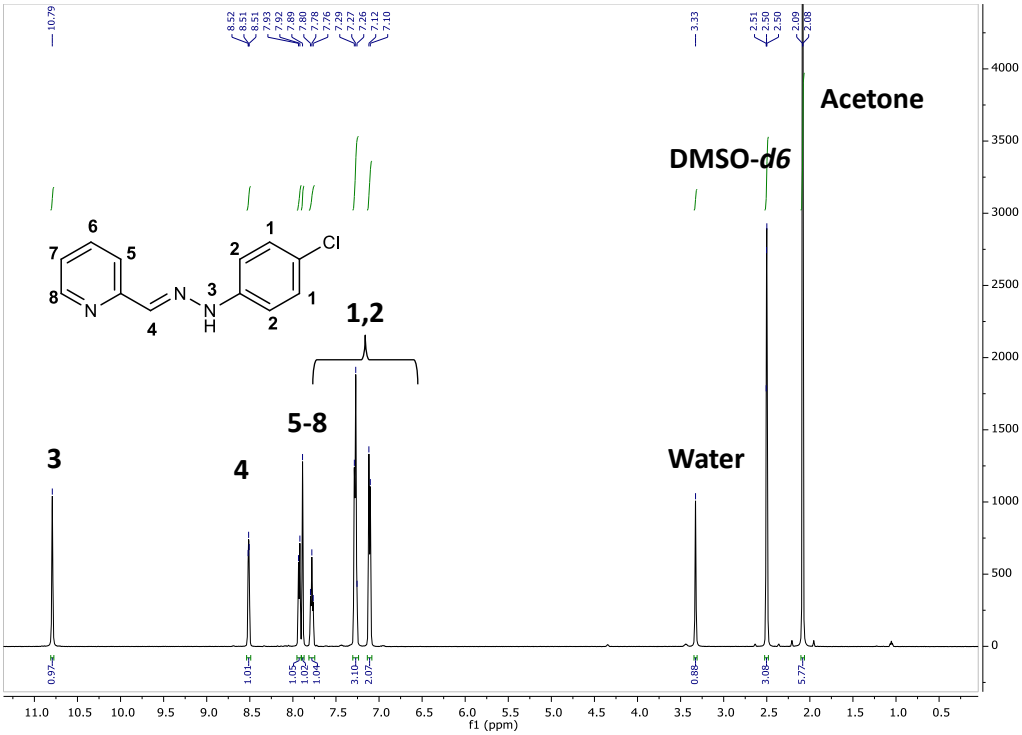

Figure 2.33: ^{1}H NMR spectrum of **16** in DMSO-*d6* (500 MHz, 300K).

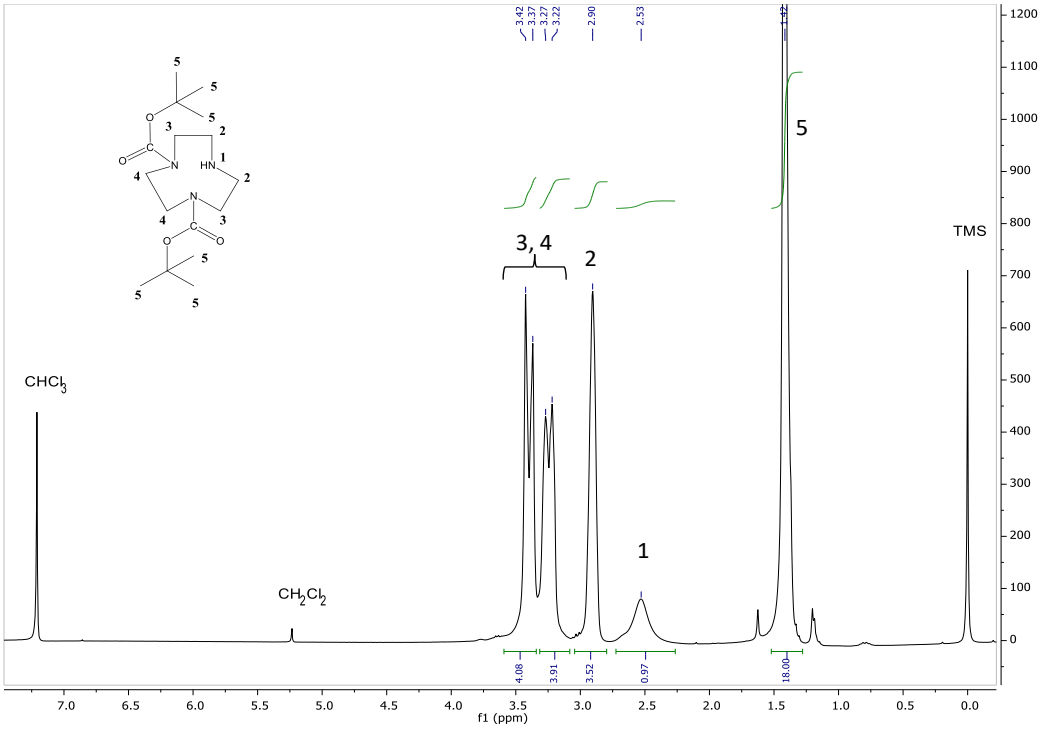

Figure 2.34: ^{1}H NMR spectrum of **21** in $CDCl_3$ (300 MHz, 300K).

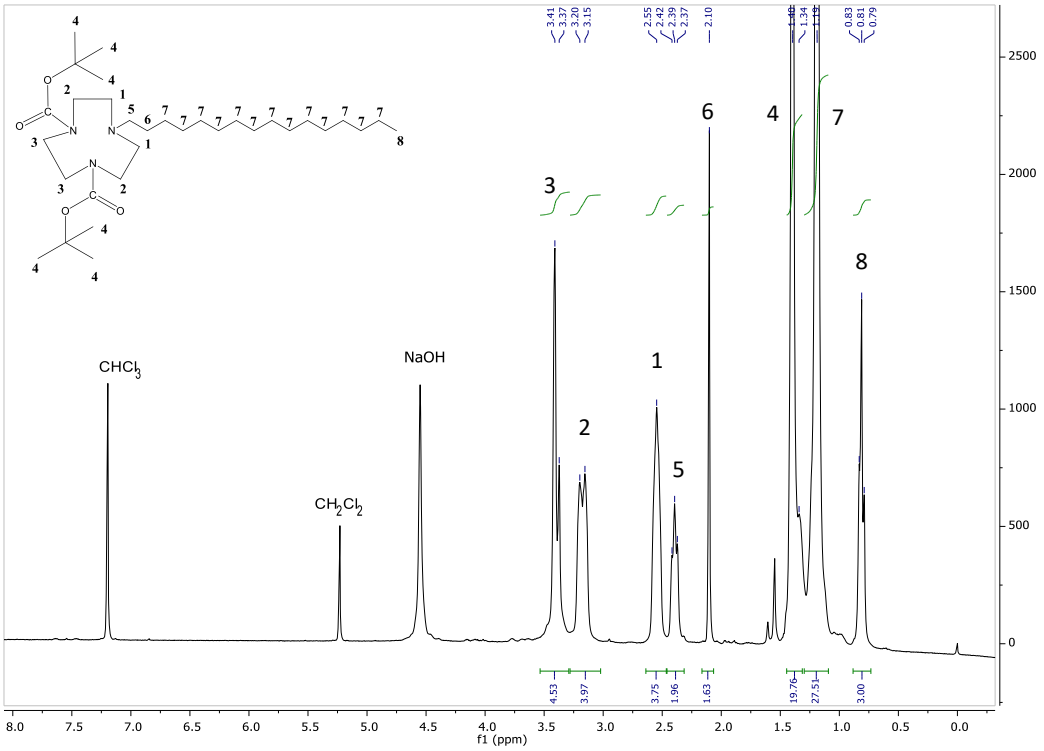

Figure 2.35: ^{1}H NMR spectrum of **22** in $CDCl_3$ (300 MHz, 300K). (A drop of NaOH was added to the solution).

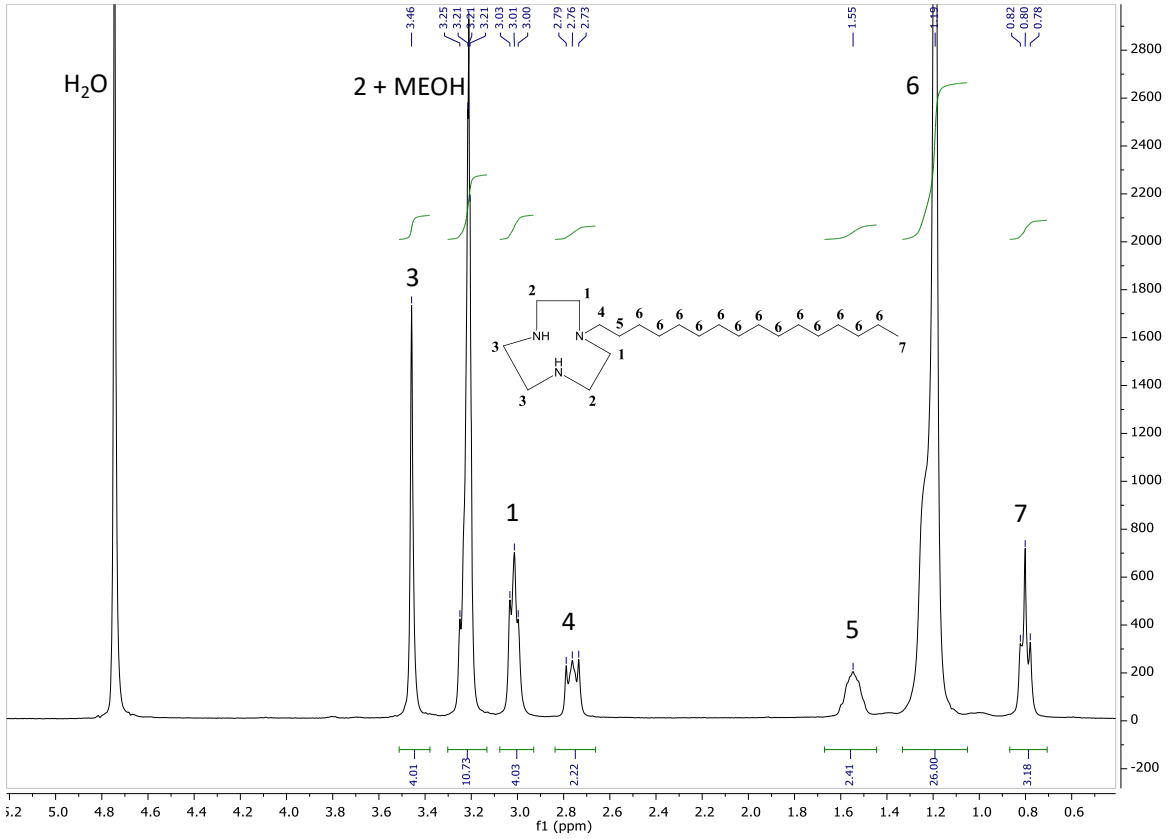

Figure 2.36 ^{1}H NMR spectrum of **23** in $CDCl_3$ (300 MHz, 300K).

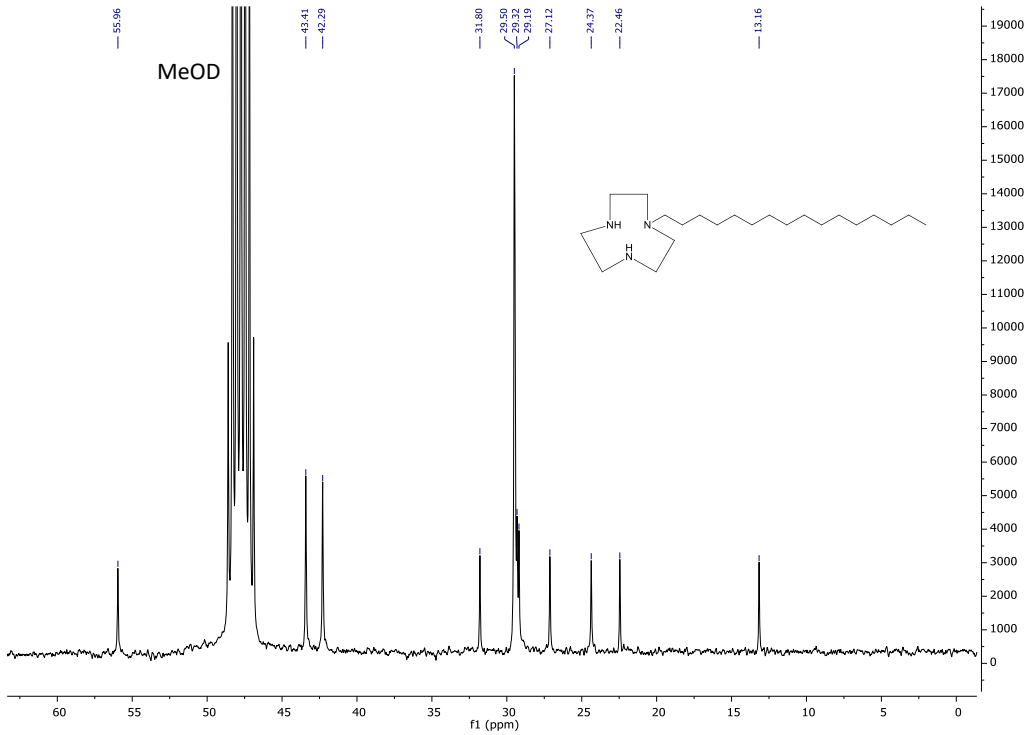

Figure 2.37: ^{13}C NMR spectrum of **23** in MeOD (125 MHz, 300K).

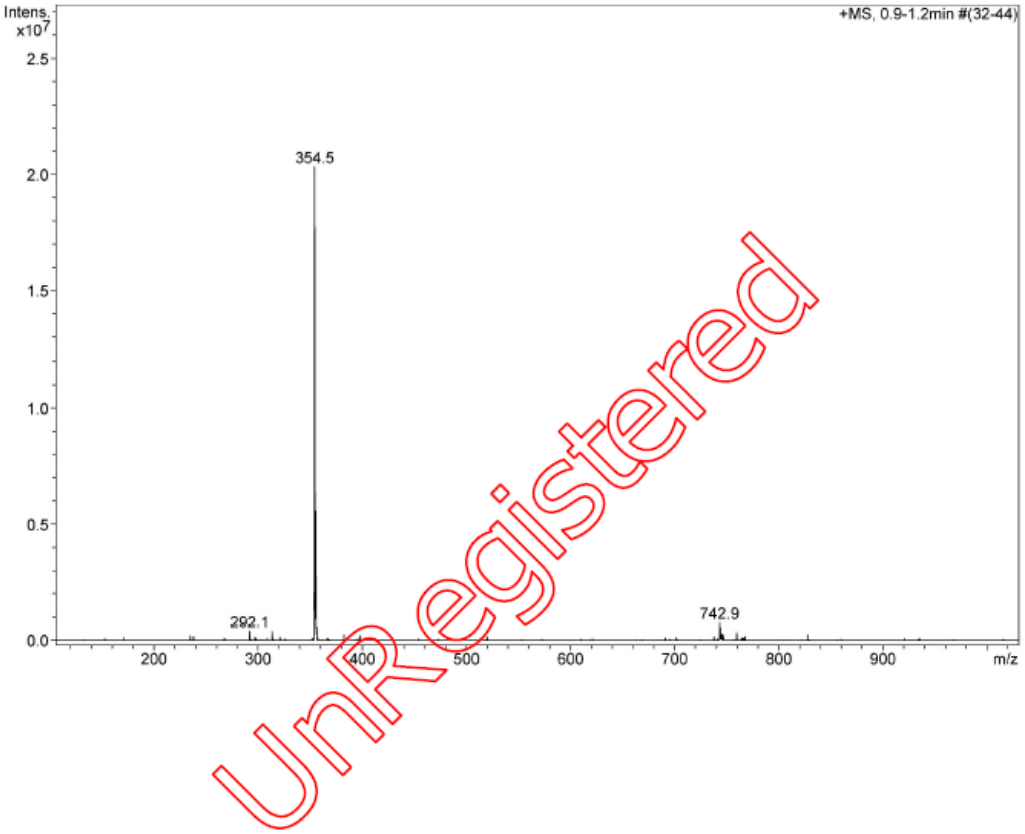

Figure 2.38: ESI-MS (ESI+, H_2O:CH_3CN = 1:1) spectrum of **23**.

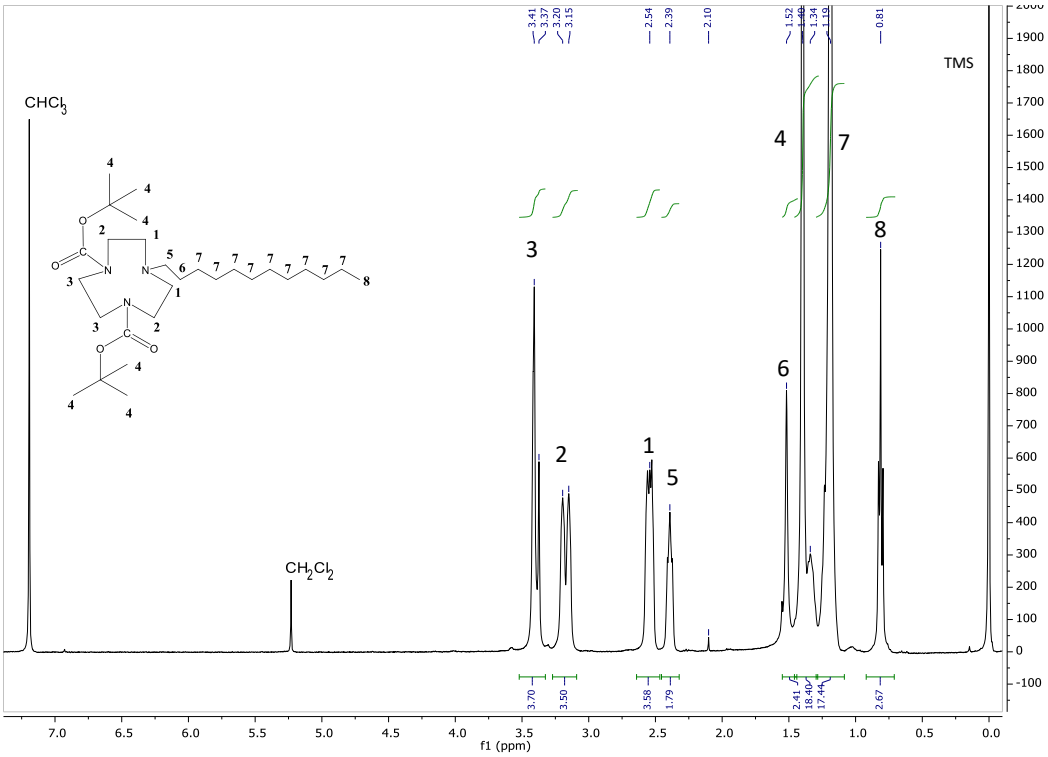

Figure 2.39: ^1H NMR spectrum of **24** in $CDCl_3$ (400 MHz, 300K).

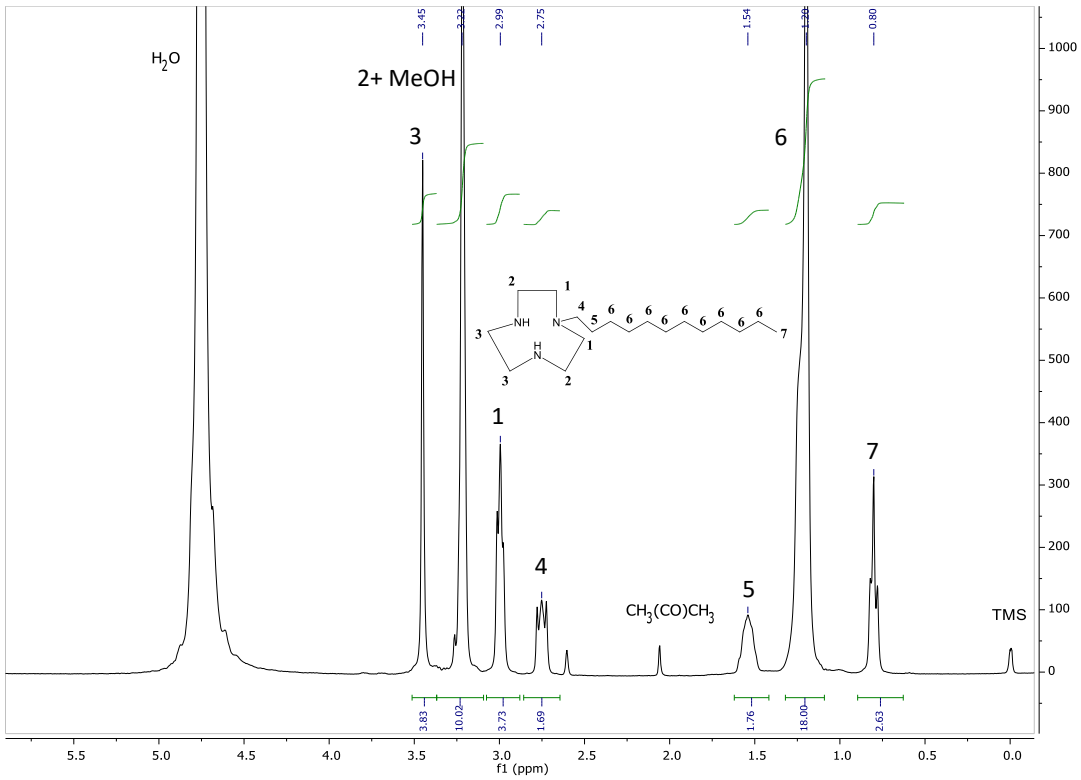

Figure 2.40: ^{1}H NMR spectrum of **25** in MeOD (300 MHz, 300K).

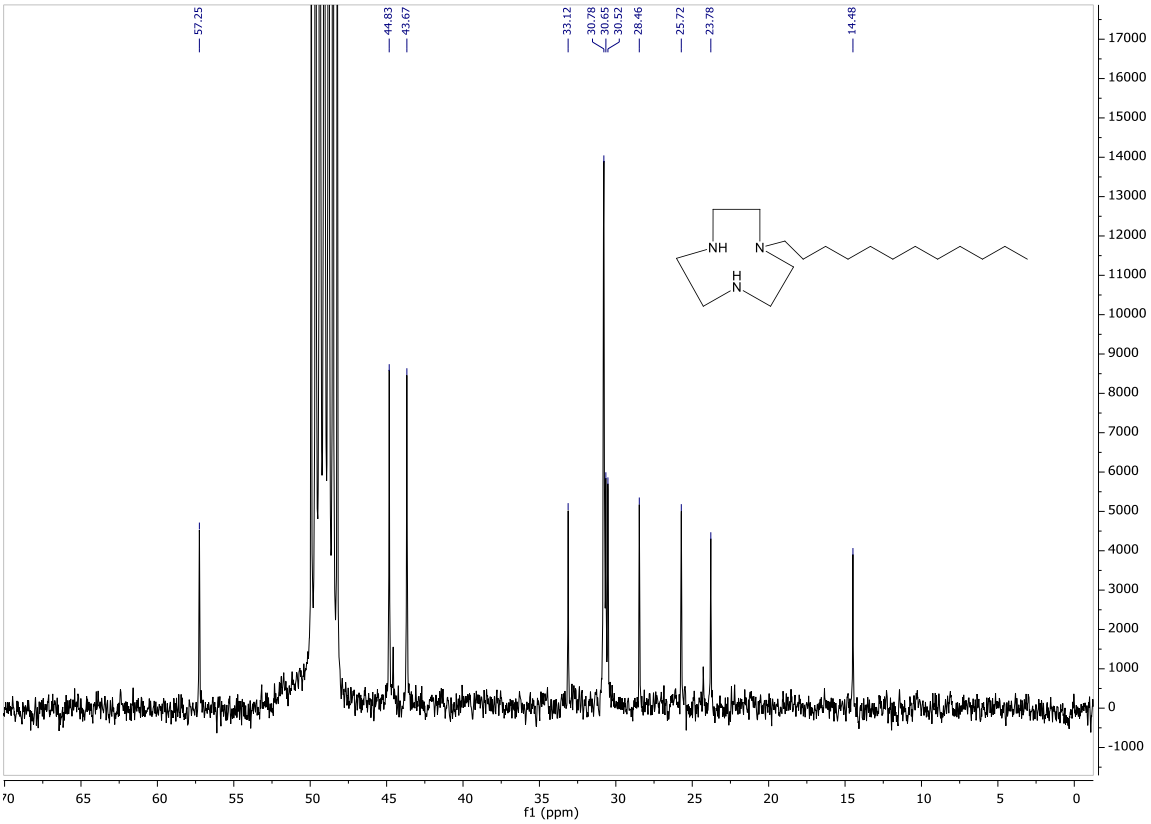

Figure 2.41: ^{13}C NMR spectrum of **25** in MeOD (125 MHz, 300K).

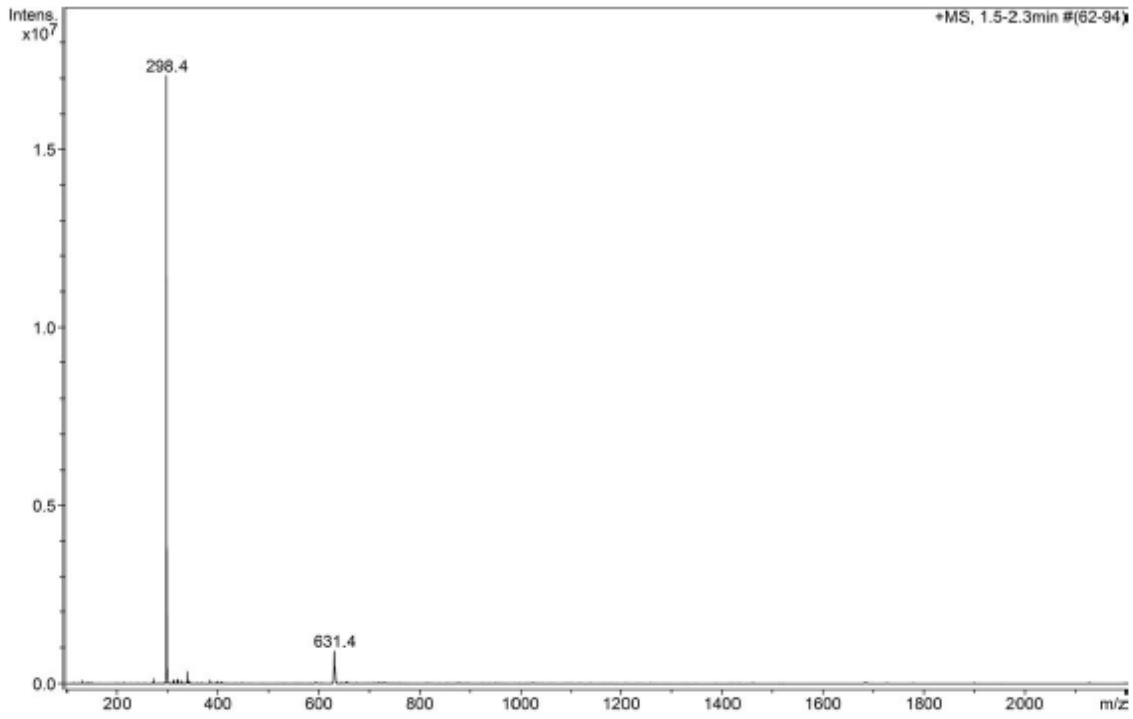

Figure 2.42: ESI-MS (ESI+, H_2O:CH_3CN = 1:1) spectrum of **25**.

2.7.2 TEM of 100 µM C_{12}TACN.Zn^{2+}

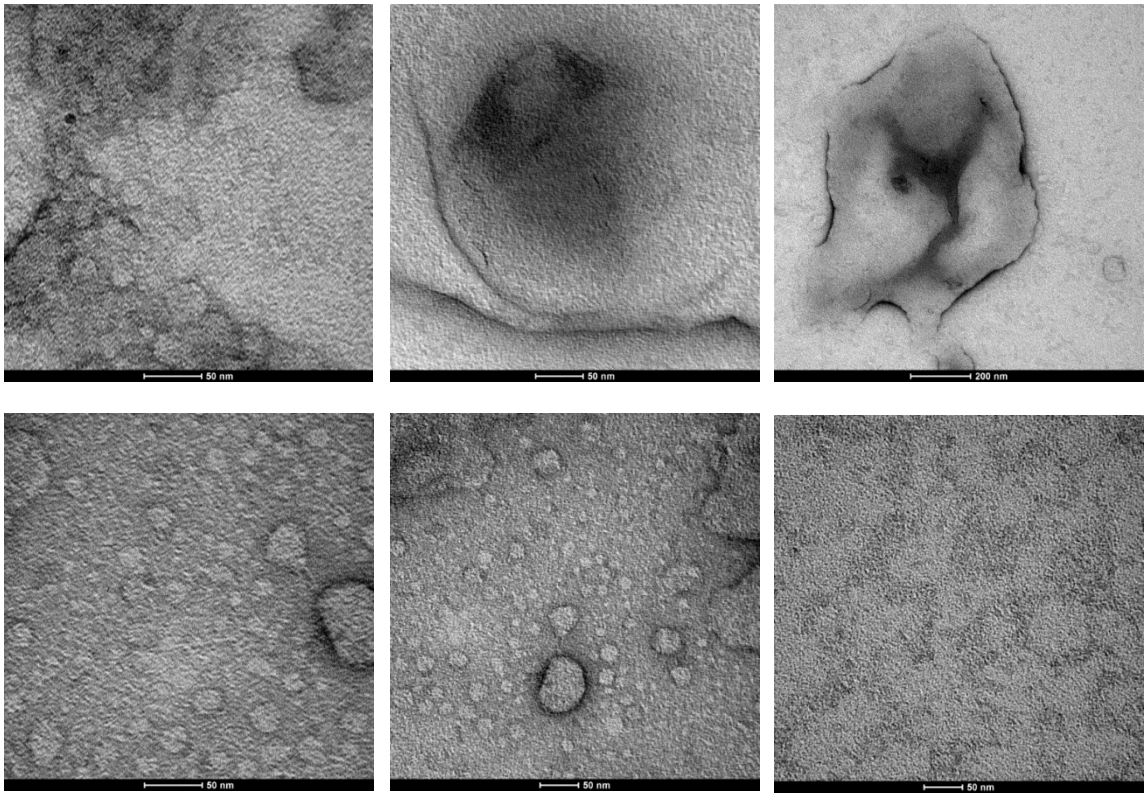

2.7.3 TEM of C_{12}TACN.Zn^{2+} at 100 µM and 50 µM ATP

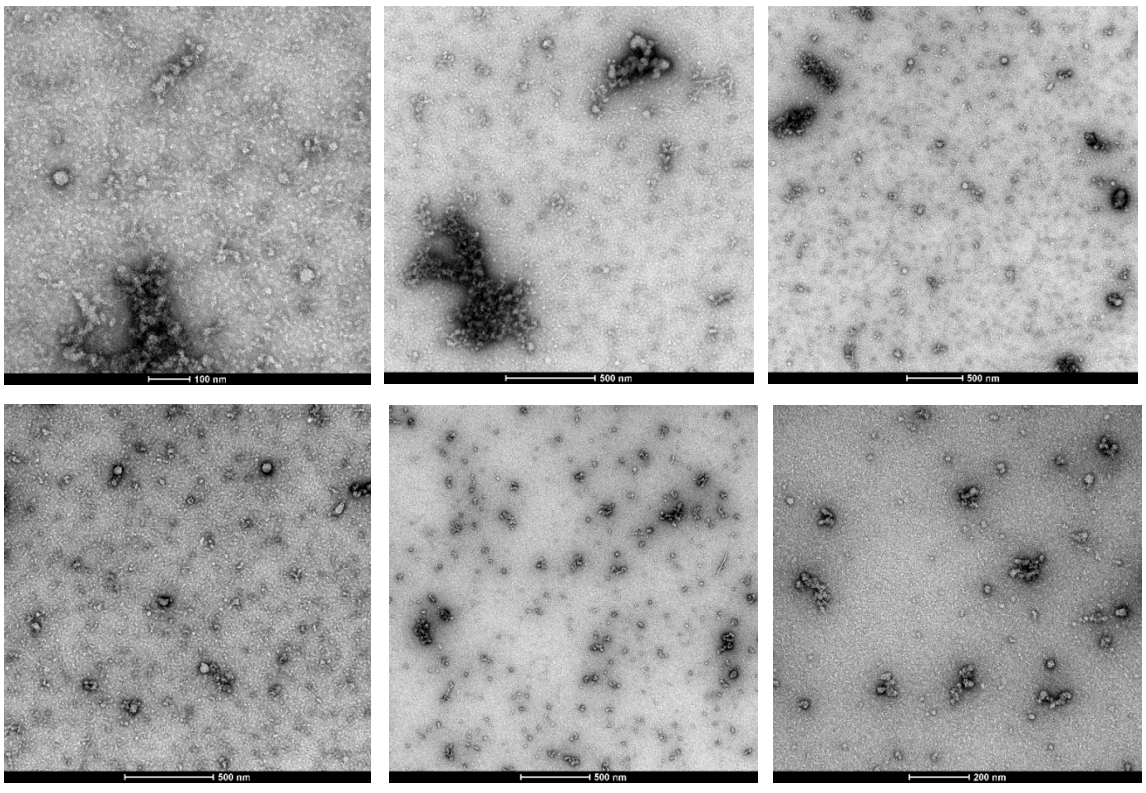

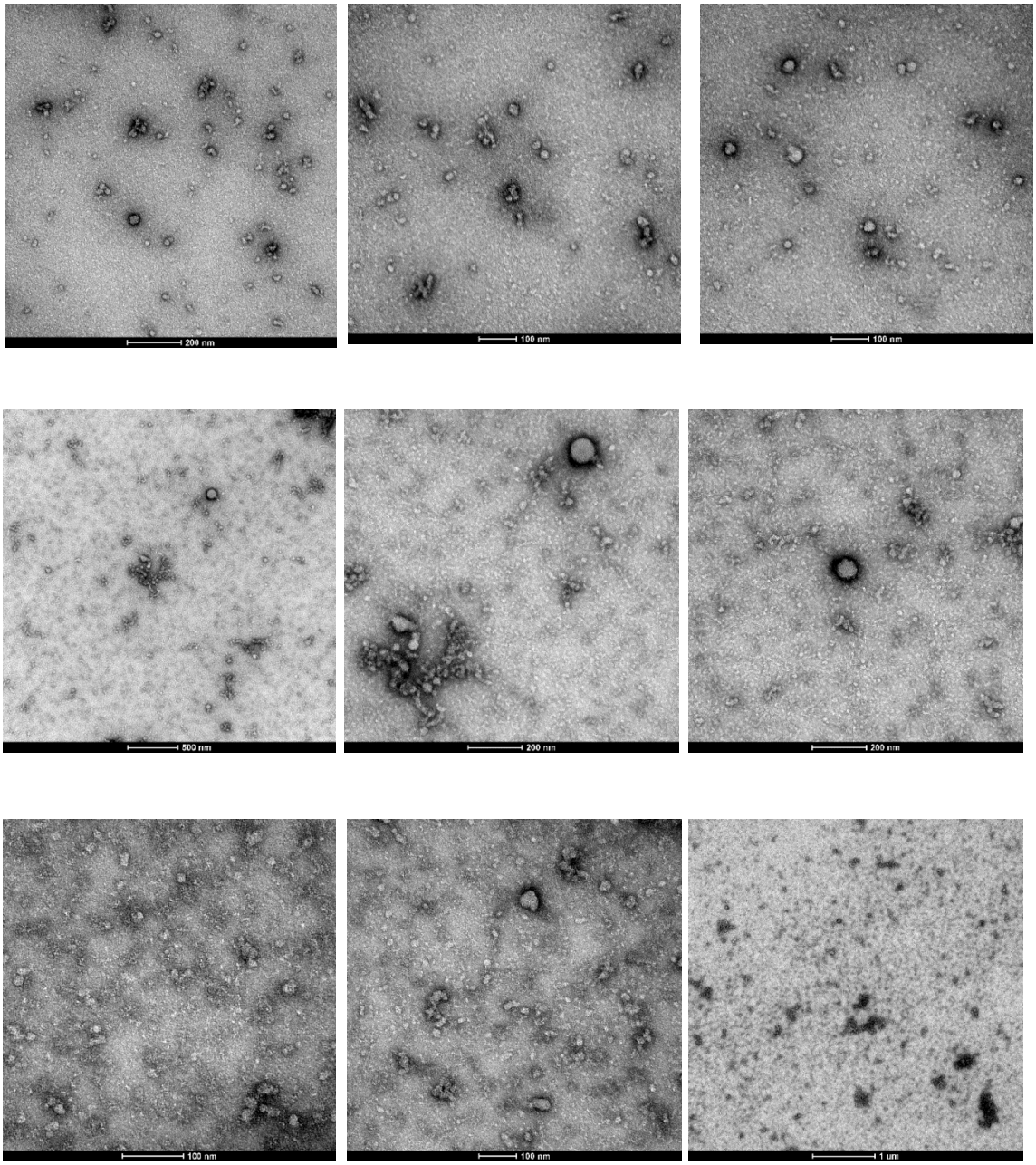
200 nm
100 nm
100 nm
500 nm
200 nm
200 nm
100 nm
100 nm
1 um

2.7.4 TEM of $C_{12}TACN.Zn^{2+}$ at 100 µM and 100 µM ATP

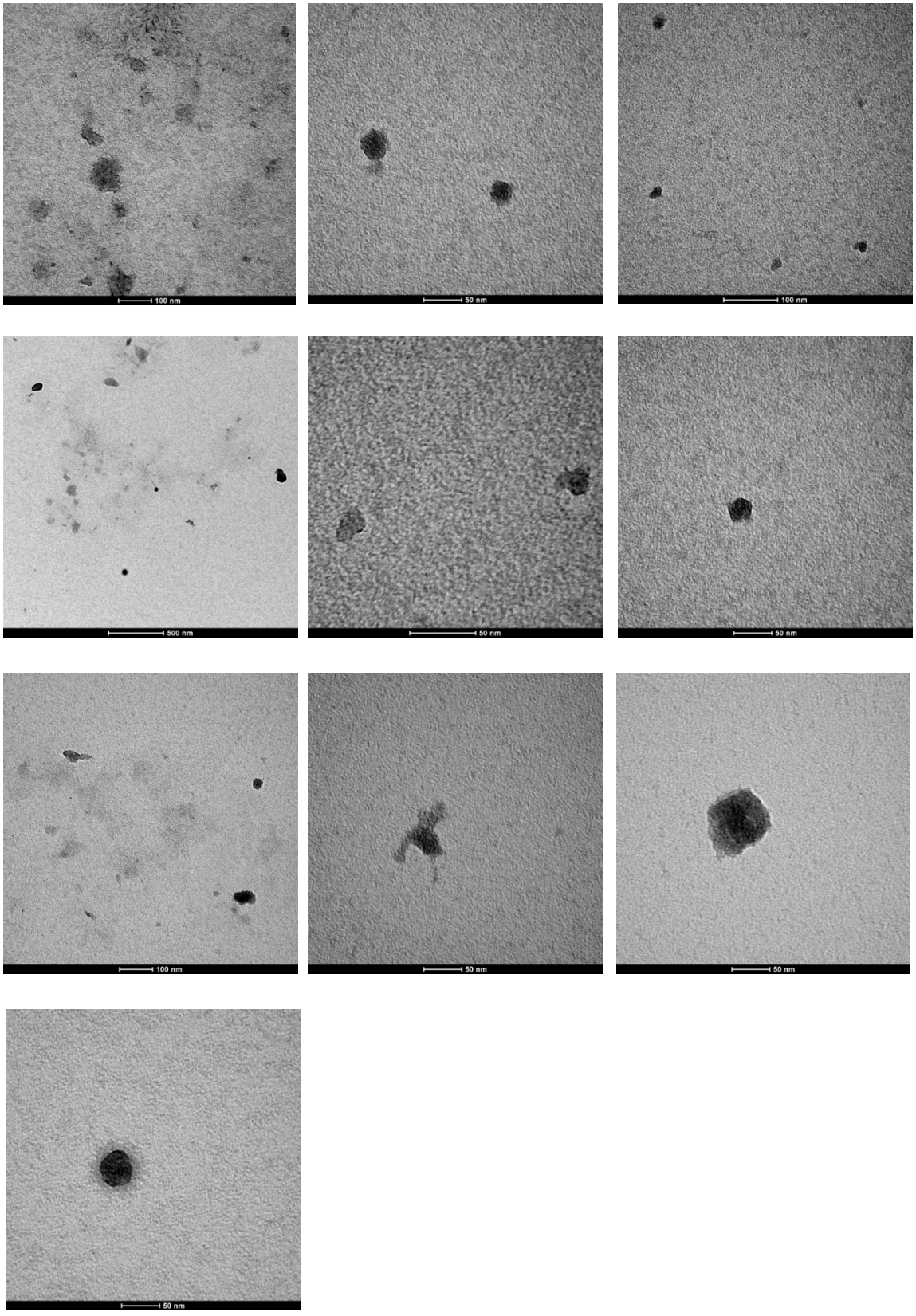

2.7.5 TEM of $C_{12}TACN.Zn^{2+}$ at 100 µM and 200 µM ATP

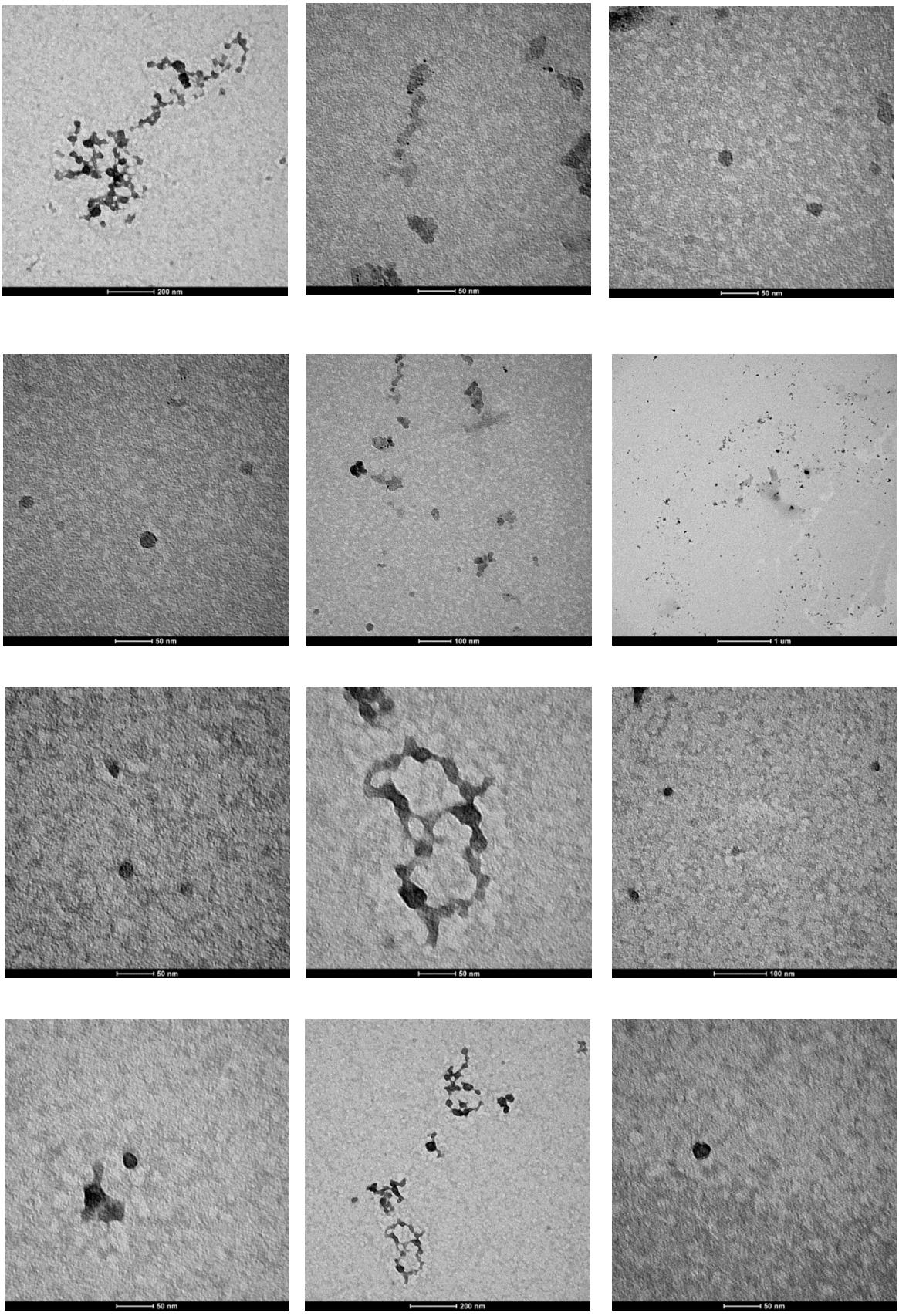

2.7.6 TEM of $C_{12}TACN.Zn^{2+}$ at 200 µM and 50 µM ATP

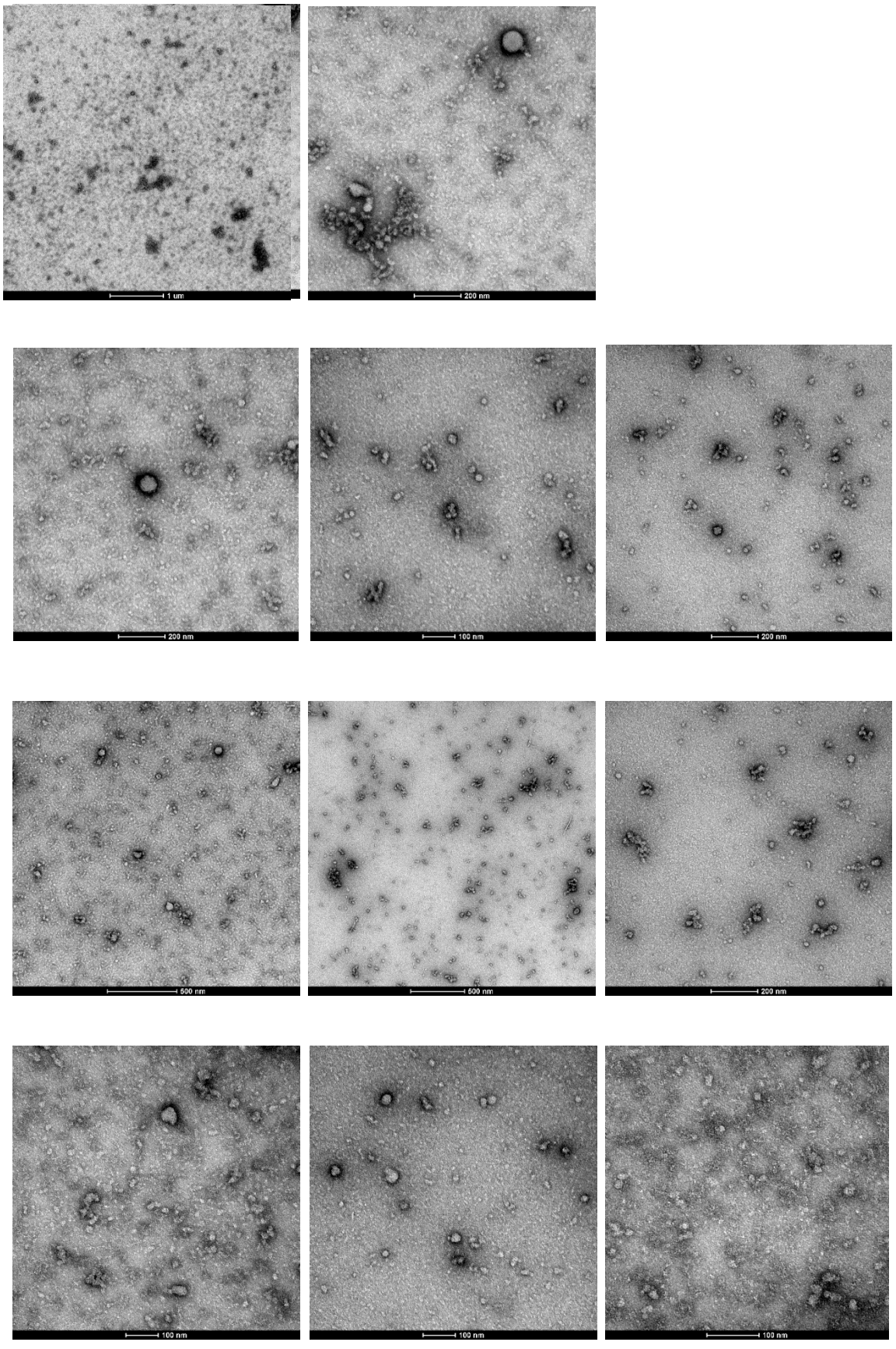

2.7.7 NMR spectra obtained upon allowing 2 M ATP to stand in the presence of 100 µM C_{12}TACN•Zn^{2+} and 0.4 U potato apyrase.

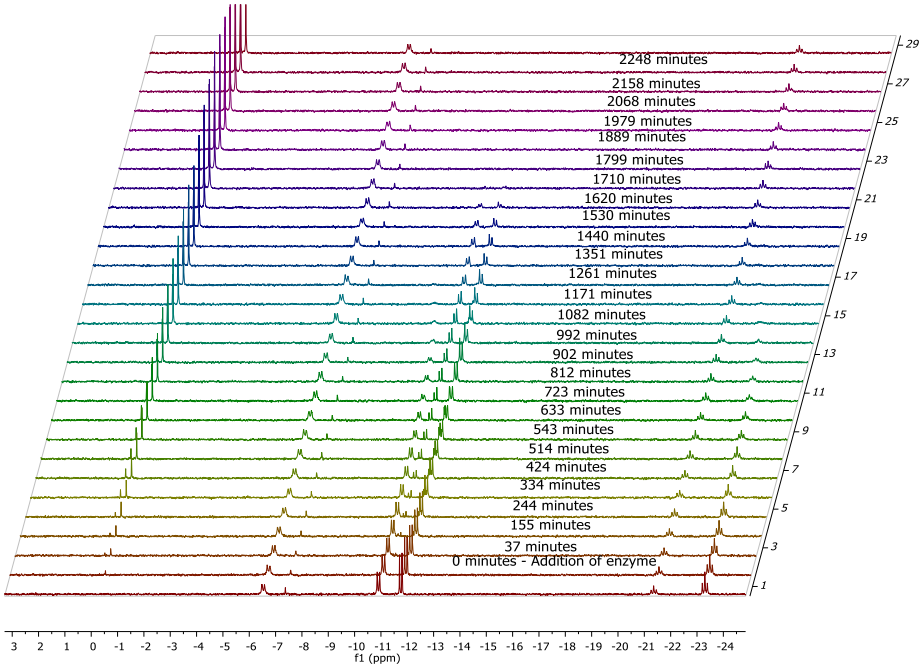

Figure 2.43: Figure showing all the ^{31}P NMR spectra obtained upon allowing 2 mM ATP to stand in the presence of 100 µM C_{12}TACN•Zn^{2+} and 0.4 U potato apyrase. (10% D_2O, 202 MHz, 300 K) [HEPES] = 5 mM, pH 7.0.

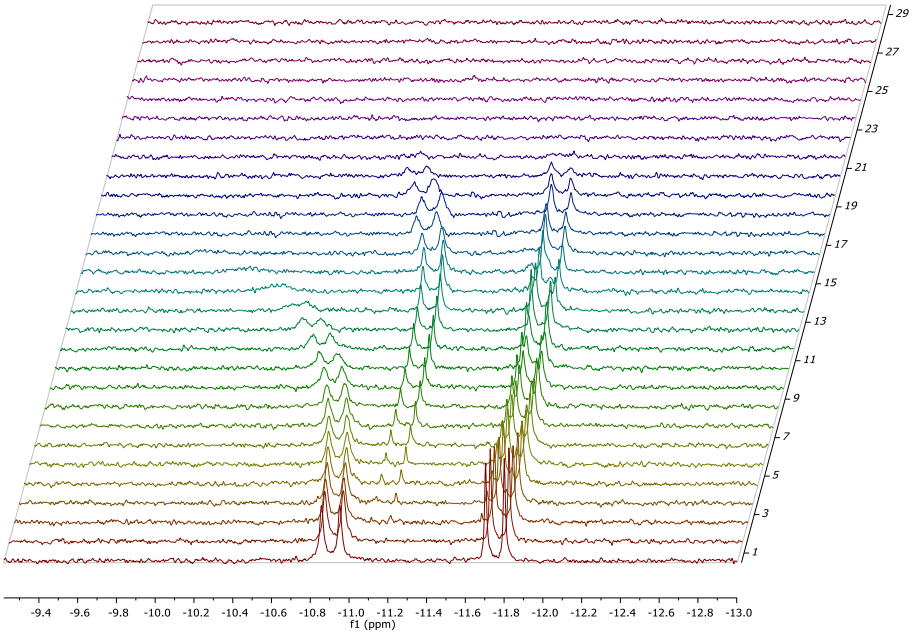

Figure 2.44: Figure showing the spectra of Figure 2.43 focusing on the region between -9.4 ppm and -13.0 ppm showing how the doublet of ATP at -10.93 ppm is eventually replaced by a doublet due to ADP at -11.19 ppm and the ATP doublet at -11.73 ppm is slightly shifted and eventually diminished in intensity. (10% D_2O, 202 MHz, 300 K) [HEPES] = 5 mM, pH 7.0.

2.7.8 NMR spectra of 2 mM ATP in the presence of 0.4 U potato apyrase (no surfactant or metal salts.)

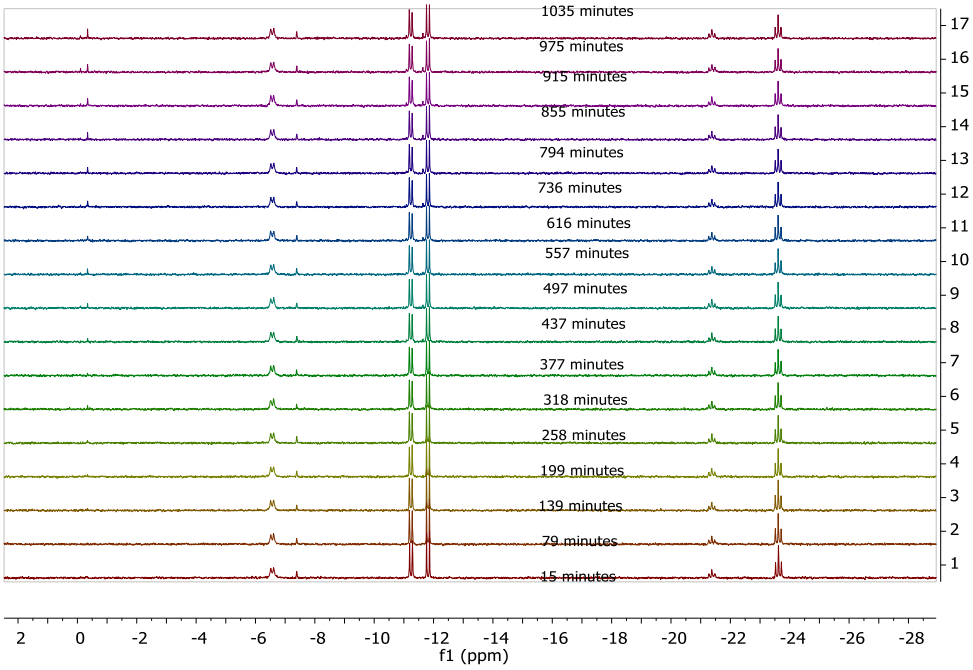

Figure 2.45: ^{31}P NMR spectra of 2 mM ATP with 0.4 U potato apyrase over time. (10% D_2O, 202 MHz, 300 K) [HEPES] = 5 mM, pH 7.0.

2.7.9 NMR spectra of 2 mM ATP in the presence of 0.6 mM C16TACN•Zn2+ (no apyrase)

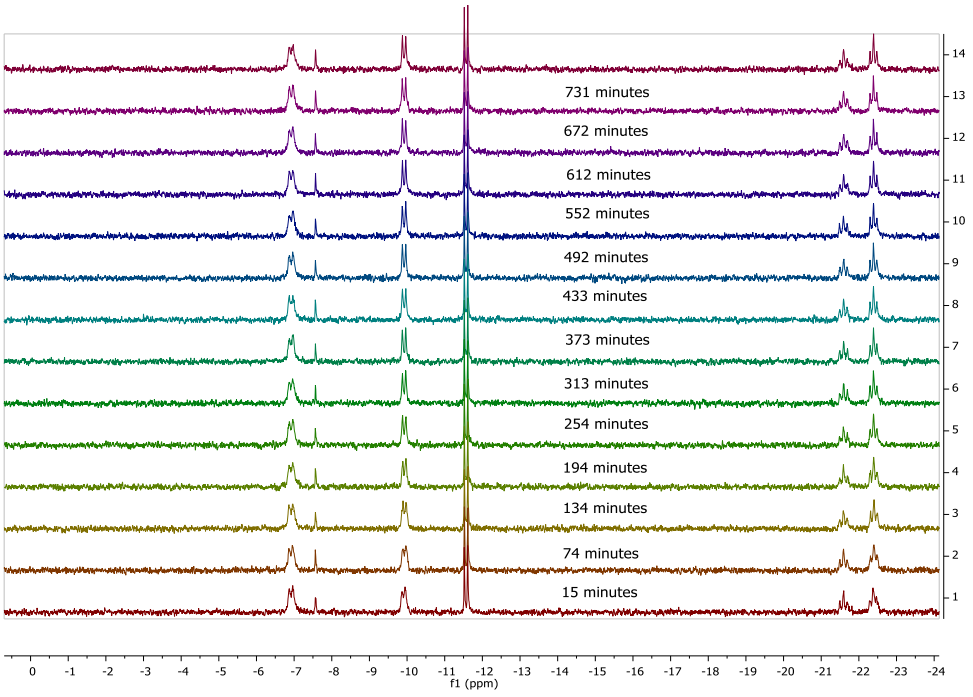

Figure 2.46: ^{31}P NMR spectra of 2 mM ATP with 0.6 mM C_{16}TACN•Zn^{2+} over time. (10% D_2O, 202 MHz, 300 K) [HEPES] = 5 mM, pH 7.0.

Chapter 3

Control of Chemical Reactivity in Transiently Stable Vesicles

3.1 Introduction

Natural selection is a biological process in which genetic information of a species mutates over time as a result of the adaptation of a species towards a particular environment, contributing to the survival of the species. In biological evolution, a system selects a particular option from a number of available ones as a way of adapting to an external parameter. In chemistry, the term "evolution" can be applied to multicomponent systems in which the different components interact with each other and undergo structural changes as a result of selective adaptation to specific external influences. As a result of adaptation, the composition of the multicomponent system changes.[1] In this Chapter we will use self-assembled vesicles under dissipative control to regulate a chemical reaction and use the triggers for the self-assembly process as a selective influence to determine the outcome of a particular reaction given a number of possibilities.

Self-assembled vesicles possess properties which are absent in the non-assembled amphiphiles from which the vesicles originate.[2,3] Therefore self-assembled vesicles can exhibit functions, so called emergent properties, which are not possible in the unassembled state.[4,5] One example of such an emergent properties is the chemical reactivity exerted by vesicles.[4,6] Vesicles provide a hydrophobic environment which is fundamentally different from the aqueous environment from which they originate and which is capable of concentrating reagents in a small region of space. This property makes them attractive as chemical nanoreactors for reactions.[4] Chemical reactivity is determined by the presence of the vesicles and, therefore, control over the formation and lifetime of the vesicles provides control over the associated chemical reaction. In this Chapter, we will explore the self-assembly of vesicles under dissipative conditions as a means of regulating chemical reactions.

The promotion of a nucleophilic aromatic substitution reaction by a self-assembled system under dissipative conditions has recently been described in our group.[7] It was decided to expand on this work and investigate a hydrazone bond-formation reaction. Hydrazones, a class of compound with a general formula $R^1R^2C{=}NNHR^3$, are formed through a condensation reaction between a hydrazide and an aldehyde (Scheme 3.1). Hydrazones are analogous to imines, but have a higher stability in aqueous solutions due to a mesomeric effect, which decreases the electrophilicity of the C=N bond.[8] Indeed, hydrazones are kinetically stable at neutral pH even in purely aqueous solutions, whilst imines are unstable under the same conditions.[9] The kinetics are very sensitive to pH, and hydrolysis, exchange and methathesis can be observed under acidic conditions (between pH 2.5 to 5.0).[8,10]

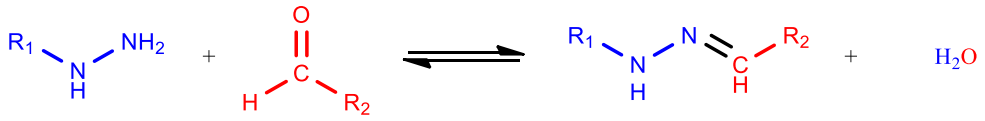

Scheme 3.1: Scheme for hydrazone bond formation between a hydrazine and an aldehyde resulting in a hydrazone and water.

The choice to study a hydrazone bond-formation reaction was driven by its versatility, which has led to numerous applications.[8] Hydrazone bond formation has been extensively studied not only within the context of supramolecular chemistry,[11,12] where it has been applied for the development of molecular switches,[13-15] sensors[16-19] and metallo-assemblies,[20,21] but also in other fields such as organic synthesis[22,23] and medicinal chemistry.[24,25] Examples include covalent and metal organic frameworks,[26] dynamic combinatorial chemistry,[10,27,28] dyes[29] and hole-transporting materials.[30]

Hydrazones have been applied in numerous fields.[8] One such example is the selective formation of products depending on the input of different chemical stimuli. This is possible because of the reversible nature of the reaction under suitable conditions. In particular, selection experiments have been carried out within the field of dynamic combinatorial chemistry.[1,8,10] In one such self-selection experiment, carried out in our lab, a number of hydrazides **1-9** were reacted with an aldehyde bearing a phosphonate group functionality, **A.** The aldehyde bearing a phosphonate group was chosen because it acts as a model for the transition state of carboxylic ester hydrolysis. Preferential hydrazone formation occurred with hydrazides which could form an intramolecular, electrostatic interaction with

the phosphonate groups, for example a quaternary ammonium group,[31] a pyridinyl group or an amine group (Figure 3.1). The extent of amplification in the dynamic library was subsequently correlated to the efficiency of the resulting products to catalyse the cleavage of the corresponding carboxylic ester. The results suggested that the aldehyde functionalised with a phosphonate group self-selects hydrazides which enhance the cleavage rates of the corresponding carboxylic ester.[32-34]

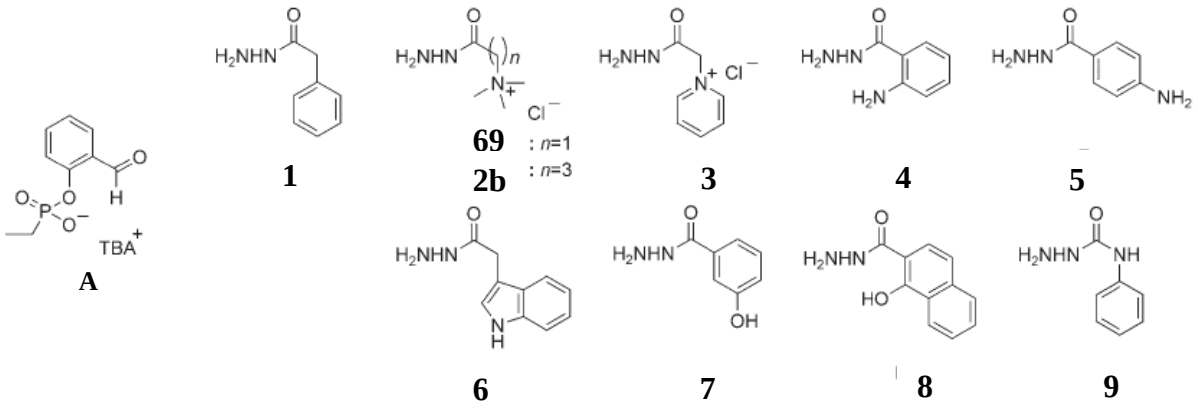

Figure 3.1: Structure of the aldehyde containing a phosphonate group (**A**) and the hydrazide library used (**1**-**9**). The hydrazide **1** was used as a reference hydrazide. TBA = tetra-*n*-butylammonium. Hydrazones from hydrazide **2**, **3** and **9** were amplified due to the favourable interaction with the phosphonate group.

3.2 Concept of the study

The excellent applications of hydrazones makes them attractive targets for study. Since the reaction between a hydrazide and an aldehyde to give a hydrazone is an equilibrium reaction involving the release of water as a by-product, the product distribution can be expected to be sensitive to the presence of local apolar phases in the reaction medium. Hydrazone bond formation reactions occur readily in organic solvents but the kinetics of formation and dissociation are much slower in aqueous solution, especially at low concentrations.[35] It is expected that the hydrophobicity of the vesicles' bilayer would provide a stimulus to shift the equilibrium towards product formation. Temporal control over the vesicle formation using dissipative conditions would then permit temporal control over the hydrazone equilibrium composition.

In Chapter 2, a dissipative self-assembly process was developed based on the self-assembly of the monomeric surfactant $C_{12}TACN \bullet Zn^{2+}$, **10**, using ATP as the chemical fuel (Figure

3.2). In this Chapter, we investigate the capacity of the aggregates to accelerate a hydrazone bond-formation reaction. The self-assembly of the vesicles was investigated at pH 7.0 and therefore these conditions were chosen for the study of hydrazone formation as well.[8]

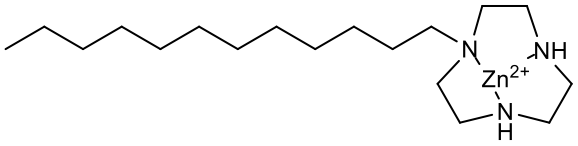

10

Figure 3.2: Structure of $C_{12}TACN \bullet Zn^{2+}$, **10**.

.

3.3 Vesicles as nanoreactors for the preferential formation of a hydrazone bond formation reaction.

3.3.1 Concept

The reaction between *trans*-cinnamaldehyde, **11** and 3-hydroxy-2-napthoic hydrazide, **12** to afford **13** (Scheme 3.2) emerged for detailed investigation after a screening of a series of hydrazides (*vide* Appendix 3.8.2). Selection criteria were based on the right balance between water solubility and hydrophobicity to enable the reaction to occur preferentially inside the vesicles and the possibility to follow the reaction spectrophotometrically. Both **11** and **12** are hydrophobic reagents which are expected to be preferentially located in the vesicular bilayer, but are sufficiently water-soluble to allow complete solubility at micromolar concentrations in the reaction medium. Furthermore **11** gives hydrazones which are highly conjugated with characteristic absorbances in the UV-Vis spectrum.[36,37]

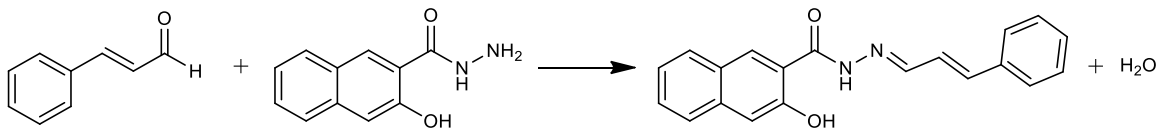

λ_{max} = 291 nm λ_{max} = 231 nm λ_{max} = 332 nm

11 **12** **13**

Scheme 3.2: Hydrazone bond-forming reaction between *trans*-cinnamaldehyde, **11** and 3-hydroxy-2-napthoic hydrazide, **12**.

Hydrazone bond formation is generally slow in aqueous media at neutral pH[38] so it is expected that the reaction between **11** and **12** would not occur to a great extent in the presence of aqueous buffer (HEPES (5 mM, pH 7.0)) and in the presence of just surfactant

10. Addition of ATP would result in the formation of vesicles, entrapment of the reagents and an improved reaction rate due to the spatial confinement of the reagents as well as a change in the polarity.[4] However, if the reaction is indeed dependent on the presence of the vesicles, carrying out the reaction under dissipative conditions, installed by the presence of an enzyme which cleaves ATP, would mean that the reaction can occur only during a limited time interval (Figure 3.3). In this manner, it is aspired to take advantage of the temporal dimension of vesicle formation to develop an innovative way of regulation of a chemical reaction.

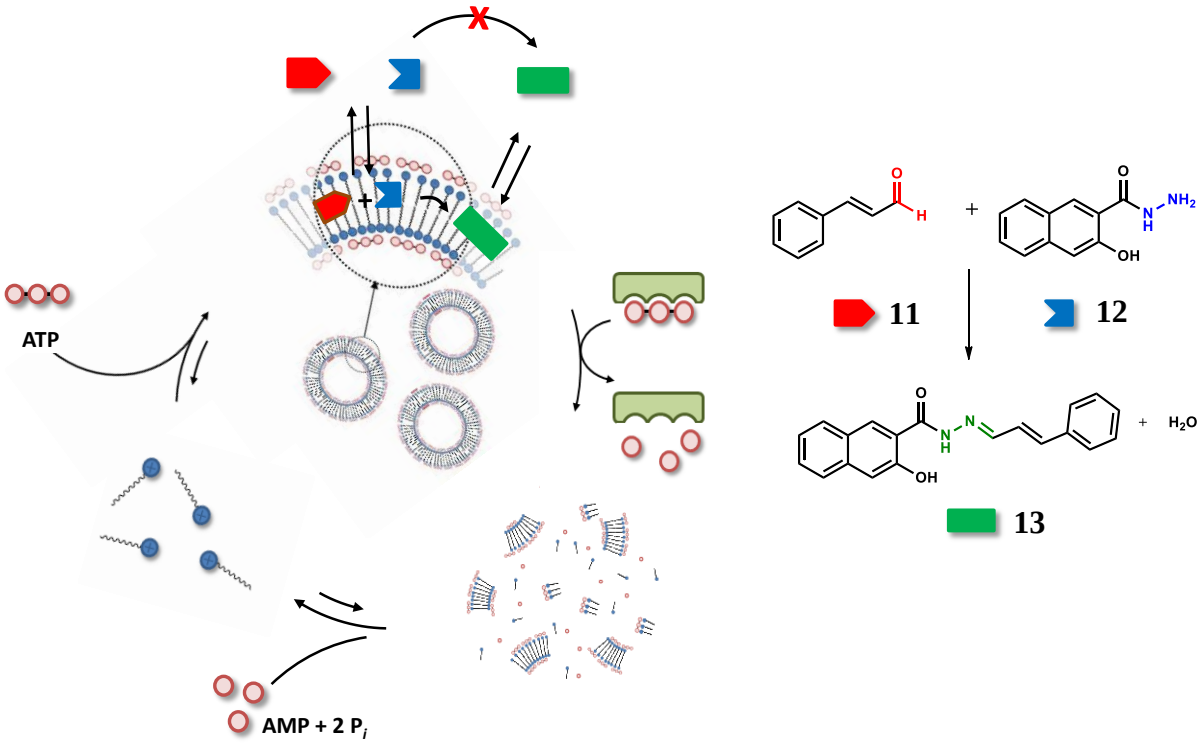

Figure 3.3: Schematic representation of the dissipative self-assembly of vesicles and how vesicles can act as chemical nanoreactors for the hydrazone bond-formation reaction.

3.3.2 UV-Vis and UPLC characteristics of the components of the reaction

The reaction between **11** and **12** was monitored principally by UV-Vis spectroscopy (Figure 3.4) and results were verified by UPLC (Figure 3.5). The UV-Vis characteristics of the components of the reaction are presented in Table 3.1. In aqueous buffer (HEPES (5 mM), pH 7.0), **11** displays a UV-Vis spectrum with λ_{max} = 291 nm (ε = 34,100 mol^{-1} dm^3 cm^{-1}) while **12** shows a maximum at 231 nm (ε = 87,000 mol^{-1} dm^3 cm^{-1}). The hydrazone product **13**, on the other hand, gives an absorption band with a λ_{max} of 332 nm (ε = 25,800 mol^{-1} dm^3 cm^{-1}) which does not overlap with that of the starting reagents (Figure 3.4a). Interestingly, when the pre-formed hydrazone was added to the vesicles (100 µM **10**, 200 µM ATP), the UV-Vis spectrum was red-shifted and the absorption changed over a period of two hours from a broad absorption band with one maximum at 339 nm to a broad absorption band with three maxima at λ_{max} of 366 nm, 384 nm and 408 nm (Figure 3.4b and Section 3.8.3 in the Appendix). This can be interpreted as evidence of the change in environment as the hydrazone migrates from the aqueous buffer to the inner, more hydrophobic interior of the vesicles.

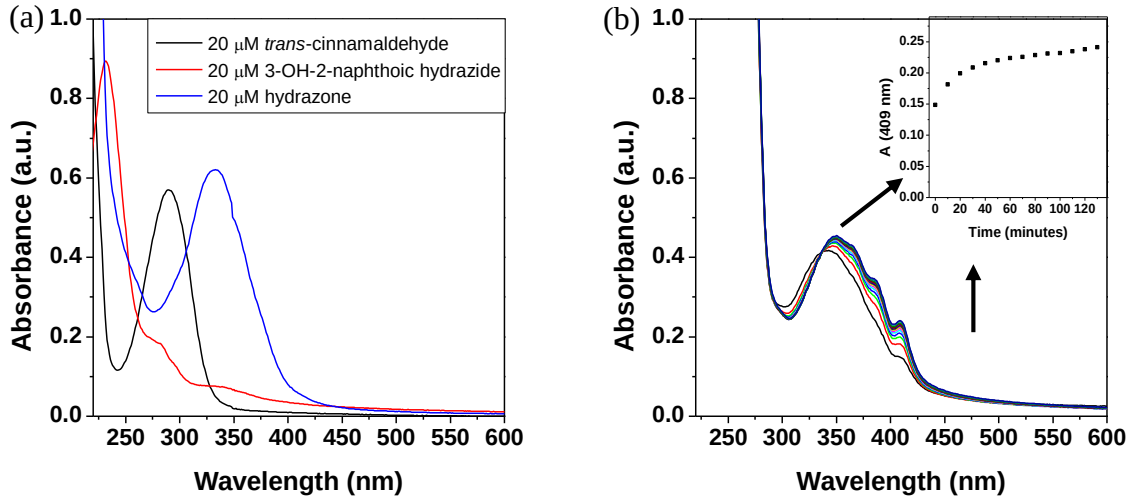

Figure 3.4: (a). UV-Vis spectrum of 20 µM reagents in HEPES buffer pH 7.0. (b). UV-Vis spectrum of 14 µM hydrazone **13** in 100 µM surfactant **10** and 200 µM ATP over time (130 minutes). Spectra were taken every 10 minutes. Inset: The change in absorbance at a fixed wavelength (409 nm) over time. [HEPES] = 5 mM, pH 7.0, [Surfactant **10**] = 100 µM, [ATP] = 200 µM.

	ε ($mol^{-1}dm^3cm^{-1}$)			
	λ_{max} (nm)	Buffer	Surfactant	Vesicles
Hydrazone, 13	332	25,800	30,600	16,330
***Trans*-cinnamaldehyde, 11**	291	34,100	21,000	N/A
3-hydroxy-2-napthoic hydrazide, 12	231	87,000	86,200	N/A

Table 3.1: The molar extinction coefficient of the starting reagents and hydrazone **13** in buffer, surfactant **10** (100 μM) and vesicles (100 μM surfactant **10**, 200 μM ATP) using UV-Vis spectroscopy. [HEPES] = 5 mM, pH 7.0.

The information obtained from the UV-Vis measurements was used to set up a method of analysis by UPLC, which uses UV-Vis as a detection method. The concentration of **12** was monitored at a wavelength of 235 nm and appeared as a single peak with a retention time of 2.8 minutes while **11** was retained more strongly by the column, appearing as a single peak at 3.5 minutes at 259 nm. Hydrazone **13** was more hydrophobic and was visible at 331 nm as a single peak with a retention time of 4.4 minutes when injected from the reference solution (Figure 3.5). When the hydrazone was formed as a result of reaction, the peak frequently showed a tail at slightly longer retention time. This could possibly originate from co-injection of the surfactant.

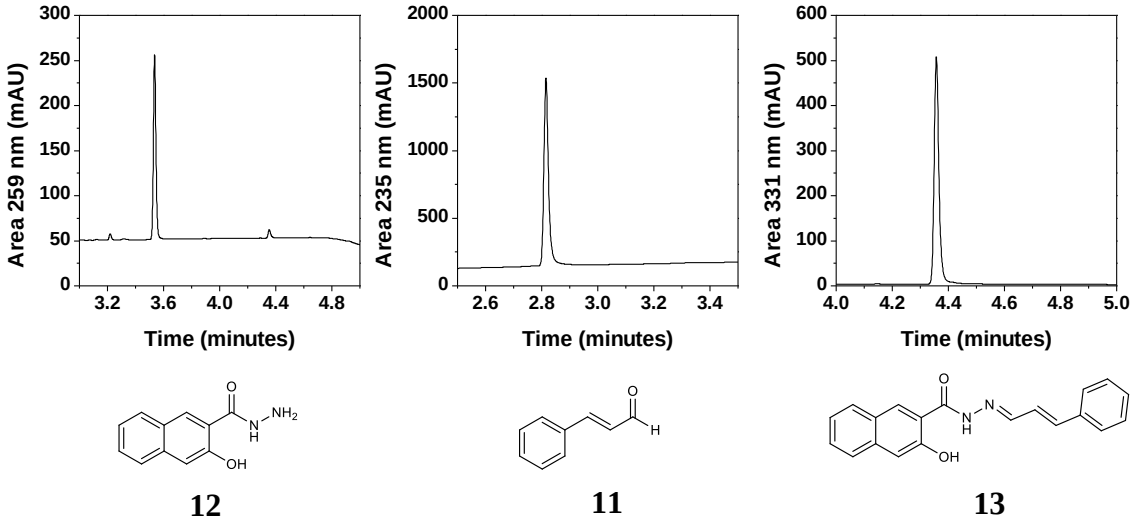

Figure 3.5: Graphs showing the peaks of the components visible as single peaks at their respective absorption by UPLC on a C3 column. [**11**] = [**12**] = [**13**] = 20 μM, [HEPES] = 5 mM, pH 7.0.

3.3.3 Investigating the formation of hydrazone 13

The attention was subsequently shifted towards the formation of hydrazone **13** from **11** and **12**. The formation of **13** was monitored by UV-Vis spectroscopy by acquiring spectra at regular intervals and tabulating the absorbance at 408 nm. In aqueous buffer (5 mM HEPES, pH 7.0), the reactants **11** and **12** do not readily form the hydrazone **13**. Even after 800 minutes no significant amount of product could be detected. The presence of surfactant **10** (without ATP) led to an increased formation of product, but the amount was still rather low (Figure 3.6a). Nevertheless, increasing the amount of surfactant **10** led to a slight increase in the initial rate of reaction (defined as the initial linear slope of the graph showing the concentration of product formed against time), in particular above a concentration of 100 μM (Figure 3.6b). This is still well below the *cac* of the surfactant.

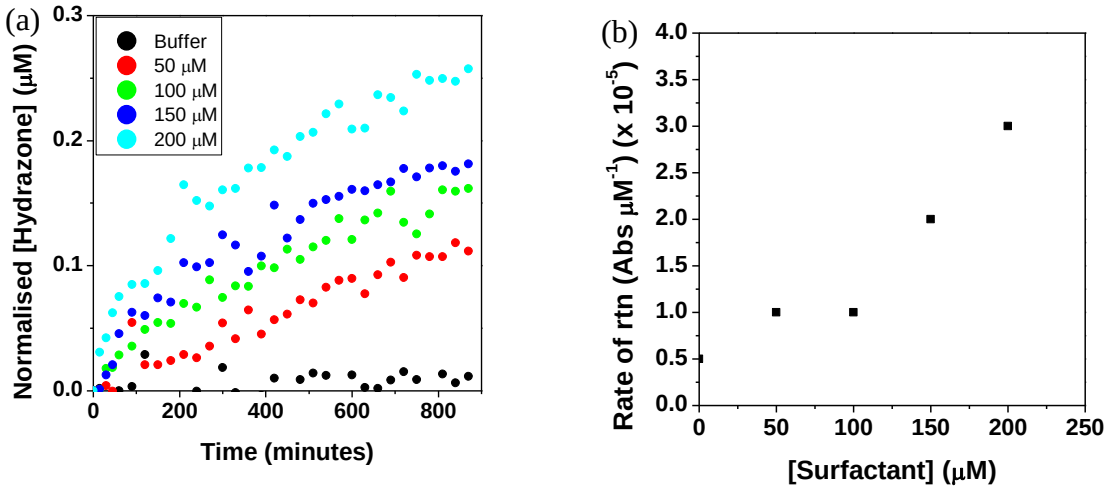

Figure 3.6: (a). A graph showing the change in the absorption band of the product over time as the surfactant **10** concentration increases. N.B. The absorbance of the product was estimated from the absorbance of the furthest maximum (to ensure minimal interference from the absorbance of *trans*-cinnamaldehdye) and subtracting the absorbance at the nearest baseline. (b). The rate of reaction as a function of surfactant concentration. The initial linear part of the graphs in (a) were used to calculate the rate of reaction. [HEPES] = 5 mM, pH 7.0, [**11**] = [**12**] = 20 μM.

A series of preliminary experiments were then conducted in order to determine the appropriate conditions for carrying out the reaction in vesicles formed upon the addition of ATP. The reaction between **11** and **12** was investigated by UV-Vis spectroscopy in the presence of 50 μM, 100 μM and 200 μM surfactant **10** and at various ATP concentrations (0 μM to 200 μM). In all cases, the reaction was faster in the presence of ATP than in the presence of the free surfactant **10**. In 50 μM surfactant **10** the hydrazone formation reaction was not enhanced much at all concentrations of ATP. However, in 100 μM and 200 μM surfactant **10** there was a strong enhancement of the reaction in the presence of ATP with

respect to that in the free surfactant solution without ATP, especially at higher concentrations of 100-200 μM ATP (Figure 3.7). UPLC experiments for the formation reaction in 100 μM surfactant **10** (Figure 3.8) and 200 μM surfactant **10** (Figure 3.9) yielded similar trends. The concentration of product formed was enhanced in the presence of increasing concentrations of ATP in both cases. Confirmation for the formation of hydrazone **13** was obtained from UPLC-MS, which gave m/z value of 317 g/mol [M+H] for the product peak with retention time at 3.9 minutes (Figure 3.8b).

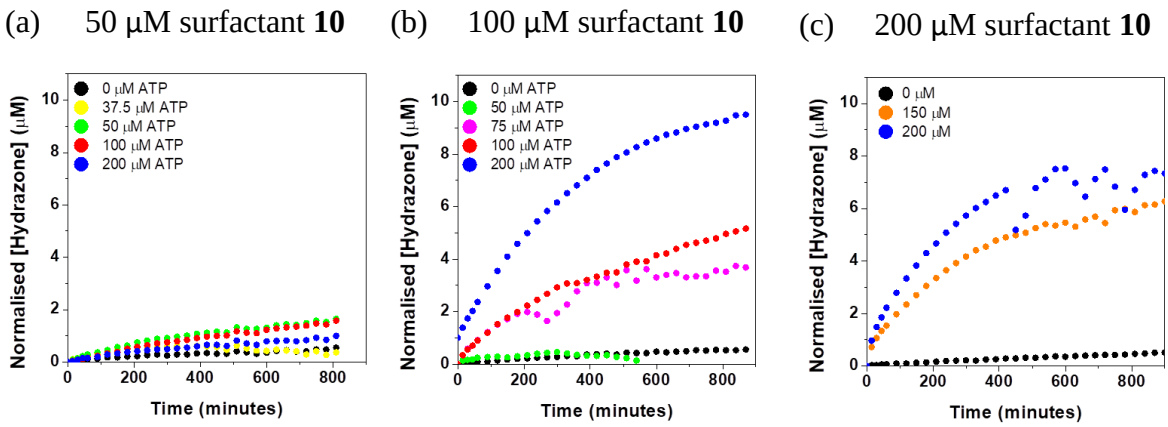

Figure 3.7: Figure showing the concentration of **13** formed over time when the reaction was carried out in (a) 50 μM, (b) 100 μM and (c) 200 μM surfactant **10** at increasing ATP concentrations. Certain combinations of concentrations of surfactant gave results which could not be analysed, namely 12.5 μM and 25 μM ATP with 50 μM surfactant **10**, 25 μM ATP with 100 μM surfactant **10**, 50 μM and 100 μM ATP with 200 μM surfactant **10**. [HEPES] = 5 mM, pH 7.0, [**11**] = [**12**] = 20 μM.

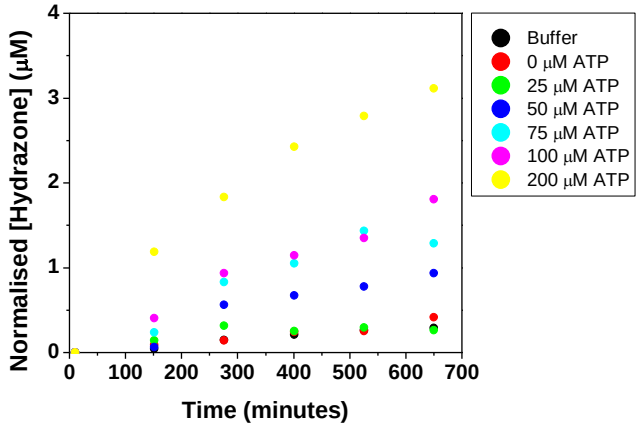

Figure 3.8: Figure showing the increase in hydrazone **13** concentration when **11** and **12** were reacted in buffer and 100 μM surfactant **10** in the presence of increasing amounts of ATP. [HEPES] = 5 mM, pH 7.0, [Surfactant **10**] = 100 μM, [**11**] = [**12**] = 20 μM.

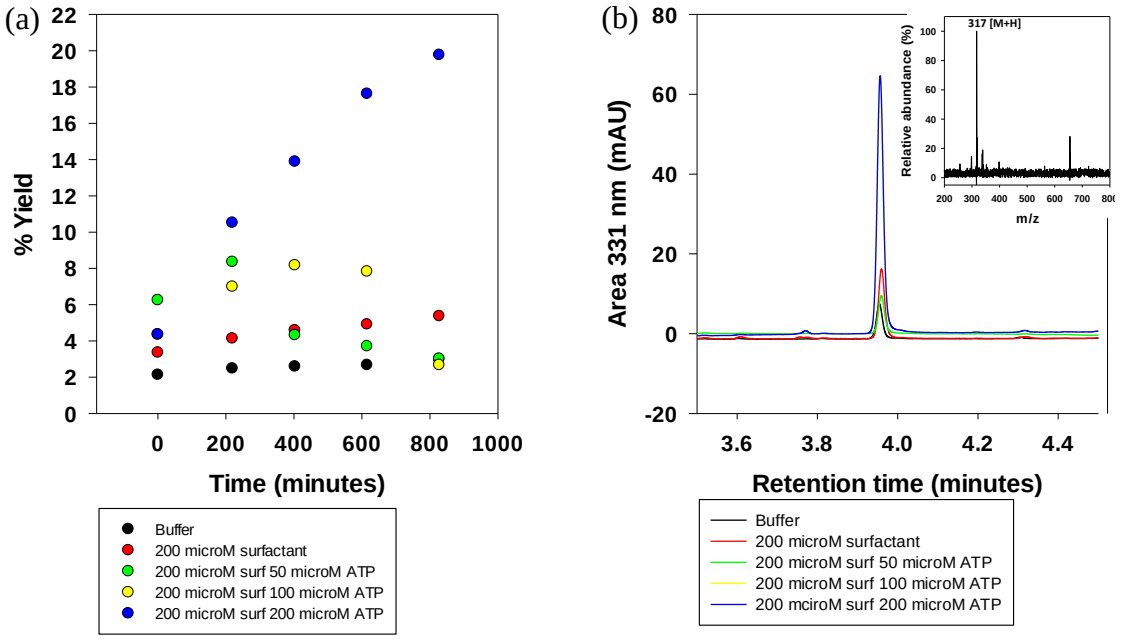

Figure 3.9: (a). Figure showing the % yield for the reaction between **11** and **12** in 200 μM surfactant **10** in the presence of increasing amounts of ATP. (b). Overlaid UPLC chromatograms for the peak of **13** obtained overnight for the different conditions. Inset shows the MS-spectrum of the peak. [HEPES] = 5 mM, pH 7.0, [Surfactant **10**] = 200 μM, [**11**] = 5 μM, [**12**] = 25 μM.

In particular, hydrazone formation in a solution containing 100 μM surfactant **10** and 200 μM ATP gave a very distinctive UV-Vis absorbance with three broad absorption maxima with minimal interference from turbidity. Comparison of the reaction of 20 μM reagents under these conditions in aqueous buffer (HEPES (5 mM), pH 7.0), surfactant **10** (100 μM) and vesicles (100 μM surfactant **10**, 200 μM ATP) by both UV-Vis (Figure 3.10) and UPLC (Figure 3.11) suggested that the rate of reaction for 20 μM reagents under these conditions was strongly enhanced in the vesicles when compared to the reaction in surfactant and aqueous buffer. The initial rate of formation was calculated from the slope of the initial linear part of the graphs showing the concentration of hydrazone against time by UPLC. The rate of formation of **13** increased from 2.8×10^{-4} μM minute^{-1} in aqueous buffer (HEPES (5 mM), pH 7.0) to 3.5×10^{-3} μM minute^{-1} in 100 μM surfactant **10** to 1.3×10^{-2} μM minute^{-1} in vesicles (100 μM surfactant **10**, 200 μM ATP). These conditions were therefore chosen for further studies.

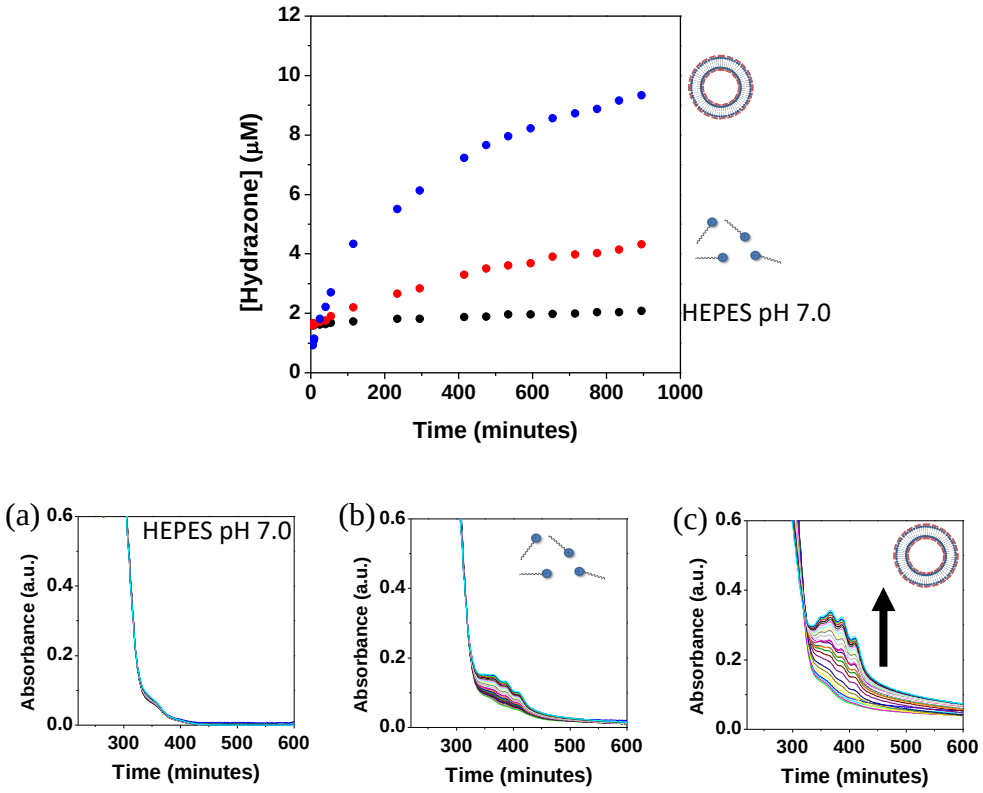

Figure 3.10: Concentration of hydrazone **13** as a function of time (top) and UV-Vis spectra at regular intervals (bottom) of the reaction of 20 μM reagents in (a) aqueous buffer (b) surfactant **10** and (c) vesicles. [HEPES] = 5 mM, pH 7.0, [Surfactant **10**] = 100 μM, [ATP] = 200 μM, [**11**] = [**12**] = 20 μM.

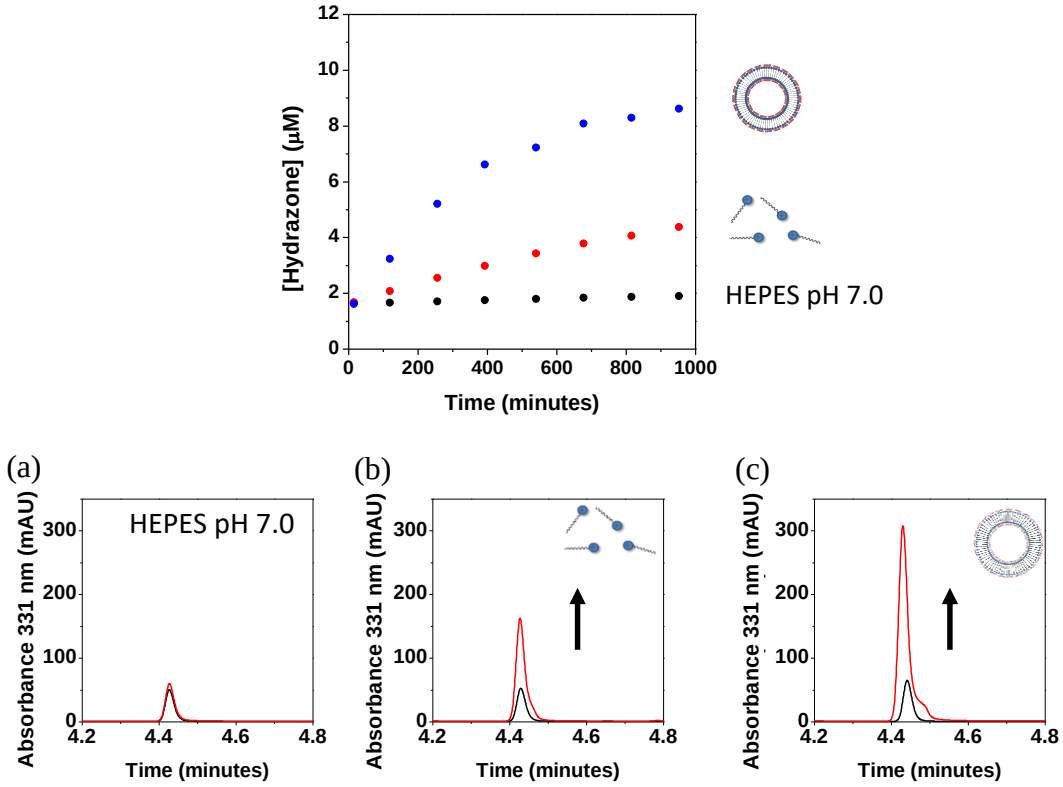

Figure 3.11: Concentration of hydrazone **13** as a function of time (top) and UPLC chromatograms (initial and final) (bottom) of the reaction of 20 μM reagents in (a) aqueous buffer (b) surfactant **10** and (c) vesicles. [HEPES] = 5 mM, pH 7.0, [Surfactant **10**] = 100 μM, [ATP] = 200 μM, [**11**] = [**12**] = 20 μM.

Finally, visible evidence for the increase in reaction rate upon formation of vesicles was observed when the reaction was initially carried out in surfactant **10** (100 μM) for 12 hours and ATP was added to the solution afterwards. The rate of reaction was slow in the free unassembled surfactant **10**. Addition of ATP resulted in a dramatic increase in the rate of product formation (slope of the graph showing the concentration of hydrazone against time), as evidenced by UV-Vis spectroscopy (Figure 3.12) as well as by UPLC (Figure 3.13).

A control experiment in which ATP was added in the absence of surfactant **10** did not cause any increased product formation compared to the background reaction in aqueous buffer (Figure 3.14a). It was also found that the reaction was affected adversely by an excess of divalent metal ions such as Ca^{2+} and carrying out the reaction in the vesicles (100 μM surfactant **10**, 200 μM ATP) in the presence of 1 mM Ca^{2+} resulted in a decreased yield of

reaction with respect to the sample without Ca^{2+} (Figure 3.14b). The amount of reaction was still, however, higher than that occurring in the free surfactant **10**.

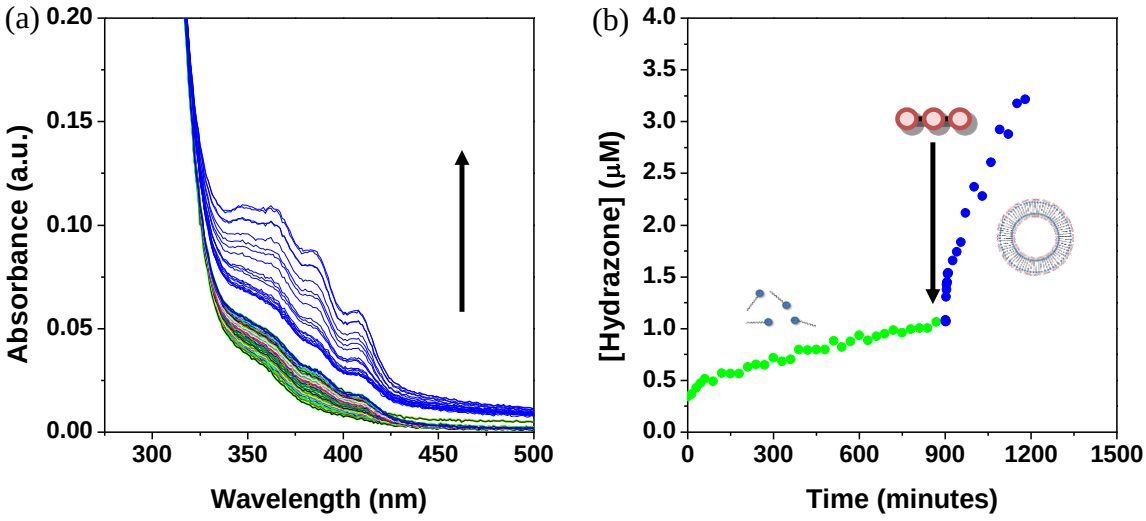

Figure 3.12: Figure showing (a) the UV-Vis spectra of hydrazone **13** at regular intervals and (b) the concentration of hydrazone **13** as a function of time upon mixing together 20 μM reagents in 100 μM surfactant **10** (green) and upon addition of ATP (200 μM) after around 900 minutes. [HEPES] = 5 mM, pH 7.0, [Surfactant **10**] = 100 μM, [ATP] = 200 μM, [**11**] = [**12**] = 20 μM.

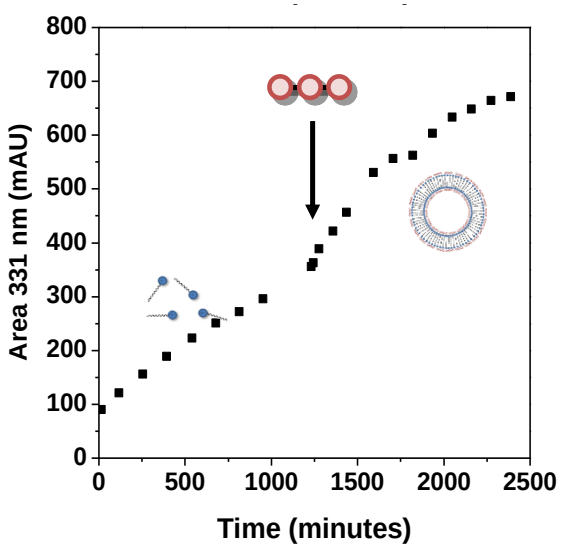

Figure 3.13: Figure showing the increase in the absorbance of the peak of hydrazone **13** at 331 nm as a function of time upon mixing together 20 μM reagents in 100 μM surfactant and after the addition of ATP (200 μM) by UPLC. [HEPES] = 5 mM, pH 7.0, [Surfactant **10**] = 100 μM, [ATP] = 200 μM, [**11**] = [**12**] = 20 μM.

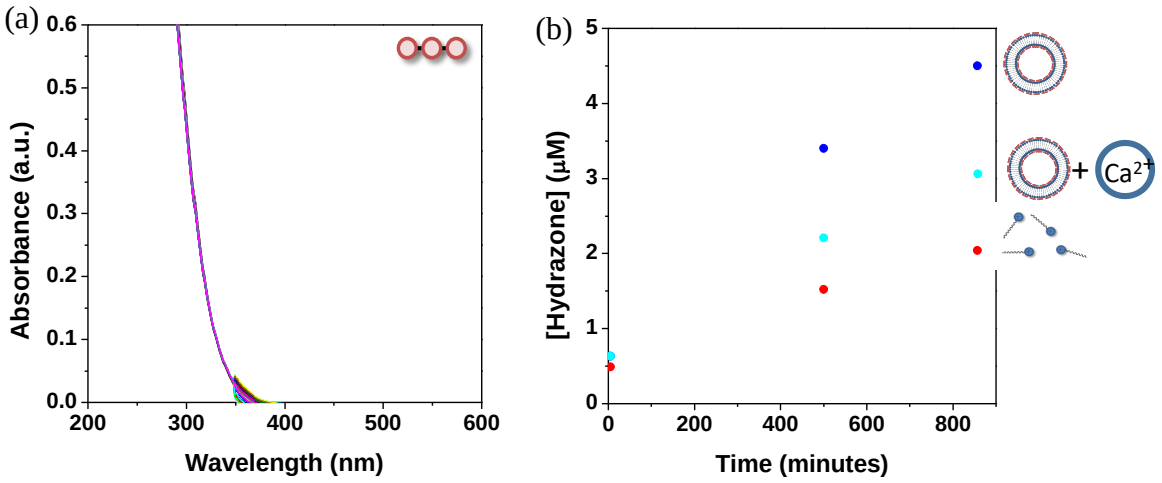

Figure 3.14: (a) UV-Vis spectra at regular intervals of the reaction of 20 μM reagents in 200 μM ATP. (b) Plot showing the change in the concentration of hydrazone **13** over time in the surfactant **10** (100 μM), in the vesicles (100 μM surfactant **10** and ATP) and in the vesicles in the presence of 1 mM Ca^{2+} by UPLC. [HEPES] = 5 mM, pH 7.0 [**11**] = [**12**] = 20 μM.

Finally, the reaction was also carried out in surfactant **10** (100 μM) in the presence of the waste products of ATP hydrolysis by the enzyme potato apyrase, namely 200 μM AMP and 400 μM P_i. Very little product was formed in this case as well, as determined by both UV-Vis (Figure 3.15a) and UPLC (Figure 3.15b). This suggests that the waste products of ATP hydrolysis did not induce product formation. Similar plots were obtained for product formation in the presence of 200 μM adenosine and 600 μM Pi, which are the waste products for ATP hydrolysis by the enzyme alkaline phosphatase. This suggests that even in this case there was no product formation induced (Figure 3.16).

This difference in reactivity between the assembled and disassembled state could not be observed with the previously studied surfactant $C_{16}TACN{\bullet}Zn^{2+}$, **14**, under the same conditions (Figure 3.17). In fact, when the reaction was carried out under the same conditions with surfactant **14** (i.e. 100 μM surfactant **14**, 200 μM ATP), the amount of product formed was generally much higher and there was little difference between the surfactant and the vesicles, probably because at this concentration of surfactant micelles are already formed, providing a different hydrophobic environment conducive to reaction even in the absence of ATP.

6

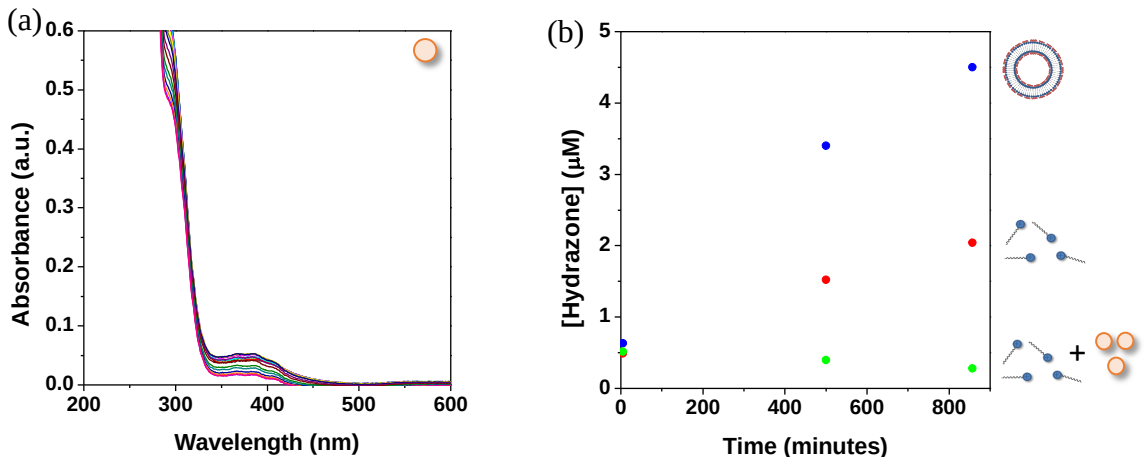

Figure 3.15: (a) UV-Vis spectra at regular intervals of the reaction of 20 μM reagents in surfactant **10** (100 μM) and waste products of ATP hydrolysis (200 μM AMP and 400 μM Pi). (b) UPLC plot of concentration of hydrazone **13** against time for the formation reaction in the surfactant **10**, in the vesicles (surfactant **10** and ATP) and in the surfactant **10** in the presence of AMP + Pi. [HEPES] = 5 mM, pH 7.0 [Surfactant **10**] = 100 μM, [ATP] = 200 μM, [AMP] = 200 μM, [Pi] = 400 μM, [**11**] = [**12**] = 20 μM.

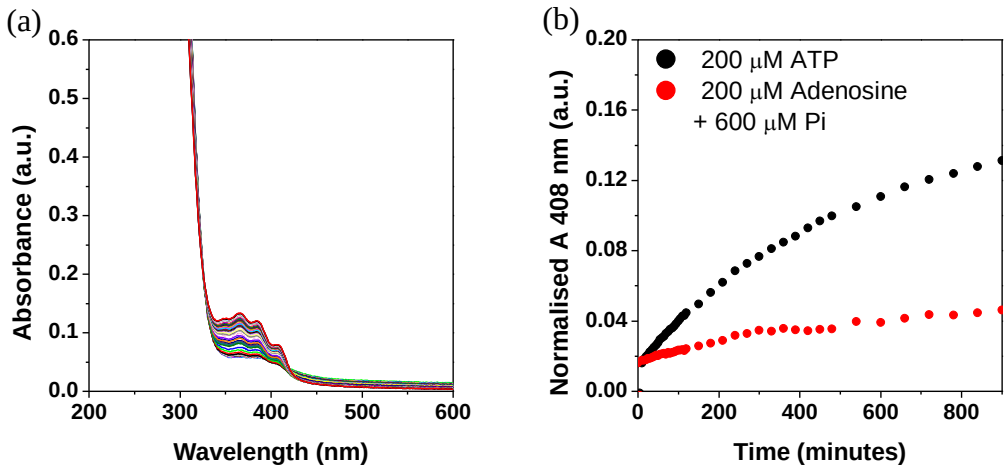

Figure 3.16: (a) UV-Vis spectra at regular intervals of the reaction of 20 μM reagents in surfactant **10** (100 μM) and waste products of ATP hydrolysis (200 μM Adenosine and 600 μM Pi). (b) UV-Vis kinetic traces showing the change in Absorbance of hydrazone **13** in the presence of 100 μM surfactant **10** and (a) 200 μM ATP and (b) 200 μM adenosine + 600 μM Pi. [HEPES] = 5 mM, pH 7.0 [Surfactant **10**] = 100 μM, [ATP] = 200 μM, [Adenosine] = 200 μM, [Pi] = 600 μM, [**11**] = [**12**] = 20 μM.

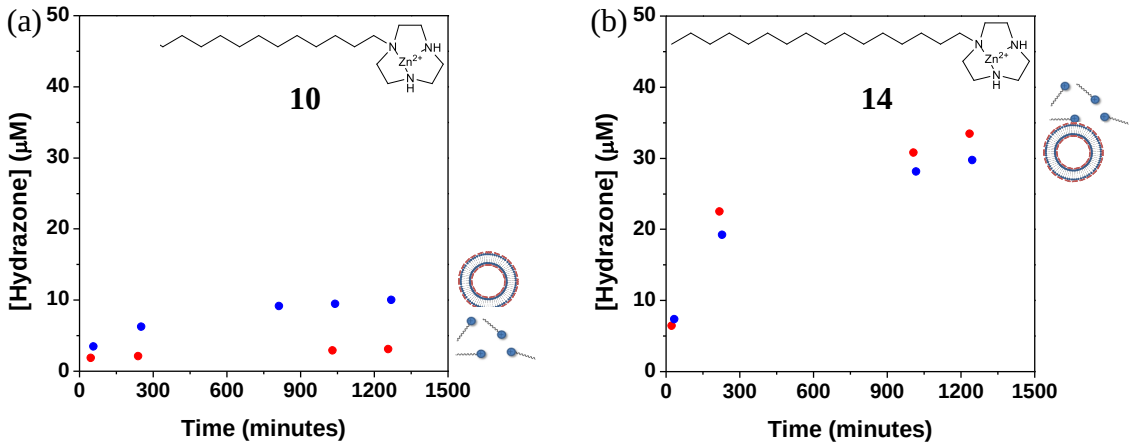

Figure 3.17: Graph showing the concentration of hydrazone **13** formed under the same conditions using (a) surfactant **10** and (b) surfactant **14** as determined by UPLC. [HEPES] = 5 mM, pH 7.0, [Surfactant **10**] = [Surfactant **14**] = 100 μM, [ATP] = 200 μM, [**11**] = [**12**] = 20 μM.

3.3.4 Determination of the order of reaction

The reaction between **11** and **12** in the vesicles (100 μM surfactant **10**, 200 μM ATP) was studied in more detail in order to better understand the dynamics of the reaction inside the vesicles. The initial rates of reaction were measured by fixing the concentration of one reagent (**11** or **12**) at 20 μM and varying the concentration of the other reagent (**12** and **11** respectively). All reaction kinetics were monitored by UV-Vis spectroscopy (Figure 3.18, Figure 3.19). The linear portion of the plot of concentration of hydrazone **13** against time was used to determine the initial rate of reaction. It was found that the rate of reaction was linearly dependent on the concentration of reactants. In the case of the hydrazide **12**, the rate of reaction did not continue to increase beyond a concentration of 30 μM, suggesting that the bilayer had a limited capacity for **12**. A plot of the log rate against the log of the concentration gives the order of reaction (Figure 3.20). From these experiments, the order of reaction was determined to be first order with respect to the aldehyde **11** and 0.5 order with respect to the hydrazide **12**. The latter could be a result of the competition with aldehyde **11** for occupation of the bilayer. Thus, an increase in concentration of **12** in the medium does not lead to the same relative increase in the bilayer.

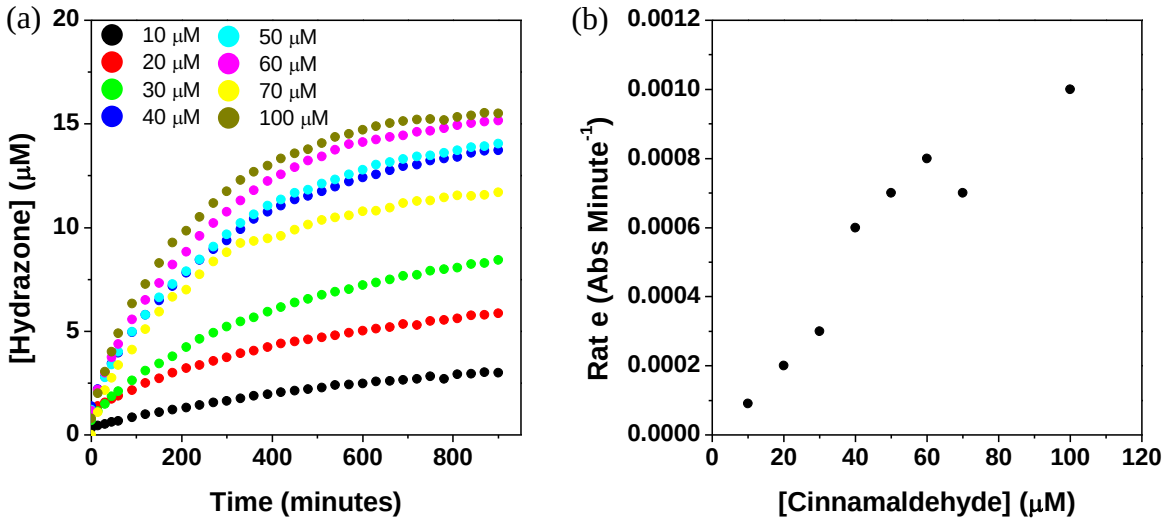

Figure 3.18: Figure showing plots of hydrazone **13** concentration against time for different concentrations of aldehyde **11** at a fixed concentation of 20 µM **12**. A plot of the rate of reaction at different concentrations of **11**, calculated from the slope of the linear portion of the graph showing absorbance against time. [HEPES] = 5 mM, pH 7.0, [Surfactant **10**] = 100 µM, [ATP] = 200 µM.

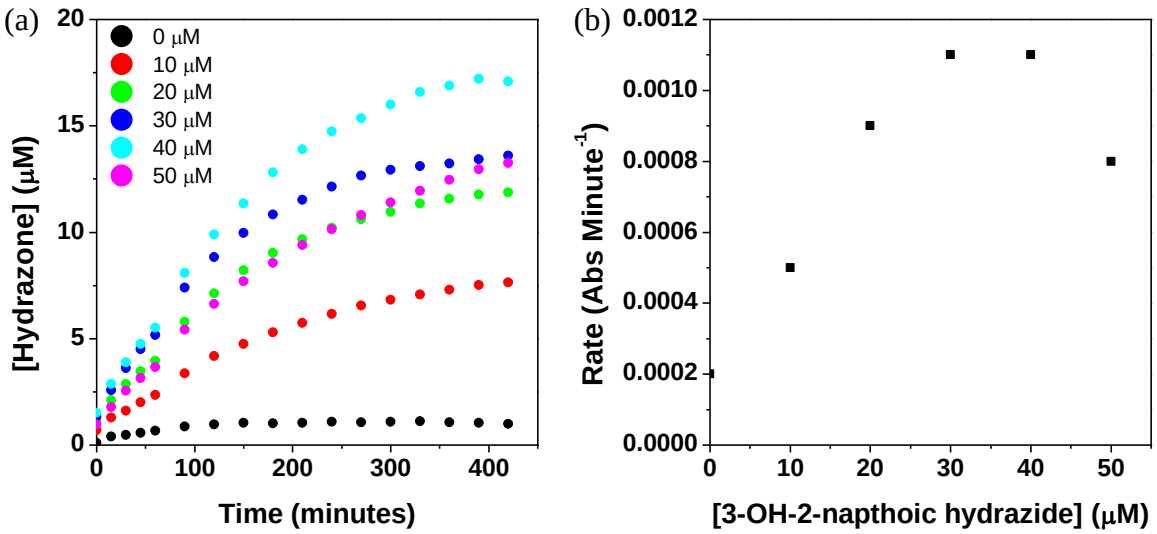

Figure 3.19: (a) Figure showing plots of hydrazone **13** concentration against time for different concentrations of hydrazide **12** at a fixed concentation of 20 µM **11**. (b) A plot of the rate of reaction for the different concentrations of hydrazide **12**, calculated from the slope of the linear portion of the graph showing absorbance against time. [HEPES] = 5 mM, pH 7.0, [Surfactant **10**] = 100 µM, [ATP] = 200 µM.

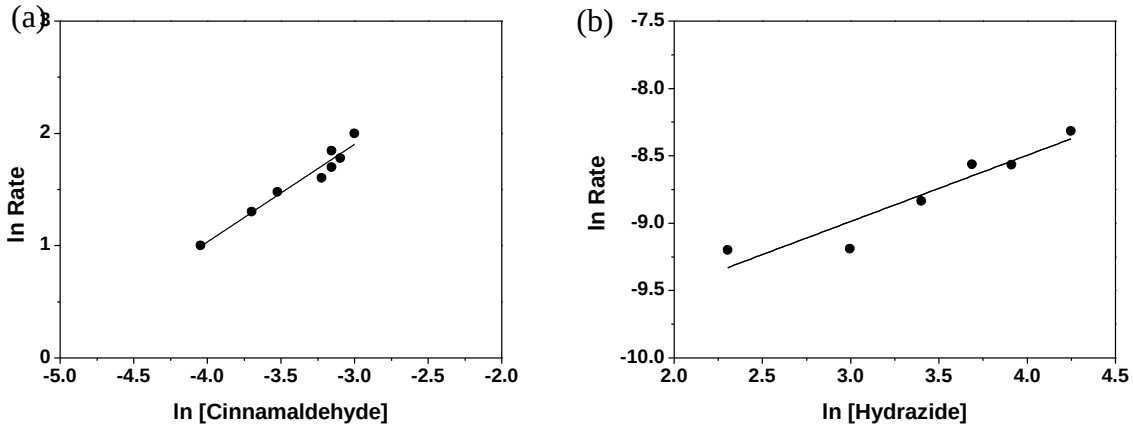

Figure 3.20: A plot of log of the rate of reaction as a function of the log of the reagent concentrations. The gradient gives the order of the reaction. [HEPES] = 5 mM, pH 7.0, [Surfactant **10**] = 100 μM, [ATP] = 200 μM. Results taken from the average of duplicate experiments.

3.3.5 Effect of pH

Like all imine-like bonds, the rates of hydrazone formation and cleavage are pH dependent. Therefore, the formation reaction between **11** and **12** was studied at pH-values varying from 5.5 to 9.0 in aqueous buffer (HEPES (10 mM), pH 7.0), surfactant **10** (100 μM) and vesicles (100 μM surfactant **10**, 200 μM ATP) by UPLC. The rate of reaction was calculated from the slope of the plots showing the concentration of hydrazone **13** formed against time (Figure 3.21). The rate of reaction in aqueous buffer (HEPES (5 mM), pH 7.0) and surfactant **10** (100 μM) was relatively indifferent of the pH. However, the rate of reaction in the vesicles was strongly pH dependant. Indeed, at pH 8.0 and 9.0, the rate of reaction in the vesicles was similar to that in the free surfactant **10** and in the aqueous buffer. The rate of reaction at pH 7.0 was moderately fast but it increased exponentially at pH 6.0 and pH 5.5 (Figure 3.21, see also Sections 3.8.5 and 3.8.6 in the Appendix).

Whilst the formation reaction in vesicles at pH 5.5 was very fast, it was found that the vesicular system was highly unstable at this pH. Indeed, when equimolar quantities of **11** and **12** are reacted inside the vesicles (100 μM surfactant **10**, 200 μM ATP), there was an initial fast increase in product formation followed by a rapid decrease in the amount of product (Figure 3.22). This decrease was attributed to instability of the vesicular system at pH 5.5 leading to precipitation (*vide infra*).

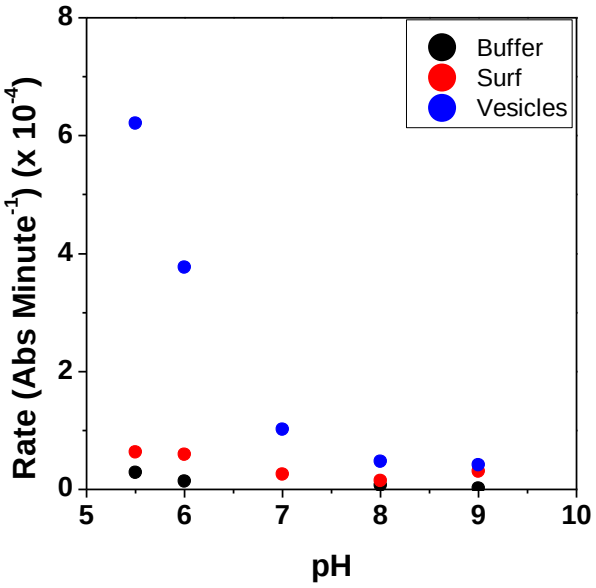

Figure 3.21: A graph showing the rate of reaction in vesicles for the reaction of 20 μM starting reagents at different pHs (pH 5.5- 9). [HEPES] = 5 mM, pH 7.0, pH 8.0, pH 9.0, [MES] = 5 mM, pH 5.5, pH 6.0, pH 6.5, [Surfactant **10**] = 100 μM, [ATP] = 200 μM, [**11**] = [**12**] = 20 μM.

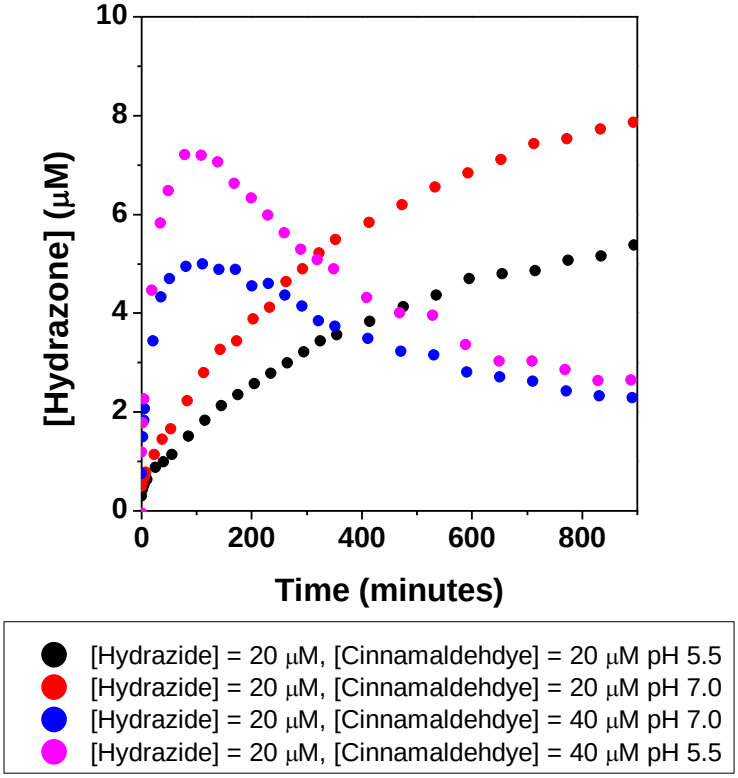

Figure 3.22: The concentration of **13** over time at pH 5.5 and pH 7.0 when reacting 20 μM **12** with 20 μM and 40 μM **11**. [HEPES] = 5 mM, pH 7.0 [Surfactant **10**] = 100 μM, [ATP] = 200 μM.

Further analyses were therefore carried out on the vesicles formed from 100 µM surfactant **10** and 200 µM ATP at pH 5.5 in order to study the stability of the system at this pH. Fluorescence spectroscopy showed that vesicles formed from 100 µM surfactant **10** and 200 µM ATP were stable overnight at pH 7.0, but the intensity of fluorescence of DPH underwent a gradual decrease in the case of the system at pH 5.5 (Figure 3.23a). This was confirmed by DLS measurements (Figure 3.23b). The count rate is a measure of the number of photons detected per second and is a measure of the stability of the sample, with lower values indicative of instability due to factors such as aggregation or precipitation.[45] The count rate of the vesicles remained approximately constant at pH 7.0 for over 600 minutes (overnight). On the other hand, the count rate decreased gradually over 350 minutes in the case of pH 5.5. The quality of the DLS data remains good throughout the time of measurement in the case of the data for pH 7.0 but the quality of the measurements degenerates after around three hours, in the case of the measurements at pH 5.5 (Data not shown). Finally, instability of the system at pH 5.5 was supported by optical density measurements (Figure 3.23c). When the optical density at 600 nm was monitored for the vesicles at different pHs, it was evident that the baseline at pH 6 and pH 7 was much more stable than at pH 5.5. It was therefore concluded that studying the system at a different pH requires a more thorough investigation of the vesicular system at that particular pH and therefore studies were continued at pH 7.0, where the system was well-behaved.

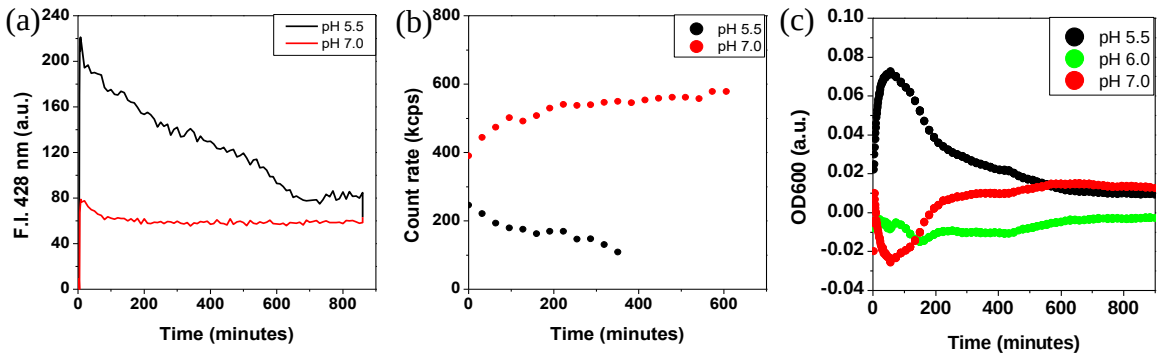

Figure 3.23: (a) The fluorescence intensity of DPH as a function of time for 100 µM surfactant **10**, 200 µM ATP at pH 5.5 and pH 7.0. [DPH] = 2.5 µM, $\lambda_{ex}/\lambda_{em}$ = = 355/428 nm, Slit: 5/5 nm, 37 °C. (b) The count rate of vesicles from 100 µM surfactant **10**, 200 µM ATP at pH 5.5 and pH 7.0 over time. (c) The optical density at 600 nm as a function of time for 100 µM surfactant **10**, 200 µM ATP at pH 5.5, pH 6.0 and pH 7.0. [HEPES] = 5 mM, pH 7.0, [MES] = 5 mM, pH 5.5.

3.3.6 Stability of hydrazone 13

Hydrazones are normally kinetically inert at neutral pH. This arises from a mesomeric effect, as a consequence of which there is a reduction in the electrophilicity of the C=N bond.[8] The stability of hydrazone **13** was tested by monitoring the absorbance of a solution of **13** in aqueous buffer (HEPES (10 mM), pH 7.0), surfactant **10** (100 μM) and vesicles (100 μM surfactant **10**, 200 μM ATP) over time. As expected, hydrazone **13** was stable in all three conditions overnight (around 800 minutes) (Figure 3.24). This meant that the self-assembled system could be used as a chemical nanoreactor for this hydrazone bond-forming reaction. However, under the conditions used it was not possible to exploit the dynamicity of equilibrium between the aldehdye **11** and the hydrazide **12**.

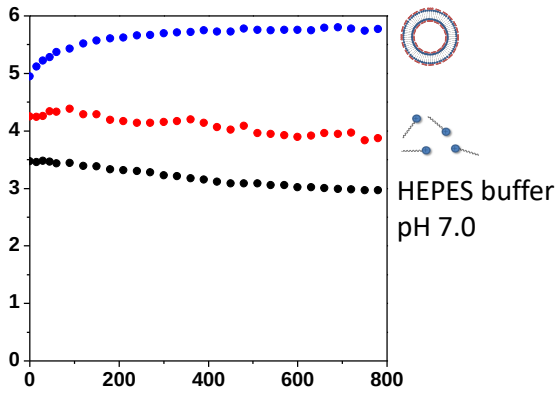

Figure 3.24: Graph showing the concentration of **13** over time for the hydrazone in aqueous buffer, 100 μM surfactant **10** and vesicles (100 μM surfactant **10**, 200 μM ATP) at pH 7.0. [HEPES] = 5 mM, pH 7.0.

3.3.7 Effect of the hydroxyl group in hydrazide 12 on the formation reaction

One potential hypothesis for the improved reaction in vesicles with hydrazide **12** was that **12** could have the capability of interacting with the positively charged headgroups in the vesicles through the hydroxy group and the nitrogen of the hydrazide group. It was therefore intriguing to investigate whether the hydroxy group in **12** had any role in determining the selective preference for the formation reaction in the vesicles. The formation reaction was thus carried out using aldehyde **11** and 2-naphthoic hydrazide, **15** to give hydrazone **16** (Scheme 3.3) in aqueous buffer (HEPES (10 mM), pH 7.0), surfactant **10** (100 μM) and vesicles (100 μM surfactant **10**, 200 μM ATP). Interestingly, when the reaction was monitored by UV-Vis spectroscopy, no new distinctive product peak was observed in the vesicles, suggesting that any product peaks are being obscured by the

absorbances of the other reagents in solution. However, analysis of the reaction by UPLC revealed that the reaction with **16** was amplified inside the vesicles (100 μM surfactant **10**) with respect to the aqueous buffer and the unassembled surfactant **10** (Figure 3.25). When compared to the reaction of **11** with **12**, a similar amount of **13** and **16** were formed overnight. This suggests that the enhanced formation of these reactions inside the vesicles from other factors, such as the hydrophobicity of **12** and **15**.

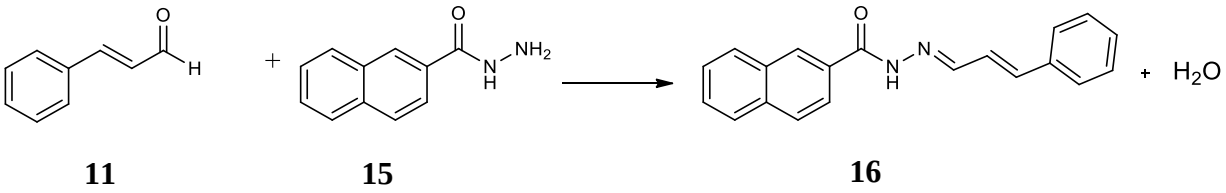

11 **15** **16**

Scheme 3.3: The reaction between **11** and **15** to give the hydrazone, **16**.

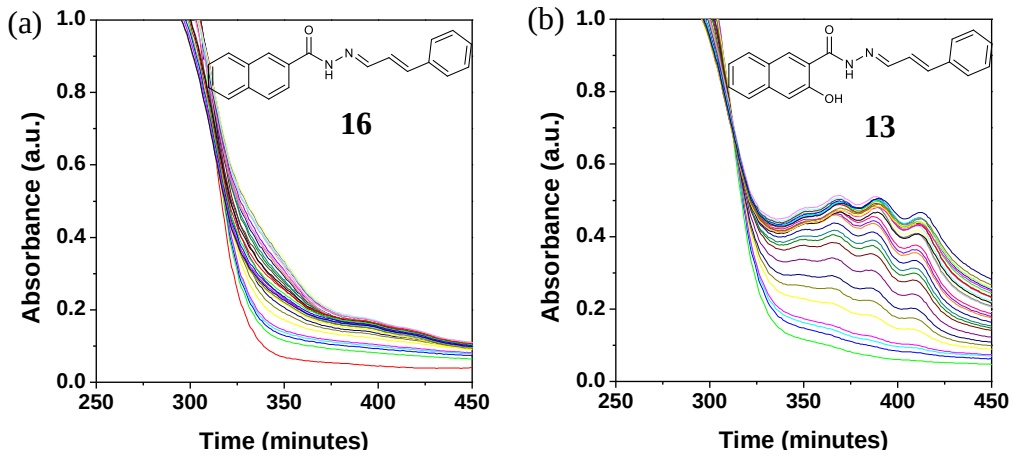

Figure 3.25: (a) Figure showing the UV-Vis spectra taken at regular intervals when reacting **11** with **15** in vesicles. Similar spectra were obtained for the same reaction in aqueous buffer and surfactant **10** (see Section 3.8.4 in the Appendix). (b) Figure showing the UV-Vis spectra taken at regular intervals when reacting **11** with **12** in vesicles, for comparison with (a). [HEPES] = 5 mM, pH 7.0 [Surfactant **10**] = 100 μM, [ATP] = 200 μM, [**11**] = [**12**] = [**15**] = 20 μM.

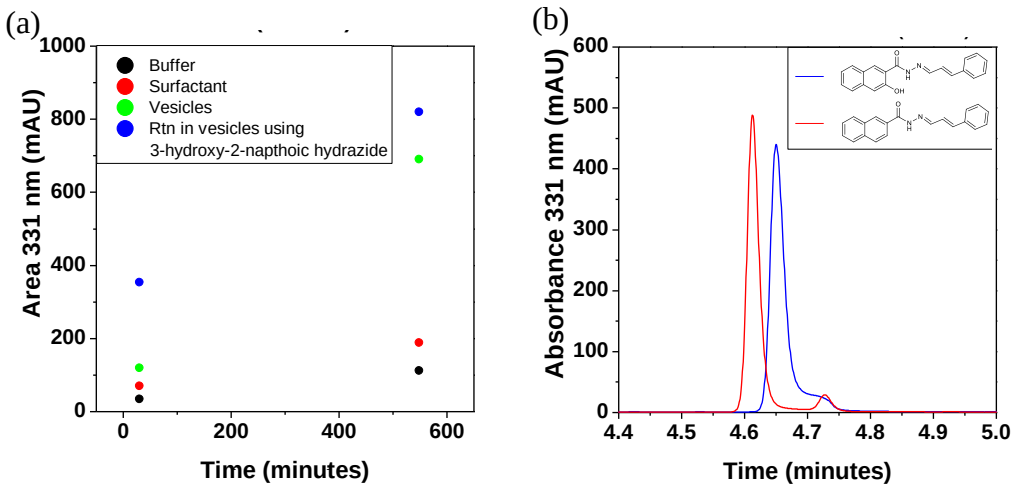

Figure 3.26: (a) The integrated area for the reaction of **11** with **15** in aqueous buffer, surfactant and vesicles. The integrated area for the reaction of **11** and **12** under the same experimental conditions is also included. (b) The final UPLC chromatogram for the formation of **13** and **16** in vesicles, suggesting that both hydrazones were formed in similar quantities under the same conditions. [HEPES] = 5 mM, pH 7.0, [Surfactant **10**] = 100 µM, [ATP] = 200 µM, [**12**] = [**15**] = 20 µM, [**11**] = 40 µM.

3.3.8 Conclusions

In summary, we have exploited the self-assembly of the surfactant **10** to form a chemical nanoreactor for controlling the reactivity of the reaction between *trans*-cinnamaldehyde, **11** and 3-hydroxy-2-napthoic hydrazide, **12**. The reaction was significantly accelerated in the ATP-templated vesicles compared to the unassembled state. The rate of reaction depends on factors such as reagent, surfactant and ATP concentration and pH. A function was thus assigned to the assembled state which was not possible to attain in the unassembled surfactant. In the next section further control over chemical reactivity will be exerted by controlling the self-assembly process.

3.4 Control over reaction selectivity in responsive self-assembly

3.4.1 Concept

Although formation of hydrazone bonds is generally slow at neutral pH, very rapid reactions have been observed even in the absence of a catalyst.[39-43] Thus, *ortho*-substituted benzaldehydes[44,45] with electron-withdrawing groups,[46,47] such as imino, hydroxy or carboxy groups have been reported to undergo uncatalysed rapid hydrazone formation in water.[39] In the system developed in the previous section, it would be expected that such aldehydes would react with hydrazide **12** in the free surfactant **10** in the non-aggregated state. Because of their polar nature it is expected that they would preferentially remain in

the aqueous phase rather than being encapsulated in the vesicles, and thus the rate of reaction would not be expected to change much in the presence of ATP.

The choice fell on 2-pyridinecarboxylaldehyde, **17** since it is an aromatic aldehyde which forms hydrazones with a characteristic absorbance in the UV-Vis spectrum. Aldehyde **17** has been reported to undergo hydrazone formation reaction with phenylhydrazine (k_{obs} = 0.045 min^{-1}) 23 times faster than methoxybenzaldehyde (k_{obs} = 0.0020 min^{-1}).[39] The reaction of aldehyde **17** with hydrazide **12** to form the hydrazone **18** is shown in Scheme 3.4. It was thus speculated that it might be possible to obtain preferential hydrazone bond formation between aldehyde **12** and **17** in the presence of the unassembled surfactant **10** in the nonaggregated state, but to invert the selectivity and obtain preferential reaction between *trans*-cinnamaldehyde, **11** and **12** in the presence of the vesicles (Figure 3.27).

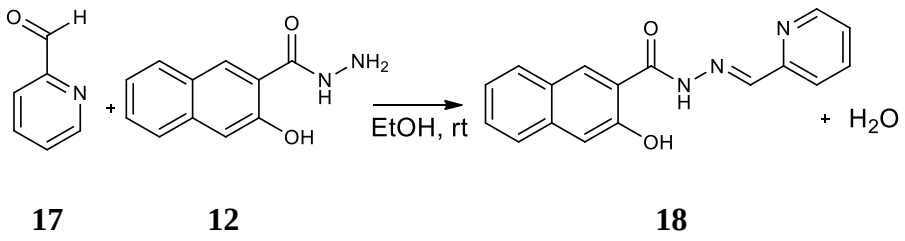

Scheme 3.4: Scheme showing the hydrazone-bond formation reaction to form **18**.

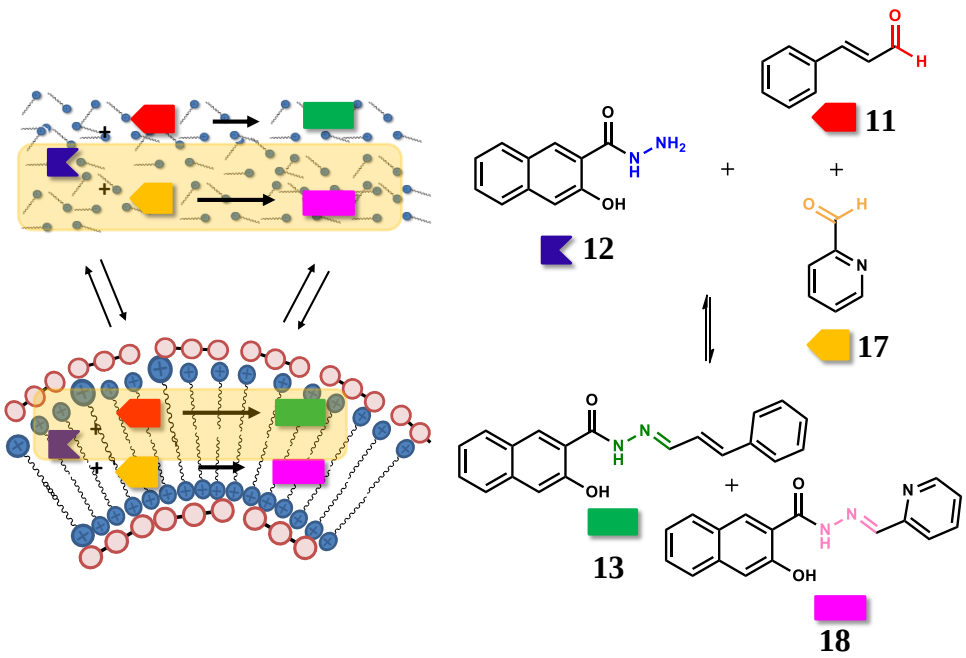

Figure 3.27: Illustration of selectivity study in the absence and presence of ATP. The hydrazide 3-hydroxy-2-napthoic hydrazide, **12**, preferentially reacts with carboxyaldehyde, **17**, to give hydrazone **18** in the presence of surfactant **10** but preferentially reacts with **11** to give **13** in the presence of vesicles formed from the addition of ATP.

3.4.2 Investigating the hydrazone bond formation reactions between 12 and aldehydes 11 and 17 separately

We initially studied the formation reaction between **12** and the two aldehydes **11** and **17** at a concentration of 10 μM in aqueous buffer (HEPES (5 mM), pH 7.0), surfactant **10** (100 μM), vesicles (100 μM surfactant **10**, 200 μM ATP). The reaction between **12** and **17** was carried out in a separate reaction flask from the reaction between **11** and **12**. The UV-Vis and UPLC retention properties of the components of the reaction between **12** and **17** are shown in Table 3.2.

	UV-*vis*	**UPLC**	
	λ_{max} (nm)	**λ (nm)**	**R_t (mins)**
2-pyridine-carboxylaldehyde, **17**[56]	260	259	1.147
3-hydroxy-2-naphtoic hydrazide, **12**	287 356	235	2.824
Hydrazone **18**	329	331	3.345

Table 3.2: Table showing the absorption properties of the solutions as determined from the UV-Vis spectra in aqueous buffer (HEPES (5 mM, pH 7.0) and the retention times obtained by UPLC.

In aqueous buffer (HEPES (5 mM), pH 7.0), the formation of **13** was highly unfavoured (υ_{init} = 4.65 × 10^{-5} μM $minute^{-1}$), as described in Section 3.3. On the other hand, the formation of **18** occurred to an appreciable extent (υ_{init} = 9.77 × 10^{-4} μM $minute^{-1}$). A similar rate of reaction was observed for hydrazone **18** in 100 μM surfactant **10** (υ_{init} = 6.95 × 10^{-4} μM $minute^{-1}$) while the formation of **13** was also slightly improved with respect to the reaction in aqueous buffer (υ_{init} = 4.36 × 10^{-4} μM $minute^{-1}$), as discussed previously in Section 3.3. The rate of formation of **13** in surfactant **10** was however, still lower than the rate of formation of hydrazone **18**. In the presence of the vesicles, on the other hand, hydrazone **18** reacted with a slightly lower rate than in the aqueous buffer and in the surfactant (υ_{init} = 3.77 × 10^{-4} μM $minute^{-1}$), but, importantly, the formation of **13** was greatly enhanced (υ_{init} = 2.07 × 10^{-3} μM $minute^{-1}$) in the presence of the vesicles (Figure 3.28, Table 3.3a).

This is in agreement with the hypothesis that the unassembled state favours the formation of hydrazone **18** while the assembled state does not significantly affect hydrazone **18** but highly favours the formation of hydrazone **13**. This leads to a change in the selectivity of the reaction upon addition of ATP to the surfactant solution (Figure 3.28).

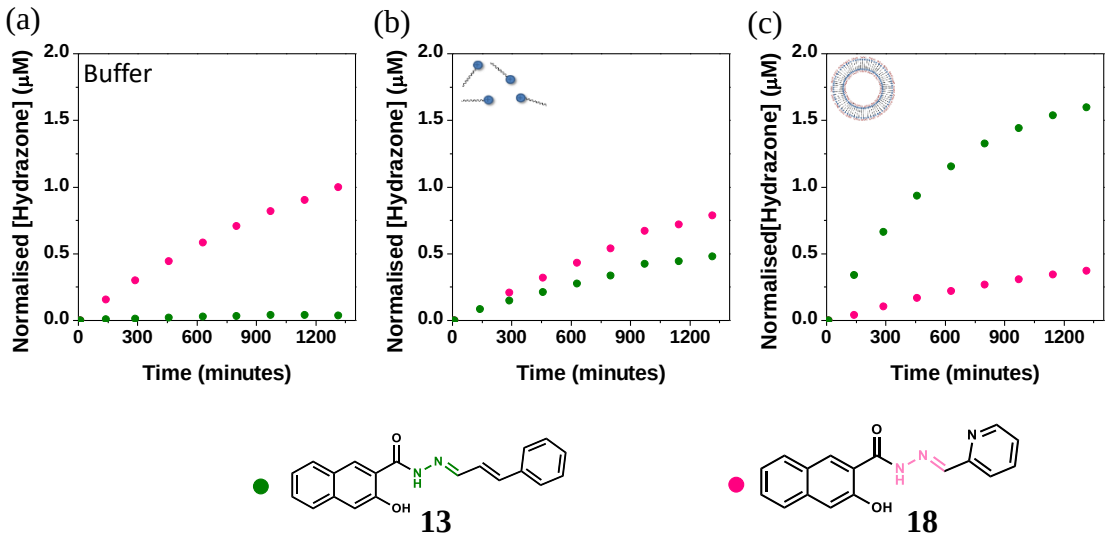

Figure 3.28: Graphs showing the concentration of hydrazones **13** and **18** over time in the presence of (a) aqueous buffer, (b) surfactant and (c) vesicles. The hydrazone **18** is preferred in the presence of aqueous buffer and surfactant while the hydrazone **13** is formed in higher yield in the presence of vesicles. [HEPES] = 5 mM, pH 7.0, [Surfactant **10**] = 100 μM, [ATP] = 200 μM. [**11**] = [**12**] = [**17**] = 10 μM.

The rate of reaction was dependent on the concentration of reagents. Doubling the concentration of reagents from 10 to 20 μM while keeping them at a ratio of 1:1 resulted in an increase in the rate of reaction in all cases by approximately five times. The individual rate enhancements upon doubling the concentrations are found in Table 3.3. The rate enhancements were calculated by dividing the initial rate for the formation reaction with 20 μM reagents by the initial rate for the formation reaction with 10 μM reagents (Table 3.4).

Two kinds of experiments were set up. In the first case, the reaction between **12** and **17** was carried out in a separate reaction vessel from the reaction between **11** and **12**. In the second case, the reagents **11**, **12** and **17** were reacted in the same reaction vessel. It was found that the rate of reaction did not show much variation between the two cases (Table 3.5), whether the reaction was carried out in aqueous buffer (HEPES (5 mM), pH 7.0) or in surfactant **10** (100 μM) or in vesicles (100 μM surfactant **10**, 200 μM ATP). This was true even if one of

the aldehydes was present in huge excess (20 μM) with respect to the hydrazide (5 μM). Further experiments were therefore carried out using reactants at 20 μM concentration in 1:1 ratio.

υ_{init} (μM minute^{-1})	(a) 10 μM reagents (× 10^{-4})			(b) 20 μM reagents (× 10^{-4})		
	Buffer	**Surfactant**	**Vesicles**	**Buffer**	**Surfactant**	**Vesicles**
13	0.47	4.36	20.70	12.00	18.00	89.00
18	9.77	6.95	3.77	31.00	65.00	23.00

Table 3.3: Table showing the initial rate of reaction for the reaction of (a) 10 μM and (b) 20 μM **11, 12** and **17** in aqueous buffer, surfactant and vesicles. The graph showing the change in concentration against time can be found in Section 3.8.7 in the Appendix. [HEPES] = 5 mM, pH 7.0, [Surfactant **10**] = 100 μM, [ATP] = 200 μM.

υ_{init} (20 μM) / υ_{init} (10 μM)	**Buffer**	**Surfactant**	**Vesicles**
13	25.53	4.13	4.30
18	3.17	9.35	6.10

Table 3.4: Table showing the rate enhancement of the reaction between **11**/**17** and **12** to give hydrazones **13** and **18** when carrying the formation reaction in the presence of 10 μM and 20 μM reagents. The rate enhancement was calculated by dividing the initial rate for the formation reaction with 20 μM reagents by the initial rate for the formation reaction with 10 μM reagents.

υ_{init} (μM minute^{-1})	Separate reaction vessel (× 10^{-4})			Same reaction vessel (× 10^{-4})		
	Buffer	**Surfactant**	**Vesicles**	**Buffer**	**Surfactant**	**Vesicles**
13	0.64	2.33	17.20	0.76	1.82	17.90
18	0.80	9.50	6.92	7.15	7.50	5.11

Table 3.5: Table showing the initial rate of reaction for the hydrazone bond formation reaction when (a) the reaction between **12** and **17** to give **18** was carried out in a separate reaction vessel from the reaction between **11** and **12** to give **18** and (b) the reaction between **11** and **12** and **17** was carried out in the same reaction vessel. [HEPES] = 5 mM, pH 7.0, [Surfactant **10**] = 100 μM, [ATP] = 200 μM, [**11**] = [**17**] = 5 μM, [**12**] = 20 μM. The initial rate of reaction, υ_{init} was calculated from the slope of a graph showing the concentration of hydrazone formed as a function of time. The graphs are found in Section 3.8.5 in the Appendix.

3.4.3 Selectivity studies in the absence and presence of ATP

The different reactivities of **11** and **17** with **12** in the assembled and disassembled state prompted us to investigate whether it would be possible to change the selectivity of the system using ATP as a trigger. Equimolar concentrations of the reagents **11**, **17** and **12** (20 μM) were therefore mixed with surfactant **10** (100 μM). Under these conditions, the formation of **18** proceeded faster (υ_{init} = 2.64 × 10^{-3} μM $minute^{-1}$) than the formation of **13** (υ_{init} = 6.90 × 10^{-4} μM $minute^{-1}$) (Figure 3.29a). ATP was added after approximately 400 minutes. The rate of formation of **18** proceeded at a slightly lower rate than before (υ_{init} = 1.34 × 10^{-3} μM $minute^{-1}$). However, there was a huge increase in the rate of formation of **13** (υ_{init} = 3.46 × 10^{-3} μM $minute^{-1}$). Consequently, after a certain period of time, the concentration of **13** exceeded the concentration of **18**.

A similar effect could be clearly observed when the reaction was initially carried out in aqueous buffer and ATP (Figure 3.29b). Under these conditions, **18** was preferentially formed over **13** (υ_{init} for **18** = 2.98 × 10^{-3} μM $minute^{-1}$ while υ_{init} for **13** = 5.22 × 10^{-4} μM $minute^{-1}$). Addition of surfactant **10** results in the formation of vesicles. Indeed, when the surfactant **10** was added to the solution, the rate of formation of **18** proceeded at approximately the same rate (υ_{init} = 3.04 × 10^{-3} μM $minute^{-1}$). There was however an immediate, sudden increase in the rate of formation of **13** (υ_{init} = 9.87 × 10^{-4} μM $minute^{-1}$). After some time, **13** exceeded **18** in concentration. These two experiments clearly show that it is possible to selectively control which reaction occurs preferentially in the reaction medium by controlling the self-assembly of the surfactant **10** with ATP.

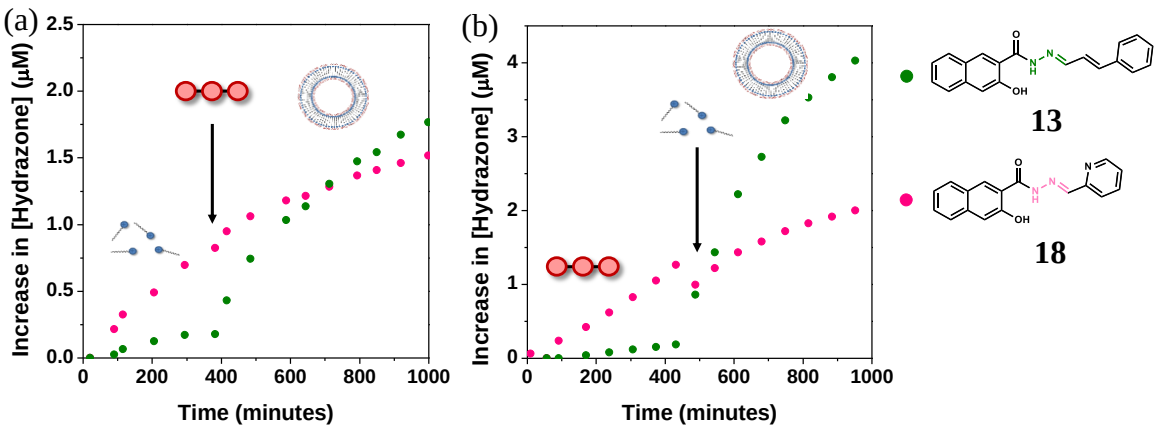

Figure 3.29: (a) Graph showing the increase in **13** and **18** in surfactant **10** on its own and upon addition of ATP to form vesicles. (b) Graph showing the increase in **13** and **18** in aqueous buffer and ATP and upon addition of surfactant **10** to form vesicles. [Surfactant **10**] = 100 μM, [ATP] = 200 μM, [**11**] = [**12**] = [**17**] = 20 μM.

3.4.4 Selectivity study under dissipative conditions

Temporal control over the reactions could be obtained by dissipating the energy stored in ATP. The enzyme potato apyrase has been used in earlier studies as an external additive to hydrolyse the ATP and destabilise the assembly in the process.[7] Earlier studies have shown that the waste products of ATP hydrolysis, AMP and inorganic pyrophosphate, Pi stabilise the vesicles under the conditions used (*vide* Chapter 2), and therefore it was necessary to modify the conditions in order to obtain a balance between the stabilisation of the vesicular structure by AMP and product enhancement by the vesicles.

The reaction between **12** and the aldehydes **11** and **17** was therefore studied in 100 μM surfactant **10** and increasing concentrations of ATP. As expected, the formation of **13** was sensitive to the amount of ATP present, with higher concentrations being formed upon increasing the ATP concentration. This agrees with the UV-Vis results described previously. On the other hand, the formation of **18** was relatively independent of the concentration of ATP, as expected based on the previous observation that **11** reacts with **17** irrespective of the presence of the vesicles. From this experiment it was determined that sufficient amount of **13** was obtained when carrying out the reaction with 50 μM ATP (Figure 3.30). Experiments in the presence of the enzyme were therefore carried out in the presence of 100 μM C_{12}TACN•Zn^{2+} and 50 μM ATP.

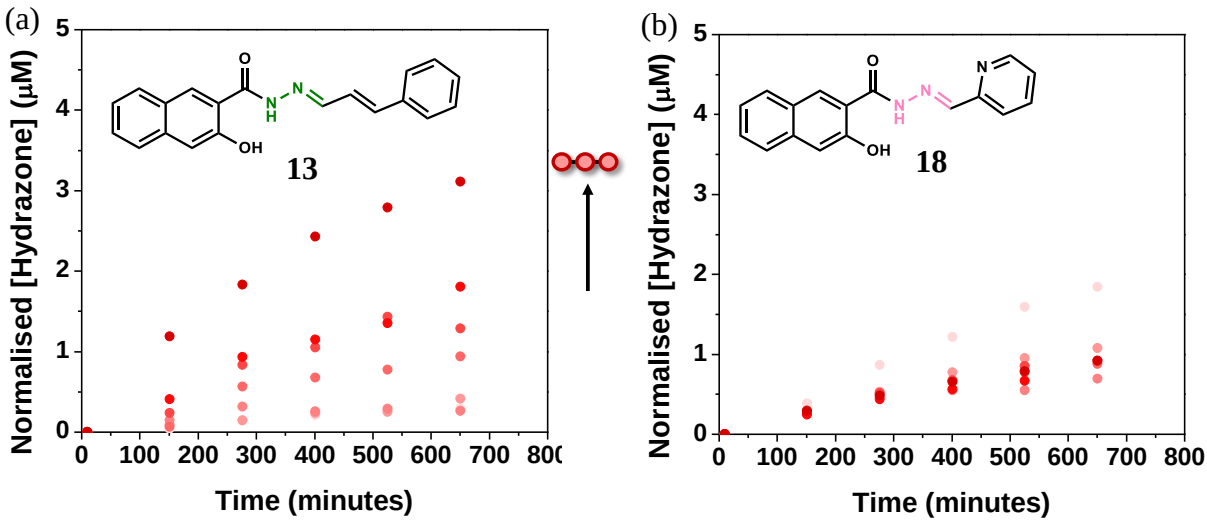

Figure 3.30: Graph showing the increase in the concentration of (a) **13** and (b) **18** when carrying out the reaction between aldehydes **11** and **17** and hydrazide **12** in the presence of 100 μM surfactant **10** and increasing concentrations of ATP. Graphs are plotted from the same experiment. [HEPES] = 5 mM, pH 7.0, [Surfactant **10**] = 100 μM, [**11**] = [**12**] = [**17**] = 20 μM.

A control was initially carried out to make sure that the enzyme potato apyrase does not react with the reactants. The reaction was therefore carried out in the unassembled surfactant **10** in the absence and presence of apyrase. The amount of hydrazone formed was similar in the both cases, both for the formation of **13** as well as for the formation of **18**. It could thus be concluded that the enzyme was not affecting the reaction. The enzyme potato apyrase is usually used in the presence of divalent Ca^{2+} ions in order to activate it. Separate studies have shown that TACN is capable of catalysing the cleavage of ATP in conjunction with potato apyrase (Chapter 2 and Chapter 4) and therefore it was decided to proceed to the enzyme studies without the use of Ca^{2+}, thereby avoiding increasing the complexity of the system further. An additional motivation for not using Ca^{2+} in the experiments was that earlier it has been shown that divalent metal ions affect the yield of the reaction in vesicles (Section 3.3.3).

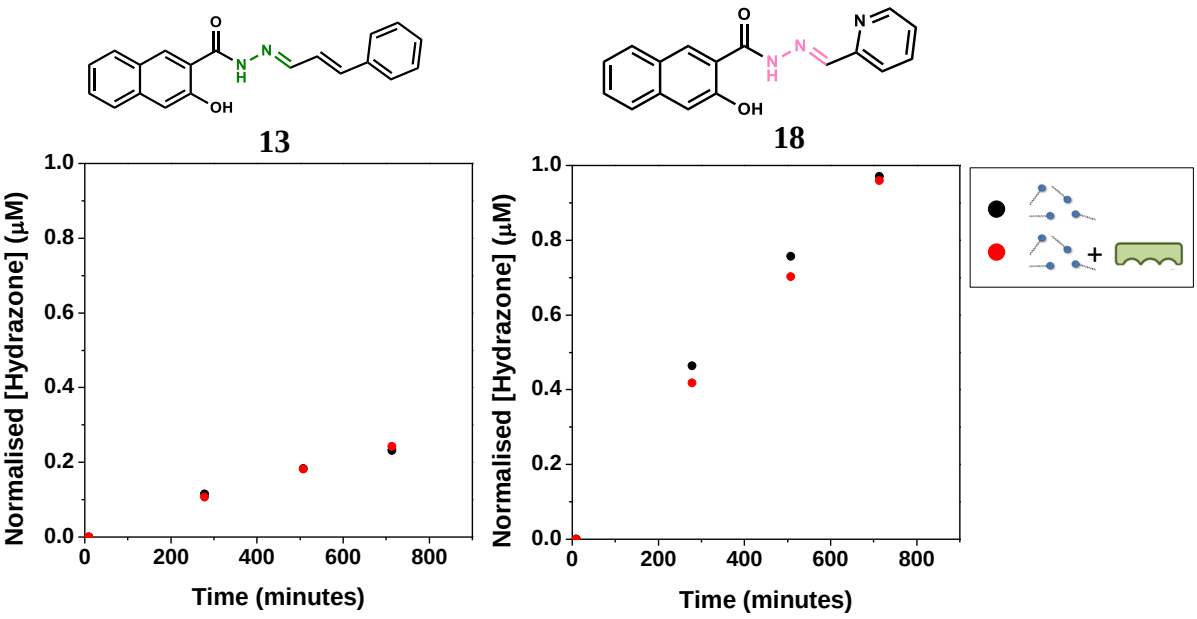

Figure 3.43: Graph showing the increase in the concentration of (a) **13** and (b) **18** when carrying out the reaction between aldehydes **11** and **17** and hydrazide **12** in the presence of 100 µM surfactant **10** with and without 1.0 U potato apyrase. Graphs are plotted from the same experiment. [HEPES] = 5 mM, pH 7.0, [Surfactant **10**] = 100 µM, [**11**] = [**12**] = [**17**] = 20 µM.

In Section 3.3.3 it was also shown that waste products of ATP hydrolysis do not induce product formation in the case of hydrazone **13.** Both the waste products of ATP hydrolysis by potato apyrase (AMP + 2Pi) as well as the waste products generated due to the action of alkaline phosphatase (adenosine + 3Pi) were unable to induce product formation even at high concentrations. Studies are underway to determine whether there is any effect from the waste products on hydrazone **18**.

For reasons of time, only some preliminary studies have been carried out for the formation reaction of hydrazones **13** and **18** in vesicles (100 μM surfactant 10, 50 μM ATP) in the presence of the enzyme potato apyrase. The enzyme was added at the beginning of the experiment and the reaction was started by the addition of ATP. Preliminary results suggest that the formation of **18** is not significantly affected by the enzyme while the formation of **13** decreases with increasing enzyme concentration. This is expected according to the mechanism of self-assembly under dissipative conditions. Hydrazone **18** forms irrespective of the presence of the vesicles since **17** is not encapsulated. In the presence of the enzyme, hydrazone **13** initially starts to form as the vesicles are formed. However, as the enzyme destabilises the assembly, it is expected that product formation ceases, leading to lower quantities of product formation with increasing enzyme concentration.

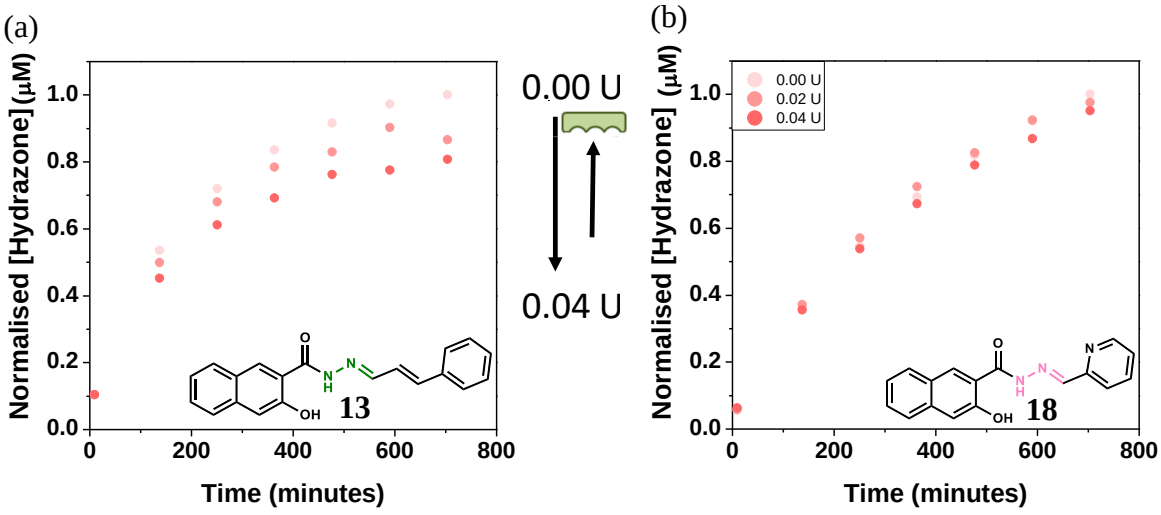

Figure 3.44: Graphs showing the increase in hydrazone concentration for (a) **13** and (b) **18** when carrying out the reaction in the presence of increasing concentration of potato apyrase. [Surfactant **10**] = 100 μM, [ATP] = 50 μM [**11**] = [**12**] = [**17**] = 20 μM.

However, these results were limited by the fact that only a low amount of potato apyrase could be used to avoid precipitation. Moreover, although ^{31}P NMR provided evidence that the enzyme potato apyrase was cleaving ATP into AMP and Pi (*vide* Chapter 2.2.6), it was not possible to prove the dissipation of energy by fluorescence spectroscopy using potato apyrase under these conditions (100 μM surfactant **10**, 50 μM ATP) (*vide* Chapter 2.2.8). Since then, it has been possible to demonstrate that under the conditions used (100 μM surfactant **10**, 50 μM ATP) it is possible to dissipate the energy of ATP using alkaline phosphatase (*vide* Chapter 2.2.8). This process could be followed by fluorescence

spectroscopy. DLS confirmed that vesicles were disassembled and no stable vesicles were discernible upon letting the vesicles (100 μM surfactant **10**, 50 μM ATP) stand in the presence of alkaline phosphatase overnight. Visual inspection of the samples also suggested a clear solution devoid of vesicular structures.

These latest results suggest that alkaline phosphatase could be a more suitable enzyme to use with surfactant **10**. Studies are underway to study the formation of hydrazones **13** and **18** using self-assembly under dissipative conditions in the presence of the enzyme alkaline phosphatase. It is expected that the reactivity can be further tuned by the presence of the enzyme (Figure 3.31). Thus, for example, it would be expected that the formation of **18** is favoured in the presence of surfactant **10** in the presence of alkaline phosphatase. Addition of ATP would result in the formation of vesicles and a consequent preference of the system for the formation of hydrazone **13**. However, as the assembly is disaggregated by the enzyme alkaline phosphatase, the formation of hydrazone **13** should cease to increase. The formation of **18** is not expected to be affected. It could thus be possible to achieve conditions where the formation of **18** becomes preferred once again, inverting the selectivity of the reaction once again.

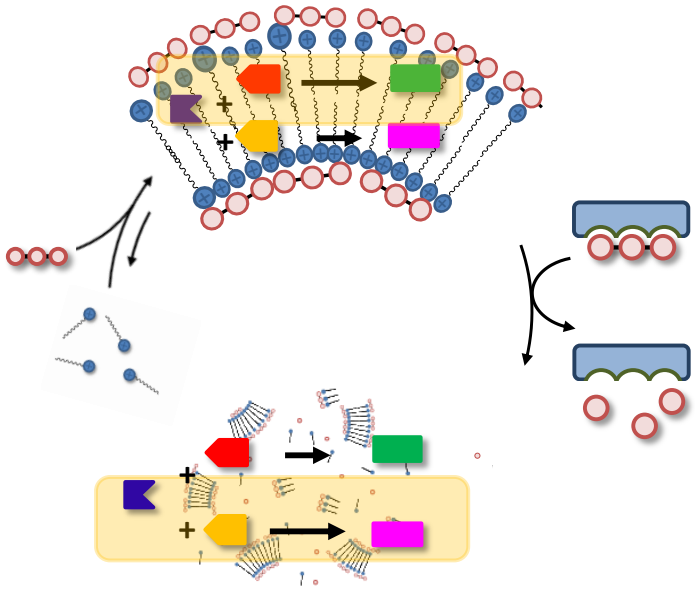

Figure 3.31: (a) Diagram showing self-assembly under dissipative conditions in the studied system and the change in the preferred reaction occurring in the assembled and disassembled states.

3.5 Conclusions

Self-assembly under dissipative conditions brings synthetic systems closer to biological ones. It provides new ways to control functions which are not possible under classical thermodynamic conditions. In this work we have made initial steps to develop a synthetic system which shows responsive and adaptive behaviour. Templates were used to induce self-assembly leading to the formation of vesicles which do not spontaneously form in aqueous conditions at those concentrations. It can thus be compared to a very primitive biological cell, providing a compartment where reactions can proceed away from the aqueous outside enviornment. It was shown that the templated vesicles were able to significantly enhance hydrazone formation between apolar hydrazides and aldehydes.

The templated self-assembly process was further exploited for controlling chemical reactivity. The addition of ATP acted as a trigger to change the selectivity of a hydrazone formation reaction. Whilst in the absence of the assembly one reaction was favoured, the assemblies formed upon the additon of template enhanced the rate of another reaction. By adding a temporal dimension to the assembly it would be possible to transiently alter the selectivity of the reaction.

3.6 Experimental

3.6.1 Materials and methods

3.6.1.1 Instrumentation

^{1}H were recorded using a Bruker spectrometer operating at 300 MHz for ^{1}H. ^{13}C NMR (proton decoupled) were recorded on a Bruker AV500 operating at 500 MHz for ^{1}H and at 126 MHz for ^{13}C. Chemical shifts, δ are reported in ppm and are referenced against TMS (δ_H = 0.00 ppm) or the solvent residual peak (δ_H = 7.26 for $CDCl_3$, δ_H = 2.49 ppm for DMSO-d_5 residual peak, δ_H = 3.31 for CD_3OD residual peak), (δ_C = 77.16 ppm for $CDCl_3$, δ_C = 39.52 ppm for DMSO-d_5 residual peak, δ_C = 49.00 for CD_3OD residual peak).[48] Abbreviations for multiplicity are as follows: s = singlet, br s = broad singlet, d = doublet, t = triplet, q = quartet, m = multiplet, dd = doublet of doublet, etc.).

MS Measurements

ESI-MS measurements were acquired on an Agilent Technologies 1100 Series LC/MSD Trap-SL spectrometer, equipped with an ESI source, hexapole filter and ionic trap.

pH Measurements

The pH of buffer solutions was determined at room temperature using a Metrohm-632 pH meter equipped with a Ag/AgCL/KCl reference electrode and calibrated with standard buffer solutions at pH 7.00 and pH 10.00.

UV-Vis Measurements

UV-Vis measurements were recorded on a Varian Cary50 spectrophotometer holding a thermostated cuvette holder hosting a maximum of 14 cuvettes or a Varian Cary100 spectrophotometer hosted with a thermostated multiple cuvette holder. Individual spectra were acquired in Scan Mode while kinetics were followed in Scanning Kinetics Mode. The spectra were then exported and analysed using Excel and plotted using Origin. Analysis were conducted using 1 mL Quartz cuvettes.

UPLC Analysis

The UHPLC analysis were performed on an Agilent Technologies 1290 Infinity equipped with a DAD detector and a Quadrupole LC/MS. Conditions: Flow rate: 0.6 ml/min, Gradient: 5-95 %B to 95-5%B (A: H_2O+0.1%HCOOH, B: CH_3CN + 0.1% HCOOH) from 0.00 to 5.00 min; 95-100 % B in 5 to 5.10 min; 100 % B from 5.10 to 8.10 min; 100-5 %

B in 8.10 to 9.10 min; and finally 5% B from 9.10 to 10.00 min. Column: Agilent Zorbax SB-C3 Rapid Resolution HT 3.0 × 100 mm 1.8 micron. Injection volume: 20 µL Column temperature: 40 ^{o}C

Fluorescence Spectroscopy

Fluorescence measurements were recorded on a Varian Cary Eclipse Fluorescence spectrophotometer equipped with a thermostated cell holder hosting a maximum of 4 cuvettes. Experiments were typically conducted in 1 mL fluorescence quartz cuvettes.

DLS Analysis

DLS measurements were recorded on a Malvern Zetasizer Nano-S instrument. Samples were analysed in disposable low volume cuvettes.

TEM Analysis

TEM images were recorded on a Jeol 300 PX electron microscope. One drop of sample was placed on the sample grid and the solvent evaporated. TEM images were elaborated using the software ImageJ (http:// rsb.info.nih.gov/ij/).

3.6.1.2 Materials

All commercially available reagents were used as received. The final solutions for analysis by UV-Vis and UPLC were prepared from stock solutions prepared in the respective solvent and diluted in MilliQ water.

ATP and AMP were obtained from Sigma Aldrich. Solutions were prepared as an approximately 10 mM solution in MilliQ water by weight and the exact concentration was calculated by UV-Vis spectroscopy using the molar extinction coefficients: ε_{259} (ATP, AMP, adenosine) = 15400 M^{-1} cm^{-1}.[49] Inorganic phosphate solution was prepared as a 20 mM stock solution by weight in MilliQ water.

The aldehydes *trans*-cinnamaldehyde, **11** and 2-pyridinecarboxylaldehyde, **17** and the hydrazides 3-hydroxy-2-napthoic hydrazide, **12**, and napthoic hydrazide, **15**, together with furoic hydrazide, phenyl acetic hydrazide, indole acetic hydrazide, toluic hydrazide, and 4-nitrobenzoic hydrazide were purchased from Sigma Aldrich and used without further purification. Solutions were prepared by weight in acetonitrile at the required

concentration, typically 20 mM, fresh before use. The concentration of *trans*-cinnamaldehyde, **11**, and 2-pyridinecarboxyaldehyde, **17**, were further determined by UV-Vis spectroscopy using the molar extinction coefficients: ε (*trans*-cinnamaldehyde) = 25300 M^{-1} cm^{-1}[50], ε (2-pyridinecarboxylaldehyde) = 5290 M^{-1} cm^{-1}.[51]

The $Zn(NO_3)_2$ stock solution was standardized using EDTA following standard procedures. $CaCl_2$ was procured as an analytical grade reagent from Sigma Aldrich.

The buffers 4-(2-hydroxyethyl)-1-piperazineethanesulfonic acid (HEPES) and 2-(N-morpholino)ethanesulfonic acid (MES) were procured from Sigma-Aldrich and used without further purification. The buffers were prepared as 100 mM solutions in MilliQ water and adjusted to the required pH. HEPES buffer was used for solutions requiring a pH of 7-9 while MES buffer was used for solutions requiring a pH of 5.5-6.5.

The fluorophore 1,6-diphenyl-1,3,5- hexatriene (DPH) was procured from Sigma-Aldrich and used without further purification.

The enzymes potato apyrase and alkaline phosphatase were obtained from Sigma Aldrich and used without further purification. The apyrase was dissolved in 1.0 mL of MilliQ water to give a concentration of 100 U/mL, divided into working aliquots of 20 µL and preserved at -20 ºC. The solution was further diluted by a factor of 10 in order to obtain a stock solution of 10 U/mL when necessary. The enzyme alkaline phosphatase was dissolved in 1 mL water to obtain a concentration of 1000 U ml^{-1}.

3.6.2 Synthesis of hydrazones

Hydrazones were synthesized using general published procedures.[31,52] Generally, the solid hydrazide was dissolved in the minimum amount of ethanol in a round-bottomed flask and the solution was stirred with a magnetic stirrer. An equimolar quantity of the respective aldehyde was added dropwise to the solution whilst stirring the solution. A few drops of TFA were sometimes added as a catalyst. The hydrazones precipitated out of solution as white or yellow solids, which were filtered and if necessary, recrystallised from methanol.

The identity and purity were confirmed by ^{1}H NMR spectroscopy. When obtained in DMSO-d_6, the NMR spectra of the hydrazones generally showed the presence of two isomers.[31] On the other hand, only one isomer was observed when the ^{1}H NMR spectrum

of the product was obtained in CD_3OD. *E*, *Z*-isomerism around the NH-C(O) bond is an intrinsic property of the double bond functionality in hydrazones,[53,54] with the *E* isomer being more favoured over the *Z* isomer (Figure 3.32).[55,56]

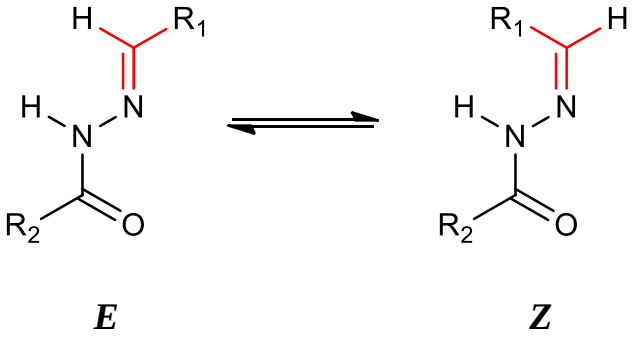

E ***Z***

Figure 3.32: *E* -> Z configurational switching in hydrazones.

Hydrazone 13

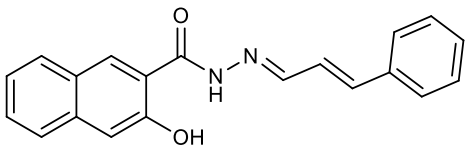

Hydrazone **13** was synthesized from 382.8 mg (1.89 mmol) 3-hydroxy-2-napthoic hydrazide, **12**, and 293.44mg (2.22 mmol) cinnamaldehyde, **11**, in 50 ml absolute ethanol. The solid crystallised out upon concentration of solution and recrystallised from ethanol to give 314.2 mg of **13** (52.5% yield).

R_f = 0.5 (hexane:ethyl acetate 80:20)

UV-Vis: λ_{max} = 331 nm (methanol)

^{1}H NMR (only major isomer: 88%) (DMSO-*d6*, 300 MHz, 300 K, ppm): δ 7.08 (d, *J* = 4.3 Hz, 2H), 7.25 – 7.41 (m, 6H), 7.48-7.50 (m, 1H), 7.62 (d, *J* = 7.4 Hz, 2H), 7.73 (d, *J* = 8.3 Hz, 1H), 7.87 (d, J = 8.3 Hz, 1H), 8.21-8.23 (m, 1H), 8.41 (s, 1H), 11.28 (s, 1H), 11.85 (s, 1H)

^{1}H NMR (MeOD-d_4, 300 MHz, 300 K, ppm): δ 7.10 (d, *J* = 4.3 Hz, 2H), 7.29 – 7.40, (m, 6 H), 7.45-7.55 (m, 1H), 7.55-7.64 (m, 2H), 7.70 (d, *J*= 8.3 Hz, 1H), 7.88 (d, *J* = 8.3 Hz, 1H), 8.18 – 8.20 (m, 1H), 8.52 (s, 1H)

^{13}C NMR (DMSO-*d6*, 126 MHz, 300 K, ppm): δ 111.02, 120.77, 124.27, 125.97, 126.32, 127.25, 127.67, 128.70, 129.14, 129.35, 129.46, 130.71, 136.31, 140.13, 150.97, 154.57, 164.17

MS (ESI,+, MeOH:H_2O 1:1): m.z calculated for $C_{20}H_{16}N_2O_2$ [M+H]+ 317.349, found 317.2.

Hydrazone 16

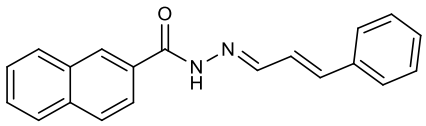

Hydrazone **16** was synthesized from 15.4 mg (0.1 mmol) naphthoic hydrazide, **15**, and 10.9 mg (0.1 mmol) *trans*-cinnamaldehyde **11** in 4 mL absolute ethanol. The hydrazone precipitated out of solution and was filtered, dried and recovered as a pure white solid in 50.3% yield.

UV-Vis: λ_{max} = 231 nm, 279 nm (methanol)

^{1}H NMR (DMSO-*d6*, 300 MHz, 300 K, ppm): δ 11.88 (s, 1H), 8.50 (s, 1H), 8.30 (1, 1H), 8.10-7.90 (m, 4H), 7.62 (m, 4 H), 7.50-7.30 (m, 3H), 7.07 (s, 2H)

^{13}C NMR (DMSO-*d6*, 126 MHz, 300 K, ppm): δ 126.25, 127.66, 128.83, 129.05, 129.82, 129.95, 130.04, 130.79, 130.85, 132.68, 134.01, 136.25, 137.88, 140.98, 151.71, 165.01

MS (ESI,+, MeOH:H_2O 1:1): m.z calculated for $C_{20}H_{16}N_2O_2$ [M+H]+ 301.350, found 301.2.

Hydrazone 18

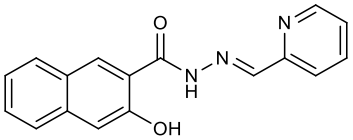

Hydrazone **18** was synthesized from 254 mg (1.25 mmol) 3-hydroxy-2-napthoic hydrazide **12** and 134.5 mg (1.25 mmol) pyridine carboxylaldehyde **17** in 150 mL absolute ethanol.

The orange-yellow solid precipitated out of solution upon evaporation of some of the solution, was filtered, dried and recrystallised from methanol to afford 128.3 mg of **18** (35% yield).

UV-Vis: λ_{max} = 329 nm

^{1}H NMR (only major isomer: 86%) (DMSO-*d6*, 300 MHz, 300 K, ppm): δ 7.21 – 7.55 (m, 4H), 7.74 (d, *J* = 8.1 Hz, 1H), 7.89 (d, *J* = 7.2 Hz, 2H), 8.00 (d, *J* = 8.1 Hz, 1H), 8.40 - 8.44 (m, 2H), 8.62 (s, 1H), 11.10 (s, 1H), 12.11 (s, 1H).

^{13}C NMR (DMSO-*d6*, 126 MHz, 300 K, ppm): δ 110.97, 120.57, 121.34, 124.29, 125.04, 126.34, 127.26, 127.37, 128.71, 129.12, 130.77, 136.31, 137.43, 148.96, 150.07, 153.61, 154.33, 164.49
MS (ESI,+, MeOH:H_2O 1:1): m.z calculated for $C_{17}H_{13}N_3O_2Na$ [M+Na]+ 314.284, found 314.1.

3.6.3 Stability of *trans*-cinnamaldehyde solution

The photooxidation of cinnamaldehyde has been documented.[50] The solution was therefore prepared fresh before use every time. Evidence of limited stability of the solution was obtained by UV-Vis spectroscopy (Figure 3.33a) and the formation of cinnamic acid was visible in UPLC chromatograms when attempting to use older solutions (Figure 3.33b). The identity of the by-product was verified to be cinnamic acid by MS [M+H] = 149 g mol^{-1} and by the injection of a standard cinnamic acid solution, which gave a peak at the same retention time (R_t = 3.2 minutes) and same mass spectrum. These problems could however be avoided by using a freshly bought sample, prepared fresh before use.

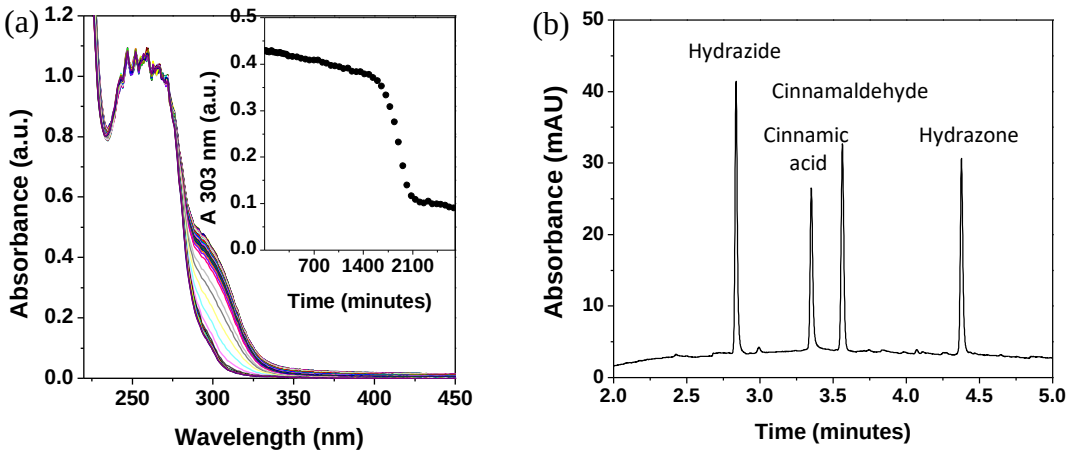

Figure 3.33: (a) UV-Vis spectrum of 20 µM cinnamaldehyde, **11**, over time. Inset shows the change in the peak at 303 nm over time, showing that cinnamaldehyde solutions were stable for approximately 1600 minutes, which was more than the duration of the experiments, after which the absorbance decreased, suggesting degradation in the solution. (b). UPLC chromatograph showing the formation of an extra peak of cinnamic acid when using an older solution of cinnamaldehdye.

3.6.4 Following the reactions by UV-Vis spectroscopy

For the reactivity studies, the concentration of reagents (**11** and **12**) was fixed at 20 µM since at this concentration all measurements could be easily quantified. The molar extinction coefficients were determined from the linear plots obtained from UV-Vis calibration curves of the starting reagents and the hydrazone in buffer, surfactant (100 µM) and vesicles. The linearity of those plots showed that all reagents and products are water-soluble at the concentrations used.

The solutions of reagents needed to follow the reactions by UV-Vis spectroscopy were prepared in 1 mL quartz cuvettes. The required volumes of the appropriate stock solutions were added to the cuvette and the solution made up with MilliQ water to give a final volume of 1 mL. The order of addition of solutions was the following (as needed): buffer, MilliQ water, surfactant, Zn^{2+}, reagents added sequentially, ATP. The baseline was taken on individual cuvettes prior to the addition of the reagents. One of the reagents was then added and the spectrum taken. The reaction was started by the addition of the second reagent in the case of the reaction in buffer and surfactant and the addition of the second reagent followed by the addition of ATP in the case of the reaction in vesicles. The solution was shaken well after the addition of each reactant to ensure homogenous solution and to minimise immediate reaction due to local concentrations of reagents. ATP was added after the reagents in order to entrap the reagents inside the vesicles since diffusion of the

reactants to the inside of the bilayer would require crossing a charged barrier, which might prove to be difficult, thus affecting the results.

Spectra were taken in Scanning Kinetics mode, taking spectra between 220 nm and 600 nm at regular intervals. Using Scanning Kinetics was more laborous than using Kinetics mode, but enabled better monitoring of the reaction with the possibility of monitoring multiple wavelengths and checking whether the reaction was proceeding as expected. The individual spectra were exported to excel where they were separated according to the different samples. From the data, the absorbance of the baseline at 600 nm was subtracted from the absorbance at the λ_{max} of the hydrazone in the corresponding solvent (buffer, surfactant, vesicles) and the corrected absorbance was converted to concentration of hydrazone by using the calibration curve of the hydrazone in the appropriate solvent.

It was necessary to correct for the baseline at 600 nm because the formation of vesicles resulted in a degree of turbidity in the solution which was evident in the UV-Vis spectrum as an increase in the baseline of the spectrum (Figure 3.34). Correction of the values for the baseline minimised the effect of this turbidity on the results obtained. The following is an example of how the baseline in the UV-Vis spectrum changed over time during experiments, illustrating the importance of correcting for the baseline in order to obtain reliable measurements.

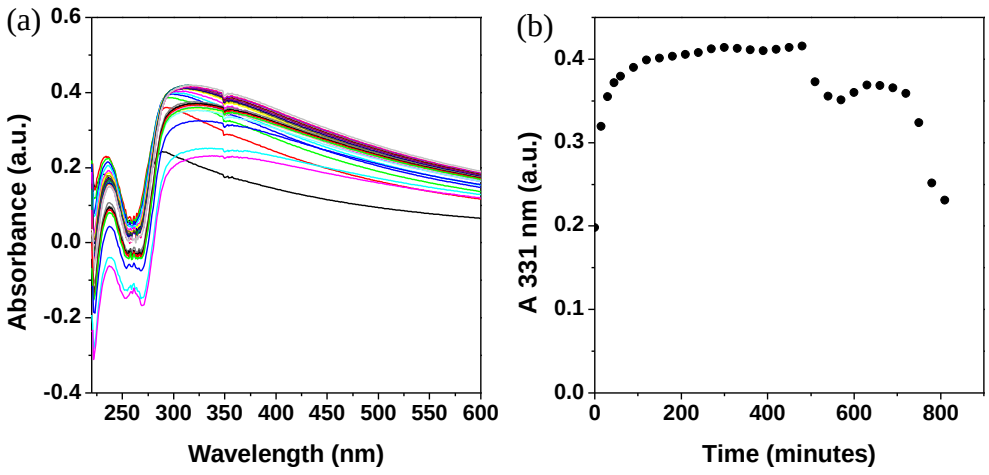

Figure 3.34: (a) Changes in the baseline of the UV-Vis spectrum when monitoring the absorbance in the presence of 200 μM surfactant **10** and 200 μM ATP. (b) Changes at an absorbance of 331 nm over time.

3.6.5 Following the reactions by UPLC

The components were separated on a C3 column, which enabled the direct injection of samples in the column without any work-up, on account of the reduced interaction of the surfactant with the shorter-chain stationary phase. The stationary phase in a standard C18 column interacts strongly with the surfactant, leading to blocking of the column. The components were separated using a gradient method using CH_3CN:H_2O mixtures with formic acid going from 5% CH_3CN to 95% CH_3CN in 5 minutes and keeping the concentration of CH_3CN at 100% for a further 2 minutes before returning back to the initial conditions.

In order to follow the reactions, samples were prepared in HPLC amber vials. Amber vials were used to minimise photooxidation of the aldehydes. As an additional precaution, the light in the UPLC sample holder was switched off during analysis. The suitability of the UPLC system in each experiment was verified by periodic injection of a solution of the hydrazide, which was known to be stable. The area of the sample was monitored regularly and ensured to be constant throughout the analysis.

The reaction solution was prepared from the appropriate stock solutions to give a final volume of 1 mL. The order of addition of solutions was the following (as needed): buffer, MilliQ water, surfactant, Zn^{2+}, reagents added sequentially, ATP. Any other reagent which needed to be added, e.g. potato apyrase or Ca^{2+} were added just before the addition of the reactants. The last reagents to be added were introduced in the solution just before injection in order to minimise the time difference from sample preparation to sample injection. The solution was shaken well after the addition of each reactant to ensure homogenous solution and to minimise immediate reaction due to local concentrations of reagents. Samples were injected at regular intervals, allowing some washing steps with 100% CH_3CN + 0.1% HCOOH in between analysis to ensure that the column was clean from the surfactant.

The reagents were monitored at an appropriate wavelength as determined by UV-Vis spectroscopy. The identity of the components was verified by MS, carried out once, and when verification was necessary. The area of the component of interest was monitored over time and then converted to concentration through the use of the appropriate calibration curve constructed using the appropriate standard solutions.

3.6.6 Stability of hydrazones under UPLC conditions

Hydrazones are unstable in acidic conditions, and it was therefore opportune to study how hydrazone **13** behaved during the HPLC-conditions. Two samples of 20 μM hydrazone **13** were prepared. In one sample, the hydrazone **13** was dissolved in 5:95 $CH_3CN:H_2O$ + 0.1% HCOOH and the other sample was dissolved in 95:5 $CH_3CN:H_2O$ + 0.1% HCOOH. The concentration of **13** was monitored over time. The hydrazone in acidic conditions at 5% CH_3CN degraded moderately quickly over a period of 300 minutes (Figure 3.35a) but increasing the concentration of the organic content to 95% improved the stability greatly and there was barely any change in hydrazone concentration over the same period of time (Figure 3.35b). The gradient used changes the organic content from 5% to 95% over a period of 5 minutes, and from the results obtained, it can safely be assumed that degradation of the hydrazone does not occur during the time of analysis under the conditions used.

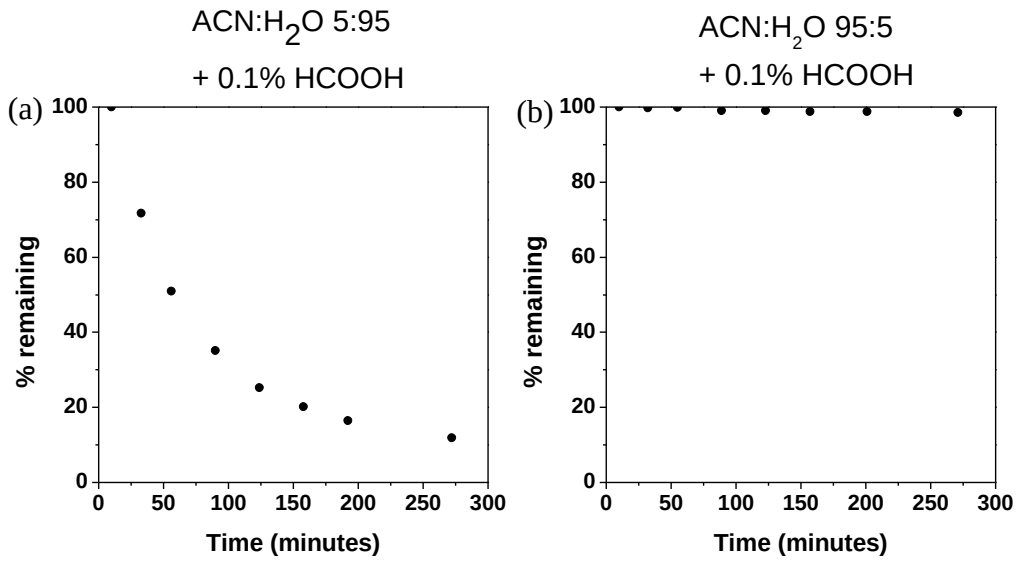

Figure 3.35: A graph showing the % hydrazone **13** remaining at periodic intervals in (a) 5:95 $CH_3CN:H_2O$ + 0.1% HCOOH and (b) 95:5 $CH_3CN:H_2O$ + 0.1% HCOOH.

3.6.7 Effect of organic content on reaction

The stock solutions of the reactants were prepared in acetonitrile and a volume of 2 μl of the appropriate concentration was added to the reaction solution in all cases. The small percentage of organic solvent could be responsible for some initial reaction upon mixing the reactants, which was more pronounced in the case of the reaction between **11** and **12**. To investigate whether the volume of organic solvent affected this initial amount of hydrazone formed, different volumes (2, 4 and 8 μL) of different stock solutions (10 mM,

5 mM and 2.5 mM respectively) were added to the vesicles and the sample injected immediately after mixing (Figure 3.40). It was found that the amount of product formed upon mixing was relatively constant and independent of the volume and identity of the organic solvent used. Sonication of the solution prior to the addition of the last reagent did nothing to reduce the initial amount of product formed. The values were therefore normalised by correcting for this initial amount of product formed, thereby enabling better comparison between the two reactions.

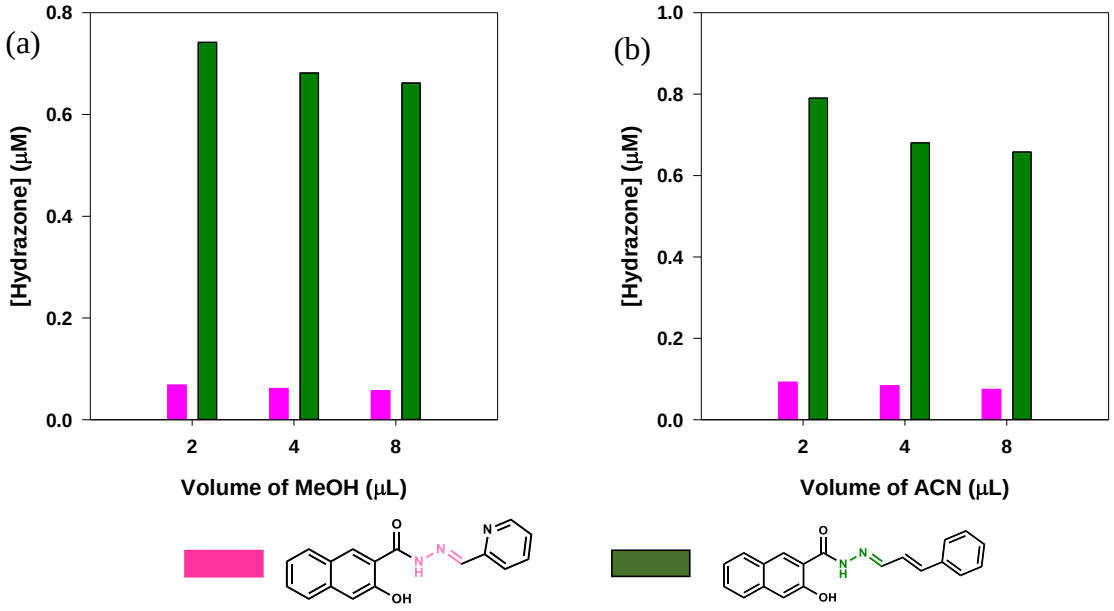

Figure 3.40: Concentration of hydrazones obtained at the first time-point from mixing together 20 μM **11** and **12** and **17** in different volumes (2, 4 or 8 μL) from different stock solutions (10 mM, 5 mM, 2.5 mM respectively) prepared in (a) MeOH and (b) CH_3CN. [Surfactant **10**] = 100 μM, [ATP] = 200 μM, [**11**] = [**12**] = [**17**] = 20 μM.

3.6.8 Quantification of the results (UV-Vis and UPLC)

The stock solutions of reactants were prepared in acetonitrile to ensure adequate solubility. Mixing the reactants in buffer, surfactant and vesicles resulted in an initial quantity of product at the inital time-point. This effect was probably due to the small percentage of organic solvent in the solution. In cases where reactions needed to be compared, the values were normalised for this initial quantity of product formed upon mixing. The exact concentration of the aldehydes was determined by UV-Vis spectroscopy. The reagent solutions were prepared fresh prior to each experiment.

The corrected absorbance obtained by UV-Vis spectroscopy and the integrated area obtained by UPLC at the appropriate wavelength were converted to concentration by using the appropriate calibration curves in the appropriate solvent. Solutions were prepared with the reagents at different concentration and the absorbance at the λ of analysis or the area under the peaks at the appropriate wavelength was plotted against the concentration. The slope of the linear curve thus obtained was used to determine the ε in the case of UV-Vis measurements and the conversion factor in the case of the UPLC measurements.

3.6.8.1 Calibration curve for quantification of hydrazone 13 formed between trans-cinnamaldehyde, 11 and 3-hydroxy-2-napthoic hydrazide, 12 by UPLC

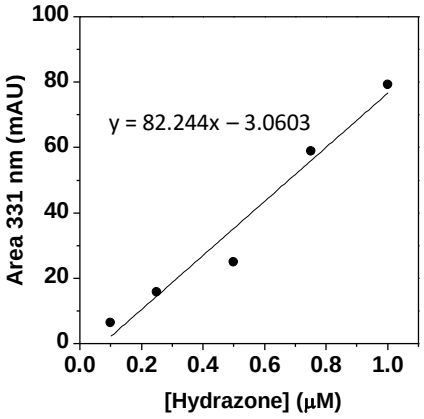

Figure 3.36: Figure showing the area of the hydrazone **13** peak at 331 nm at the various hydrazone concentrations and linear regression of the ponts to give the equation for the straight line. [HEPES] = 5 mM, pH 7.0.

3.6.8.2 Calibration curves for components of the reaction between 11 and 12 to form 13 by UV-Vis Spectroscopy

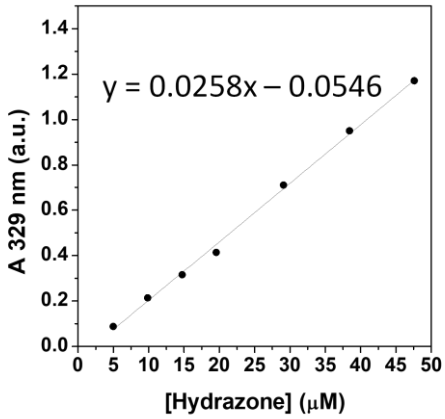

Figure 3.37: Calibration curve for hydrazone **13** in HEPES buffer pH 7.0 monitoring the λ_{max} peak at 329 nm. [HEPES] = 5 mM, pH 7.0.

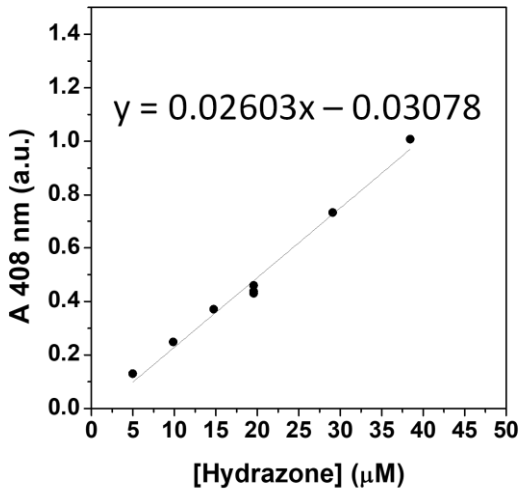

Figure 3.38: Calibration curve for hydrazone **13** in 200 μM surfactant **10** at pH 7.0 monitoring the λ_{max} peak at 408 nm. [HEPES] = 5 mM, pH 7.0.

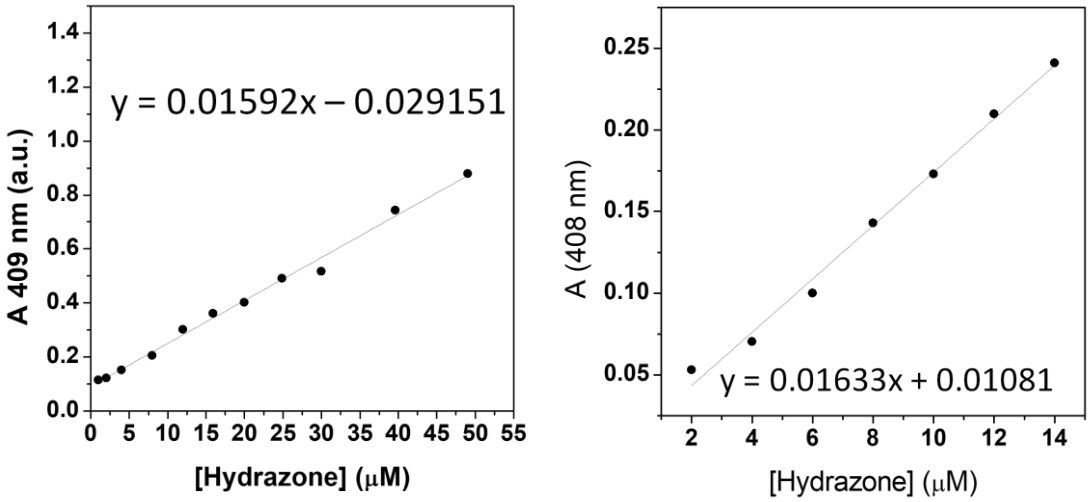

Figure 3.39: Calibration curve for hydrazone **13** in 200 μM surfactant **10**, 200 μM ATP at pH 7.0 monitoring the λ_{max} peak at 408 nm. [HEPES] = 5 mM, pH 7.0.

3.6.8.3 Calibration curves for components of the reaction between 11 and 12 to form 13 by UPLC

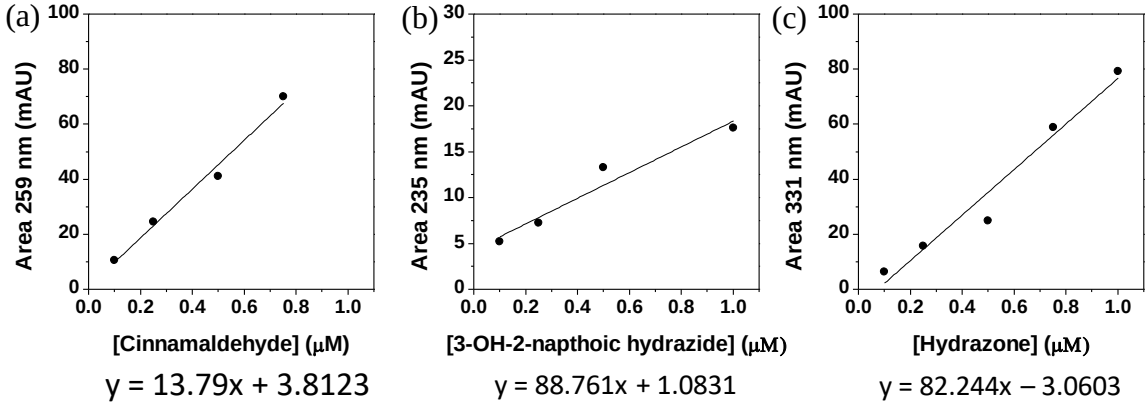

Figure 3.40: Calibration curve for hydrazone **13** in HEPES buffer pH 7.0 between 0-1 µM monitoring the area at 235 nm for cinnamaldehyde, **11**, 259 nm for 3-hydroxy-2-napthoic hydrazide, **12** and 331 nm for hydrazone **13.** [HEPES] = 5 mM, pH 7.0.

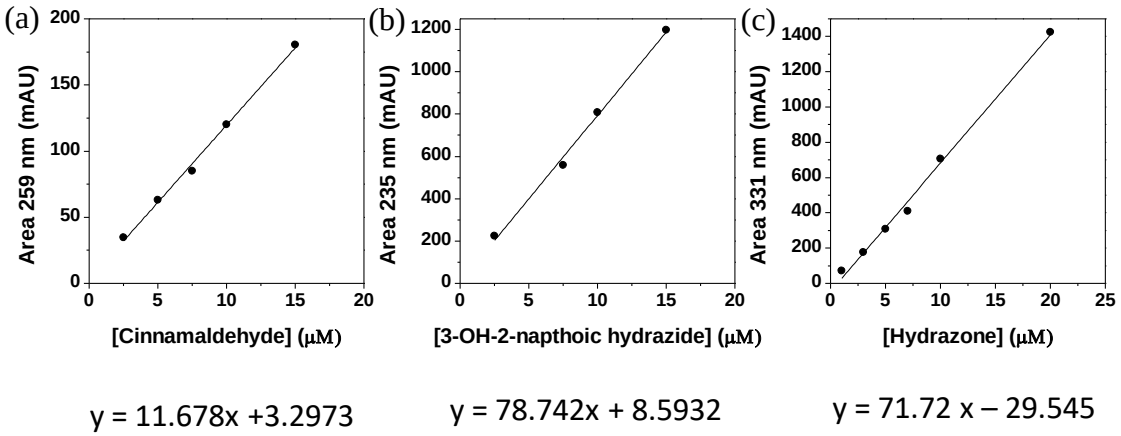

Figure 3.41: Calibration curve for hydrazone **13** in HEPES buffer pH 7.0 between 0-25 µM monitoring the area at 235 nm for cinnamaldehyde, **11**, 259 nm for 3-hydroxy-2-napthoic hydrazide, **12** and 331 nm for hydrazone **13**. [HEPES] = 5 mM, pH 7.0.

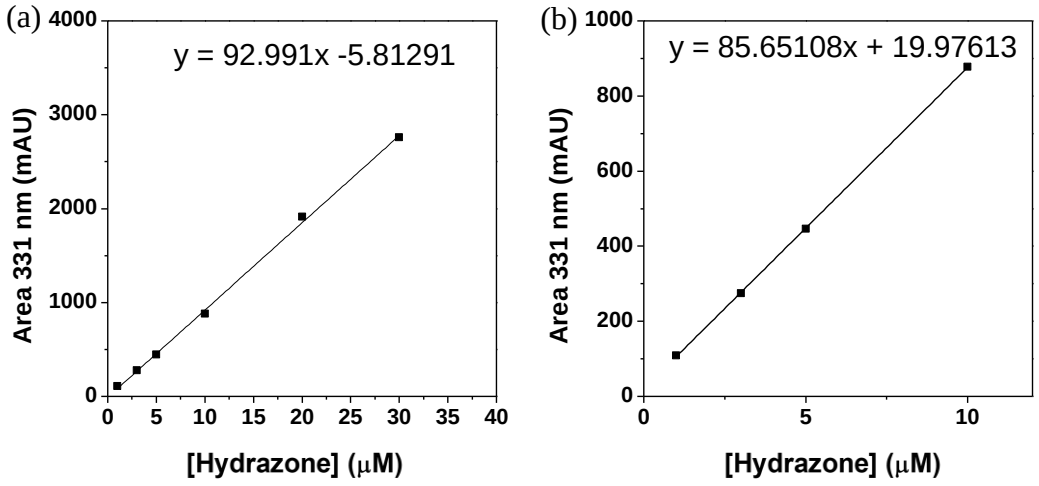

Figure 3.42: Calibration curves for hydrazone **13** in acetonitrile, monitoring the area of the hydrazone peak at 331 nm. [HEPES] = 5 mM, pH 7.0.

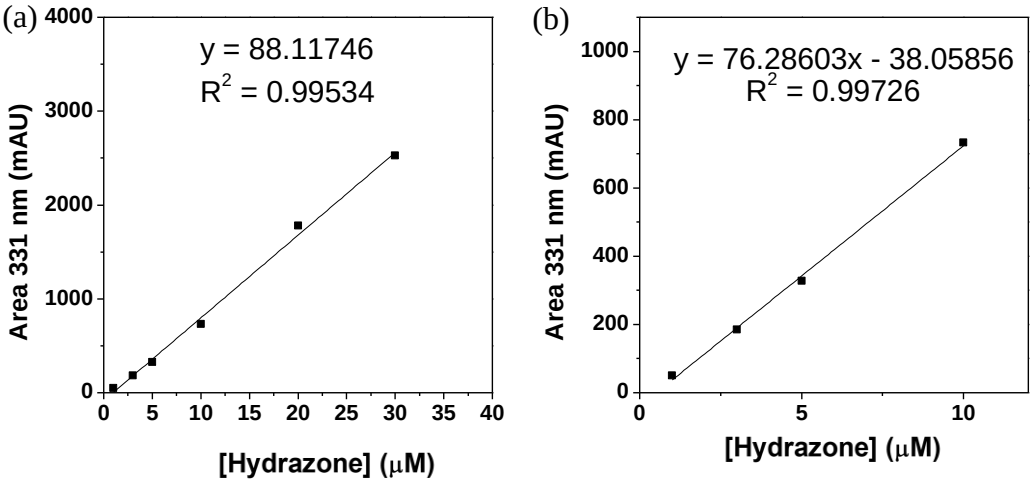

Figure 3.43: Calibration curves for hydrazone **13** in 100 μM surfactant **10**, monitoring the area of the hydrazone peak at 331 nm. [HEPES] = 5 mM, pH 7.0.

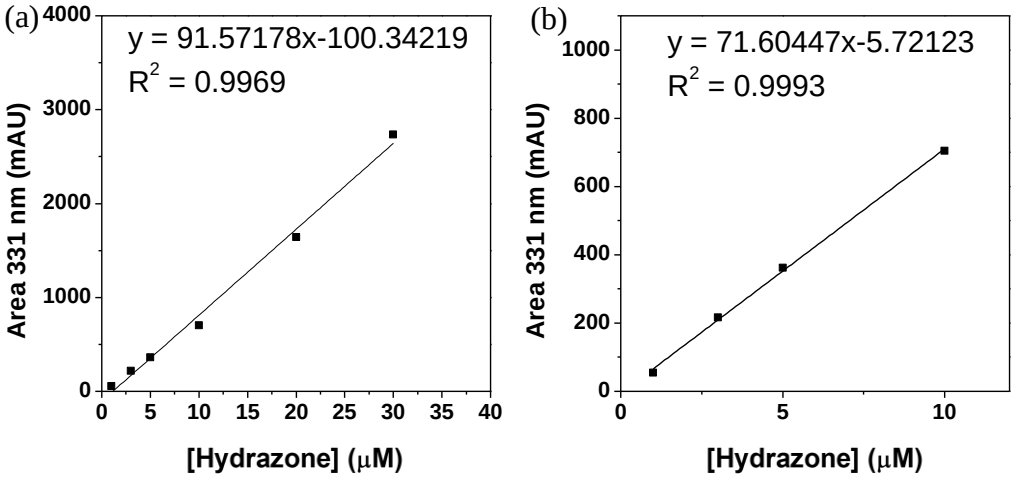

Figure 3.44: Calibration curves for hydrazone **13** in 100 μM surfactant **10**, 200 μM ATP (vesicles), monitoring the area of the hydrazone peak at 331 nm. [HEPES] = 5 mM, pH 7.0.

3.6.8.4 Calibration curves for components of the reaction between and 11 and 17 to give 18 by UPLC

Calibration curves of hydrazone were prepared separately for the hydrazone **18** in buffer, in 100 µM surfactant **10** and for vesicles obtained from mixing 200 µM ATP with 100 µM surfactant **10** at five different concentrations. They were injected in the UPLC and the area of **18** was plotted against the concentration. Linear regression of the plots gave an equation which was used to change the area into concentration.

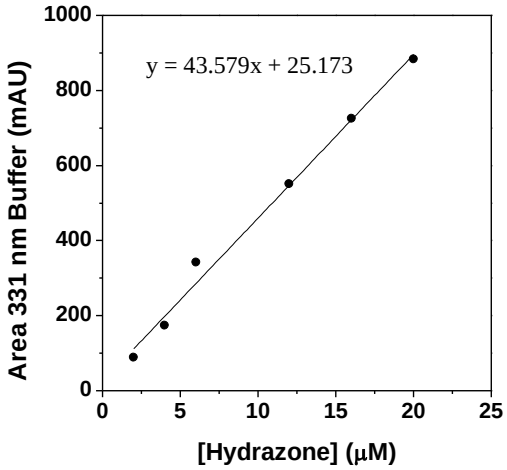

Figure 3.45: Calibration curves showing plots of the intergrated area against the concentration of **18** for standard solutions of **18** in aqueous buffer. [HEPES] = 5 mM, pH 7.0.

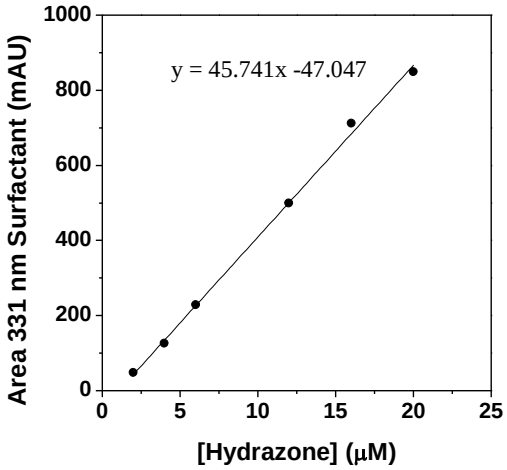

Figure 3.46: Calibration curves showing plots of the intergrated area against the concentration of **18** for standard solutions of in 100 µM surfactant **10**. [HEPES] = 5 mM, pH 7.0.

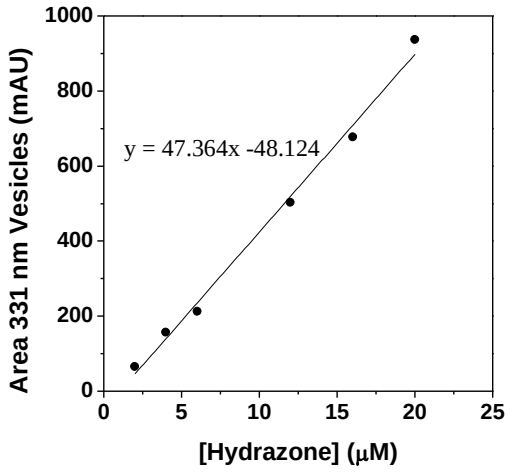

Figure 3.47: Calibration curves showing plots of the intergrated area against the concentration of **18** for standard solutions of **18** in 100 μM surfactant **10**, 200 μM ATP. [HEPES] = 5 mM, pH 7.0.

3.6.9 Determination of the order of the reaction

The progression of the formation of the hydrazone was monitored by measuring the absorbance at 331 nm due to hydrazone **13** as a function of time. The concentration of the reagents **11** or **12** was fixed at 20 μM and the concentration of the other reagent **12** or **11**, respectively, was changed between 0 and 100 μM. The absorbance at 331 nm (corrected for the baseline) against time for the different concentrations of the second reagent was plotted and the slope of the initial linear portion of the curve gave the initial rate of the reaction.

$$\text{Absorbance (331 nm)} \propto [\text{Hydrazone } \mathbf{13}]$$

$$\text{Initial rate of reaction} = \frac{\Delta\, Absorbance\ (331\ nm)}{\Delta\, Time}$$

The rate of reaction is directly proportional to the concentration of the individual starting reagent to the power of the order of the reaction. Thus for the reaction between **11** and **12** to give **13**, the

$$\text{Rate of reaction} \propto [\mathbf{11}]^{\text{Order}}[\mathbf{12}]^{\text{Order}}$$

For each individual reactant,

$$\text{Rate of reaction} \propto [\mathbf{11}]^{\text{Order}}$$

$$\text{and Rate of reaction} \propto [\mathbf{12}]^{\text{Order}}$$

In other words:

$$\text{Rate of reaction} = k[\mathbf{11}]^{\text{Order}}$$

$$\text{and Rate of reaction} = k[\mathbf{12}]^{\text{Order}}$$

Taking the logs:

$$\ln \text{Rate} = \text{Order}.\ln[\mathbf{11}] + k$$

$$\text{and } \ln \text{Rate} = \text{Order}.\ln[\mathbf{12}] + k$$

Therefore the order of the reaction could be determined by plotting the ln Rate of reaction as determined above against the ln of the concentration of the changing reagent. The slope of the resulting curve gave the order of the reaction.

3.7 References

(1) Herrmann, A. *Org. Biomol. Chem.* **2009**, *7*, 3195.
(2) Whitesides, G. M.; Grzybowski, B. *Science* **2002**, *295*, 2418.
(3) Chen, I. A.; Walde, P. *Cold Spring Harbor Perspectives in Biology* **2010**, *2*.
(4) Walde, P.; Umakoshi, H.; Stano, P.; Mavelli, F. *Chem. Commun.* **2014**, *50*, 10177.
(5) Ashkenasy, G.; Hermans, T. M.; Otto, S.; Taylor, A. F. *Chem. Soc. Rev.* **2017**, *46*, 2543.
(6) Scrimin, P. *Supramolecular Control of Structure and Reactivity* **1996**, 101.
(7) Maiti, S.; Fortunati, I.; Ferrante, C.; Scrimin, P.; Prins, L. J. *Nat. Chem.* **2016**.
(8) Belowich, M. E.; Stoddart, J. F. *Chem. Soc. Rev.* **2012**, *41*, 2003.
(9) Conant, J. B.; Bartlett, P. D. *J. Am. Chem. Soc.* **1932**, *54*, 2881.
(10) Corbett, P. T.; Leclaire, J.; Vial, L.; West, K. R.; Wietor, J.-L.; Sanders, J. K.; Otto, S. *Chem. Rev.* **2006**, *106*, 3652.
(11) Lehn, J.-M. *Chem. Soc. Rev.* **2007**, *36*, 151.
(12) Lehn, J. M. *Angew. Chem., Int. Ed.* **2015**, *54*, 3276.
(13) Greb, L.; Eichhöfer, A.; Lehn, J. M. *Angew. Chem., Int. Ed.* **2015**, *54*, 14345.
(14) *Molecular Machines and Motors*; Springer-Verlag Berlin Heidelberg, 2001.
(15) *Molecular Switches*; Second Edition ed.; Wiley-VCH Verlag GmbH & Co. KGaA.
(16) Cho, D.-G.; Sessler, J. L. *Chem. Soc. Rev.* **2009**, *38*, 1647.
(17) Teresa Albelda, M.; Frías, J. C.; García-España, E.; Schneider, H.-J. *Chem. Soc. Rev.* **2012**, *41*, 3859.
(18) Wenzel, M.; Hiscock, J. R.; Gale, P. A. *Chem. Soc. Rev.* **2012**, *41*, 480.
(19) Gale, P. A.; Busschaert, N.; Haynes, C. J. E.; Karagiannidis, L. E.; Kirby, I. L. *Chem. Soc. Rev.* **2014**, *43*, 205.
(20) Ruben, M.; Lehn, J.-M.; Müller, P. *Chem. Soc. Rev.* **2006**, *35*, 1056.
(21) Hardy, J. G. *Chem. Soc. Rev.* **2013**, *42*, 7881.
(22) Kobayashi, S.; Mori, Y.; Fossey, J. S.; Salter, M. M. *Chem. Rev.* **2011**, *111*, 2626.
(23) Lazny, R.; Nodzewska, A. *Chem. Rev.* **2010**, *110*, 1386.
(24) Vicini, P.; Incerti, M.; La Colla, P.; Loddo, R. *Eur. J. Med. Chem.* **2009**, *44*, 1801.
(25) Masunari, A.; Tavares, L. C. *Bioorganic Med. Chem.* **2007**, *15*, 4229.
(26) Zhou, X.-P.; Wu, Y.; Li, D. *J. Am. Chem. Soc.* **2013**, *135*, 16062.
(27) Jin, Y.; Yu, C.; Denman, R. J.; Zhang, W. *Chem. Soc. Rev.* **2013**, *42*, 6634.
(28) Rowan, S. J.; Cantrill, S. J.; Cousins, G. R. L.; Sanders, J. K. M.; Stoddart, J. F. *Angew. Chem., Int. Ed.* **2002**, *41*, 898.
(29) Raue, R.; Brack, A.; Lange, K. H. *Angew. Chem., Int. Ed.* **1991**, *30*, 1643.
(30) Lygaitis, R.; Getautis, V.; Grazulevicius, J. V. *Chem. Soc. Rev.* **2008**, *37*, 770.
(31) Gasparini, G.; Martin, M.; Prins, L. J.; Scrimin, P. *Chem. Commun.* **2007**, 1340.

(32) Gasparini, G.; Prins, L. J.; Scrimin, P. *Angew. Chem., Int. Ed.* **2008**, *47*, 2475.
(33) Gasparini, G.; Rastrelli, F.; Prins, L. J. *Org. Biomol. Chem.* **2013**, *11*, 6580.
(34) Gasparini, G.; Dal Molin, M.; Corrà, S.; Galzerano, P.; Scrimin, P.; Prins, L. J. *Isr. J. Chem.* **2013**, *53*, 122.
(35) Larsen, D.; Pittelkow, M.; Karmakar, S.; Kool, E. T. *Org. Lett.* **2015**, *17*, 274.
(36) Gasparini, G.; Bettin, F.; Scrimin, P.; Prins, L. J. *Angew. Chem., Int. Ed.* **2009**, *48*, 4546.
(37) Levrand, B.; Ruff, Y.; Lehn, J.-M.; Herrmann, A. *Chem. Commun.* **2006**, 2965.
(38) Crisalli, P.; Kool, E. T. *J. Org. Chem.* **2013**, *78*, 1184.
(39) Kool, E. T.; Park, D.-H.; Crisalli, P. *J. Am. Chem. Soc.* **2013**, *135*.
(40) Dirksen, A.; Dawson, P. E. *Bioconjugate Chem.* **2008**, *19*, 2543.
(41) Wu, B.; Wang, Z.; Huang, Y.; Liu, W. R. *ChemBioChem* **2012**, *13*, 1405.
(42) Rayo, J.; Amara, N.; Krief, P.; Meijler, M. M. *J. Am. Chem. Soc.* **2011**, *133*, 7469.
(43) Kool, E. T.; Crisalli, P.; Chan, K. M. *Org. Lett.* **2014**, *16*, 1454.
(44) Wolfenden, R.; Jencks, W. P. *J. Am. Chem. Soc.* **1961**, *83*, 2763.
(45) French, T. C.; Auld, D. S.; Bruice, T. C. *Biochemistry* **1965**, *4*, 77.
(46) Cordes, E. H.; Jencks, W. P. *J. Am. Chem. Soc.* **1962**, *84*, 4319.
(47) Anderson, B. M.; Jencks, W. P. *J. Am. Chem. Soc.* **1960**, *82*, 1773.
(48) Fulmer, G. R.; Miller, A. J. M.; Sherden, N. H.; Gottlieb, H. E.; Nudelman, A.; Stoltz, B. M.; Bercaw, J. E.; Goldberg, K. I. *Organometallics* **2010**, *29*, 2176.
(49) Missoouri, USA; Vol. 2018.
(50) Ceppan, M.; Fiala, R.; Brezová, V.; Panák, J.; Motlíková, V. *Chem. Papers*, **1994**, *48*, 45.
(51) Nakamoto, K.; Martell, A. E. *J. Am. Chem. Soc.* **1959**, *81*, 5857.
(52) A.I. Vogel, A. R. T., B.S. Furnis, A.J. Hannaford, P.W.G. Smith *Vogel's Textbook of Practical Organic Chemistry*; 5 ed.; John Wiley & Sons: New York, 1991.
(53) Su, X.; Aprahamian, I. *Chem. Soc. Rev.* **2014**, *43*, 1963.
(54) Patorski, P.; Wyrzykiewicz, E.; Bartkowiak, G. *J. Spectrosc.* **2012**, *2013*.
(55) Pichon, R.; Le Saint, J.; Courtot, P. *Tetrahedron* **1981**, *37*, 1517.
(56) Courtot, P.; Pichon, R.; Le Saint, J. *Tetrahedron Lett.* **1976**, *17*, 1181.

3.8 Appendix

3.8.1 ^{1}H NMR, ^{13}C NMR and MS Spectra

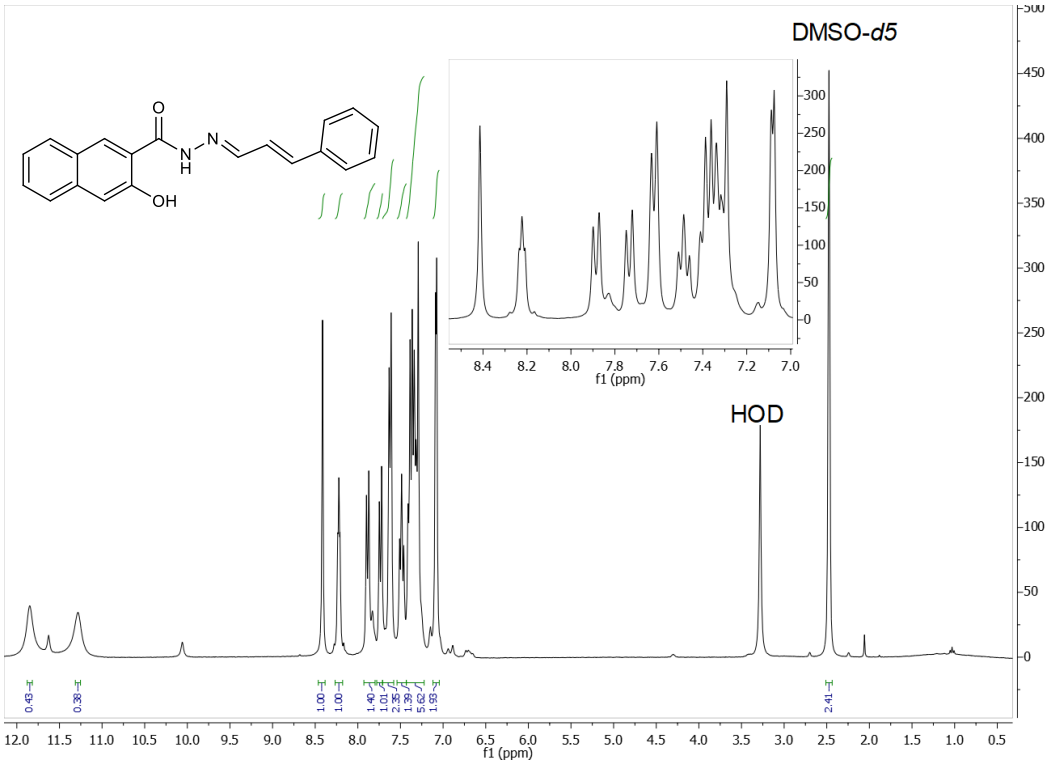

Figure 3.48: ^{1}H NMR spectrum of **13** in DMSO-*d6* (300 MHz, 300K).

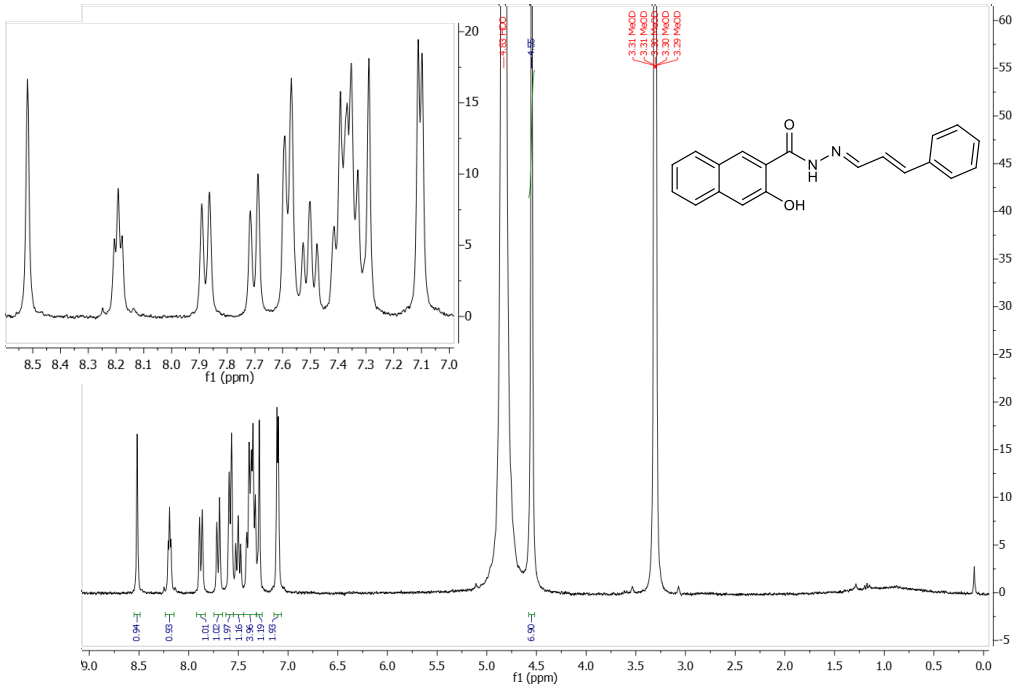

Figure 3.49: ^{1}H NMR spectrum of **13** in MeOD (300 MHz, 300K).

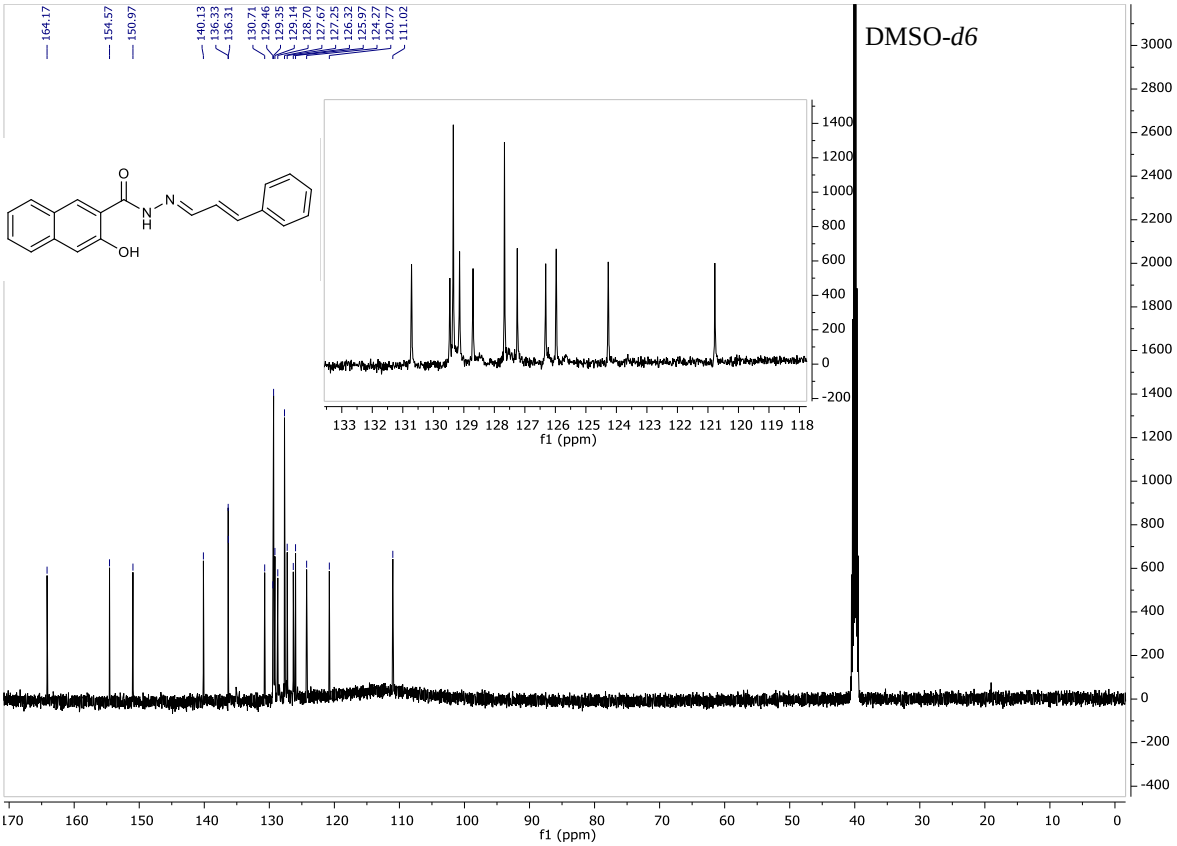

Figure 3.50: ^{13}C NMR spectrum of **13** in DMSO-*d6* (126 MHz, 300K).

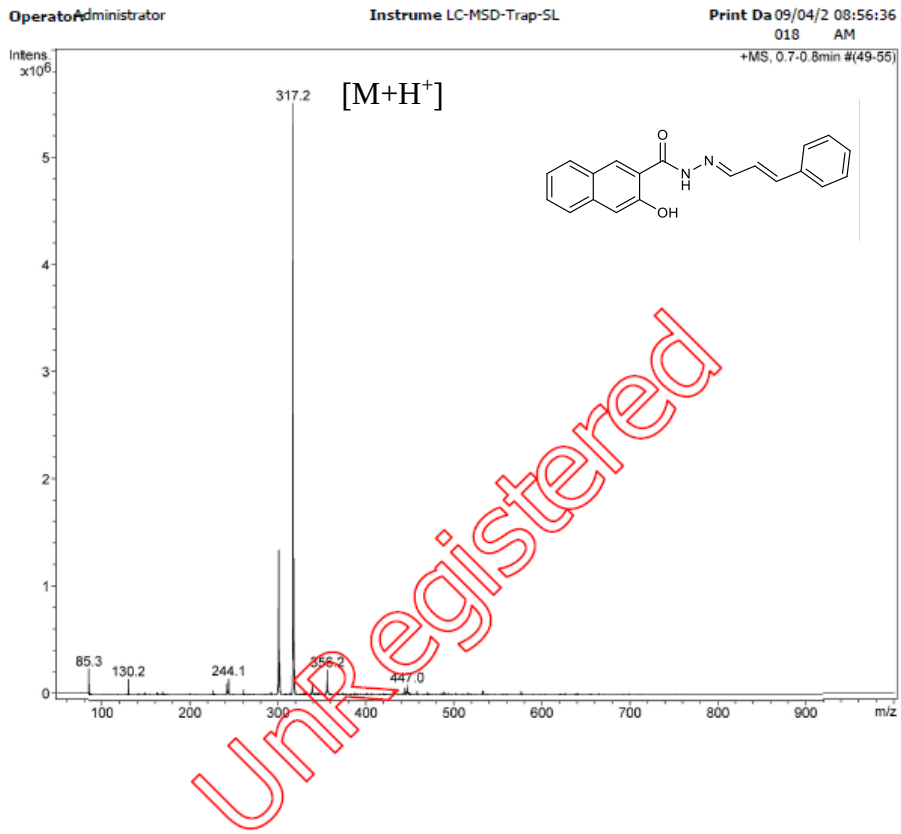

Figure 3.51: ESI-MS (ESI+, MeOH:H_2O 1:1) spectrum of **13**.

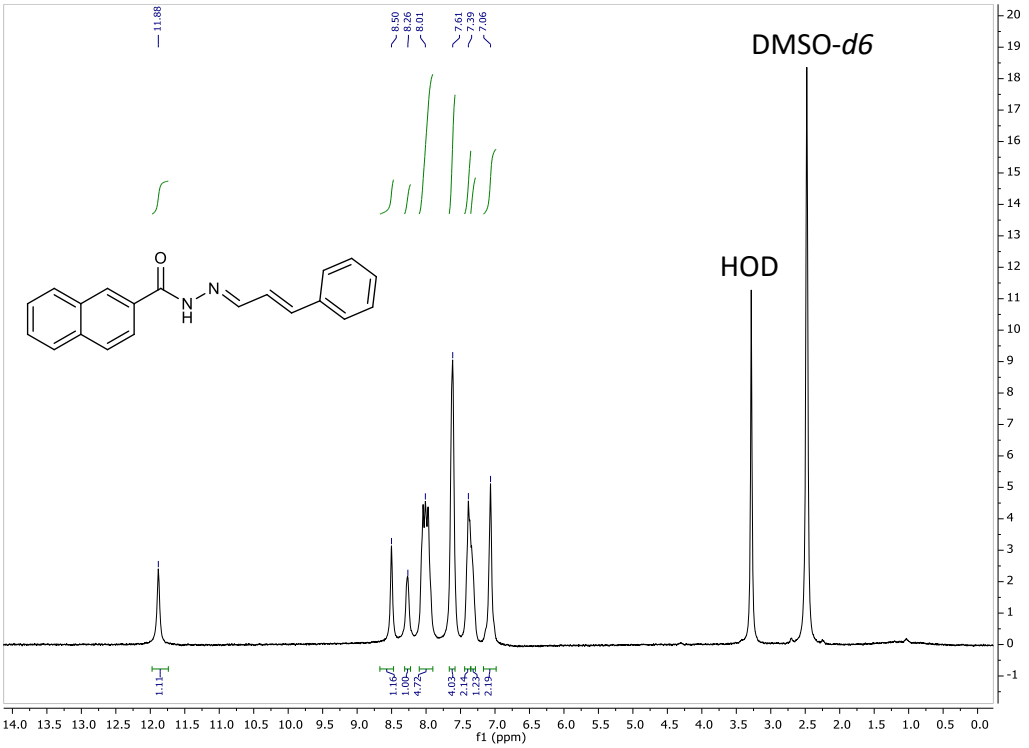

Figure 3.52: ^{1}H NMR spectrum of **16** in DMSO-*d6* (300 MHz, 300K).

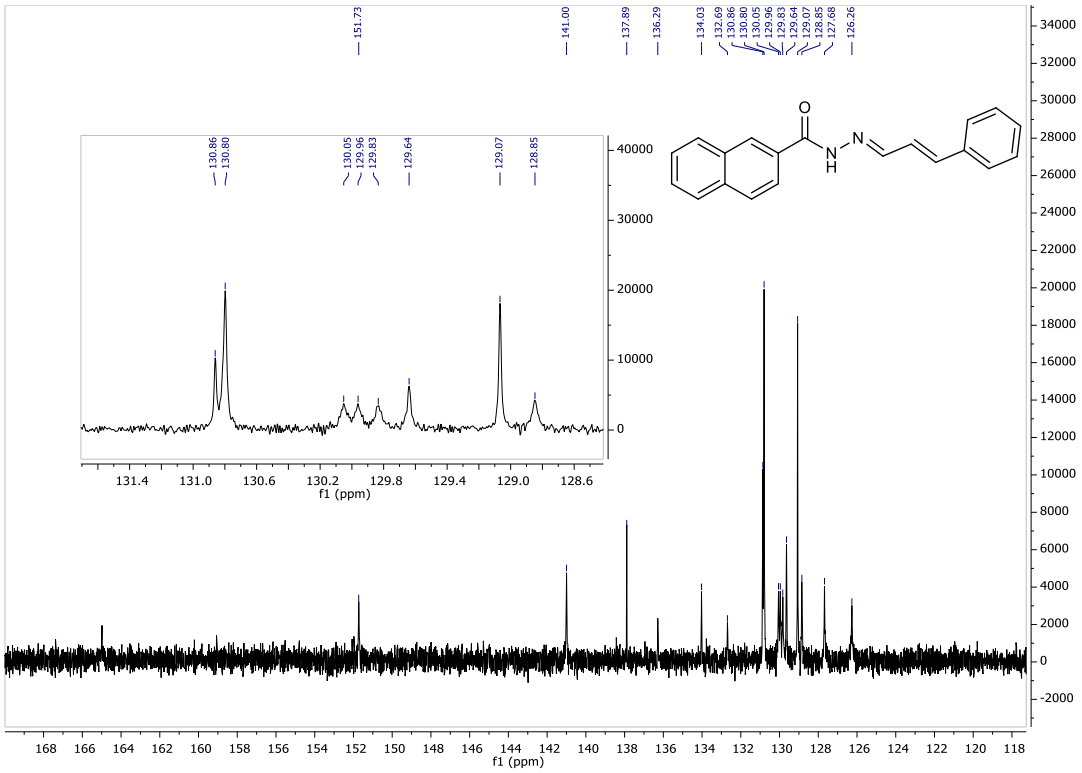

Figure 3.53: ^{13}C NMR spectrum of **16** in DMSO-*d6* (126 MHz, 300K).

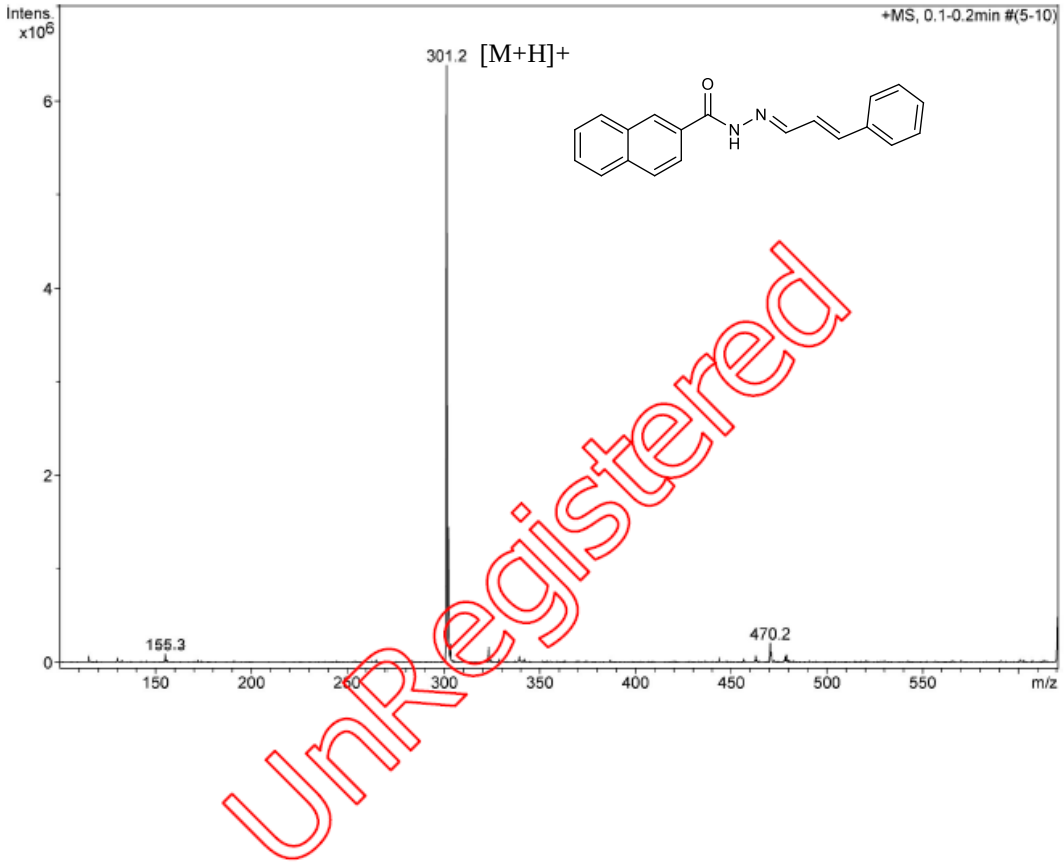

Figure 3.54: ESI-MS (ESI+, MeOH:H_2O 1:1) spectrum of **16**.

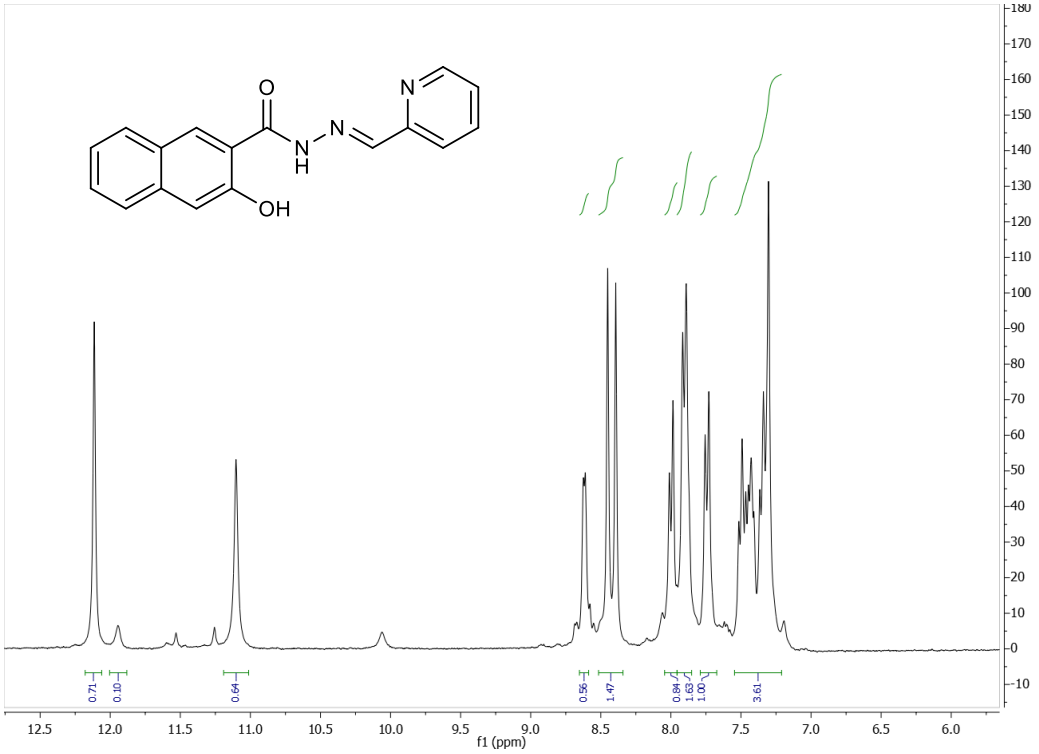

Figure 3.55: ^{1}H NMR spectrum of **18** in DMSO-*d6* (300 MHz, 300K).

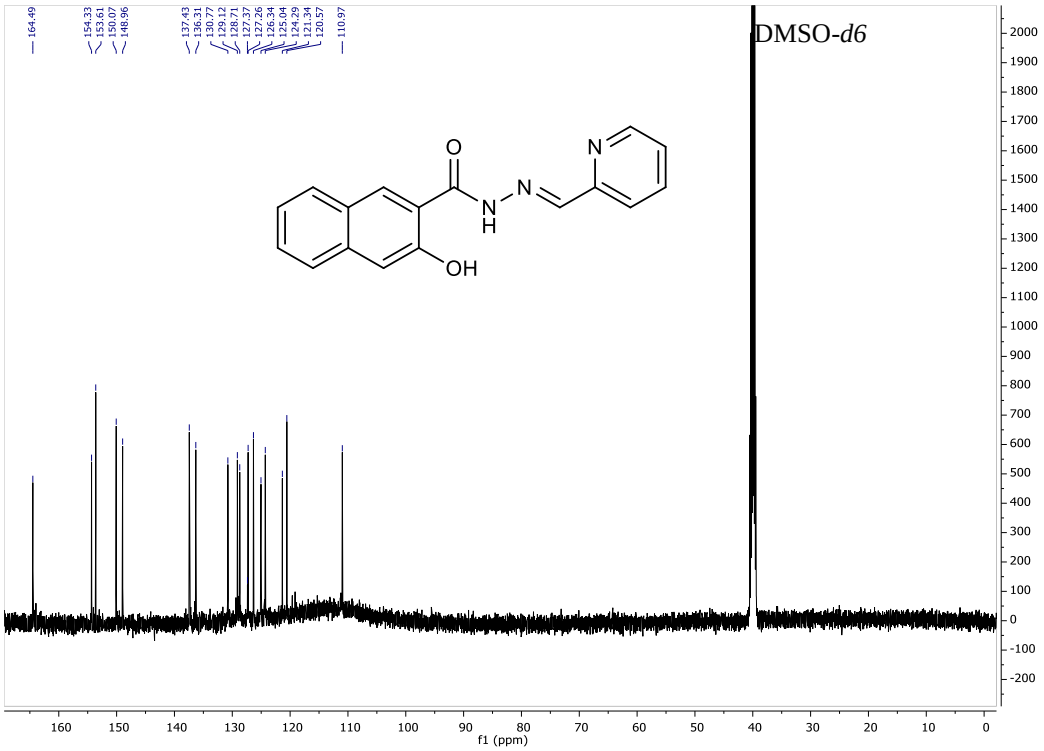

Figure 3.56: ^{13}C NMR spectrum of **18** in DMSO-*d6* (126 MHz, 300K).

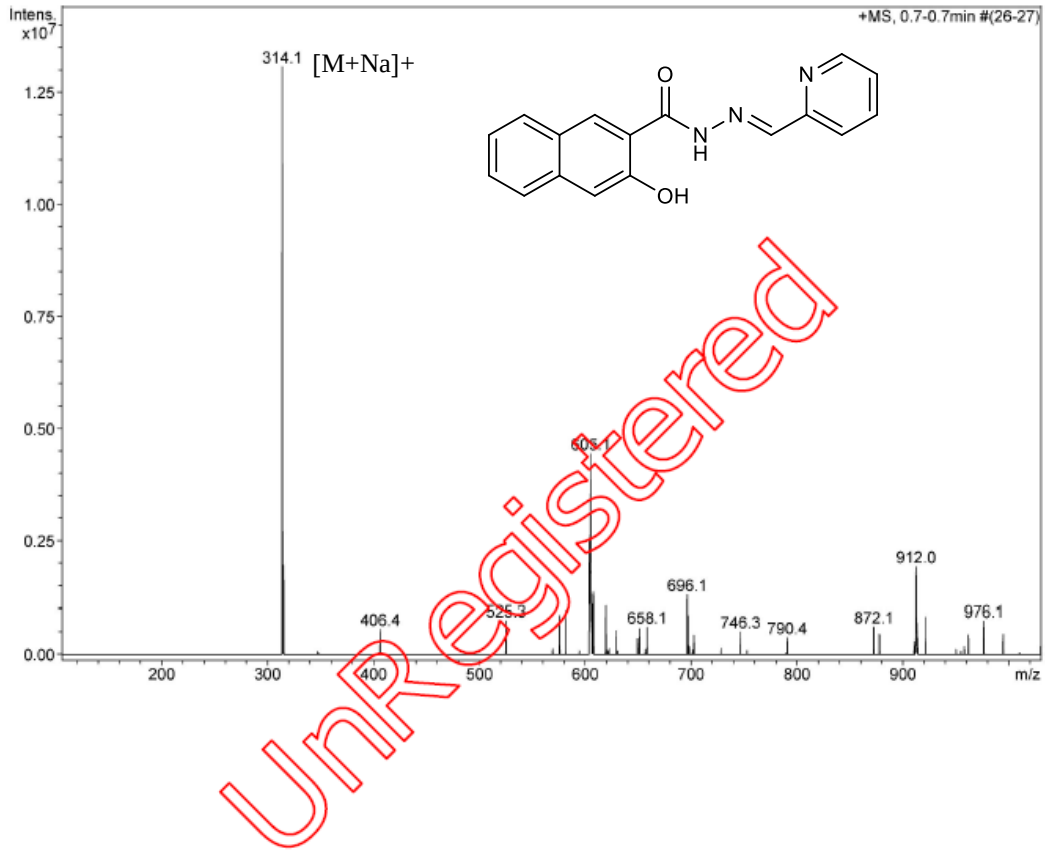

Figure 3.57: ESI-MS (ESI+, MeOH:H_2O 1:1) spectrum of **18**.

3.8.2 Screening exercise to identify a suitable reaction to study using vesicles from surfactant 10

One assumption for the preferential formation of hydrazone bond-formation in the vesicles is that the reagents need to be hydrophobic enough to prefer residing in the bilayer instead of in the aqueous solution but on the other hand to be sufficiently soluble in micromolar concentrations in aqueous buffer. It was decided to use the hydrophobic aldehyde *trans*-cinnamaldehyde, **11**, for reaction. In order to identify a suitably hydrophobic hydrazide, a number of available hydrazides, namely furoic hydrazide, **19**, phenylacetic hydrazide, **20**, indole acetic hydrazide, **21**, toluic hydrazide, **22**, and 4-nitrobenzoic hydrazide, **23**, and 3-hydroxy-2-napthoic hydrazide, **12**, (Figure 3.54) were injected in a UPLC column. The corresponding retention time is tabulated in Table 3.6, together with the wavelength used for analysis. The R_t of the hydrazide was taken as an indication of the hydrophobicity. A higher retention time was taken to signify a higher degree of hydrophobicity. From this, furoic hydrazide, **19** was found to be the least hydrophobic while 3-hydroxy-2-napthoic hydrazide, **12** was found to be the most hydrophobic. Trials were therefore carried out using **11** and **12**. It was found that the reaction was greatly enhanced in the vesicles compared to the free surfactant **10** and therefore studies were continued using these reagents.

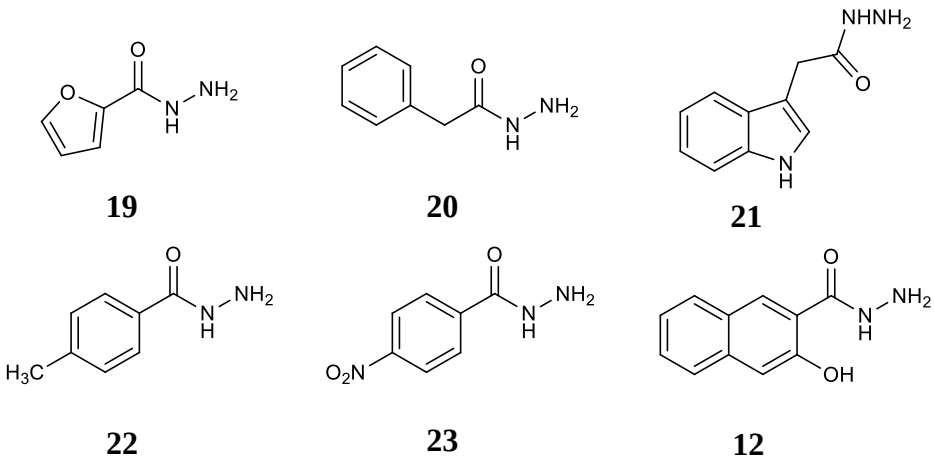

Figure 3.58: Structure of the hydrazides used in this study.

Hydrazide	λ_{max} (nm)	R_t by UPLC (minutes)
19	254	1.197
20	259	1.453
21	280	1.644
22	235	1.697
23	263	1.724
12	231	2.412

Table 3.6: Table showing the hydrazides studied by UV and their R_t by UPLC. Table is arranged in order of increasing hydrophobicity of the hydrazides.

3.8.3 UV-Vis of hydrazone in buffer pH 7.0 overlaid on the hydrazone in vesicles

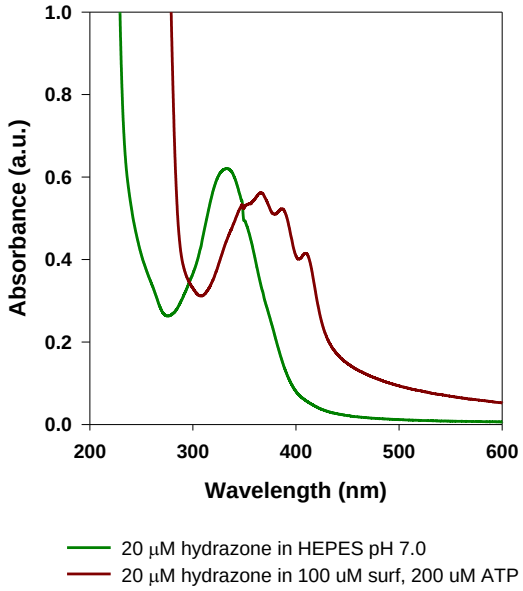

Figure 3.59: UV-Vis spectrum of 20 µM **13** in HEPES buffer pH 7.0 and in vesicles (100 µM surfactant **10**, 200 µM ATP) showing the red shift and change in absorption maximum of **13** as a result of the different hydrophobicity of the medium.

3.8.4 UV-Vis spectra for the reaction of cinnamaldehyde, 11, with napthoic hydrazide, 15, in buffer and 100 µM surfactant 10

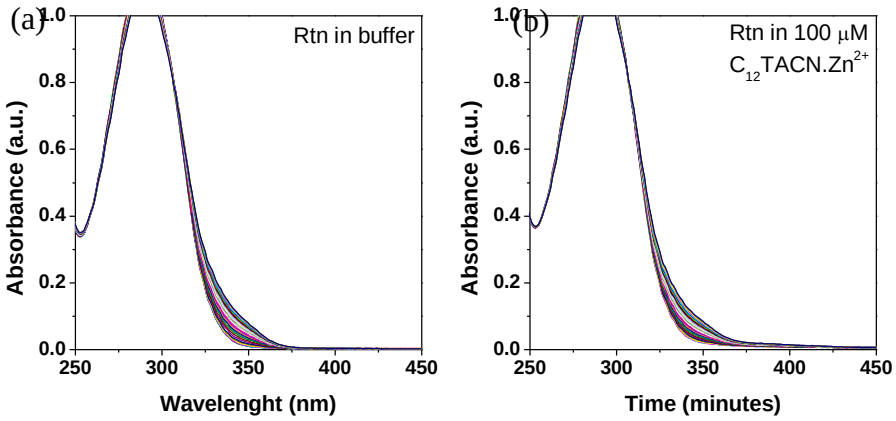

Figure 3.60: Figure showing the UV-Vis spectra taken at regular intervals when reacting **11** with **15** in (a) HEPES buffer pH 7.0 and (b) surfactant. [HEPES] = 5 mM, pH 7.0 [Surfactant **10**] = 100 µM, [ATP] = 200 µM, [**11**] = 40 µM, [**15**] = 20 µM.

3.8.5 Concentration of hydrazone 13 at different pHs by UPLC over time

MES buffer was used for pHs 5.5 and 6.0 while HEPES buffer was used for pHs 7-9

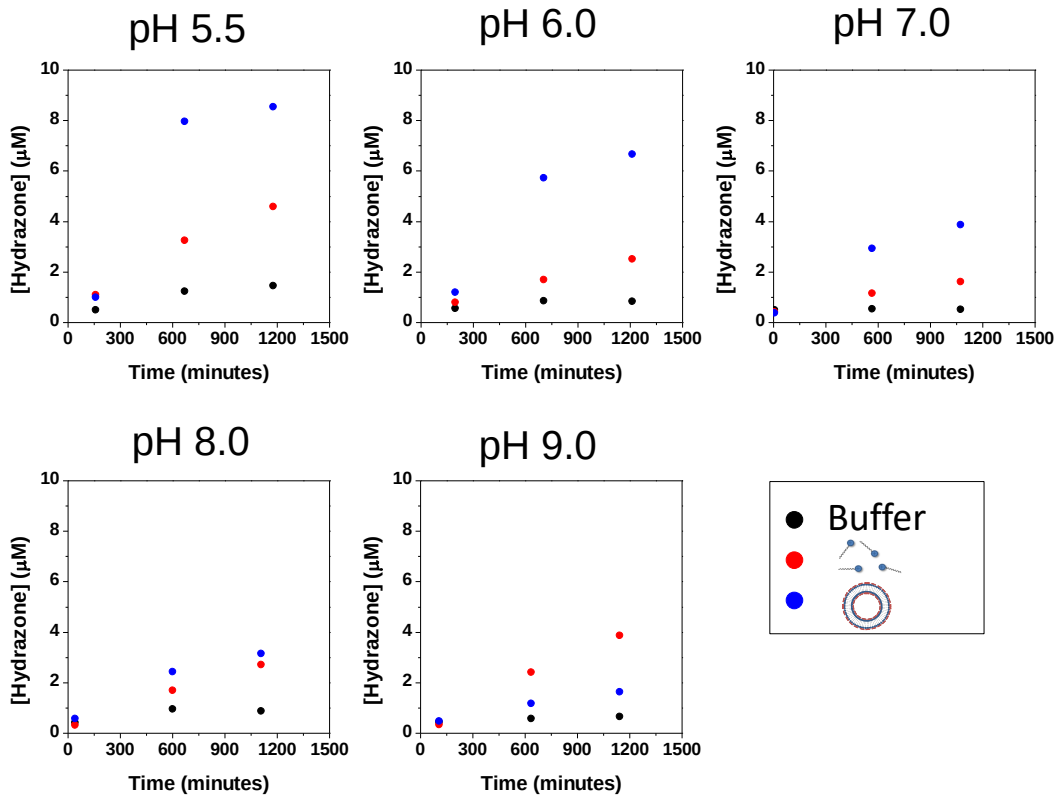

Figure 3.61: Graph showing the concentration of hydrazone **13** obtained in buffer, surfactant and vesicles at different pHs. [Buffer] = 5 mM. [Surfactant **10**] = 100 µM, [ATP] = 200 µM. [**11**] = [**12**] = 20 µM.

3.8.6 Concentration of hydrazone 13 at different pHs by UV-Vis spectroscopy over time

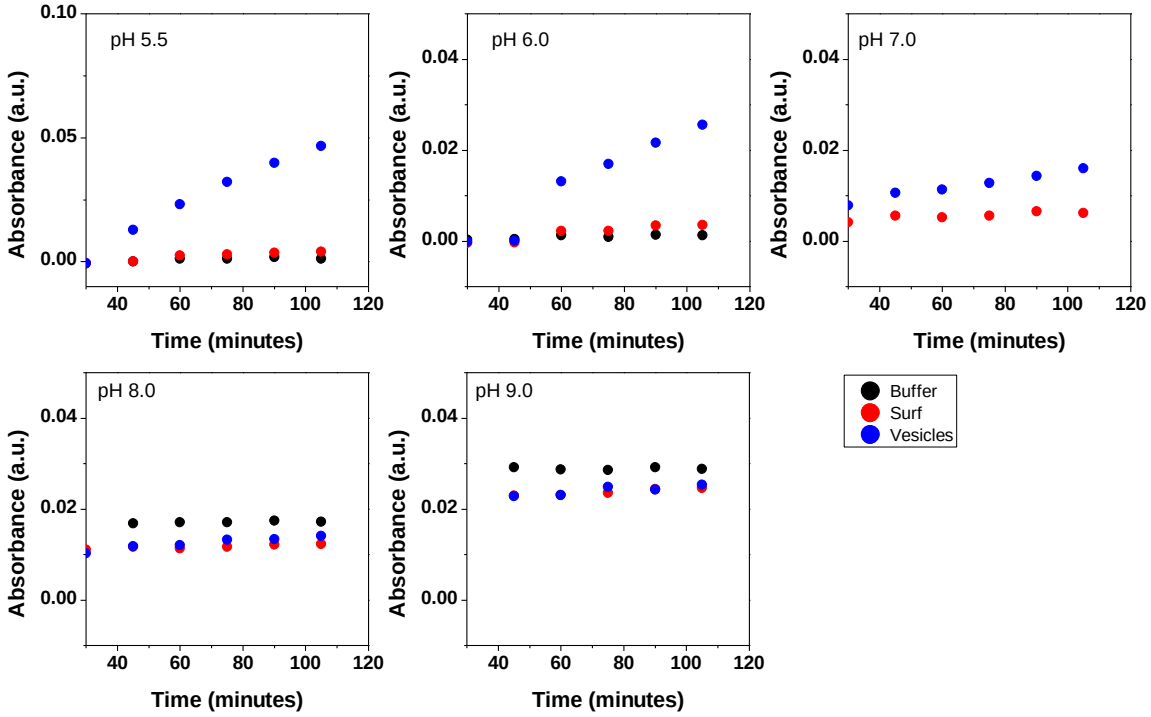

Figure 3.62: Graph showing the concentration of hydrazone **13** obtained in buffer, surfactant and vesicles at different pHs for the purpose of determinine the intial rate of reaction. [Buffer] = 5 mM, [Surfactant **10**] = 100 µM, [ATP] = 200 µM. [**11**] = [**12**] = 20 µM.

3.8.7 Comparison of formation of hydrazones 13 and 18 in aqueous buffer, surfactant and vesicles (10 μM and 20 μM reagents)

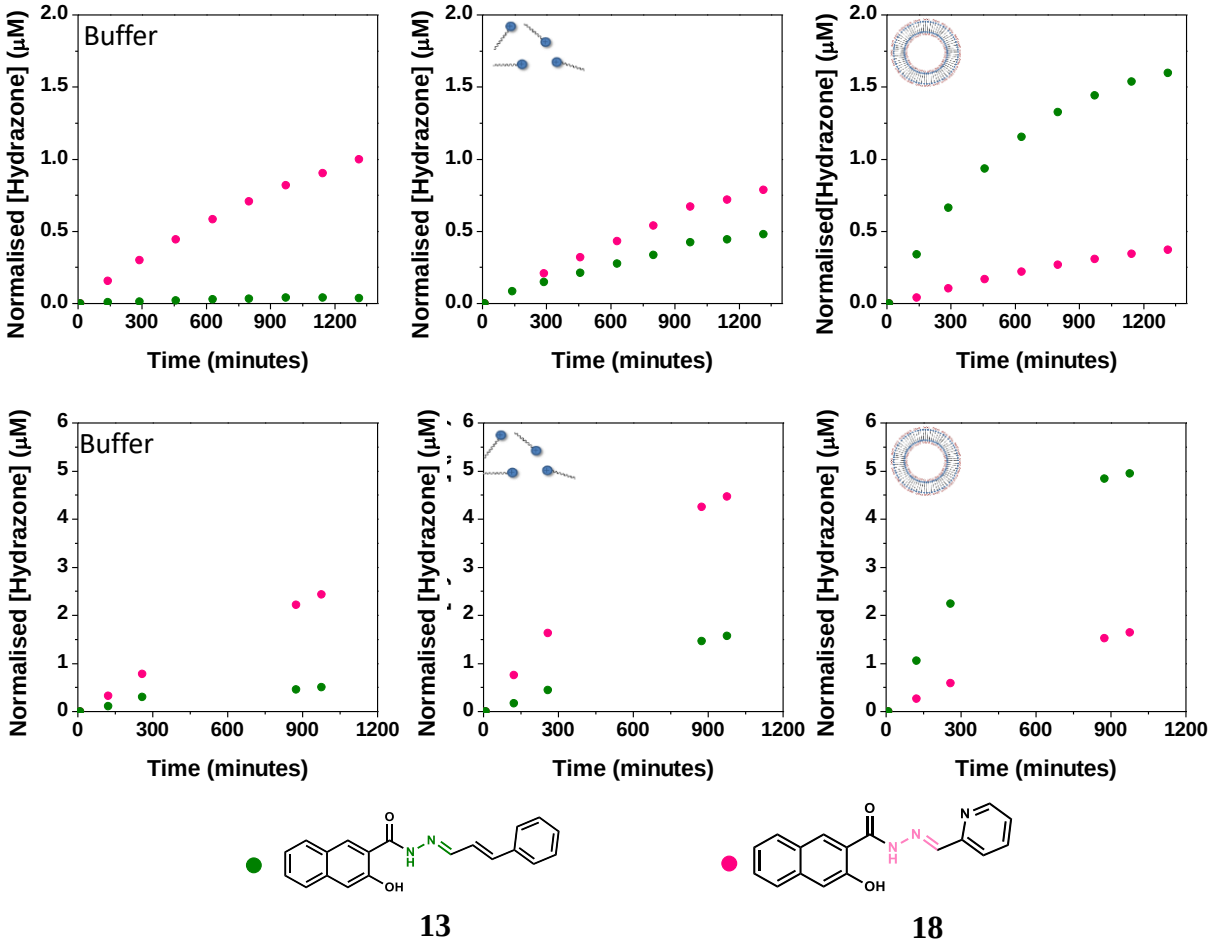

Figure 3.63: Graphs showing the concentration of hydrazones **13** and **18** over time in the presence of (a) buffer, (b) surfactant only and (c) surfactant and ATP, using 10 μM (top) and 20 μM (bottom) starting reagents. The hydrazone **18** is preferred in the presence of surfactant while the hydrazone **13** is formed in higher yield in the presence of vesicles. [Surfactant **10**] = 100 μM, [ATP] = 200 μM.

3.8.8 Comparison of formation of hydrazones 13 and 18 from mixing the reagents separately or in in one reaction pot

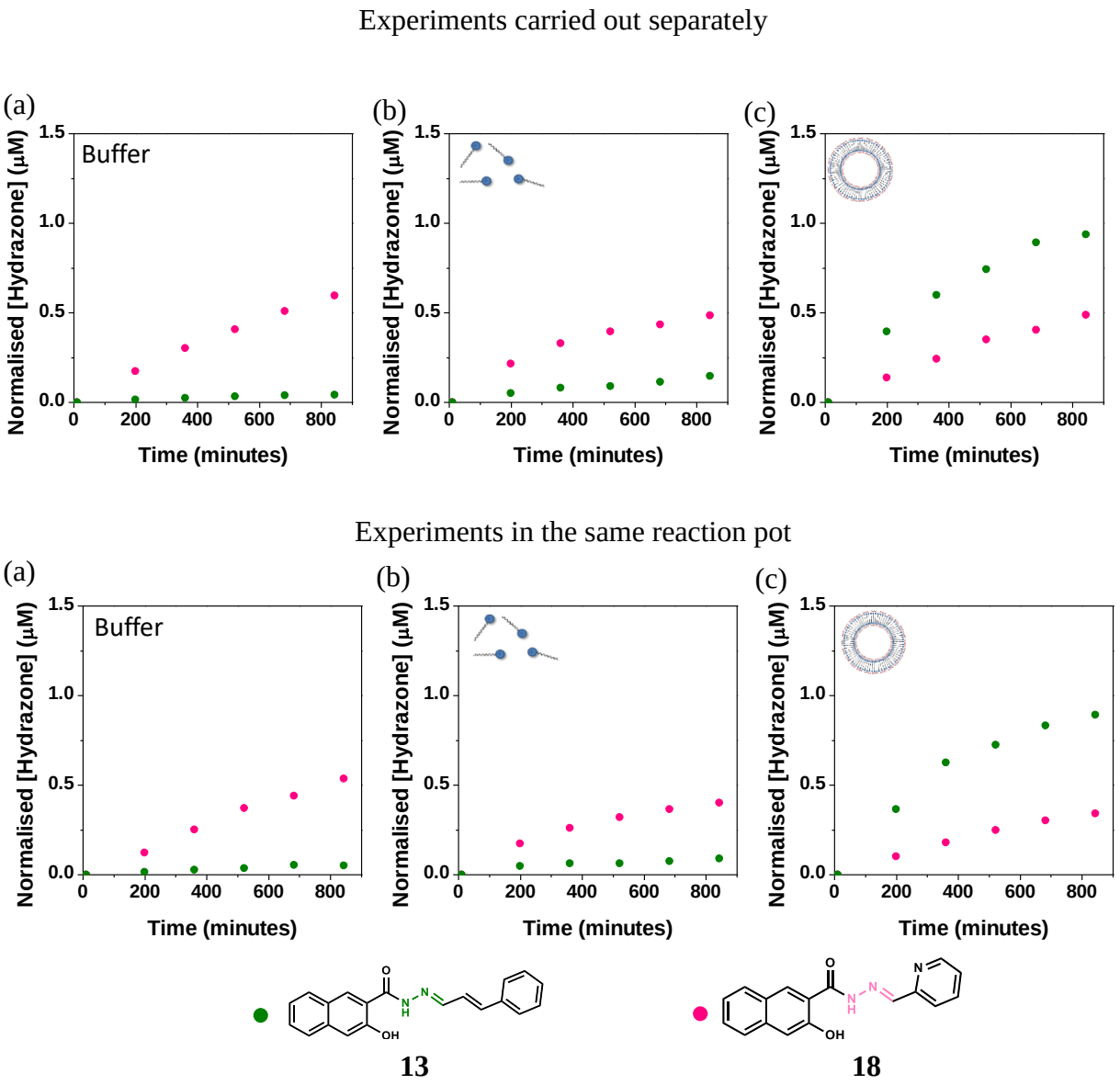

Figure 3.64: Graphs showing the concentration of hydrazones **13** and **18** over time in the presence of (a) buffer, (b) surfactant only and (c) surfactant and ATP. Top: Reaction between **11** and **12** was carried out separately from reaction between **12** and **17**. Bottom: Reaction between aldehydes **12**/**17** and **11** carried out in the same reaction pot. [Surfactant **10**] = 100 μM, [ATP] = 200 μM, [**12**] = 5 μM, [**11**] = [**17**] = 20 μM.

Chapter 4

Enhanced Enzymatic ATP Hydrolysis in Dissipative Systems

4.1 Introduction

Traditionally, supramolecular chemistry has dealt with the study of self-assembled systems under thermodynamic or kinetic control. Although such systems are also frequently observed in nature,[1-3] on occasion nature exploits another approach to self-assembly as well. This approach relies on the use of energy to activate chemical processes for defined periods of time before returning to the equilibrium state.[4,5] In recent years, supramolecular chemistry is undergoing a transition towards the study of out-of-equilibrium systems, which indeed bear a closer analogy to living systems (see Chapter 1 and 2).[6-8] Such systems require the consumption of fuel to maintain the high energy functional state populated[9,10] and therefore the associated function is only transiently present and depends on the presence of the chemical fuel (Figure 4.1).

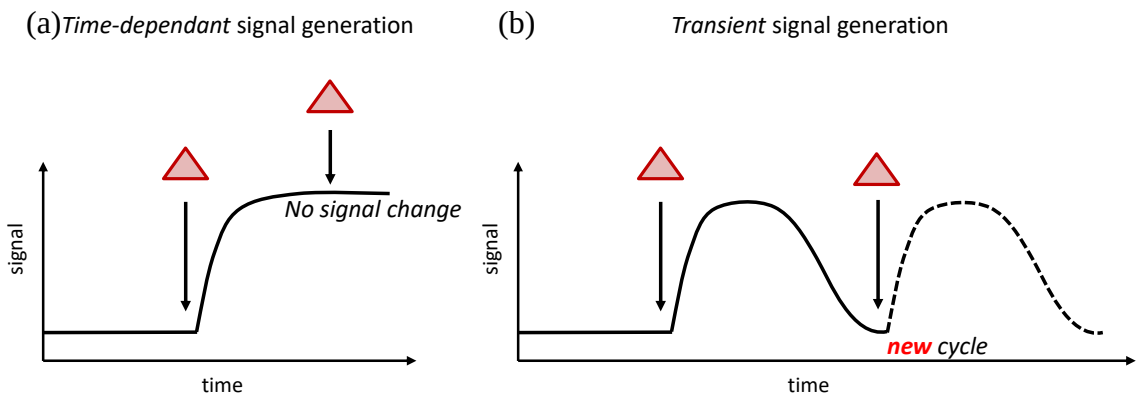

Figure 4.1: Time-dependent (a) and transient (b) signal generation upon addition of a trigger to a chemical system.

One example of such transient signal generation in nature is synaptic transmission, which is used for communication between nerve cells. Neurotransmittor release into the synaptic cleft generates a signal response in the postsynaptic neuron, but neurotransmittor degradation causes transientness and the system returns spontaneously to its basal resting state.[11] In our lab, transient signal generation was obtained based on monolayer-protected gold nanoparticles passivated with thiols terminating with a positively charged 1,4,7-triazacyclononane (TACN)•Zn^{2+} complex, Au NP **1**•Zn^{2+} (Figure 4.2a) and ATP.[12]

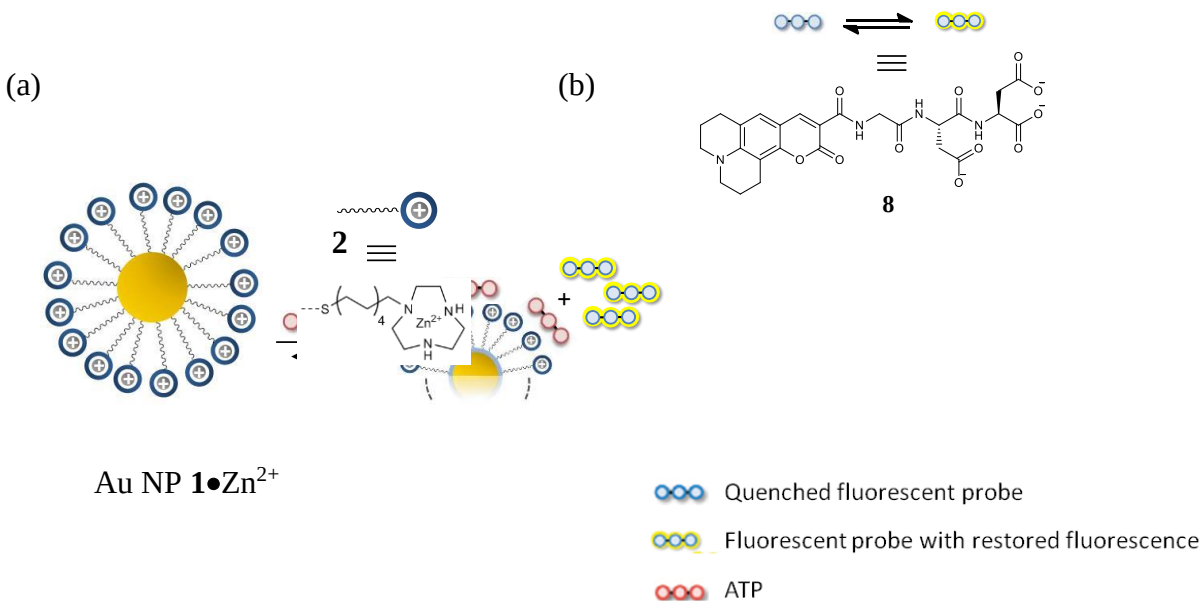

Figure 4.2: (a) Schematic representation of Au NP **1**•Zn^{2+} showing the attachment of the monomeric TACN•Zn^{2+} complex to the gold core. (b) Illustration of the displacement of the fluorescent probe **2** from Au NP **1**•Zn^{2+} upon addition of ATP as a stronger competitor.

Au NP **1**•Zn^{2+} has a high affinity for negatively-charged species. Therefore, when fluorescent probes containing a carboxylate group, such as **2**, are added to a solution of Au NP **1**•Zn^{2+}, the surface of the nanoparticle becomes covered with the probe (Figure 4.2b). The close proximity of the fluorophores to the gold core results in a quenching of its fluorescence.[13,14] However, phosphate groups have a higher affinity for Au NP **1**•Zn^{2+} compared to carboxylate groups.[15] ATP strongly binds to the Au NP **1**•Zn^{2+} because of multiple, electrostatic interactions between the phosphate groups and the TACN•Zn^{2+} complexes on the surface. Consequently, addition of ATP results in the displacement of the fluorescent probes from the nanoparticle surface. As a result, fluorescence is restored and

a fluorescence signal is generated. Multivalent interactions ensure that ATP binds the nanoparticle surface two orders of magnitude stronger compared to the products of ATP hydrolysis, AMP and P_i. Thus, when ATP is added in the presence of a hydrolytic enzyme, such as potato apyrase, an initial displacement of the probe is observed (Figure 4.3a), but progressively the signal decays as ATP is converted in the low affinity waste products AMP and P_i through the hydrolytic action of potato apyrase on the ATP. The cycle can be repeated upon the addition of a new batch of ATP.[15] This process can be monitored by monitoring the change in the fluorescence intensity of the fluorescent probe over time (Figure 4.3b). The general applicability was demonstrated by showing that similar transient signals could be generated using other phosphorylated chemical fuels and the enzyme alkaline phosphatase,[16] which is a less substrate-specific enzyme.[17]

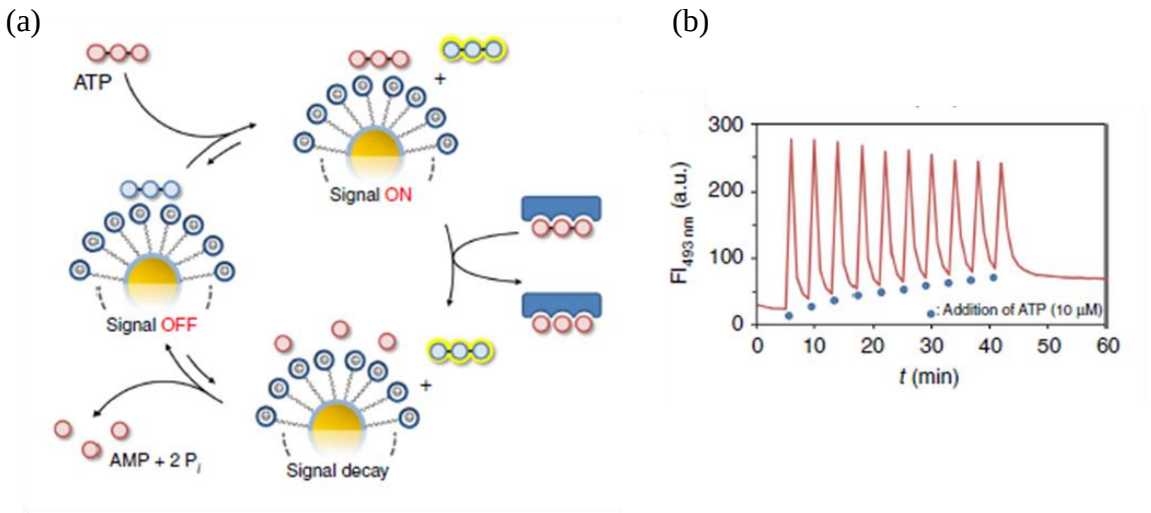

Figure 4.3: (a) Schematic representation of the system used for transient signal generation. In the absence of ATP, fluorescent probes containing carboxylate groups bind the Au NP **1**•Zn^{2+} and the fluorescence is quenched. Addition of ATP displaces the fluorescent probes from the surface and generates a fluorescent signal. The enzyme hydrolyses ATP and restores the preferential binding of **2** to the Au NP **1**•Zn^{2+} surface. This quenches the fluorescence of the probe once again. The cycle can be repeated upon re-addition of ATP. (b) The fluorescence intensity at 493 nm (λ_{em} of the dye) upon 10 repetitive additions of ATP to a solution of Au NP **1**•Zn^{2+} and fluorescent probe in the presence of potato apyrase which cleaves ATP.

Self-assembly under dissipative conditions in Nature is further used for the formation of transient structures, where the chemical fuel is essential in order to drive the assembly process.[18-22] For instance, microtubules are formed during cell division and destroyed when they are not needed any longer, as described in Chapter 2. In the Prins group, this process

was mimicked by developing an approach towards the transient self-assembly of vesicles, as described in Chapter 1 (Figure 4.4a).[23] ATP was capable of assembling vesicles from a surfactant bearing a TACN•Zn^{2+} head group, **3**. The presence of the enzyme potato apyrase was responsible for the transient nature of the assembly. ATP was hydrolysed into the waste products AMP and Pi by the enzyme potato apyrase, which were unable to stabilise the assembly. The monomeric state was therefore restored. It was possible to monitor this process by following the fluorescence intensity of a hydrophobic fluorescent dye (Figure 4.4b). Dyes like DPH, **4**, are not soluble in aqueous buffer and thus do not emit any fluorescence when the surfactant is unassembled. Formation of the vesicles provides a suitable hydrophobic environment for the dye to be solubilised and fluorescence is turned-on upon addition of ATP to the surfactant. Subsequent disassembly of the vesicles upon enzymatic hydrolysis turns off the fluorescent signal once again.[23] Chemical fuels other than ATP in combination with the enzyme alkaline phosphatase were also shown to induce transient self-assembly by hydrolysing ATP.[16]

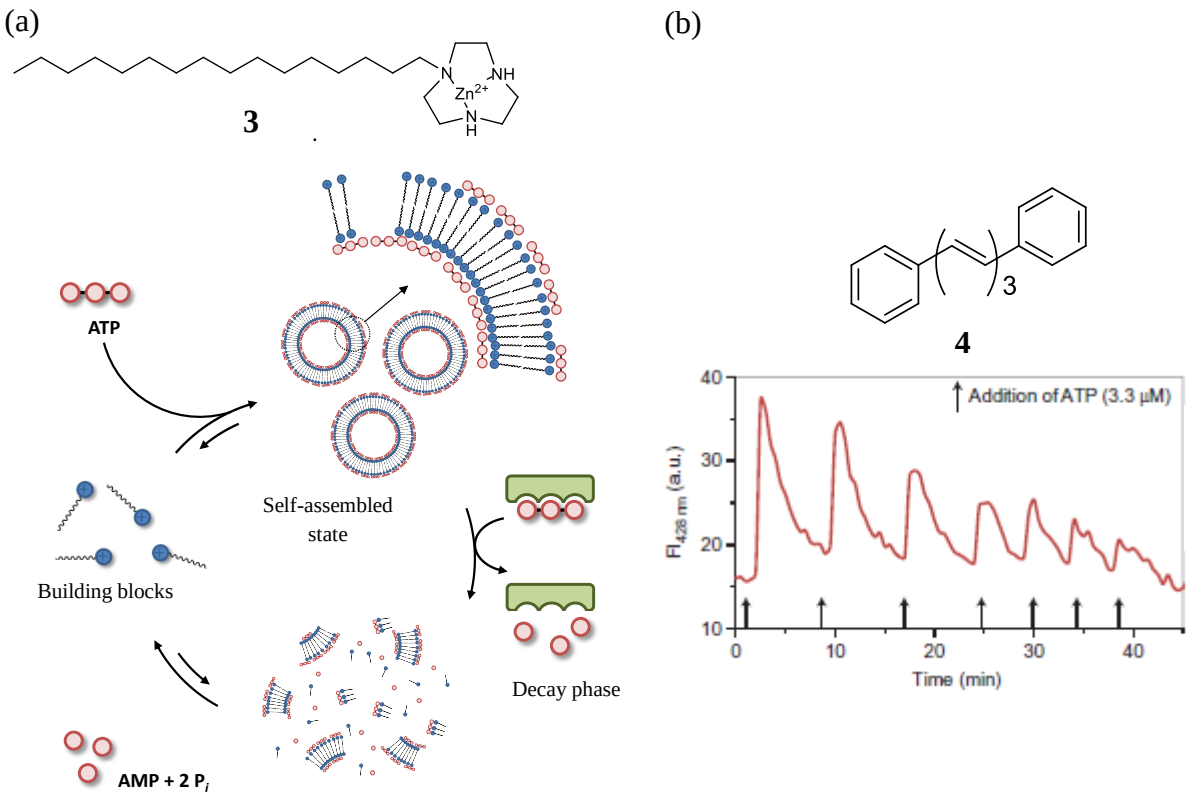

Figure 4.4: (a) Schematic representation of transient signal generation in the C_{16}TACN•Zn^{2+} surfactant (**3**) system and (b) monitoring the assembly and disassembly by monitoring the fluorescent signal from the dye DPH, **4**.

In these studies on self-assembled systems under dissipative conditions, the fuel to waste conversion occurs through the addition of an external additive, namely an enzyme capable of cleaving ATP. Here, the enzyme is responsible for fuel-to-waste conversion. It is assumed that the monomers or assembled state never actually participate in the conversion of the fuel to waste.[24] This contrasts natural dissipative self-assembled processes such as microtubule and actin formation, described in Chapters 1 and 2, in which the building blocks themselves are involved in the fuel-to-waste conversion process. Moreover, the rate of this process is enhanced in the assembled state.

The experiments typically used potato apyrase as an enzyme for hydrolysis.[25] The enzyme has low substrate specificity and requires the presence of metal ions, ideally Ca^{2+} or Mg^{2+}, for optimal activity.[26,27] The final products of ATP hydrolysis are AMP and inorganic phosphate, Pi with ADP being an intermediate product. The precise mechanism of action of the enzyme is still unclear but it probably involves a single site for ATP and ADP hydrolysis.[28,29] The metal ion is thought to directly coordinate to the β- and γ- phosphates of the ATP or to take part in the positioning of ATP through a network of hydrogen bonds involving water molecules of the metal coordination sphere. This also helps to maintain the conformation of the triphosphate needed for hydrolysis.[29] It has also been determined that the metal ion-nucleotide complex approaches the active site through the phosphate group and that another metal ion might be required as a cofactor to activate the enzyme at another site.[30]

The self-assembly studies under dissipative conditions typically rely on fluorescence spectroscopy to monitor the assembly and disassembly processes. Advantages are the sensitivity and the ease of use.[31] However, fluorescence spectroscopy is an indirect analysis method, and does not provide a direct insight into the chemical modifications occurring. In this Chapter, we will use ^{31}P NMR spectroscopy as a direct method for obtaining evidence for the conversion of ATP into waste products in the presence of building blocks typically used in our group. Since most of the dissipative studies in our lab were performed using Au NP **1**•Zn^{2+}, the study will use these Au NPs rather than the amphiphiles studied in the previous Chapters. This study is aimed at addressing the question whether the presence of Au NP **1**•Zn^{2+} affects ATP hydrolysis by potato apyrase.

Au NP **1**•Zn^{2+} have been used as nanozymes for the transphophorylation of 2-hydroxy propyl 4-nitrophenyl phosphate (HPNPP), **5**, an RNA model substrate (Figure 4.5).[32-36] Nanozymes are defined as catalytic nanomaterials possessing enzyme-like behaviour.[37,38] Previous detailed studies have shown that the strong catalytic effect of Au NP **1**•Zn^{2+} originates from the cooperative effect between neighbouring TACN•Zn^{2+} complexes embedded in the monolayer.[39] Indeed, a sigmoidal plot was observed when the initial rate was plotted as a function of the amount of Zn^{2+} metal ions, and this reached a maximum at a 1:1 ratio of Zn^{2+}:TACN. These studies also showed that in the absence of metal ions, the system is not catalytically active. Studies of the initial rates as a function of substrate concentration revealed that the catalytic behaviour can be described by Michaelis-Menten saturation kinetics.[32]

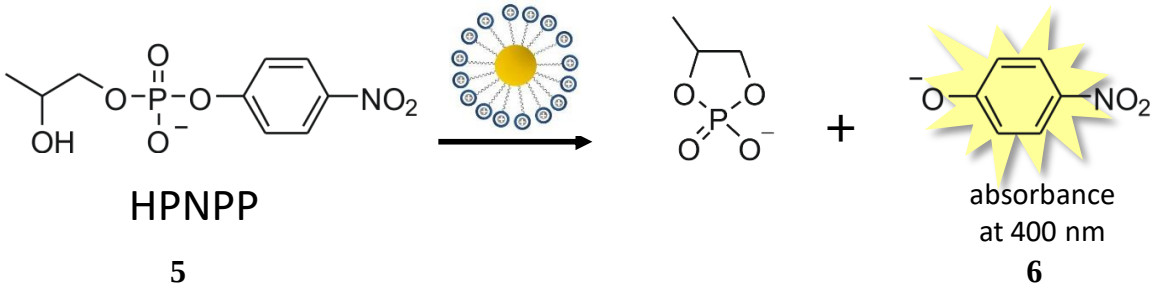

Figure 4.5: Schematic representation of the transphosphorylation of HPNPP, **5**, catalysed by Au NP **1**•Zn^{2+}. The reaction could be monitored by the formation of product **6** which is highly coloured.

Considering that Au NP **1**•Zn^{2+} acts as an efficient transphosphorylation catalyst, we were interested to investigate whether it could also play a role in ATP hydrolysis. This would bring the system closer to natural systems, in which energy dissipation occurs by the system itself, without the need for external additives.

4.2 Results and discussion

The spectrum of ATP (1 mM) in aqueous HEPES buffer (10 mM) displays two doublets at -11.13 ppm and -11.70 ppm corresponding to the α- and γ- phosphorus atoms, respectively, and a multiplet at -23.37 ppm corresponding to the β-phosphorus atom. ADP on the other hand, shows only two doublets at -11.11 ppm and -11.64 ppm, whereas AMP has only one peak at 3.34 ppm.[40] Inorganic phosphate, Pi, on the other hand, exhibits a single peak at 2.17 ppm (Figure 4.6). The addition of divalent metal ions such as Ca^{2+} and Zn^{2+} (0.6 mM) shifts the peaks of ATP downfield indicating that the divalent metal ions bind the nucleotides (Figure 4.7 and Table 4.1). The α-phosphorus peak of ATP undergoes only a slight shift upon addition of metal ions. Thus, a shift of 0.8 ppm was observed in the presence of Ca^{2+} and a shift of 0.4 ppm was observed in the presence of Zn^{2+}. The β- and γ-phosphorus peaks of ATP undergo larger shifts of approximately 2.0 ppm in the case of both Ca^{2+} and Zn^{2+}, suggesting that these are more involved in the binding to the metal ions.

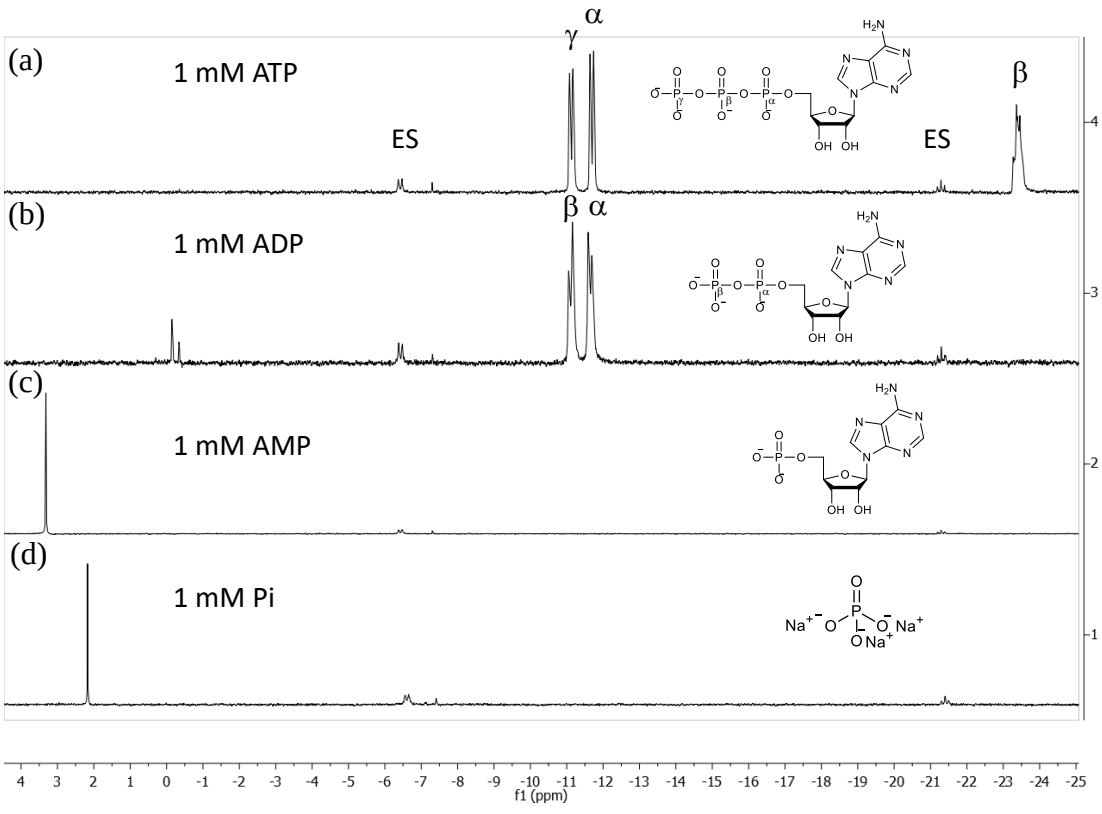

Figure 4.6: ^{31}P NMR spectrum of 1 mM reference solution of (a) ATP (b) ADP (c) AMP (d) Pi (10% D_2O, 202 MHz, 300 K) [HEPES] = 10 mM, pH 7.0. ES denotes the external standard.

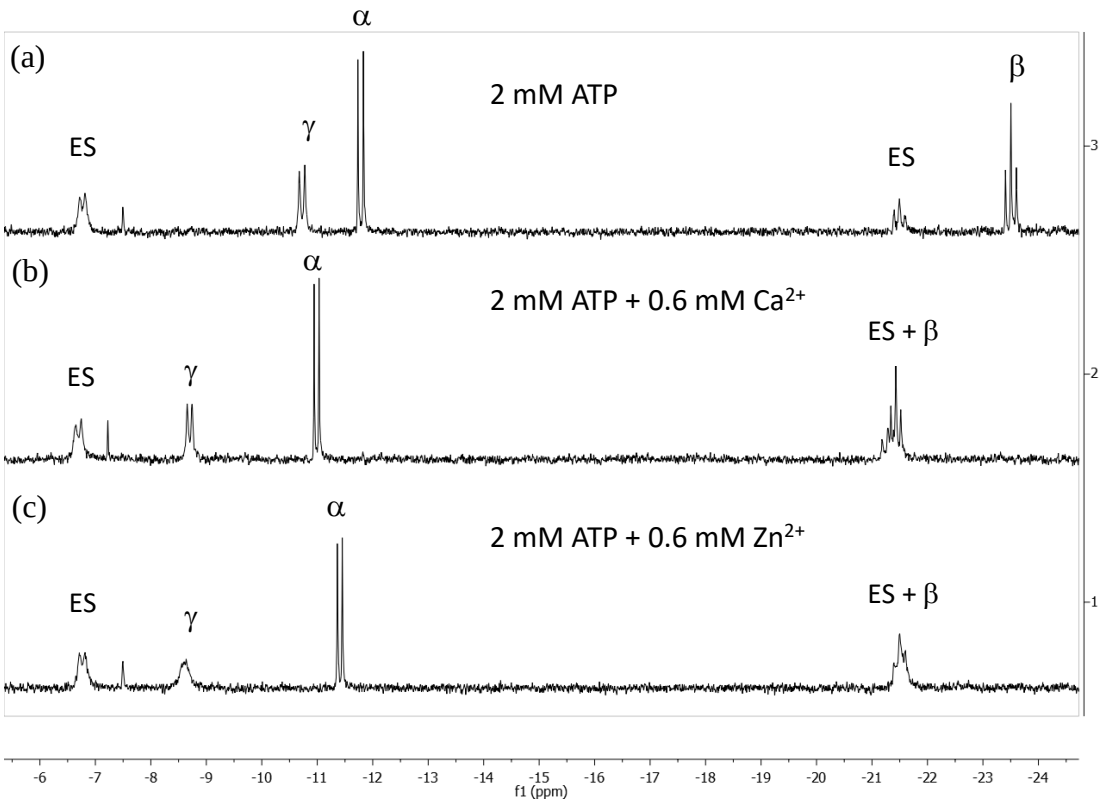

Figure 4.7: ^{31}P NMR spectrum of (a) 2 mM ATP and upon addition of (b) 0.6 mM Ca^{2+} or (c) 0.6 mM Zn^{2+}.

	α (ppm)	**β (ppm)**	**γ (ppm)**
2 mM ATP	-10.71	-11.81	-23.49
2 mM ATP + 0.6 mM Ca^{2+}	-8.69	-10.99	-21.41
2 mM ATP + 0.6 mM Zn^{2+}	-8.63	-11.43	-21.50

Table 4.1: Table showing the chemical shifts of the phosphorus atoms in ATP in the absence of metal ions and upon addition of 0.6 mM Ca^{2+} and 0.6 mM Zn^{2+}.

Longitudinal relaxation times (T_1) for ^{31}P signals were determined by an inversion – recovery method in order to set appropriate pulse delay time for quantitiative NMR experiments. The relaxation times obtained are documented in Table 4.2. The ^{31}P NMR experiment was set with a delay time of 5 s.

	P1 Chemical Shift Range (ppm)	P1 *T*1 (s)	P2 Chemical Shift Range (ppm)	P2 *T*1 (s)	P3 Chemical Shift Range (ppm)	P2 *T*1 (s)
STD $Na_5P_3O_{10}$	(-6.75) – (-7.69)	1.52	(-21.51) – (-22.26)	1.29		
ATP	(-10.40) – (-11.25)	2.03	(-11.64) – (- 12.22)	1.09	(-23.25) – (- 23.98)	1.25
ADP	(-9.52) – (- 10.48)	1.964	(-11.22) – (- 12.19)	1.25	/	/
AMP	(-6.89) – (-7.59)	1.504	/	/	/	/

Table 4.2: Table showing the relaxation times for each phosphorus atom in the standard and each of the nucleotides used.

4.2.1 Investigating the binding affinity of ATP to Au NP 1•Zn^{2+}

The binding of ATP to Au NP **1**•Zn^{2+} was monitored by titrating a 2 mM solution of ATP with aliquots of Au NP **1**•Zn^{2+} up to a final concentration of 1.5 mM. The phosphorus peaks were referenced against a 1 mM solution of $Na_5P_3O_{10}$ placed in a co-axial tube. It was decided to add Au NP **1**•Zn^{2+} to ATP, instead of the other way around, to keep a constant ^{31}P concentration. As Au NP **1**•Zn^{2+} was added, a clear downfield shift for the ATP peaks was observed (Figure 4.8), indicating complex formation with Au NP **1**•Zn^{2+}. The changes in chemical shifts were plotted against the concentration of Au NP **1**•Zn^{2+} (Figure 4.9a). The obtained binding isotherms indicate that binding occurs under saturation conditions. Saturation is reached at a Au NP **1**•Zn^{2+} concentration of 800 μM, which corresponds to 1 ATP bound every three head groups. This is in full agreement with previously reported data obtained from fluorescence titrations.[12] Similar saturation profiles were also obtained for ADP and AMP ((Figure 4.9b and c), but in this case binding stoichiometries of 1:2 and 1:0.8 were obtained.[41]

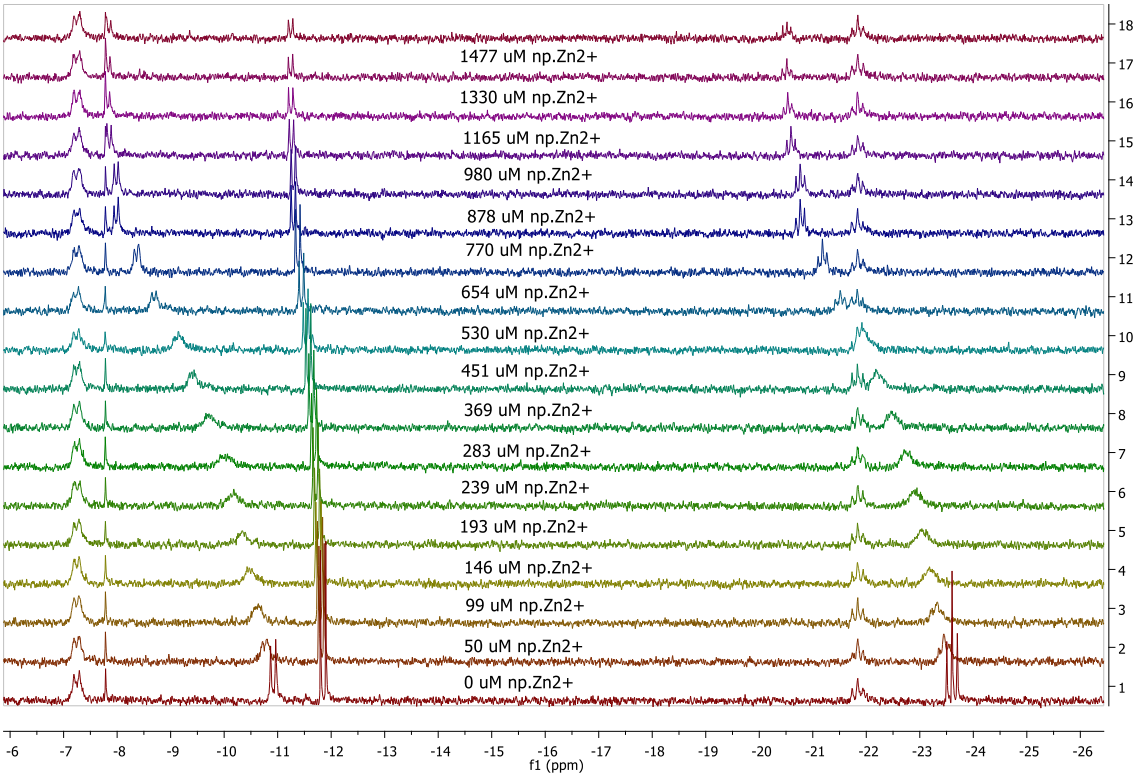

Figure 4.8: ^{31}P NMR spectra showing the peak of ATP as it shifts upon successive addition of Au NP **1**•Zn^{2+} to the solution. (10% D_2O, 202 MHz, 300 K) [HEPES] = 10 mM, pH 7.0 [ATP] = 2 mM.

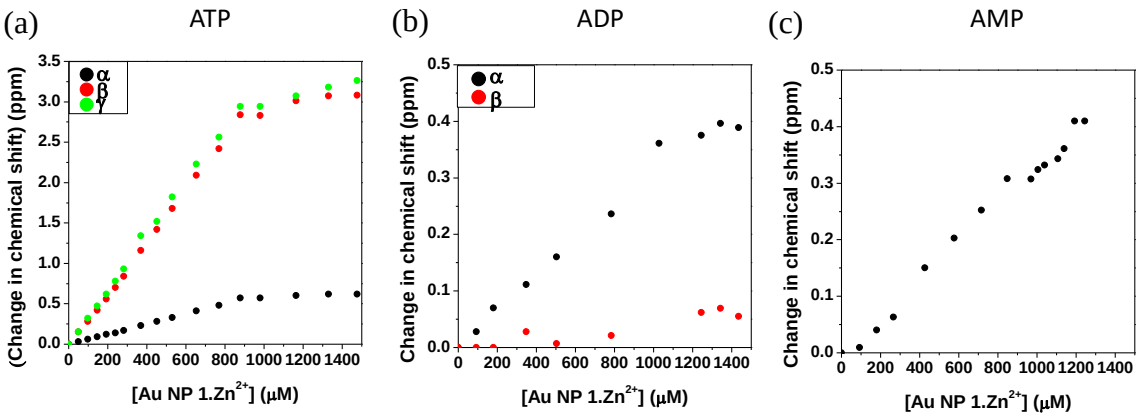

Figure 4.9: Figure showing the change in the chemical shift when titrating successive volumes of Au NP **1**•Zn^{2+} to 2 mM nucleotides ((a) ATP, (b) ADP and (c) AMP).

4.2.2 Investigating enzymatic hydrolysis of ATP by ^{31}P NMR spectroscopy

The rate of ATP hydrolysis by potato apyrase under different conditions was investigated by ^{31}P NMR spectroscopy. The rate was compared under different conditions in the absence and presence of metal salts and Au NP **1**•Zn^{2+}. In this manner, an insight could be obtained on whether Au NP **1**•Zn^{2+} plays a role in hydrolysis. A 2 mM solution of ATP buffered at pH 7.0 with HEPES buffer gave a respectable signal in a reasonable time (300 scans). Solutions were buffered with 10 mM HEPES buffer at pH 7.0. Depending on the conditions used, the peaks of ATP could be observed to decrease in intensity over time, accompanied by an increase in peaks assigned to ADP and Pi. The ADP peak initially increased in intensity, reaching a maximum before decreasing again. A peak due to AMP simultaneously appeared and this continued to increase in intensity together with the peak due to Pi (Figure 4.10).

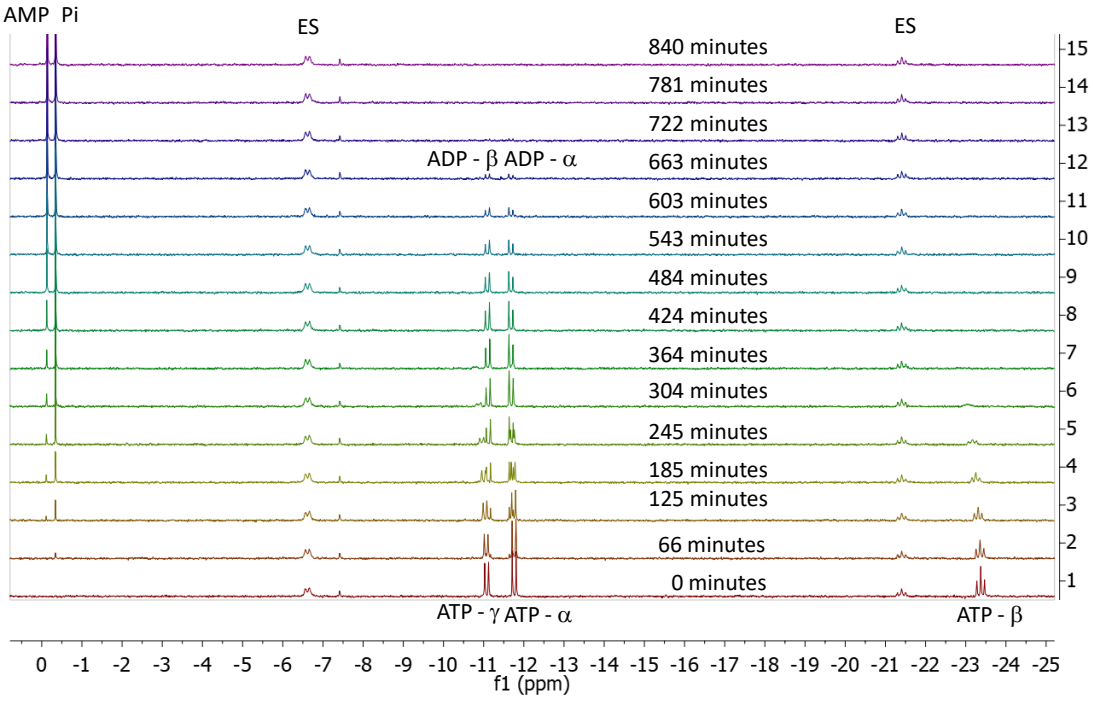

Figure 4.10: Representative spectra showing the conversion of ATP into ADP, AMP and Pi through the action of potato apyrase. [ATP] = 2 mM, [HEPES] = 10 mM, pH 7.0, [potato apyrase] = 1.0 U, [Ca^{2+}] = 0.25 mM. ES denotes the external standard.

Under these conditions, the enzyme worked under saturation conditions. The experimental data points could be fitted to a model which assumes that the substrate, ATP initially binds to the enzyme reversibly to form an enzyme-substrate complex (Equation 4.1). This step is characterised by a dissociation constant K_m. The enzyme-substrate constant in turn releases the products ADP and Pi, regenerating the enzyme in a rate-determining, irreversible step. That step is characaterised by a first-order rate constant k_{cat}. A similar behaviour is assumed for ADP. ADP binds the enzyme reversible to form an enzyme-substrate complex. The products AMP and Pi are subsequently released from the enzyme in a rate-determining step, regenerating the enzyme in the process.

$$ATP + E \underset{k_2}{\overset{k_1}{\rightleftharpoons}} ATPE \xrightarrow{k_{catATP}} ADP + P + E$$

$$ADP + E \underset{k_4}{\overset{k_3}{\rightleftharpoons}} ADPE \xrightarrow{k_{catADP}} AMP + P + E$$

Equation 4.1: Equations describing the hydrolysis of ATP into AMP and inorganic phosphate.

Poor fitting for K_m could be explained by the fact that the enzyme worked under saturation conditions and therefore the rate is actually described by a first–order rate constant, $v_{init} = k_{cat}[S]$. Table 4.3 shows the kinetic parameters calculated for the different conditions investigated.

	k_{catatp} (Minute^{-1})	**k_{catadp} (Minute^{-1})**
2 mM ATP + 0.6 mM Ca^{2+} + 1.0 U apyrase	14	149
2 mM ATP + 0.6 mM Zn^{2+} + 1.0 U apyrase	16	100
2 mM ATP + 0.6 mM Au NP **1**•Zn^{2+} + 1.0 U apyrase	150	3.70705E+11
2 mM ATP + 0.6 mM Au NP **1** + 1.0 U apyrase	25	99
2 mM ATP + 0.6 mM TACN + 0.6 mM Zn^{2+} + 1.0 U apyrase	7	250

Table 4.3: Table showing the k_{cat} values calculated for the hydrolysis of ATP under the different conditions investigated.

The enzyme potato apyrase requires metal ions in order to be activated.[25] In fact, when the ATP concentration was monitored over time in the presence of 1.0 U potato apyrase without any metal salts, hardly any changes in the ^{31}P NMR spectrum could be observed over time (Figure 4.11a). A tiny amount of Pi accumulated over time, suggesting a small amount of enzymatic activity.

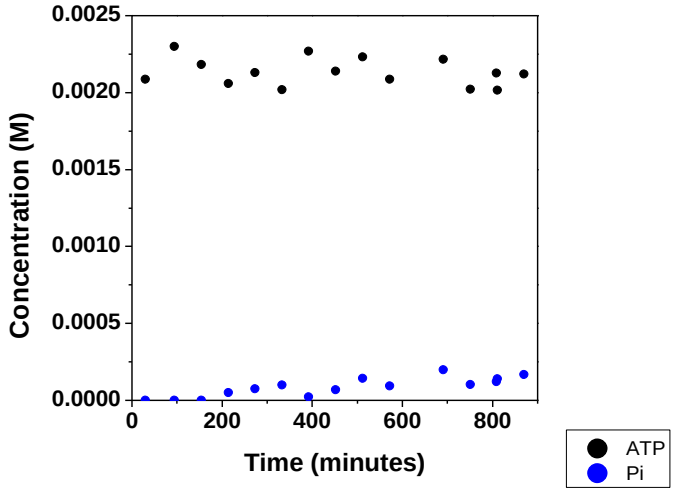

Figure 4.11: Figure showing the change in nucleotide concentration when ATP is allowed to stand in the presence of potato apyrase in the absence of metal ions. [ATP] = 2 mM, [HEPES] = 10 mM, pH 7.0, [potato apyrase] = 1.0 U.

The experiment was then carried out in the presence of 0.6 mM Ca^{2+}, which is the preferred metal ion activator for optimal enzymatic activity (Figure 4.12a).[27] In this case, the peaks due to ATP could be observed to rapidly decrease in intensity, and peaks due to ADP and Pi appeared simultaneously. The ADP peak initially increased, reached a maximum and then decreased over time. A singlet peak originating from AMP was observed to increase over time. A similar effect could be observed with Zn^{2+} (Figure 4.12b). Comparable values were obtained for the k_{cat} values in the presence of Ca^{2+} and Zn^{2+} as activating metal ions, suggesting that the metal ions had similar effects on the hydrolysis. The time required for ATP hydrolysis to go to completion appeared to be approximately the same in both cases.

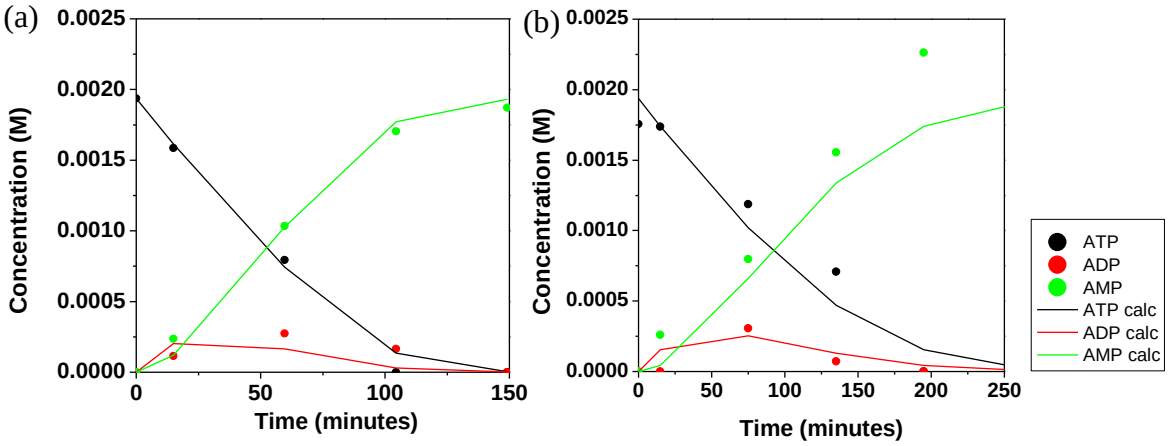

Figure 4.12: Figure showing the change in nucleotide concentration when ATP is allowed to stand in the presence of potato apyrase and (a) Ca^{2+} and (b) Zn^{2+}. [ATP] = 2 mM, [HEPES] = 10 mM, pH 7.0, [potato apyrase] = 1.0 U, [Ca^{2+}] = 0.6 mM, [Zn^{2+}] = 0.6 mM.

The hydrolysis of ATP was then repeated in the presence of Au NP **1**•Zn^{2+} (with the same amount of Zn^{2+} but complexed in the nanoparticle monolayer). The k_{cat} value for ATP increased from 16 min^{-1} in the presence of free Zn^{2+} to 150 min^{-1} in the presence of the Au NP **1**•Zn^{2+} complex. The k_{cat} value obtained for ADP could not be reliable determined in this case, because the experiment was too fast to give enough data points for a sufficiently good analysis (Figure 4.13a).

This experiment was compared to the experiment in the presence of the same amount of Au NP **1**, but without Zn^{2+}. In the absence of Zn^{2+}, ATP hydrolysis still occurred, suggesting a role of the Au NP **1** in the hydrolysis of ATP. However, the rate of ATP hydrolysis was much lower. In fact, the k_{catATP} decreased to 25 min^{-1}, more reminiscent of the situation with free Zn^{2+}. This experiment demonstrates the pivotal role of Zn^{2+} in the regulation of the function of the Au NP **1**•Zn^{2+} system, as highlighted in previous work using the same nanoparticles.[42] Metal ions have also been reported to be a requirement for the function of other multivalent systems.[43]

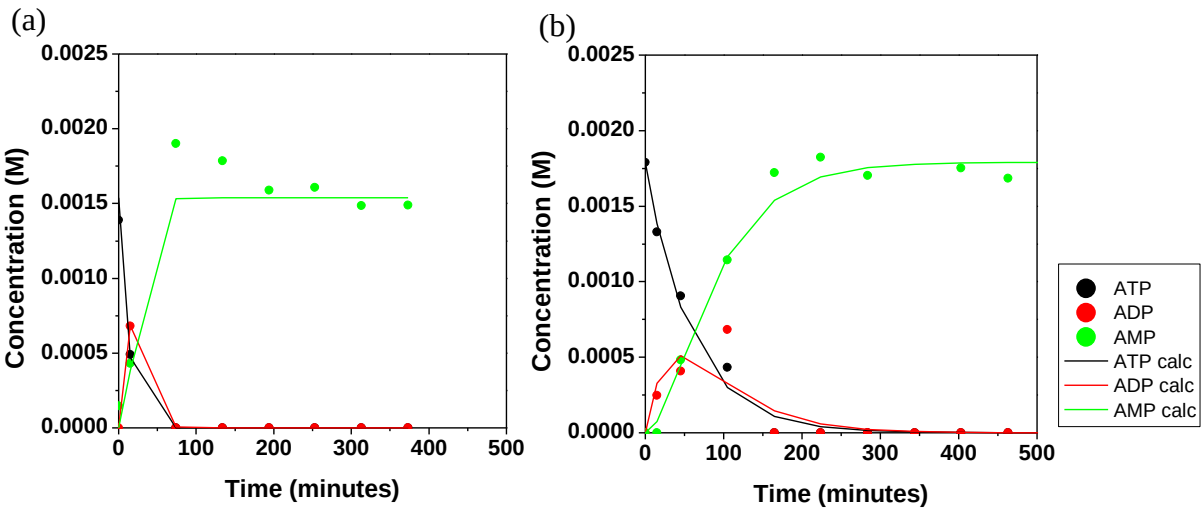

Figure 4.13: Figure showing the change in nucleotide concentration when ATP is allowed to stand in the presence of potato apyrase and Au NP **1** (a) in the presence and (b) in the absence of Zn^{2+}. [ATP] = 2 mM, [HEPES] = 10 mM, pH 7.0, [potato apyrase] = 1.0 U, [Au NP **1**] = 0.6 mM, [Zn^{2+}] = 0.6 mM.

Previous studies have shown that the catalytic effect of the Au NP **1**•Zn^{2+} arises from a cooperative effect between TACN head groups in close proximity,[39] which are able to form catalytic pockets comprising more than one neighbouring TACN•Zn^{2+} complexes.[32] A multivalent effect[44] was observed in the present study as well, as emerged from an experiment carried out in the presence of the monomeric TACN•Zn^{2+} complex (0.6 mM). Under these conditions, the system presented the slowest k_{cat} for ATP-hydrolysis. This was reflected in a longer time required for complete hydrolysis than in the presence of metal ions. The k_{catADP} was however enhanced with respect to the situation with Zn^{2+} only suggesting that the complex is better capable of activating the hydrolysis of ADP than that of ATP while the Au NP **1**•Zn^{2+} favours ATP as well. The gold nucleus is capable of inducing cooperativity between neighbouring TACN•Zn^{2+} complexes, leading to enhanced catalysis.

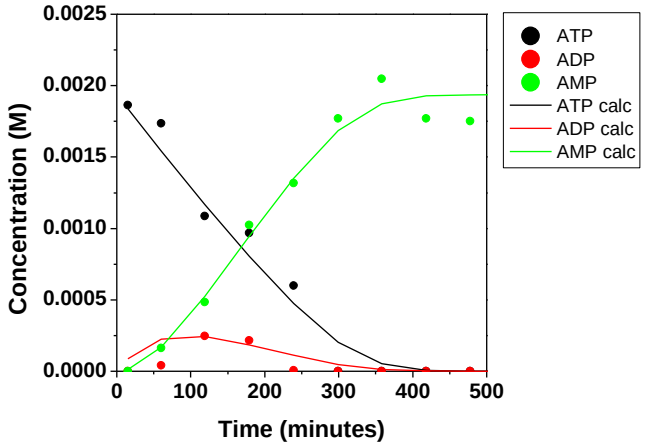

Figure 4.14: Figure showing the change in nucleotide concentration when ATP is allowed to stand in the presence of potato apyrase and TACN•Zn^{2+}. [ATP] = 2 mM, [HEPES] = 10 mM, pH 7.0, [potato apyrase] = 1.0 U, [TACN•Zn^{2+}] = 0.6 mM.

The improved rates observed with the Au NP **1**•Zn^{2+} led us to question whether the nanoparticle complex had an intrinsic ability to hydrolyse ATP without any requirement for an enzyme. Such a catalytic effect has been observed with macrocylic polyamine compounds,[45-47] which have been used as mimics for phosphoryl transfer enzymes.[40,48] Metal ion complexes have also been reported to spontaneously cleave ATP.[49] Therefore, 2 mM ATP was added to 0.6 mM Au NP **1**•Zn^{2+} with no enzyme added. There was no change in the ATP peaks in this case. A similar result was obtained for ADP. This suggests that the Au NP **1**•Zn^{2+} are not able to cleave ATP and ADP on their own but act as activators for the enzyme to exert its hydrolytic power. The Au NP **1**•Zn^{2+} potentially takes over the role of the metal ion in activating the nucleotide for hydrolysis by the enzyme.

4.3 Conclusions

In this study it was shown that Au NP **1**•Zn^{2+} acts as a promoter for enzymatic ATP hydrolysis. The enhancement is driven by the cooperative, multivalent effect induced by the clustering of cataytic TACN•Zn^{2+} complexes on the surface of gold nanoparticles. The enhanced rate of ATP hydrolysis by potato apyrase suggests a revision of the mechanism described previously for the generation of a transient signal by Au NP **1**•Zn^{2+}.[15] It has previously been assumed that energy dissipation in the Au NP **1**•Zn^{2+} system occurs exclusively through the action of the external additive, the potato apyrase. The hydrolytic enzyme modifies the building block, ATP, and changes its propensity to form an aggregate. Thus, the conversion of the fuel to waste is independent of the self-assembling building blocks.

The present study implies that transient signal generation by the Au NP **1**•Zn^{2+} is closer to true dissipative conditions than previously assumed. Addition of ATP as the chemical fuel to the monomer, Au NP **1**•Zn^{2+} provides energy to form the higher energy aggregated state. The assembled state returns to the resting state through the action of the enzyme potato apyrase mediated by the same monomeric state Au NP **1**•Zn^{2+}. The requirement for potato apyrase as an external additive distinguishes this system from true dissipative mechanisms found in nature. However, in our system the assembled state promotes the return to the basal state. The active participation of the building blocks, in this case Au NP **1**, in fuel-to-waste conversion brings the system closer to natural dissipative processes such as microtubule formation

4.4 Experimental

4.4.1 Instrumentation

^{31}P NMR spectra were recorded on a Bruker AV500 operating at 500 MHz for ^{1}H and at 202 MHz for ^{31}P. A solution of $Na_5P_3O_{10}$ at pH 7 (HEPES buffer 5 mM) was used as a coaxial reference for ^{31}P NMR spectra ($Na_5P_3O_{10}$ gives a triplet centered at $\delta = -21.16$ ppm and a doublet centered at $\delta = -6.42$ ppm).[50] Spectra were obtained with a delay time of 5 s. Analysis of spectra was carried out using MestreNova.

4.4.2 Materials

All fine chemicals were sourced from commercial suppliers and were used directly without purification unless mentioned. The final solutions for analysis were prepared from stock solutions prepared in the respective solvent and diluted in MilliQ water.

ATP, ADP and AMP were obtained from Sigma Aldrich. Solutions were prepared as an approximately 10 mM solution in MilliQ water by weight and the exact concentration was calculated by UV-Vis spectroscopy using the following molar extinction coefficient: ε_{259} (ATP, ADP AMP) = 15400 M^{-1} cm^{-1}.[51] Inorganic phosphate solution was prepared as a 20 mM stock solution by weight in MilliQ water.

4.4.3 Synthesis of thiol used for nanoparticle synthesis

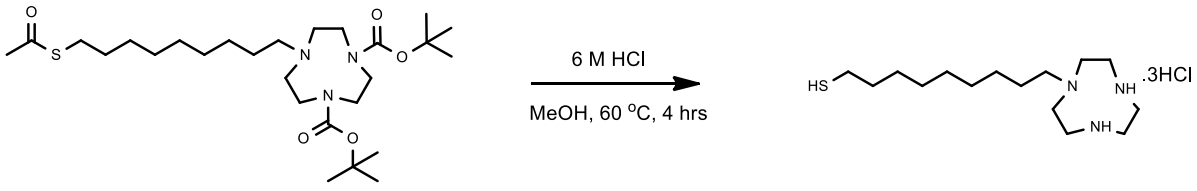

7 **8**

The synthesis of **8** has been described in literature.[12] A mass of 100 mg **7** was solubilised in 2 mL methanol. A volume of 2 mL concentrated HCl was subsequently added to yield a final concentration of HCl of 6 M. The resulting solution was left stirring for 4 hours at 60 °C and the solvent was evaporated under reduced pressure, resulting in the formation of a white solid in quantitative yield. The solid was not isolated but used directly for the synthesis of the nanoparticles.

^{1}H NMR:[52] (δ ppm, D_2O, 300 K, 500 MHz): 3.33 (s, 4H), 3.26 (m, 4H), 3.20 (m, 4H), 2.92 (m, 2H), 2.46 (t, J = 7 Hz, 2H), 1.52 (m, 4H), 1.25 (m, 12H)

4.4.4 Synthesis, purification and characterisation of gold nanoparticles

Gold nanoparticles (Au NP) are nanoclusters consisting of a gold core with a diameter between 1 and 25 nm stabilised by a monolayer of organic molecules, typically thiols, which are capable of forming a strong, stable Au-S bond upon self-assembly, due to the soft character of both the Au and S.[53,54] The organic monolayer thus formed prevents the gold nanoparticles from clustering and precipitating. The stability offerred by the Au-S bond enables the nanoparticles to be used at very low concentrations under physiological conditions while the versatility offered by thiol chemistry enables the nanoparticles to be functionalised with a number of headgroups,[55,56] allowing applications in a number of areas, such as sensing. Functionalisation of Au NP with a C_9-thiolate bearing a 1,4,7-triazacyclononane (TACN) headgroup enables the efficient complexation of a Zn^{2+} moiety, resulting in cationic nanoparticles which can interact efficiently with negatively charged molecules.

4.4.4.1 Synthesis of water-soluble monolayer-protected gold nanoparticles

The Brust-Schiffrin method for nanoparticle synthesis[57] as adapted in the procedure by Scrimin and co-workers[52] was used for the synthesis of the gold nanoparticles. The method, published in 1994, combines the two-phase colloid preparation of Faraday[58] with phase transfer and alkanethiolate/Au chemistry to provide, through a facile *in situ* synthesis in ambient conditions, nanoparticles of controlled size between 2 and 5 nm with a narrow dispersity index and high air and thermal stability which can be repeatedly isolated and re-dissolved without aggregation or decompostion and which can be functionalised relatively easily.[53,55] The resulting nanoparticles can be handled as simple chemical compounds and characterised using conventional techniques.[57] Nanoparticles synthesized using the procedure of Brust and Schriffin are typically called monolayer-protected clusters (MPCs).[53]

In the initial step, a phase transfer agent, in this case tetraoctylammonium bromide (TOABr), is used to transfer $AuCl_4^-$ from an aqueous solution to toluene. In the second step, dioctylamine reduces Au(III) to Au(I) whilst controlling the size of the growing cluster of

nanoparticles and increases their stability upon addition of $NaBH_4$, which is subsequently added to complete the reduction process. The reducing agent is then removed and the hydrophilic thiol **8** is added after being de-protected. The thiol exchanges with the dioctylamine resulting in the formation of a nanoparticle passivated with a monolayer of thiol **8**. The gold nanoparticles can then be extracted in aqueous solution leaving the hydrophobic amine and ammonium derivatives in the organic phase. The aqueous layer is subsequently washed with a number of organic solvents and further purified with size exclusion chromatography to give nanoparticles with a narrow size distribution. The synthetic protocol used is summarised in Figure 4.15. Using this procedure, 26.5 mg of Au NP were obtained and these were dissolved in 3 mL of MilliQ water and stored at 4 ^{o}C.

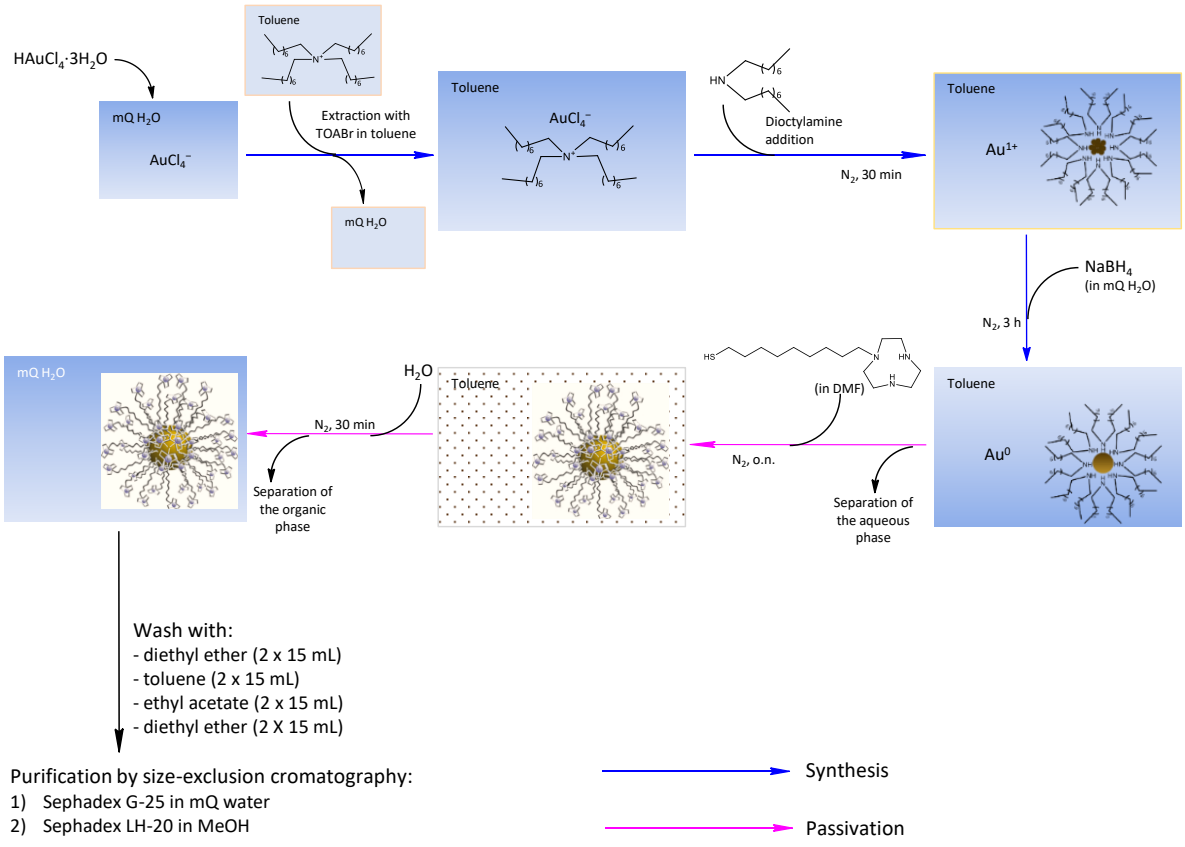

Figure 4.15: Schematic representation of the synthetic protocol used for the synthesis of the Au NP **1**•Zn^{2+}. Adapted from 59.

Experimental procedure for the synthesis of Au NP

Preparation of the nanoparticles.

$HAuCl_4 \bullet 3H_2O$ (96.7 mg, 0.25 mmol) was dissolved in 2 mL MilliQ water to provide an aqueous solution of Au(III) and transferred to a 250 ml separating funnel. A solution of tetraoctylammonium bromide (TOABr, 5.20 g, 9.51 mmol) was prepared in 250 mL of degassed toluene in a 250 mL round bottomed flask (degassed previously with nitrogen) and sonicated for 5 minutes. The TOABr solution was divided into three aliquots used to extract the aquoues solution of Au(III). $[AuCl_4^-]$ was thus transferred to the toluene organic phase, which thus turned red orange in colour. The fractions were combined in a 500 mL round-bottomed flask and stirred vigorously with a half-inch magnetic stirrer. Deprotection of the ligand was initiated at this point (see procedure above). Dioctylamine (3.85 mL, 12.7 mmol) was added to the solution with a plastic syringe which was then stirred vigourously under nitrogen for 30 minutes, resulting in progressive colour changes from red to yellow to green over a short period of time. A solution of $NaBH_4$ (92.5 mg, 1.96 mmol) in 2 mL MilliQ water was subsequently added under vigorous stirring resulting in the formation of gold nanoparticles, evident as brown colored agglomerates. The mixture was stirred for an additional three hours under nitrogen, after which the mixture was separated in a 250 mL separating funnel to discard the aqueous phase and to transfer the organic phase containing the nanoparticles to a 500 mL round-bottomed flask.

Passivation of the Nanoparticles with the Thiol

The deprotected HS-C9-TACN, **7** previously deprotected and obtained as a white solid, was dissolved in a minimum amount of DMF (1 mL) and added quickly to the organic phase, resulting in a decolorisation of the solution followed by the formation of a brown precipitate after some time. The suspension was stirred under nitrogen overnight.

Isolation, Purification and Characterisation of the Au NP **1**

A volume of 5 mL MilliQ water was added to the solution and the solution was stirred under nitrogen for an additional 30 minutes. The aqueous phase was separated as a dark layer and washed with diethyl ether (2 × 15 mL), toluene (2 × 15 mL) and ethyl acetate (2 × 15 mL). The resulting dark brown suspension was concentrated and purified in small portions through the use of a Sephadex G-25 column swollen in MilliQ water, collecting the middle fraction of nanoparticles. The resulting fractions were combined, concentrated under reduced pressure and purified through a Sephadex LH-20 column swollen in

methanol. The resulting solution was evaporated under reduced pressure to give 26.5 mg of solid, which was immediately dissolved in 3 mL of MilliQ water and stored at 4 ^{o}C. The nanoparticles were characterised by ^{1}H NMR, TEM, DLS and TGA analysis. The headgroup concentration was determined by fluorescence spectroscopy.

Au NP **1**•Zn^{2+} were obtained by mixing the Au NP **1** with $Zn(NO_3)_2$ in a 1:1 ratio.

4.4.4.2 Characterisation of gold nanoparticles

Structural and compositional analysis of the resulting monolayer protected nanoparticle was possible due to their excelling handling properties. Gold nanoparticles are usually deep-red in colour. UV-Vis spectroscopy is one of the most widely used methods for the characterization of nanoparticles. Au NPs with a core diameter less than 2 nm give a UV-Vis spectrum characterized by the absence of the surface plasmon resonance (SPR) band. The SPR band is the result of a characteristic absorption band which appears in the region of 520 nm for gold nanoparticles. This band is due to collective oscillations of the 6s electrons of the conduction band at the surface of the NPs.[54] Oscillations of the surface electrons are induced when incoming light frequency is resonant with the surface plasmon oscillation frequency, resulting in a consequnt polarization of the electron density to one surface of the particle and oscillation of the electron cloud in resonance with the light's frequency.[60] When the size of the nanoparticles decreases, the SPR band undergoes a blue shift and is broadened due to the onset of quantum size effects so that it is absent in nanoparticles of a core size less than 2 nm. The UV-Vis spectrum of the nanoparticles did not exhibit an SPR band, as shown in Figure 4.16.

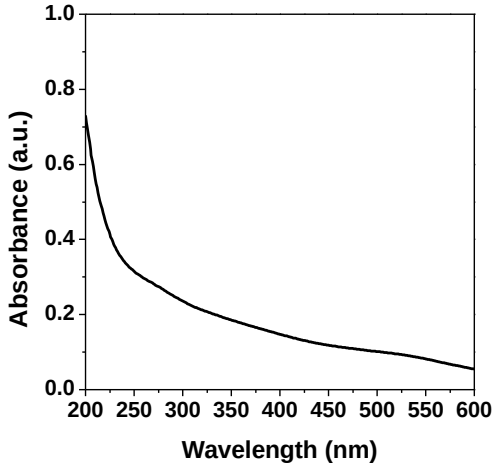

Figure 4.16: UV-Vis spectrum of Au NP **1**•Zn^{2+}.

Transmission electron microscopy, TEM is capable of providing a two dimensional picture of the Au NPs at the atomic level on account of the heavy metal gold core. This appears dark when contrasted with regions containing lighter atoms (such as carbon) with less scattered electrons. Thus, the image looks bright under in the most common bright field imaging mode. Nanopartices can be considered as spheres to a first approximation, and this enables them to be counted and their diameter estimated using common imaging software programs. The technique provides information about the nanoparticle core but the bound ligands are usually invisible using this technique. From TEM, it was determined that Au NP **1**•Zn^{2+} exhibited a core diameter of 1.4 ± 0.45 nm, which is in accordance with literature data (Figure 4.17).[42] Additional TEM images can be found in the supplementary information.

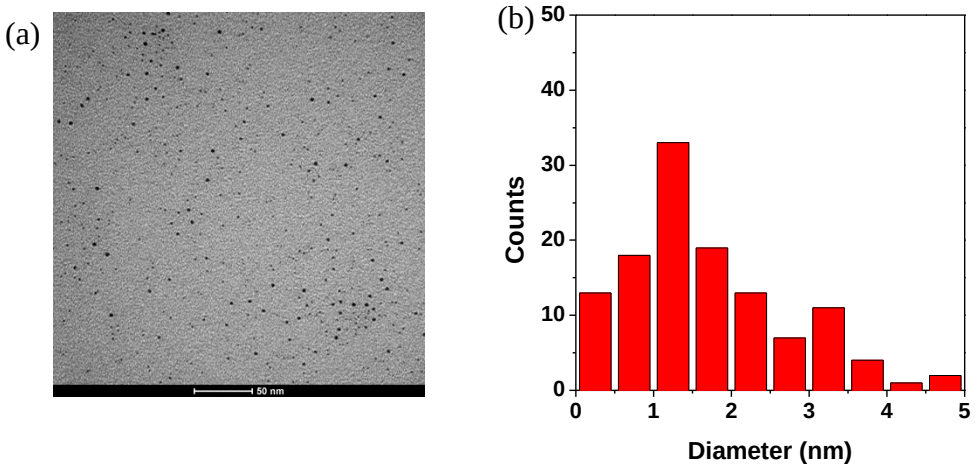

Figure 4.17: (a) TEM bright field mode micrograph of Au NP **1**•Zn^{2+} (scale bar 50 nm) (b) Au NP **1**•Zn^{2+} size distribution; average diameter 1.4 ± 0.45 nm.

The monolayer shell was then also analysed using multiple techniques. NMR spectroscopy gives information about the structure and chemical content of the monolayer. The ^{1}H resonances are broadened with respect to the free alkanethiols. This occurs due to spin-spin relaxational (T_2) broadening as well as due to a distribution in the chemical shifts because of differences in the Au-SR binding sites and due to a gradient in the monolayer packing density from near-core to the chain terminus, which is associated with dipolar broadening.[53] The ^{1}H NMR spectrum of the deprotected ligand on its own was obtained from a batch which was deprotected separately for analysis (Figure 4.18a). After attachment on the Au

NP (Figure 4.18b), it is evident that the peaks broaden significantly, providing unequivocal proof that the thiol is bound to the surface of the Au NP. The ^{1}H NMR spectrum of the ligand on the Au NP was further obtained upon applying a "longitudinal-eddy-current-delay" (LED) pulse sequence to differentiate molecules based on their diffusion coefficients (a diffusion filter) (Figure 4.18c). Comparision of the spectra obtained without (Figure 4.18b) and with (Figure 4.18c) the diffusion filter suggests that there is only minimal amount of unbound ligand in the final sample.

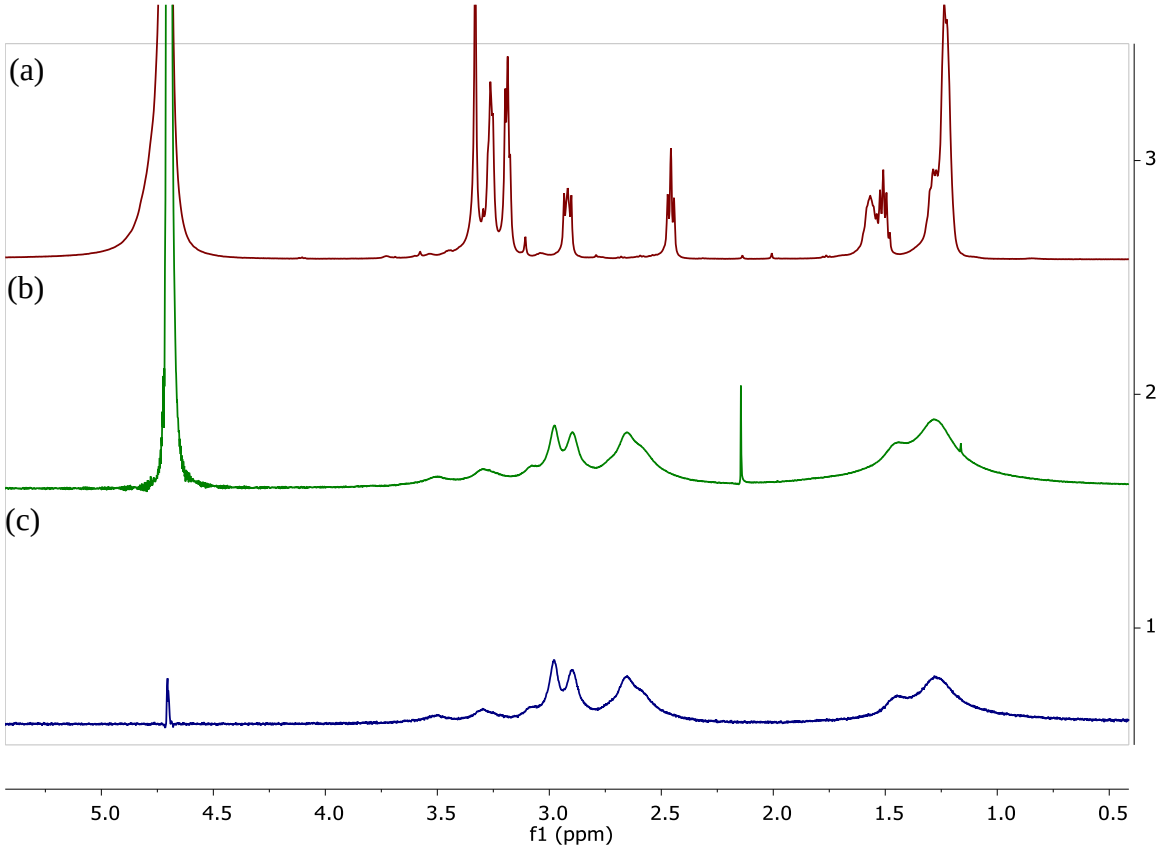

Figure 4.18: ^{1}H NMR spectrum of (a) the deprotected thiolated ligand and the ligand bound to the Au NP•**1**•Zn^{2+} (b) without diffusion filter and (c) with diffusion filter (D_2O, 300 K, 500 MHz).

DLS gives information about the overall hydrodynamic diameter of the nanoparticles while TGA gives information about the organic thiol coverage of the nanoparticles. The hydrodynamic diameter of the Au NP **1**•Zn^{2+} was determined to be 5.5 ± 1.4 nm (Figure 4.19), which is consistent with the diameter of the nucleus and twice the thiol length (ca. 1.7 mm).[42] TGA suggested that the weight loss, w_{loss} was 44.69%, which corresponds to the percentage organic content. The remaining 55.31% corresponds to the weight of the thermally stable gold core, w_{Au}.

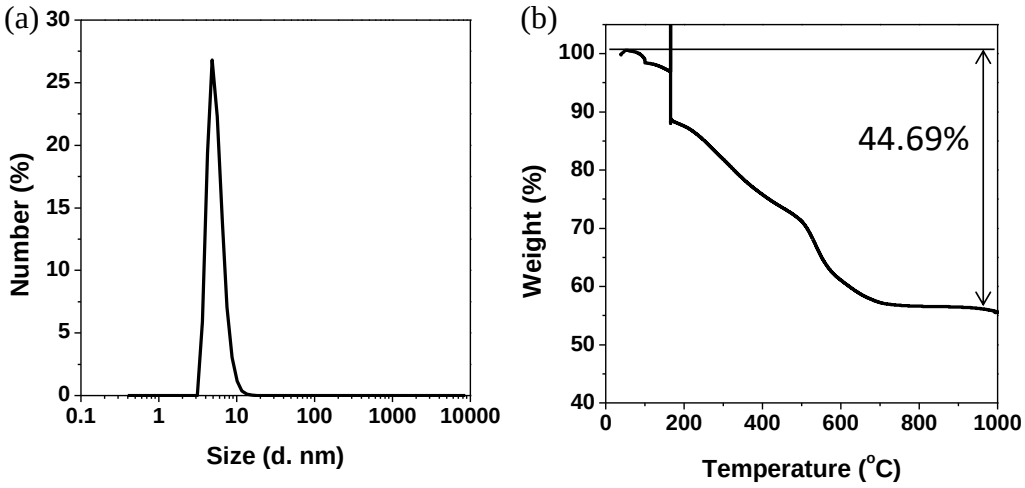

Figure 4.19: (a) DLS and (b) TGA spectrum of Au NP **1**•Zn^{2+}.

4.4.4.3 Determination of nanoparticle-bound TACN headgroup concentration

The headgroup concentration was determined by a fluorescence assay which exploits the ability of the positively charged Au NP **1**•Zn^{2+} to quench the fluorescence of negatively-charged fluorophores which are directly bound on the surface of the nanoparticles (Figure 4.20).[61] Oligoanions such as ATP have a strong affinity for the Au NP **1**•Zn^{2+} surface and binding occurs under saturation conditions even at low micromolar concentrations in aqueous media. Indeed, a fluorescent analogue of ATP, 2-aminopurine riboside-5'-o-triphosphate, ATP_f, **9**, binds the Au NP **1**•Zn^{2+} with a binding affinity of 2.4×10^8 M^{-1}.[12,62] The maximum amount of fluorophore which can be accomodated on the nanoparticle surface is defined as the surface saturation concentration (SSC). The Au NP **1**•Zn^{2+} quench the fluroescence of fluorophores up to the SSC. Above this value, the fluorophore remains free in solution and its fluorescence can be detected. The SSC of **9** has been determined to be 2.5 μM for a Au NP **1** concentration of 10 μM.[42]

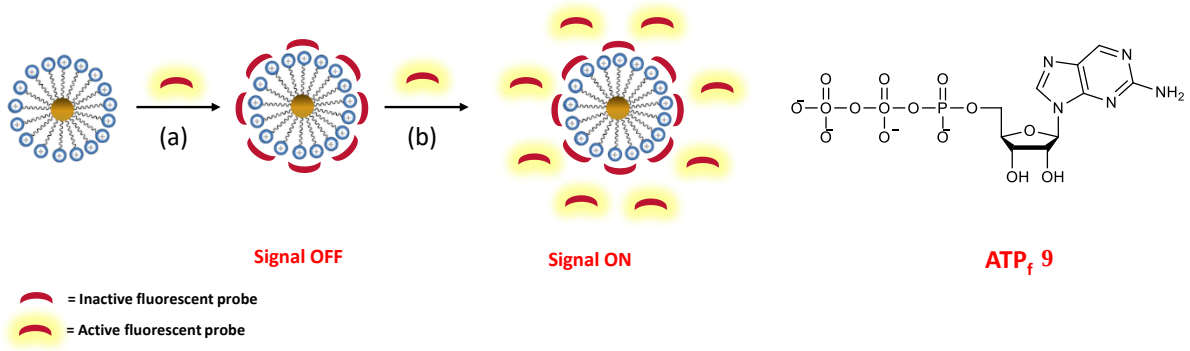

Figure 4.20: Schematic representation of the binding of a fluorescent probe on the surface of Au NP **1**•Zn^{2+} (a) until the SSC, where the fluorescence signal is off and (b) above the SSC, where the fluorescence signal is on. The structure of ATP_f, **9** as a fluorescence probe is also shown.

Approximate concentration of nanoparticle-bound TACN headgroup concentration

The approximate headgroup concentration was determined by titrating Au NP **1**•Zn^{2+} to a buffered solution of 2.5 μM **9** and 10 μM $Zn(NO_3)_2$. The concentration of **9** was determined by UV-Vis spectroscopy ([HEPES] = 10 mM, pH 7.0; λ = 254 nm, ε = 8000 M^{-1} cm^{-1}).[42] The fluorescence intensity of **9** ($\lambda_{ex}/\lambda_{em}$ = 305/370 nm, slit = 5/5 nm, 37 °C) was monitored after subsequent addition of Au NP **1**•Zn^{2+} in kinetic mode, allowing enough time for sample equilibration prior to noting the value of the fluorescence intensity (F.I.). The F.I. was plotted as a function of the added volume of Au NP **1**•Zn^{2+} to give a linear decrease in F.I. The linear part of the curve (y = ax+b where a = 23.901 and b = 501.127) was extrapolated to the value of F.I. = 0 to determine the volume of Au NP **1**•Zn^{2+} needed to give total quenching of the fluorescence (Equation 2). This value corresponds to the SSC of **9** on the Au NP **1**•Zn^{2+} and thus to [TACN] of 10 μM. The approximate concentration of the Au NP **1**•Zn^{2+} stock solution could thus be calculated as per Equation 3.

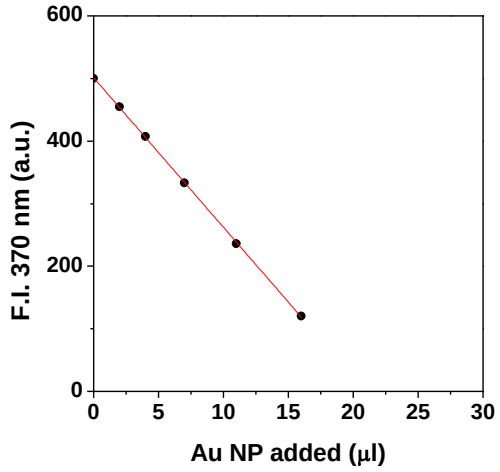

Equation	y = a + b*x		
Weight	No Weighting		
Residual Sum of Squares	14.26794		
Pearson's r	-0.99993		
Adj. R-Square	0.99983		
		Value	Standard Error
C3	Intercept	501.12658	1.21594
	Slope	-23.90149	0.14103

Figure 4.21: Determination of the approximate headgroup concentration in the Au NP **1**•Zn^{2+} stock solution by extrapolation of the calibration curve. [$Zn(NO_3)_2$] = 10 µM, [ATP_f] = 2.5 µM, [HEPES] = 10 mM, pH = 7.0; ($\lambda_{ex}/\lambda_{em}$ = 305/370 nm, slit = 5/5 nm, 37 °C).

$$V_{Au\ NP,FI=0} = \frac{b}{a} = \frac{501.127}{23.901} = 20.967$$

Equation 2

$$[\text{TACN}]_{\text{Au NP } \mathbf{TACN} \text{ stock s.}} = \frac{[\text{TACN}] \times V_{\text{TOT}}}{V_{\text{Au NP } \mathbf{TACN},\ \text{FI} = 0}} =$$

$$\frac{10 \times 10^{-6}\ \text{M} \times 1000\ \mu\text{L}}{20.967\ \mu\text{L}} = 0.00485\ \text{M} = 4.85\ \text{mM}$$

Equation 3

Accurate concentration of nanoparticle-bound TACN headgroup concentration

In order to determine the accurate concentration of nanoparticle-bound TACN headgroups, aliquots of an ATP_f, **9** solution of precisely-defined concentration (105.8 μM) were added consecutively to a buffered solution of Au NP **1**•Zn^{2+} at an assumed concentration of 10 μM ([HEPES] = 10 mM, pH 7.0; total volume: 1 mL). The F.I. was monitored following each addition in kinetic mode to ensure sample equilibration ($\lambda_{ex}/\lambda_{em}$ = 305/370 nm, slit = 5/5 nm, 37 °C). The F.I. was plotted as a function of the concentration of **9**. The F.I. remained near zero until the SSC was reached, after which a linear increase in the F.I. was noted. The linear part of the curve was extrapolated to the point where the F.I. was equal to 0. This gives the minimal concentration of **9** at which fluorescence quenching does not occur. Since this value corresponds to the SSC of Au NP **1**•Zn^{2+}, then it is equal to 2.5 μM. The titration was repeated several times, gradually modifying the assumed concentration of nanoparticle-bound TACN head groups until the value of the SSC of **9** was equal to 2.5 μM. From these calculations, the concentration of the Au NP **1**•Zn^{2+} stock solution was determined to be 3.1 mM.

(a) 4.0 mM

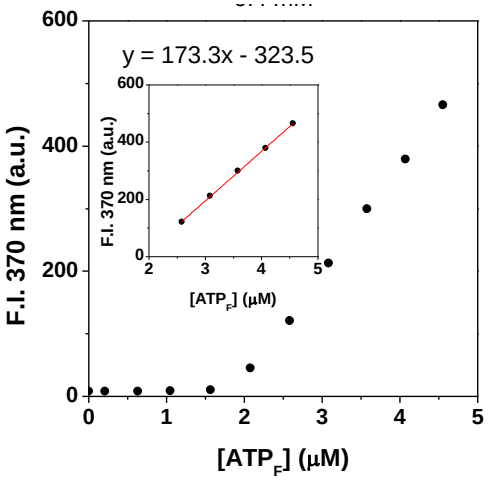

$$[ATP_F] = \frac{b}{a} = \frac{323.5}{173.3} = 1.87\ \mu M$$

(b) 3.3 mM

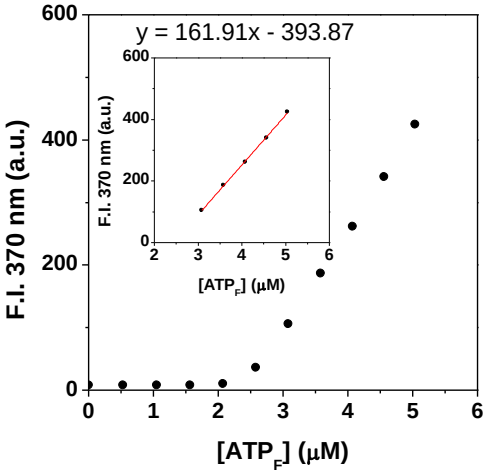

$$[ATP_F] = \frac{b}{a} = \frac{393.87}{161.91} = 2.43\ \mu M$$

(c) 3.1 mM

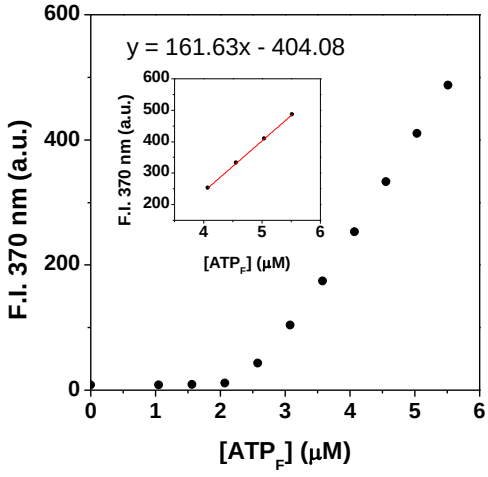

$$[ATP_F] = \frac{b}{a} = \frac{404.08}{161.63} = 2.50\ \mu M$$

Figure 4.22: Determination of the TACN headgroup concentration by extrapolating the linear part of the curve obtained upon consecutive additions of a solution of ATP_f, **9** to a solution of Au NP **1**•Zn^{2+} assuming a headgroup concentration of (a) 4.0 mM, (b) 3.3 mM and (c) 3.1 mM. [Au NP **1**•Zn^{2+}] = 10 μM, [HEPES] = 10 mM, pH 7.0; $\lambda_{ex}/\lambda_{em}$ = 305/370 nm, slit = 5/5 nm, 37 °C.

4.4.5 Quantification of results

The integrals were quantified against the standard $Na_3P_2O_5$. This showed a triplet at -21.16 ppm, corresponding to one phosphorus atom and a doublet at -6.42 ppm, corresponding to two phosphorus atoms. The latter peak was used for quantification. A 1 mM standard solution was prepared. The following reasoning was applied for quantification:

$$\int_i \alpha\, C_i . n_i$$

$$C_i \;\alpha\; \frac{\int_i}{n_i}$$

$$\frac{C_{STD}}{C_x} = \frac{\int_{STD}}{n_{STD}} . \frac{n_x}{\int_x}$$

$$C_x = C_{STD} . \frac{\int_x}{n_x} . \frac{n_{STD}}{\int_{STD}}$$

The $\int_{STD}$ is set to 1.

$$\text{Thus, } C_x = C_{STD} . \int_x . \frac{n_{std}}{n_x}$$

$$\text{In our case, } \frac{n_{std}}{n_x} = \frac{2}{1}$$

$$\text{Thus, } C_x = C_{STD} . \int_x . \frac{2}{1}$$

Where *C* = concentration,

n = number of phosphorus atoms

i = a general species,

x = an unknown

STD = standard

4.4.6 Monitoring the concentration of ATP over time in the presence of various conditions

The solution was typically prepared from appropriate stock solutions in an NMR tube. A volume of 500 μL buffered solution was prepared and NMR spectra were measured at appropriate time intervals. Each spectrum was acquired with 300 scans and a delay time of 5 s. The integrals due to the peak of the appropriate nucleotide was converted to concentration and plotted against time.

4.4.7 Kinetic model

The model was used to fit the data by varying kcatATP, kcatADP and kcatAMP, k2 and k4 while fixing k1 and k3. The model was implemented in Micromath Scientist for Windows, version 2.01:

```
// MicroMath Scientist Model File ATP hydrolysis
// E = Enzyme; A = Adenosine
IndVars: T
DepVars: ATP, ADP, AMP, P, E, ATOT, ETOT, ADPE, ATPE
Params: kcatatp, kcatadp, ATP0, ADP0, AMP0, P0, E0, ADPE0, ATPE0 k1, k2, k3, k4
ATP'=-k1*ATP*E+k2*ATPE
ATPE'= k1*ATP*E-k2*ATPE-kcatatp*ATPE
ADP'=kcatatp*ATPE-k3*ADP*E+k4*ADPE
AMP'=kcatadp*ADPE
ADPE'=k3*ADP*E-k4*ADPE-kcatadp*ADPE
E'=-k1*ATP*E+k2*ATPE+kcatatp*ATPE-k3*ADP*E+k4*ADPE+kcatadp*ADPE
//check
ATOT=ATP+ADP+AMP+ADPE+ATPE
ETOT=ADPE+E+ATPE
//initial conditions
T=0
ATP=ATP0
ADP=ADP0
AMP=AMP0
P=P0
ADPE=ADPE0
```

ATPE=ATPE0

E=E0

4.4.8 Titration of Au NP 1•Zn^{2+} to a solution of nucleotides

A volume of 400 μl solution was prepared containing 2 mM of the appropriate nucleotide, 10 mM HEPES buffer pH 7.0 and 10% D_2O. The ^{31}P NMR spectrum of the solution was taken. Au NP **1**•Zn^{2+} were then added to the solution, the solution shaken and the NMR spectrum obtained again. This was repeated with successive 50 μM aliquots of Au NP **1**•Zn^{2+} until no further shift was observed in the peaks of the nucleotides. The chemical shift of the peak of the nucleotide was plotted against the concentration of Au NP **1**•Zn^{2+} added.

4.5 References

(1) Singer, S. J.; Nicolson, G. L. *Science* **1972**, *175*, 720.
(2) Newth, D.; Finnigan, J. *Aust. J. Chem.* **2006**, *59*, 841.
(3) Carl Ivar Branden, J. T. *Introduction to Protein Structure*; 2nd Edition ed.; Garland Science, 1999
(4) Mann, S. *Angew. Chem., Int. Ed.* **2008**, *47*, 5306.
(5) Desai, A.; Mitchison, T. J. *Annu. Rev. Cell Dev. Biol.* **1997**, *13*, 83.
(6) Whitesides, G. M.; Grzybowski, B. *Science* **2002**, *295*, 2418.
(7) Grzybowski, B. A.; Wilmer, C. E.; Kim, J.; Browne, K. P.; Bishop, K. J. M. *Soft Matter* **2009**, *5*, 1110.
(8) Ashkenasy, G.; Hermans, T. M.; Otto, S.; Taylor, A. F. *Chem. Soc. Rev.* **2017**, *46*, 2543.
(9) Grzybowski, B. A.; Huck, W. T. *Nat. Nanotech.* **2016**, *11*, 585.
(10) Merindol, R.; Walther, A. *Chem. Soc. Rev.* **2017**.
(11) Rizzoli, S. O. *The EMBO journal* **2014**, *33*, 788.
(12) Pieters, G.; Cazzolaro, A.; Bonomi, R.; Prins, L. J. *Chem. Commun.* **2012**, *48*, 1916.
(13) Pieters, G.; Pezzato, C.; Prins, L. J. *Langmuir* **2013**, *29*, 7180.
(14) Bonomi, R.; Cazzolaro, A.; Prins, L. J. *Chem. Commun.* **2011**, *47*, 445.
(15) Pezzato, C.; Prins, L. J. *Nat. Commun.* **2015**, *6*.
(16) Chen, J. L. Y.; Maiti, S.; Fortunati, I.; Ferrante, C.; Prins, L. J. *Chem.–Eur. J.* **2017**, *23*, 11549.
(17) Coleman, J. E. *Annu. Rev. Biophys. Biomol. Struct.* **1992**, *21*, 441.
(18) Grzybowski, B. A.; Stone, H. A.; Whitesides, G. M. *Nature* **2000**, *405*, 1033.
(19) Lu, W.; Le, X.; Zhang, J.; Huang, Y.; Chen, T. *Chem. Soc. Rev.* **2017**, *46*, 1284.
(20) Hecht, S. *Nat. Nanotech.* **2015**, *11*, 6.
(21) Cheng, C.; McGonigal, P. R.; Schneebeli, S. T.; Li, H.; Vermeulen, N. A.; Ke, C.; Stoddart, J. F. *Nat. Nanotech.* **2015**, *10*, 547.
(22) Krabbenborg, S. O.; Veerbeek, J.; Huskens, J. *Chem.–Eur. J.* **2015**, *21*, 9638.
(23) Maiti, S.; Fortunati, I.; Ferrante, C.; Scrimin, P.; Prins, L. J. *Nat. Chem.* **2016**.
(24) Ragazzon, G.; Prins, L. J. *Nat. Nanotech.* **2018**.
(25) Traverso-Cori, A.; Mancilla, M.; Kettlun, A. M.; Valenzuela, M. A. In *Ecto-ATPases: Recent Progress on Structure and Function*; Plesner, L., Kirley, T. L., Knowles, A. F., Eds.; Springer US: Boston, MA, 1997, p 227.
(26) Kettlun, A. M.; Espinosa, V.; García, L.; Valenzuela, M. A. *Phytochemistry* **2005**, *66*, 975.
(27) Lee, K.-H.; Krezanoski, J. Z.; Eiler, J. J. *Proc. Soc. Exp. Biol. Med.* **1957**, *94*, 193.
(28) Komoszynski, M.; Wojtczak, A. *Biochim. Biophys. Acta* **1996**, *1310*, 233.
(29) Anna Kozakiewicz, P. N., Mariusz Banach, Michal Komoszynynski, Andrej Wojczak *Acta Biochimica Polonica* **2008**, *55*, 141.
(30) Valenzuela, M. A.; Kettlun, A. M.; Mancilla, M.; Calvo, V.; Fanta, N.; Traverso-Cori, A. *Phytochemistry* **1988**, *27*, 1981.

(31) Lakowicz, J., R. *Principles of Fluorescence Spectroscopy*; 3rd ed.; Springer: USA, 2006.
(32) Zaupa, G.; Mora, C.; Bonomi, R.; Prins, L. J.; Scrimin, P. *Chem.–Eur. J.* **2011**, *17*, 4879.
(33) della Sala, F.; Chen, J. L. Y.; Ranallo, S.; Badocco, D.; Pastore, P.; Ricci, F.; Prins, L. J. *Angew. Chem., Int. Ed.* **2016**, *55*, 10737.
(34) Neri, S.; Garcia Martin, S.; Pezzato, C.; Prins, L. J. *J. Am. Chem. Soc.* **2017**, *139*, 1794.
(35) Bonomi, R.; Cazzolaro, A.; Sansone, A.; Scrimin, P.; Prins, L. J. *Angew. Chem., Int. Ed.* **2011**, *50*, 2307.
(36) Guarise, C.; Manea, F.; Zaupa, G.; Pasquato, L.; Prins, L. J.; Scrimin, P. *J. Pept. Sci.* **2008**, *14*, 174.
(37) Pasquato, L.; Pengo, P.; Scrimin, P. *J. Mater. Chem.* **2004**, *14*, 3481.
(38) Lin, Y.; Ren, J.; Qu, X. *Acc. Chem. Res.* **2014**, *47*, 1097.
(39) Manea, F.; Houillon, F. B.; Pasquato, L.; Scrimin, P. *Angew. Chem., Int. Ed.* **2004**, *43*, 6165.
(40) Mertes, M. P.; Mertes, K. B. *Acc. Chem. Res.* **1990**, *23*, 413.
(41) Thordarson, P. *Chem. Soc. Rev.* **2011**, *40*, 1305.
(42) Pieters, G.; Pezzato, C.; Prins, L. J. *J. Am. Chem. Soc.* **2012**, *134*, 15289.
(43) Mancin, F.; Scrimin, P.; Tecilla, P. *Chem. Commun.* **2012**, *48*, 5545.
(44) Jurriaan Huskens (Editor), L. J. P. E., Rainer Haag (Editor), Bart Jan Ravoo (Editor) *Multivalency: Concepts, Research and Applications*; John Wiley & Sons: West Sussex, UK, 2018.
(45) Yohannes, P. G.; Plute, K. E.; Mertes, M. P.; Mertes, K. B. *Inorg. Chem.* **1987**, *26*, 1751.
(46) Hosseini, M. W.; Lehn, J. M.; Maggiora, L.; Mertes, K. B.; Mertes, M. P. *J. Am. Chem. Soc.* **1987**, *109*, 537.
(47) Papoyan, G.; Gu, K.-j.; Wiorkiewicz-Kuczera, J.; Kuczera, K.; Bowman-James, K. *J. Am. Chem. Soc.* **1996**, *118*, 1354.
(48) Bencini, A.; Bianchi, A.; Garcia-Espana, E.; Scott, E. C.; Morales, L.; Wang, B.; Deffo, T.; Takusagawa, F.; Mertes, M. P.; Mertes, K. B.; Paoletti, P. *Bioorg. Chem.* **1992**, *20*, 8.
(49) Bazzicalupi, C.; Bencini, A.; Bianchi, A.; Danesi, A.; Giorgi, C.; Lodeiro, C.; Pina, F.; Santarelli, S.; Valtancoli, B. *Chem. Commun.* **2005**, 2630.
(50) Jastrzębska, A.; Szłyk, E. *Chem. Pap.* **2009**, *63*, 414.
(51) Missoouri, USA; Vol. 2018.
(52) Manea, F.; Bindoli, C.; Polizzi, S.; Lay, L.; Scrimin, P. *Langmuir* **2008**, *24*, 4120.
(53) Templeton, A. C.; Wuelfing, W. P.; Murray, R. W. *Acc. Chem. Res.* **2000**, *33*, 27.
(54) Daniel, M.-C.; Astruc, D. *Chem. Rev.* **2004**, *104*, 293.
(55) Zhao, P.; Li, N.; Astruc, D. *Coord. Chem. Rev.* **2013**, *257*, 638.
(56) Jana, N. R.; Peng, X. *J. Am. Chem. Soc.* **2003**, *125*, 14280.
(57) Brust, M.; Walker, M.; Bethell, D.; Schiffrin, D. J.; Whyman, R. *J. Chem. Soc., Chem. Commun.* **1994**, 801.
(58) Faraday, M. *Philos. Trans. R. Soc. Lond., B, Biol. Sci.* **1857**, *147*, 145.
(59) Ceresara, E., University of Padova, 2017.
(60) Eustis, S.; El-Sayed, M. A. *Chem. Soc. Rev.* **2006**, *35*, 209.

(61) Dulkeith, E.; Morteani, A. C.; Niedereichholz, T.; Klar, T. A.; Feldmann, J.; Levi, S. A.; van Veggel, F. C. J. M.; Reinhoudt, D. N.; Möller, M.; Gittins, D. I. *Phys. Rev. Lett.* **2002**, *89*, 203002.

(62) McClure, W. R.; Scheit, K.-H. *FEBS Lett* **1973**, *32*, 267.

4.6 Appendix

4.6.1 Additional TEM images of gold nanoparticles for characterisation

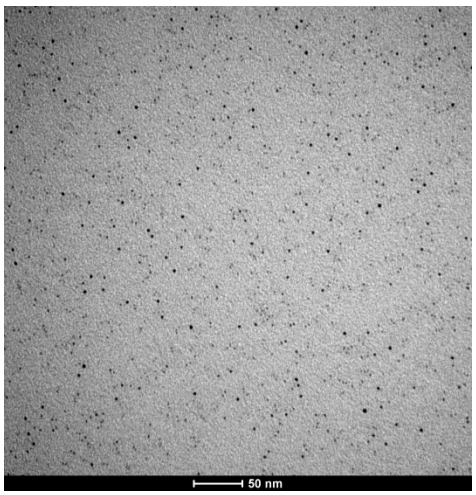

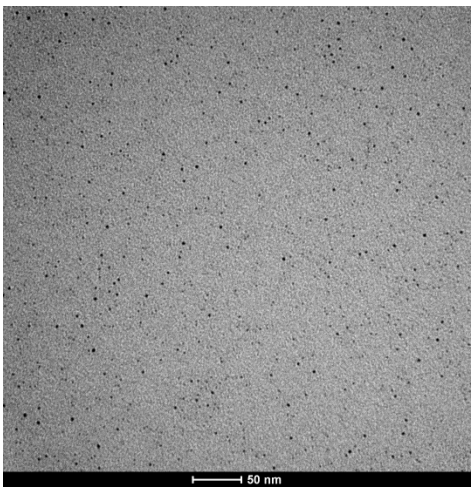

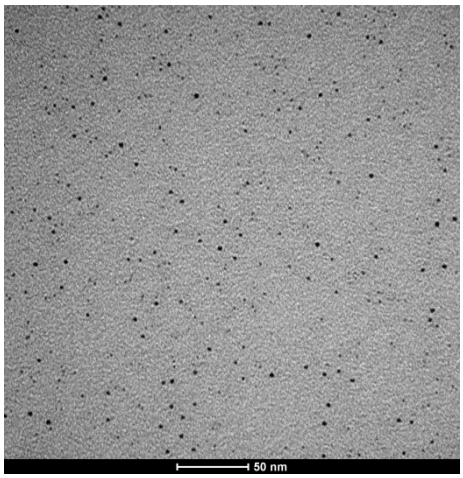

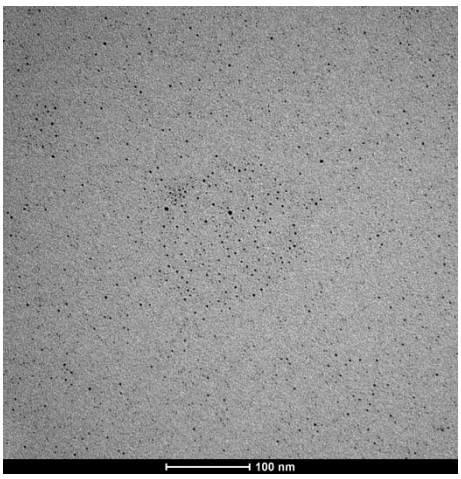

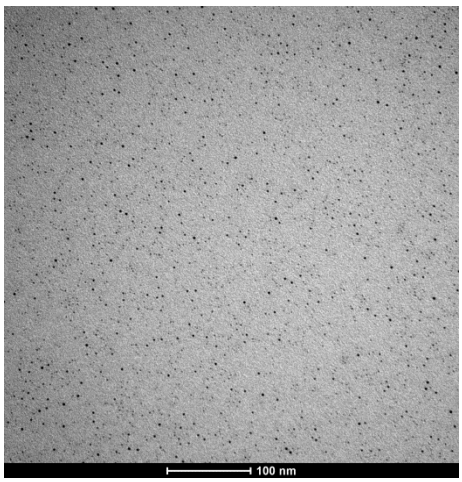

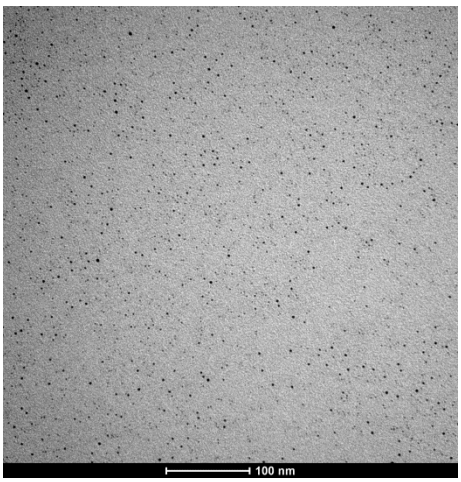

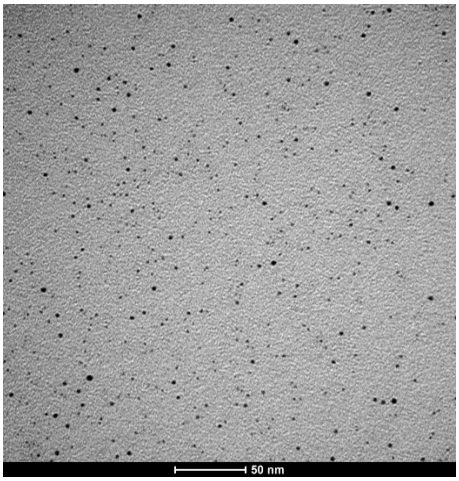
50 nm

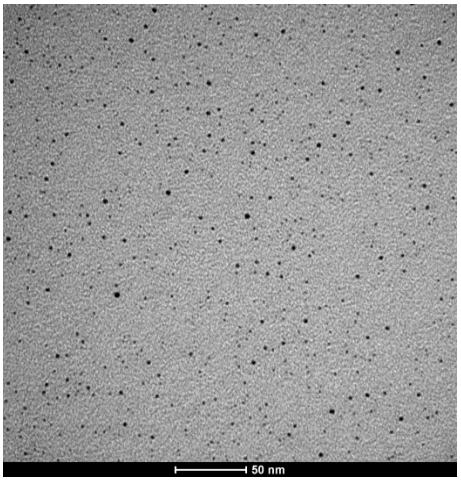
50 nm

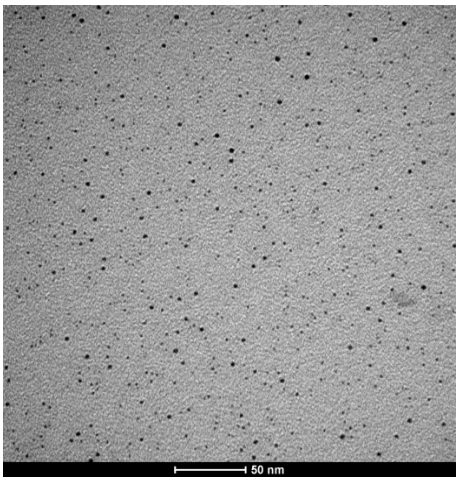
50 nm

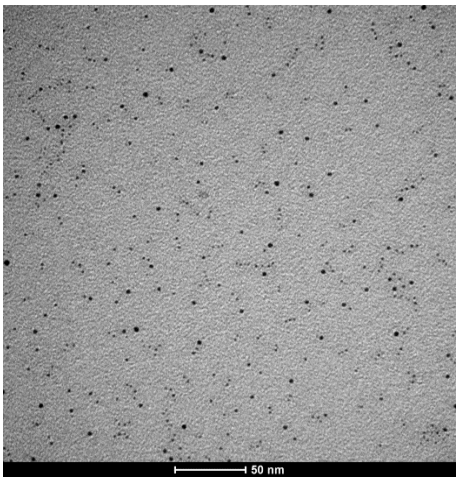
50 nm

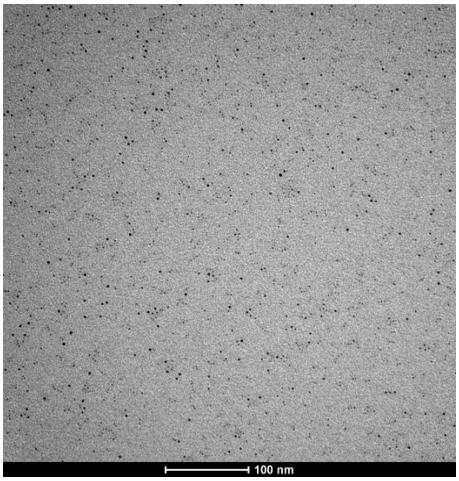
100 nm

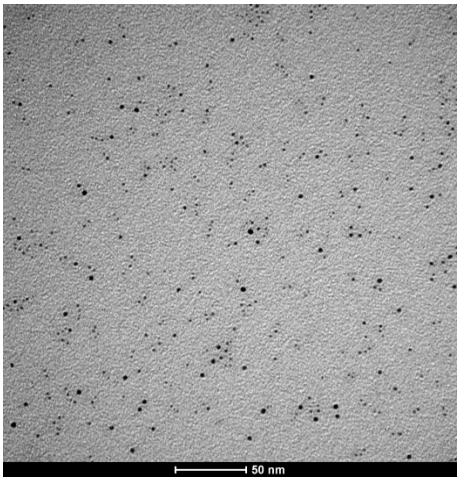
50 nm

Chapter 5

Transient Self-Assembled Aggregates Based on Cyclodextrin Vesicles and Nanoparticles

5.1 Introduction

Chemical reactions are typically carried out in solution between freely moving molecules, which allows frequent encounters. This is in contrast with what happens in nature, where reactions occur in confined spaces on a nanoscale level in a crowded environment.[1] Frequently, confinement is essential for the remarkable rate accelerations observed in enzymatic processes.[2]

Over the years, chemists have made various attempts at mimicking such nanoscale confined spaces and have investigated the reactivity of molecular guests within such spaces. It has been observed, for example, that the reactivity of molecules can be dramatically improved using nucleic acid templates, which enhances the effective molarities of bound reactants.[3,4] Numerous supramolecular and molecular hosts have been developed which are capable of influencing the chemical reactivity of reactants within them. Noteable examples of such reactions include the stabilisation of cyclic trimers of siloxanes[5] and of white phosphorus[6] and the introduction of unusual regioselectivities in the Diels-Alder reaction.[7] Various nanostructured materials have been investigated as mimics for such natural confined nanoreactors including zeolites[8,9] and other nanoporous materials,[10,11] hydrogels,[12] emulsion microdroplets,[13] lipidic cubic phases[14] and coacervate droplets.[15] Other groups have studied the reactivity of molecular guests inside nanosized pores formed from the self-assembly of inorganic nanoparticles into colloidal crystals.[16-20] However, many of these studies have been hampered by the slow diffusion of molecules in and out of such systems.[2]

Recently, the group of Klajn has developed dynamic reaction ‘nanoflasks’, which are formed through the self-assembly of azobenzene-functionalised inorganic nanoparticles upon

irradiation of the non-polar *trans*- isomer to the polar *cis*- isomer. This led to the formation of nanoparticle aggregates able to entrap polar reactants within the cavities. Entrapment led to a modulation of the chemical reactivity of these reactants.[1] The enhanced reactivity was transient in nature and could be interrupted by disaggregating the assembly with visible light irradiation. It was hypothesized that in this case trapping the reactants in the dynamic nanoflasks amends their reactivity. The advantage of Klajn's approach lies in its generality and can be applied to all systems where control of chemical reactivity is dependent on the dimensions and surface chemistry of the reaction vessel.[2]

In the present work we use gold nanoparticles passivated with thiols terminating with a positively charged 1,4,7-triazacyclononane (TACN)•Zn^{2+} headgroup, Au NP **1**, and negatively charged β-cyclodextrin vesicles containing carboxylate groups, β-CDV **2**, to develop a dynamic aggregating system which self-assembles under dissipative conditions (Figure 5.1).[21-23] These species are able to assemble as a result of electrostatic interactions and disassemble in the presence of a negatively charged competitor. The system is then used to modulate a chemical reaction. We further develop the principles of aggregation and dispersion with Au NP **1** and β-CDV **2** to design a system which is regulated by light.

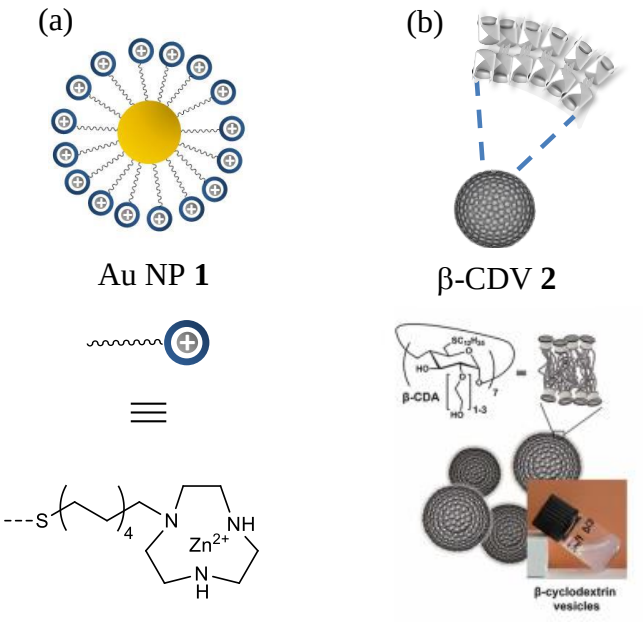

Figure 5.1: (a). Structure of gold nanoparticles covered with thiols ending with positively charged 1,4,7-triazacyclononane (TACN)•Zn^{2+} headgroups, Au NP **1**.[24] (b). Structure of the amphiphilic β-cyclodextrin vesicles, β-CDV **2**.[25]

5.1.1 Cyclodextrin vesicles

Cyclodextrins are cyclic oligo(α-(1-4)-glucopyranosides) consisting of 6-8 repeating glucose units (Figure 5.2).[26] They can be made to aggregate into bilayer vesicles by appropriate modification of the cyclodextrin core. In such bilayers the hydrophilic "headgroups" face water while the hydrophobic "tails" consisting of alkyl substituents are directed inwards. The bilayer encloses an interior consisting of an aqueous environment (Figure 5.2). The hydrophilic headgroups can be nonionic,[27-30] such as (poly(ethylene glycol), anionic,[31] such as sulfonate groups and cationic,[32] such as ammonium groups.

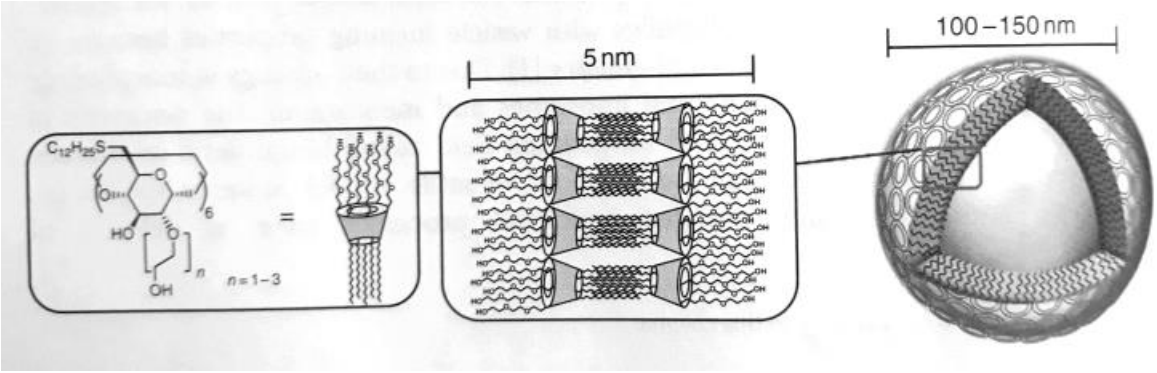

Figure 5.2: Molecular structure of amphiphilic cyclodextrin and the the assembly into vesicles.[33]

Cyclodextrin vesicles (CDV), have attracted a lot of interest due to their versatility. They have properties pertaining to liposomes,[34] they are capable of encapsulating water-soluble molecules inside their aqueous interior and they are capable of absorbing hydrophobic molecules inside the bilayer membrane.[35,36] β-CDVs are also capable of recognising and hosting guest molecules such as adamantane, ferrocene and bulky aromatics through inclusion in their surface cavities.[37] The binding constants for such interactions are in the order of 1.5-3.2 × 10^5 M^{-1}.[38] This implies that cyclodextrin (CD) vesicles can be functionalised easily with any group which has a hydrophobic anchor fitting inside the cavity of the CD. Addition of the guest to the aqueous solution of the vesicle will spontaneously decorate the CD surface through the formation of an inclusion complex.[33] This host-guest chemistry makes cyclodextrins a versatile model for the recognition of substrates by receptors on the surface of the cell membrane.[39-43] This, combined with their low toxicity, low cost of production and high availability has enabled them to find increasing applications in medicine,[44] material science[45] and catalysis[46] amongst others.

The host-guest chemistry of β-CDV **2** can be used to assemble molecules at the membrane surface, at the interface between a hydrophobic nanolayer and an aqueous environment. The high local concentrations of bound molecules are usually unmatched in homogenous solution. The interactions between CDVs and guests are often mediated by multivalent effects, making them stronger and more selective than their monovalent counterparts. Processes such as endo- and exocytosis and cell adhesion all involve aggregation/fusion of vesicular structures. It thus becomes possible to imitate aggregation, fusion and fission processes of membranes by attaching artificial binding motifs to β-CDV **2**, and such investigations can lead to a better understanding of complex natural cell-vesicle interactions.[33]

5.1.2 Adamantane as guest molecules for cyclodextrins

One very popular hydrophobic guest for CDVs is adamantane (Ad). Ad is complexed by β-CDV **2** with a high association constant of 3.2×10^4 M^{-1} at pH 7.2 at 25 ^oC.[47,48] Functionalisation of Ad with appropriate groups enables the vesicles to adhere and aggregate in aqueous solution with, for example, carbohydrates,[37,49] peptides[50,51] and guanidinium-carboxylate zwitterions.[52] In one noteable example, Förster resonance energy transfer (FRET) between a hydrophobic dye taken up into the membrane of β-CDV **2** (donor) and an Ad-functionalised acceptor fluorophore enabled the study of the dynamic multivalent molecular recognition in CDV.[53]

In another example, β-CDV **2** was mixed with an adamantyl-functionalized hydroxyethylcellulose (HED) polymer, **3** in dilute aqueous solution (< 2% organic matter). This resulted in aggregation and spontaneous formation of a hydrogel responsive to external stimuli (Figure 5.3a).[25] The gelation process was attributed to cross-linking upon formation of inclusion complexes with β-CDV **2**. Interestingly, the gel had self-healing and shear-thinning properties and could be pressed through a needle allowing it to be injected. The gel reformed after escaping the needle.

Ad groups covered with carbohydrates (maltose, mannose and lactose groups) were used to self-assemble a mimic of a glycocalix when added to β-CDVs **2** (Figure 5.3b).[49] Addition of lectins (proteins which bind to carbohydrates) resulted in selective aggregation; it was only possible to obtain aggregation if the lectins were added to a complimentary carbohydrate, i.e. the lectin peanut agglutinin bound to β-CDV **2** covered with lactose and concanavalin A (Con

A) bound to β-CDV **2** covered with mannose. This artificial system could thus mimic biological systems where multivalent interactions of lectins and carbohydrates aid the recognition and adhesion of cells. In another study, the multivalent interaction between cyclodextrin vesicles covered with mannose-adamantane conjugates containing one, two or three adamantane units as well as one or two mannose units and the lectin Con A was investigated. In this system, the cyclodextrin acts as the receptor for the Ad guest and thus the vesicle surface is covered with mannose. The mannose act as ligands for Con A, which induces agglutination because of multivalent cross-linking of the vesicles. The effective Ad concentration reflects the concentration of Ad units. Thus, a guest with two Ad units results in an effective adamantane concentration that is twice the concentration of the divalent guest while for a trivalent Ad, the effective concentration is three times the concentration of the guest.[37] It was found that di- and trivalent guests are capable of inducing cross-linking even in the absence of host and that the most efficient binder was a divalent guest with two mannose units; this was capable of inherantly binding to the β-CDV **2** surface as well as to Con A and was thus able to mediate fast agglutination at low overall concentration and low surface coverage.

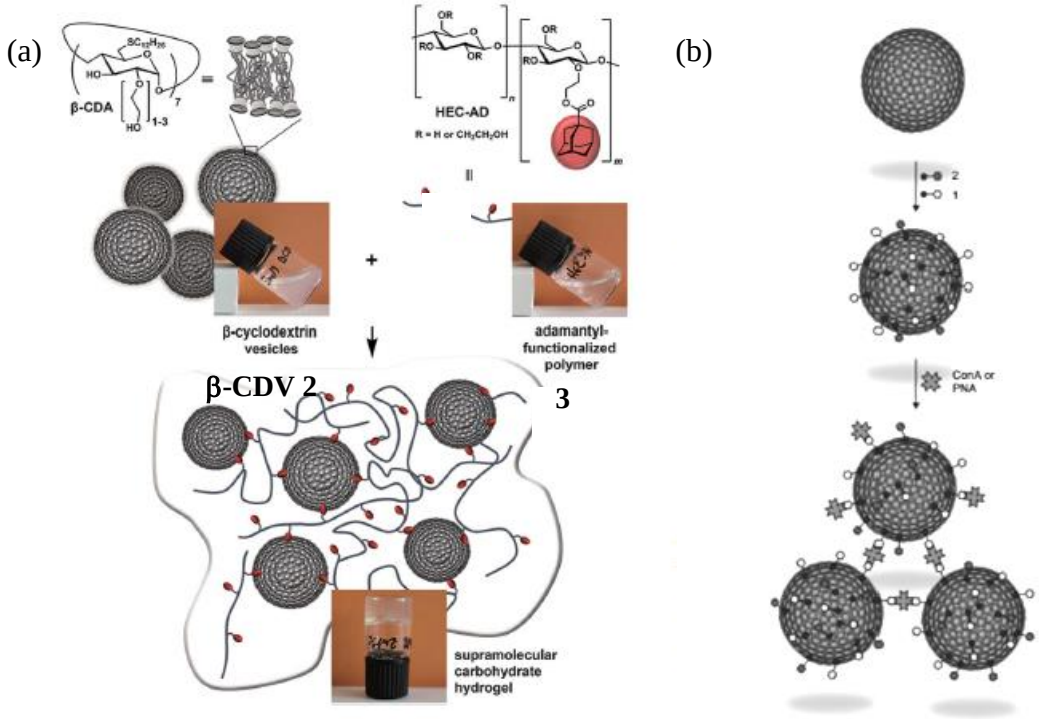

Figure 5.3: (a) Formation of a hydrogel when HEC-AD, **3** forms an inclusion complex with β-CDV, **2**.[25] (b) Agglutination of β-CDV **2** induced by the lectin Con A in the presence of maltose-adamantane conjugate.[49]

5.1.3 Arylazopyrazoles as guest molecules for cyclodextrins

Development of light-responsive systems is particulary attractive since light combines high spatio-temporal control, mild conditions, high efficiency and absence of potentially interfering additives.[54] The *cis-trans* isomerisation of azobenzenes has been exploited for the development of reversible aggregation studies with cyclodextrins.[36,55,56] The *trans*- isomers of azobenzenes are capable of binding to cyclodextrins, but the *cis*- isomers are not.[57] Studies were however limited by incomplete switching of the azobenzenes. This occurs because the *cis*- isomer has a local absorption maximum at 350 nm, so Vis light promotes the reisomerisation of the *cis*-isomer back to the *trans*- form. Ravoo's group have overcome this limitation of azobenzenes by using arylazopyrazoles (AAPs) as light-responsive molecular switches.[58] When a benzene group is substituted by a pyrazole group, this red shifts the n->π* band of the *Z*-isomer, and results in almost quantitative isomerisation from the *E*->*Z* isomer (UV light) or from the *Z*->*E* isomer (green light).

The Ravoo-group in Münster developed a series of AAPs which were water-soluble and functionalisable with carboxylate and/or fluorine atoms. The studied systems exhibited superior photoswitching characteristics with respect to azobenzenes, while maintaining water-solubility and the ability to be selectively complexed to the β-CDV **2** only in the *E*- form but not in the *Z*-form.[59] Generally, guests bind β-CDV **2** driven by hydrophobic interactions. Guests which are capable of optimally fitting and filling the host space maximise dispersion interaction. Additional hydrogen bonding is obtained when high energy water leaves the cavity and the solvation shell of the guest and becomes part of the bulk water.[60] These criteria can be satisfied for the *Z*-isomer but not for the *E*-isomer, which does not bind the β-CDV **2** due to steric hindrance and a change in polarity (Figure 5.4).[61] *E*->*Z* isomerisation can be obtained in AAPs upon irradiation with UV-Vis light at 365 nm while *Z* -> *E* isomerisation occurs upon irradiation with green light at 520 nm. Upon irradiation with UV-Vis light, the thermodynamically stable *E*-isomer is converted to the *Z*-isomer. The π-π* absorbance undergoes a blue shift and decreases in intensity while the n-π* absorbance increases in intensity and undergoes a red shift. Irradiation with green light results in a restoration of the original spectrum with more than 90% of intensity.[60]

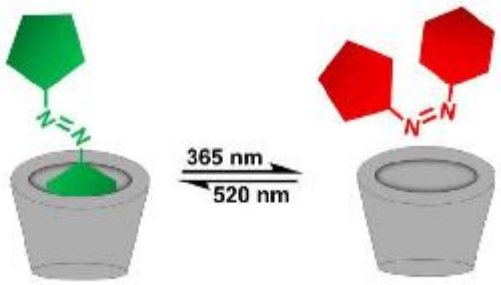

Figure 5.4: Schematic representation of the host-guest interaction between β-CDV **2** and AAPs in the *trans*- (green) and *cis*-(red) form.[60]

Arylazopyrazoles display excellent photophysical properties and almost quantitative photoisomerisation in both directions combined with very high thermal stability. Their properties can be modulated by using different substituents.[60] The AAP/CDV **2** motif was used to design several light-responsive systems and these displayed superior properties to those based on azobenzenes. Thus for example, aggregation studies could be carried out with AAPs functionalised with divalent amine groups, **4**-**6** (Figure 5.5). Two of the AAPs (AAP-**4** and AAP-**6**) were capable of undergoing *E* -> Z isomerisation with an almost quantitative efficiency of 94%. This could be attributed to the red shift of the n->π* bands of the *Z*-isomers. The AAPs **4**-**6** were incorporated into β-CDV **2** and into nanoparticles functionalised with β-CDV, **7**. Aggregation and disaggregation cycles could be induced by light irradiation and were monitored both by UV-Vis as well as by DLS. Both systems exhibited fully reversible light responsive aggregation/disaggregation behaviour over five cycles.

Other examples of systems based on AAPs include particle assemblies, DNA compaction and hydrogels (Figure 5.6).[54,61-65] In one example, AAPs were used as guests for upconversion cyclodextrin nanoparticles (UCNP), **8**. Irradiaton of **8** with NIR led to emission by **8** at 350 nm. The emission triggered the isomerisation of *trans*-AAP to *cis*-AAP. In another system, positively charged AAPs could simultaneously bind CDV **2** and DNA through hydrophobic and electrostatic interactions, respectively. Irradiation with Vis light converted the *cis*-isomer back to the *trans*-isomer over seven hours, and this was exploited for medicinal purposes.[61] Light-induced isomerisation from *trans*- to *cis*-AAP led to the release of the DNA cargo with higher efficiency than for a similar azobenzene-based system.[54] AAPs were also

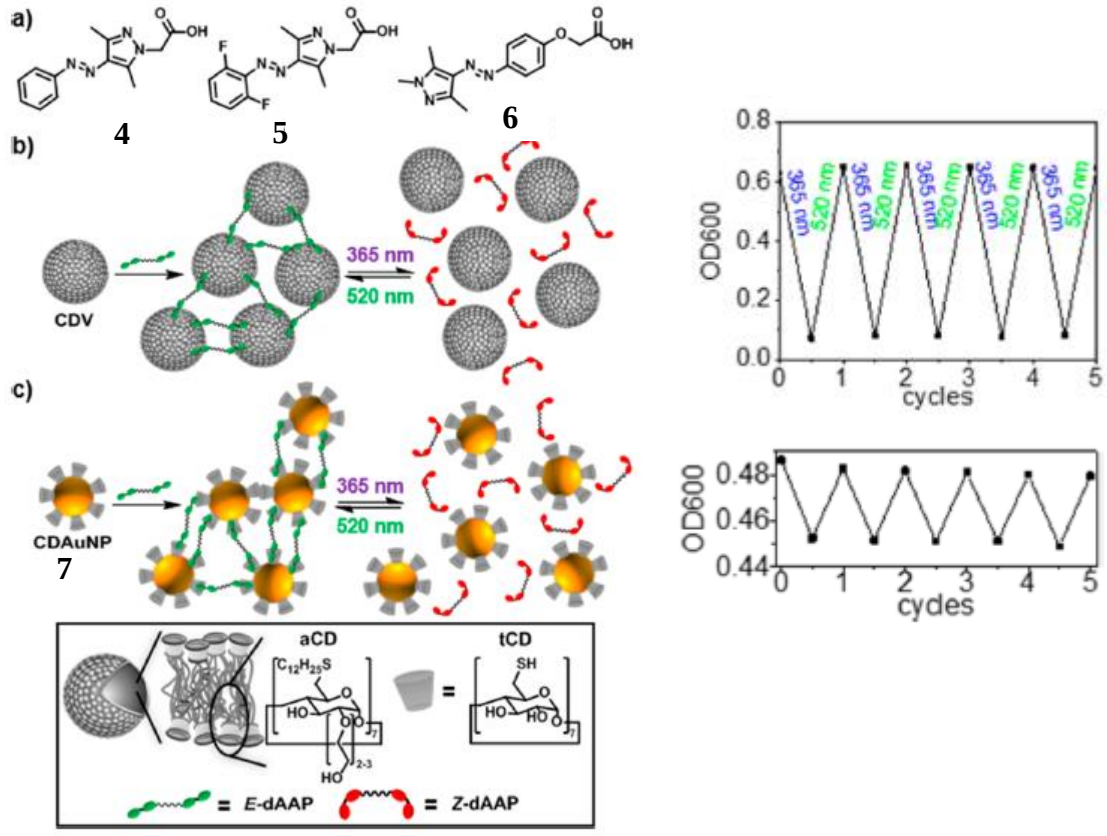

Figure 5.5: (a) Molecular structure of AAP, **4**-**6** and schematic representation of AAP and CD-based supramolecular systems including (b) β-CDV **2** and (c) CD embedded on nanoparticles, **7**. The corresponding OD600 graphs illustrate the optical density at 600 nm upon irradiation for 10 minutes.

incorporated in DNA and used as photoswitches to regulate DNA duplex hydridization. The system showed better results than a previous azobenzene-based system, with a low number of incorporations per base pair, good thermal stabilities and a red-shifted response *trans*-wavelength.[64] In yet another example, AAPs added to a hydrogelating peptide sequence and a supramolecular hydrogel gel was formed upon mixing with β-CDV **2**. These could function as multivalent non-covalent cross-linkers only when the AAP was in the *trans*- state. It was thus hypothesized that the gelation process involved both the entanglement of the self-assembled supramolecular peptides and additional host-guest interactions between the AAP and β-CDV **2**. Light-sensitive gelation was used to release both a dye as well as the cyclodextrin vesicles from the gel into solution.[63] More recently, AAPs have also been used as guests for other host molecules such as cucurbit[8]urils[66] and were also incorporated into surfactants to produce light-switchable foams.[67]

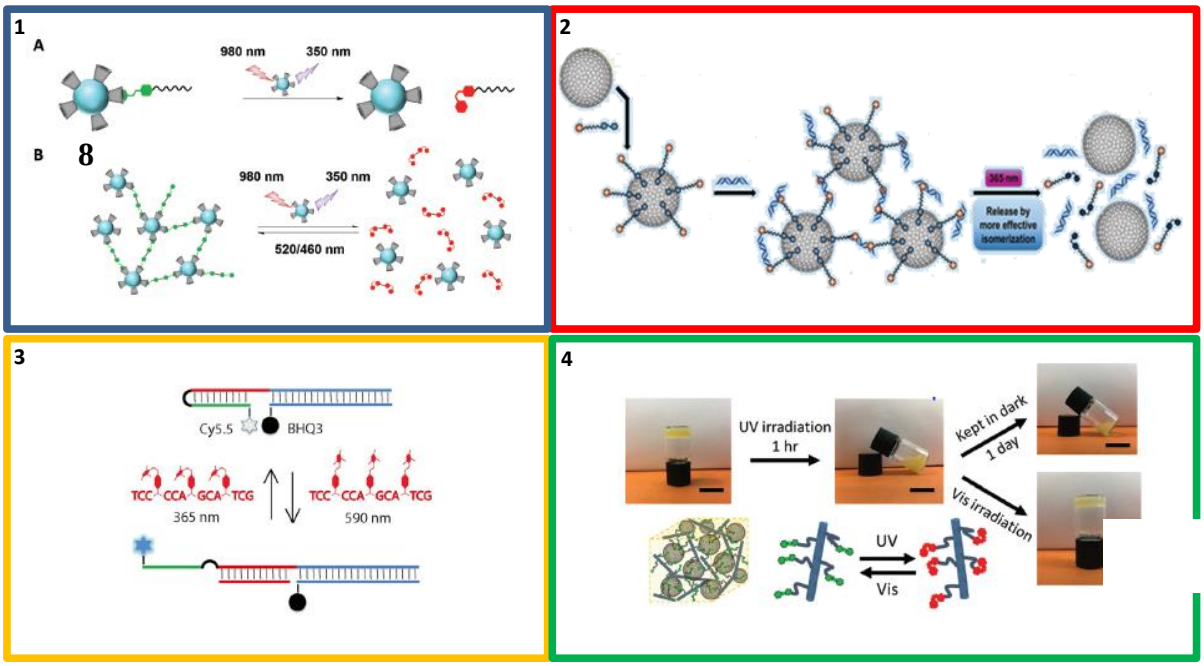

Figure 5.6: Examples of work involving light-switchable AAP-cyclodextrin complexes. (**1**). A. Host-guest complexation of AAP-based ligand in the cavity of UCNP **8** and release after NIR irradiation. B. Aggregation experiment using AAP-linker and UCNP **8**. (**2**). Capture and light-stimulated release of DNA from complexes using AAPs as a molecular switch. (**3**). Reversible DNA opening and closing with AAP-modified peptide sequences. (**4**). Reversible photoswitching of a supramolecular hydrogel.

5.2 Dynamic self-assembling nanoreactors based on transient aggregation of β-cyclodextrins and nanoparticles

In this project, the ability of β-CDV **2** to host negatively charged host guests will be used to assemble a dynamically aggregated system based on electrostatic interactions. The amphiphilicity of β-CDV **2** arises from hydrophobic *n*-dodecyl chains on one end and hydrophilic oligo(ethylene glycol) groups on the opposite end of the macrocycle (Figure 5.1b).[68] The negative charge of β-CDV **2** is increased using a carboxylate-containing Ad, **9** as a guest (Figure 5.7). Ad **9** consists of a phenylcarboxylate functionalised with two alkoxy chains ending with an Ad group. The Ad groups act as guests for the β-CDV **2** due to hydrophobic interactions. The carboxylate groups of **9** interact electrostatically with the positively charged gold nanoparticles developed in the group of Prins and co-workers, Au NP **1**, described in Chapter 4 (Figure 5.1a) and lead to aggregation of the β-CDV **2** (Figure 5.7a).

ATP is negatively charged and has a high affinity for Au NP **1** on account of the presence of multiple phosphate-groups that can coordinate to the TACN.Zn^{2+} complexes. Previous studies

have indeed shown that the nanoparticles preferentially bind phosphates rather than carboxylates.[69] Consequently, it is expected that upon addition of ATP, the Au NP **1** preferentially bind ATP instead of the vesicles, resulting in deaggregation (Figure 5.7b).

Dissipative conditions are installed when an additional process releases the chemical energy stored in ATP, which removes the stabilising interactions between the Au NP **1** and the ATP. The enzyme potato apyrase has been demonstrated to hydrolyse ATP into AMP and two molecules of inorganic phosphate Pi.[21] These waste products are singly charged and exhibit a reduced affinity for the nanoparticle surface.[21] The interaction between Au NP **1** and the β-CDV **2** becomes prominent once again and this restores aggregation (Figure 5.7c). Cycles of aggregation and disaggregation can be generated by periodic fresh addition of ATP, until the accumulation of waste products makes the assembly unfavourable.

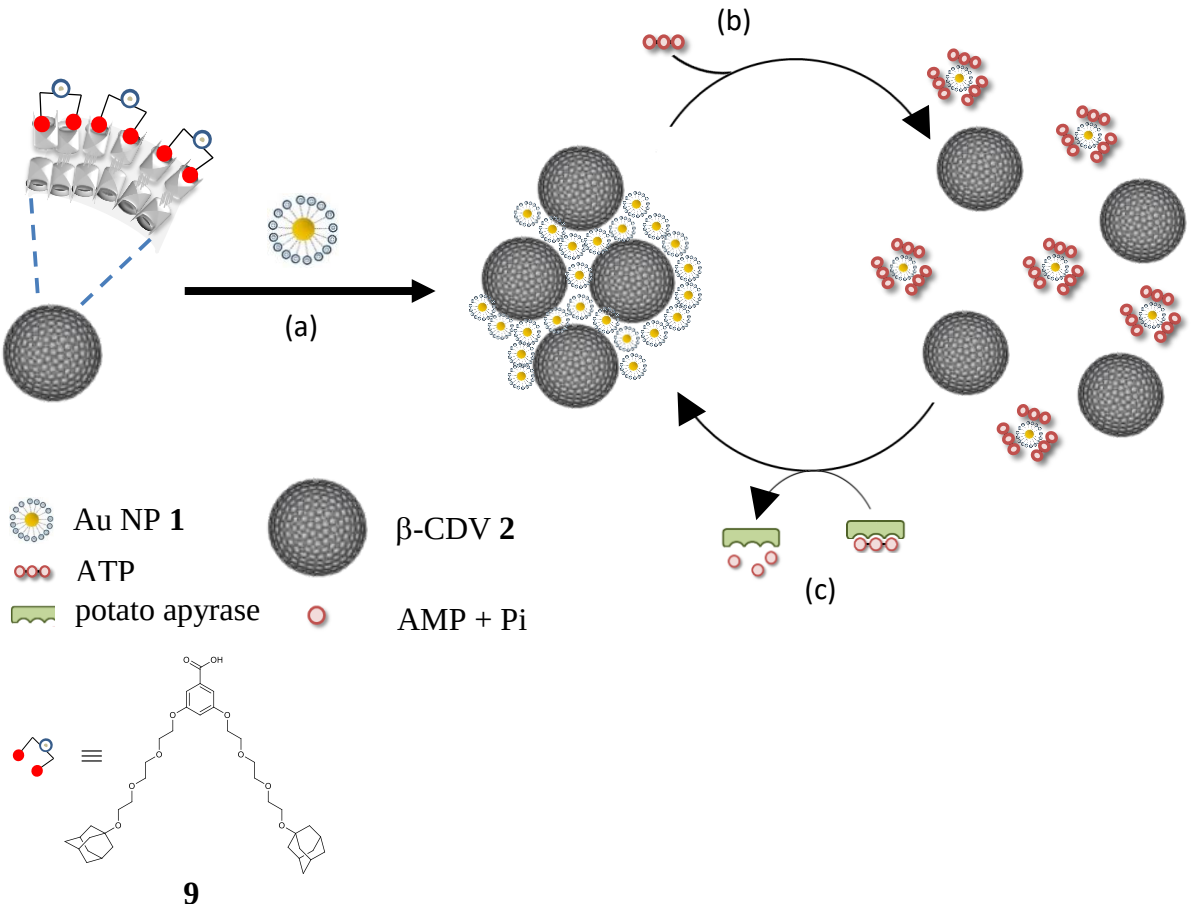

Figure 5.7: Structural representation of the system to be developed. The negatively charged **9** can be hosted by the β-CDV **2**. Addition of Au NP **1** leads to the aggregated state whereby several Au NP **1** surround the larger β-CDV **2**. Addition of ATP results in the preferential interaction between ATP and the Au NP **1** and this results in dispersion of the aggregate. Potato apyrase can however hydrolyse ATP to AMP and inorganic phosphate, Pi, which do not bind Au NP **1** well. The attractive electrostatic interactions between Au NP **1** and β-CDV **2** are restored, resulting in aggregation once again. Cycles of aggregation and disaggregation can be maintained by the fresh addition of ATP as the chemical fuel.

5.2.1 Aggregation/disaggregation cycles induced by the interaction between gold nanoparticles and adamantane-functionalised cyclodextrin vesicles under dissipative conditions

5.2.1.1 Cyclodextrin vesicles covered with carboxylate-containing adamantane

β-CDV **2** were prepared from cyclodextrin amphiphiles as described in literature.[38] A thin film cast was prepared by evaporation from an organic solution, hydrated and subsequently extruded through a 100 nm polycarbonate membrane to afford unilamellar bilayer vesicles with a homogenous size of around 67 nm, as determined by DLS. In the presence of **9** (100% decoration of vesicles), the β-CDV **2** had a similar size with a better distribution (Figure 5.8a). β-CDV **2** invariably carry a slight negative charge of -7.3 ± 0.9 mV at neutral pH as determined by ξ-potential measurements. The ξ-potential of β-CDV **2** significantly increases upon binding of the guest, **9** (-36.3 ± 0.8 mV) (Figure 5.8b). This indicates that the surface of the β-CDV **2** is covered with a high density of **9**. The host-guest interaction between β-CDV **2** and **9** was analysed by ITC assuming a 2:1 binding model. A binding constant in the order of 10^{-4} M^{-1} was calculated, which is typical for adamantane-cyclodextrin binding.[38]

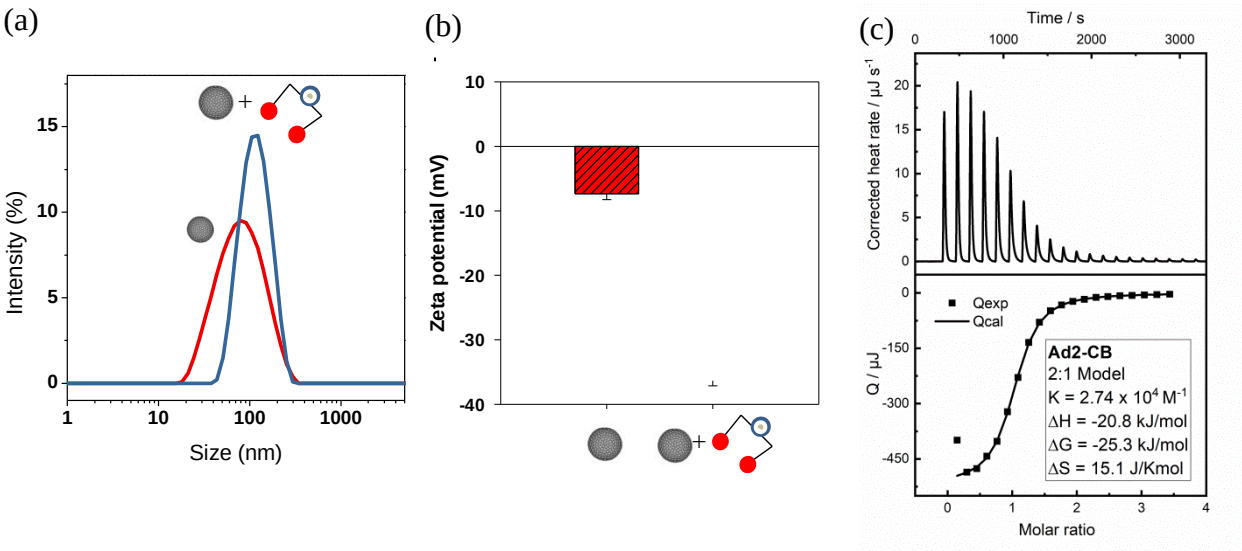

Figure 5.8: DLS (a) ξ-potential, (b) and ITC titration graph with the corresponding 2:1 fit (c) of β-CDV **2** in HEPES buffer pH 7.0 and upon addition of **9**.

5.2.1.2 Aggregation in the presence of nanoparticles and disaggregation with ATP

We initially wanted to test whether the addition of Au NP **1** to CDV **2** resulted in aggregation. Aggregation was monitored by time-dependent optical density measurements at 600 nm (OD600). Increasing aggregation was indeed observed as evidenced by an enhancement in the OD600 (Figure 5.9a). Free **9** did not induce aggregation of β-CDV **2**, as evident from the lack of increase in the OD600 (i). Addition of Au NP **1** to β-CDV **2** without any **9** resulted in a slight increase in the OD600, suggesting that β-CDV **2** on its own can also form an aggregate with Au NP **1** (ii). This is not surprising considering the slight negative charge on the β-CDV **2**. However, when Au NP **1** was added to β-CDV **2** covered with **9**, β-CDV **2●9**, a much stronger increase in the OD600 (iii+iv) was observed, implying a higher tendency to aggregate.

The next step was to investigate what happens upon the addition of ATP (Figure 5.9b). There was no effect on the OD600 upon addition of ATP to free **9** (i), but a slight decrease was noted when ATP was added to the aggregate formed between uncomplexed β-CDV **2** and Au NP **1** (ii). Addition of ATP to the β-CDV **2●9**, on the other hand, resulted in a much more significant decrease in the OD600 (iii), suggesting a much higher degree of disaggregation. As a control, without the addition of ATP, the OD600 of the system containing Au NP **1** and β-CDV **2●9** continued to increase as function of time (iv). The aggregation upon addition of Au NP **1** to the CDV **2●9** and the corresponding disaggregation upon addition of ATP could be observed with the naked eye; two separate cuvettes, both containing β-CDV **2**, **9** and Au NP **1** were set aside. Only the second cuvette contained ATP (Figure 5.9c). After two hours it was possible to observe large aggregates in the cuvette containing the Au NP **1** and β-CDV **2**. On the other hand, the cuvette to which ATP was added was visibly clearer .

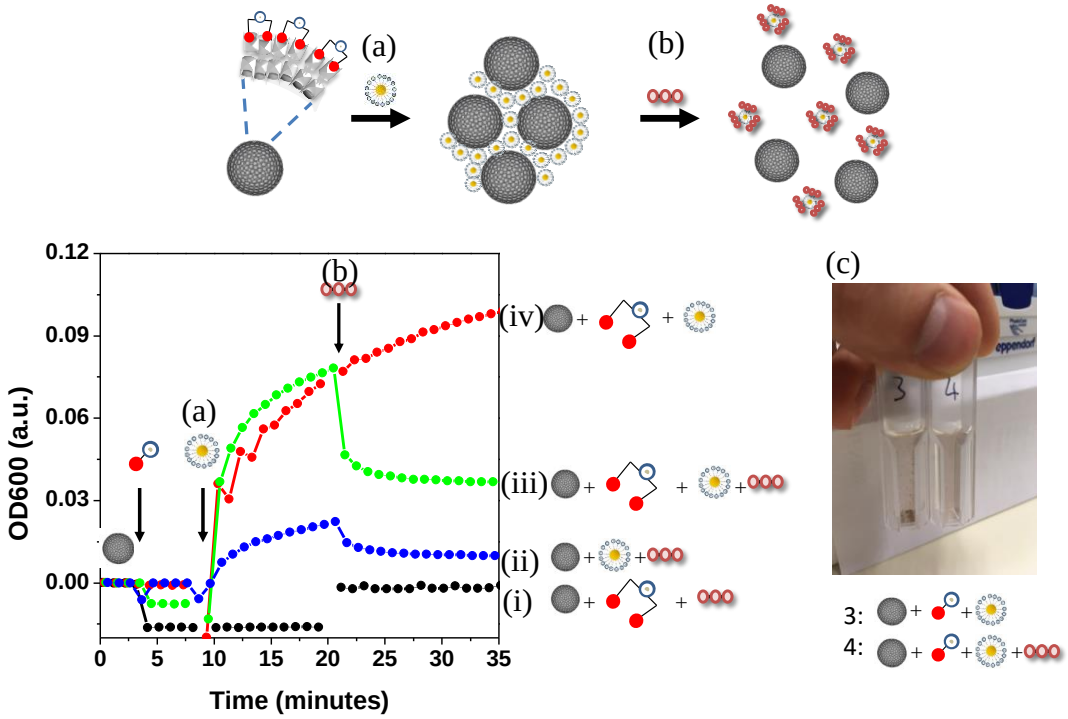

Figure 5.9: Study of aggregation and disaggregation upon addition of (a) Au NP **1** and (b) ATP to (i) the free **9**, (ii) the free β-CDV **2** and ((iii)+(iv)) the β-CDV **2** covered with **9**. (c). Observation of aggregation in cuvettes in the absence (**3**) and presence (**4**) of ATP. [Au NP **1**] =30 μM, [β-CDV **2**] = 20 μM, [ATP] = 20 μM, [HEPES] = 10 mM, pH 7.0.

The increase in OD600 upon addition of Au NP **1** to β-CDV **2** was dependent upon the amount of Au NP **1** added. Increasing amounts of Au NP **1** were added to β-CDV **2•9** and, after each addition, the OD600 was allowed to stabilise to a plateau value (0-20 minutes) (Figure 5.10a). The stabilised OD600 was plotted against Au NP **1** concentration (Figure 5.10b). A non-linear relationship between the variables was observed. Interestingly, aggregation increased only slowly with Au NP **1** concentrations up to 13 μM. This was followed by a sudden enhancement in the OD600 when the Au NP **1** concentration was increased between 13 and 15 μM. Further increase in Au NP **1** concentration did not significantly affect the maximum OD600 obtained. This suggested that a concentration of Au NP **1** higher than 15 μM was required in order to obtain maximal aggregation. In a control experiment, the background OD600 of Au NP **1** increased linearly with increasing Au NP **1** concentration, as expected according to Beer's law.

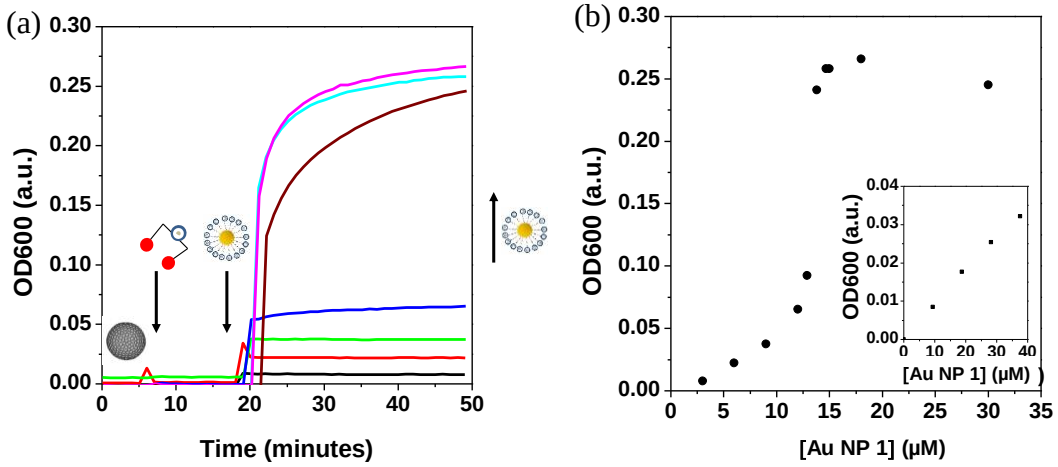

Figure 5.10: (a). Graph illustrating the increase in the OD600 upon addition of increasing [Au NP **1**] to β-CDV **2** and **9**. (b) A plot showing the final value of the OD600 as a function of [Au NP **1**]. Inset shows the linear increase in OD600 of the blank containing increasing [Au NP **1**]. Values are uncorrected for the absorbance of the [Au NP **1**]. [β-CDV **2**] = 20 μM, [**9**] = 5 μM, [HEPES] = 10 mM, pH 7.0.

The disaggregation induced by the addition of ATP was also dependent on the ATP concentration. Adding increasing amounts of ATP to aggregated β-CDV **2•9** resulted in a deeper drop in the OD600 (Figure 5.11). Initial additions of ATP led to large effects while subsequent additions resulted in a less dramatic decrease in the OD600, suggesting that the maximum dissociation level was approached. Since significant disaggregation was evident even with 5 μM ATP, it was decided to perform further experiments with this concentration of ATP.

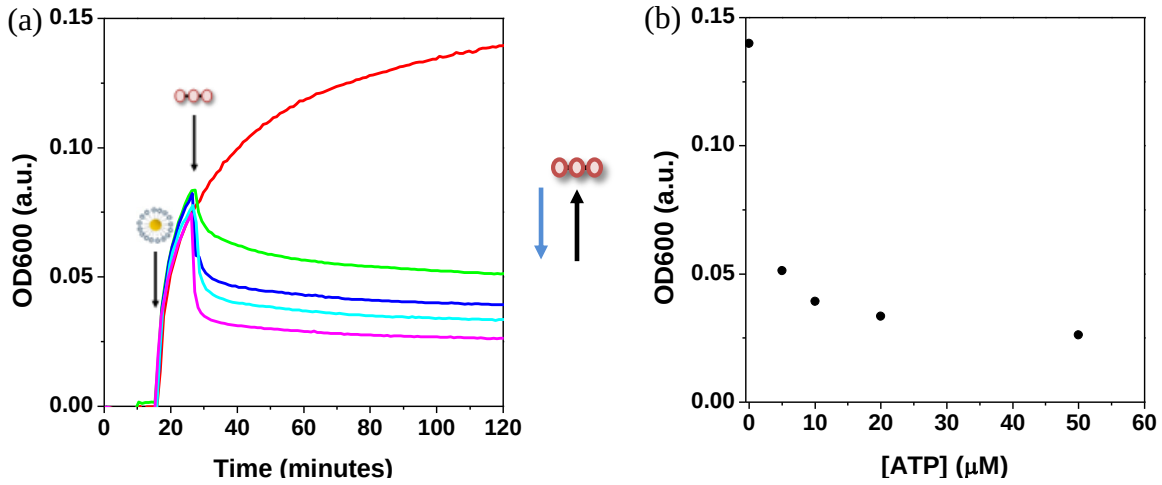

Figure 5.11: (a). A kinetic profile showing the variation in the OD600 upon addition of increasing [ATP] to β-CDV **2** covered with **9** to which Au NP **1** have been added. (b). A plot showing the OD600 at time = 120 minutes as a function of [ATP]. [β-CDV **2**] = 20 μM, [9] = 5 μM, [Au NP **1**] = 30 μM, [HEPES] = 10 mM, pH 7.0.

Further evidence for the aggregation and disaggregation processes was obtained using fluorescence and optical microspectroscopy (Figure 5.12). The fluorescent dye NBD-cholesterol, **10** was incorporated in β-CDV **2** conferring a bright green fluorescence. Au NP **1** quenches the fluorescence of **10**, so that the sample darkened upon addition of Au NP **1** to β-CDV•**9**. However, small patches of bright fluorescence could still be observed by careful observation. Addition of ATP to the solution resulted in the preferential binding of the ATP to the Au NP **1**, releasing some Au NP **1** from the aggregates. An increase in the fluorescence was evident. Optical microscopy images clearly showed the presence of aggregates upon addition of Au NP **1** to β-CDV **2•9**. Aggregates were also observed upon addition of ATP. This is understandable since the amount of ATP added was not sufficient to result in total dissociation of the aggregate. TEM spectroscopy also showed the presence of large aggregates upon addition of β-CDV **2•9** to Au NP **1** (Figure 5.13).

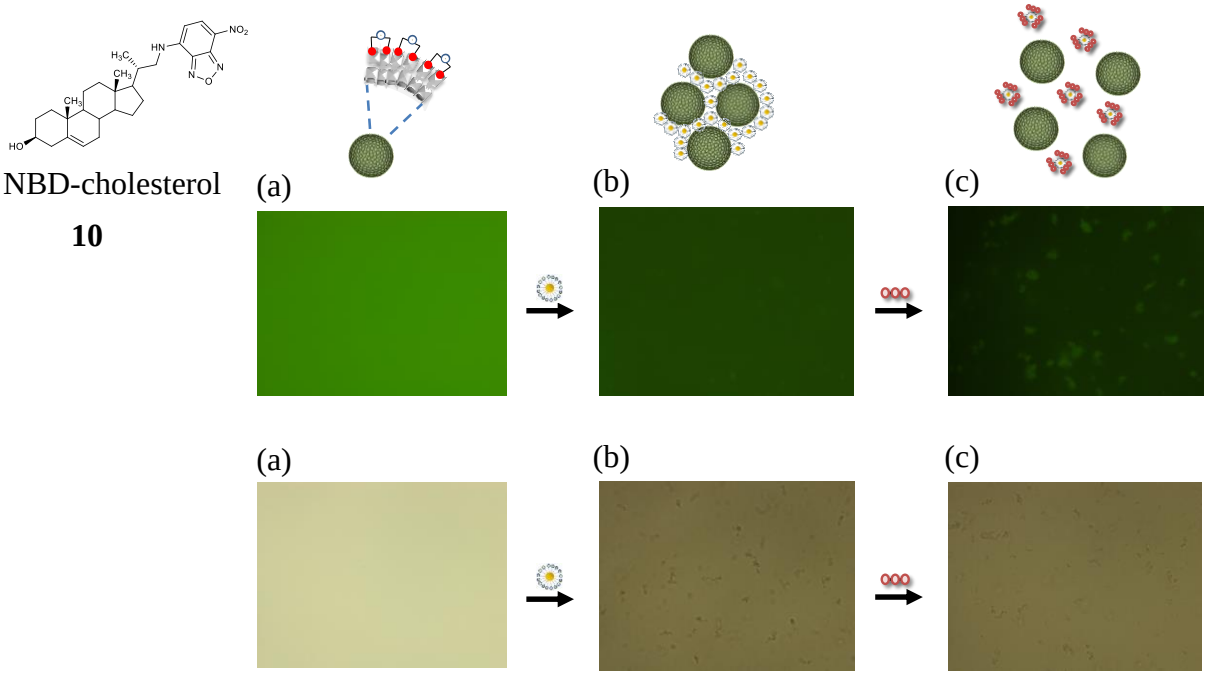

Figure 5.12: Figure showing fluorescence (top) and optical (bottom) microscope images for (a) the β-CDV **2** incorporated with NBD-cholesterol, **10**, (b) upon addition of Au NP **1** and (c) upon further addition of ATP. [β-CDV **2**] = 100 μM, [**9**] = 25 μM, [Au NP **1**] = 50 μM, [HEPES] = 10 mM, pH 7.0.

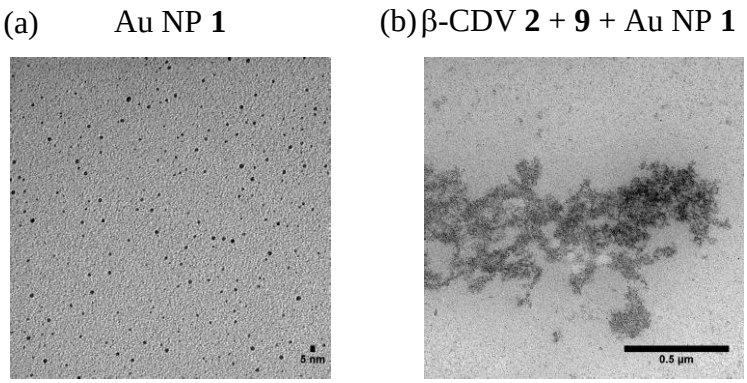

Figure 5.13: TEM images of Au NP **1** (a) on their own (b) in the presence of β-CDV **2** covered with **9**. [β-CDV **2**] = 100 µM, [**9**] = 25 µM, [Au NP **1**] = 50 µM, [HEPES] = 10 mM, pH 7.0.

5.2.1.3 Re-aggregation in the presence of potato apyrase

Addition of different concentrations of potato apyrase to the disaggregated state (the system obtained after adding ATP to the β-CDV **2●9**-Au NP **1** aggregates) causes the hydrolysis of ATP to AMP and Pi. These waste products have a much lower affinity for the Au NP **1**. In this situation, the binding of the Au NP **1** to β-CDV **2●9** becomes preferred again, restoring the aggregated state (Figure 5.7c). This was evident as an increase in the OD600 following a delay period when the potato apyrase was added (Figure 5.14). As expected the OD600 increased at a faster rate as the enzyme concentration increased.

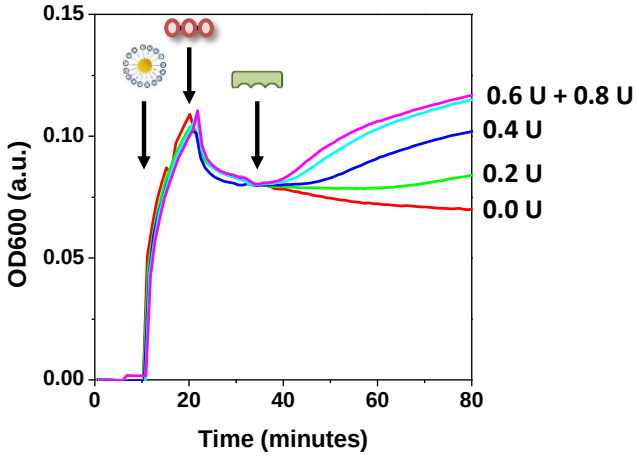

Figure 5.14: Figure showing the restoration of aggregation upon addition of increasing concentration of the potato apyrase to the disaggregated state (the β-CDV **2●9** to which Au NP **1** and ATP were added). [Au NP **1**] =30 µM, [β-CDV] = 20 µM, [ATP] = 20 µM, [HEPES] = 10 mM, pH 7.0, [potato apyrase] = 0.0 – 0.8 U.

Having established that cleaving ATP by potato apyrase restores the aggregated state, the experiment was repeated under dissipative conditions. The enzyme (0.8 U) was incorporated in the system at the start of the experiment. It was observed that the presence of enzyme did not affect the aggregation between Au NP **1** and β–CDV **2•9** complex. When the system was appreciably aggregated, ATP was added to the system. Addition of ATP initially caused the system to disaggregate but the OD600 started to increase again after some time as ATP was hydrolysed. The cycle could be repeated by re-addition of ATP (Figure 5.15a). Subsequent cycles were less efficient, possibly due to the accumulation of waste products in the system.[22] As a control, when the waste products of ATP hydrolysis, AMP and Pi, were added to the system, the OD600 continued to increase until the aggregates were large enough to precipitate (Figure 5.10b). This is consistent with previous studies which show that the waste products of ATP hydrolysis do not have a high affinity for the Au NP **1**.[21]

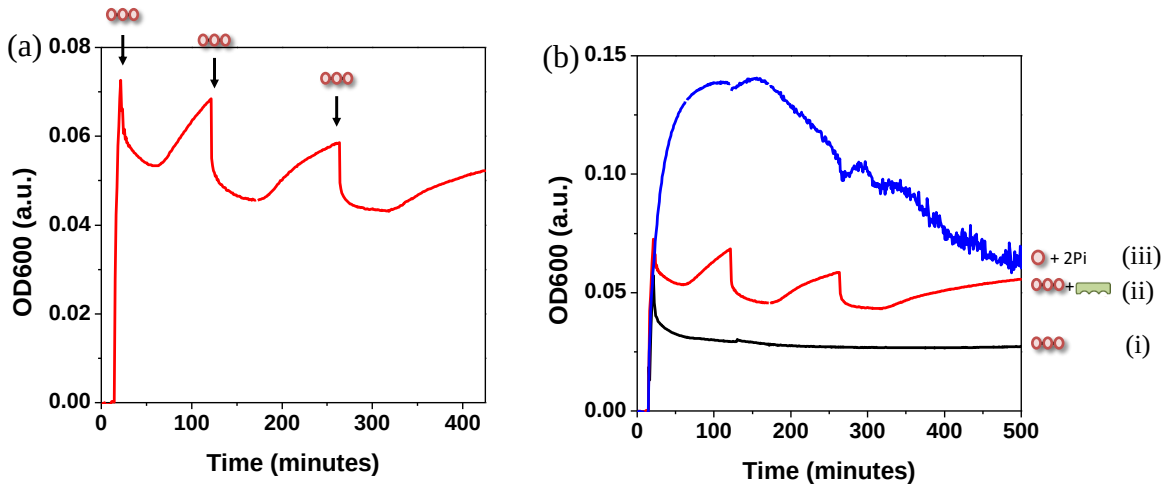

Figure 5.15: (a). Repeated addition of ATP in a system containing β-CDV **2** covered with **9**, ATP and potato apyrase. Addition of ATP results in de-aggregation and a decrease in the OD600. The hydrolysis of ATP releases the Au NP **1** for binding with the β-CDV **2** once again, and the system re-aggregates. The process could be repeated by the re-addition of ATP. (b). Comparison of the kinetic profile curves obtained in the case where ATP was added in the absence of the enzyme (i), ATP was added in the presence of the enzyme (ii), and when the waste products AMP (one equivalent) and Pi (two equivalents) were added in the absence of the enzyme (iii). [β-CDV **2**] = 20 μM, [**9**] = 5 μM, [ATP] = 5 μM, [potato apyrase] = 0.8 U, [HEPES] = 10 mM, pH 7.0.

Potato apyrase is usually activated using divalent metal ions, and the best activity is documented with calcium ions at 5 mM.[70] In our system the enzyme was active despite the absence of the calcium ions (see Chapter 4). However, we wanted to investigate whether the efficiency of the disaggregation process could be enhanced by Ca^{2+} (Figure 5.16a). This was

indeed found to be the case and re-aggregation occured much faster in the presence of 0.25 mM Ca^{2+}. This is in agreement with the results described in Chapter 4, which showed that Ca^{2+} is a better activator of potato apyrase compared to Au NP **1**. The addition of Ca^{2+} on its own in the absence of the apyrase was not capable of inducing re-aggregation. Under these conditions, it was possible to cycle the system six times in one day, without saturating the system (Figure 5.16b).

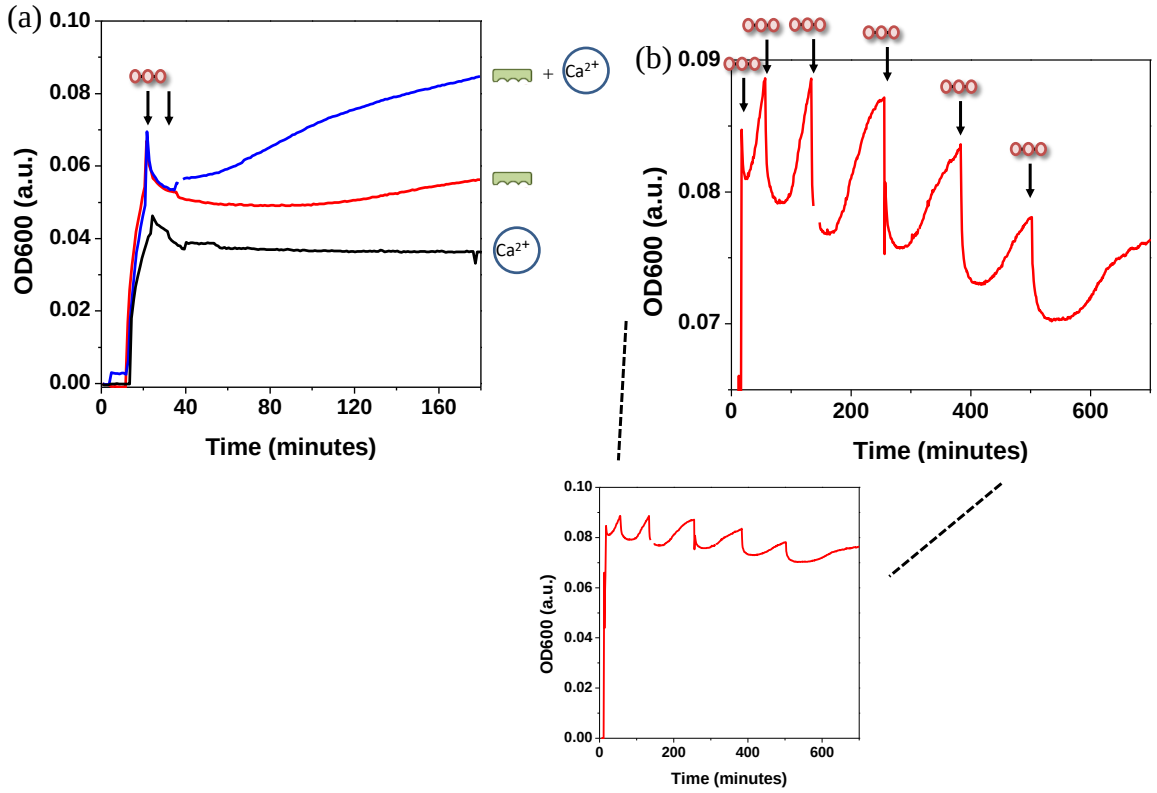

Figure 5.16: (a). Comparison of kinetic profile obtained when ATP was added to β-CDV **2** covered with **9** in the presence of (i) 0.25 mM Ca^{2+} (ii) 0.8 U potato apyrase and (iii) 0.8 U potato apyrase and 0.25 mM Ca^{2+}. (b). Kinetic profile obtained for the aggregation/disaggregation process upon repeated additions of ATP to β-CDV **2** covered with **9** in the presence of 0.25 mM Ca^{2+} and 0.8 U potato apyrase to which Au NP **1** were added. [β-CDV **2**] = 20 µM, [**9**] = 5 µM, [ATP] = 5 µM, [potato apyrase] = 0.8 U, [Ca^{2+}] = 0.25 mM, [HEPES] = 10 mM, pH 7.0.

In summary, we have developed a system which transiently aggregates under dissipative conditions. Addition of Au NP **1** to the adamantane-covered β-CDV **2** results in the aggregation of the vesicles. Addition of ATP disrupts the aggregate and causes de-aggregation. Hydrolysis of ATP through the action of the enzyme potato apyrase restores the attractive forces between

Au NP **1** and β-CDV **2●9** leading to transient de-aggregation under dissipative conditions. The cyle can be repeated again upon a fresh addition of ATP.

5.2.2 Exploiting aggregation as confined spaces for promoting chemical reactions

Aggregation of Au NP **1** and β-CDV **2** generates confined spaces which may be exploited to perform a function. We speculated that the increased effective molarity upon trapping reactants during the aggregation process with Au NP **1** could provide a distinct nanoporous environment which could potentially enhance chemical reactivity with respect to the bulk solution.[1] We decided to investigate the nucleophilic aromatic substitution reaction between 1-octanethiol (C8-SH, **11**) and 4-chloro-7-nitrofurazan (NBD-Cl, **12**) to give NBD-SC8, **13** (Scheme 4.1) which has been reported to occur preferentially in hydrophobic environments such as those provided by vesicles.[22]

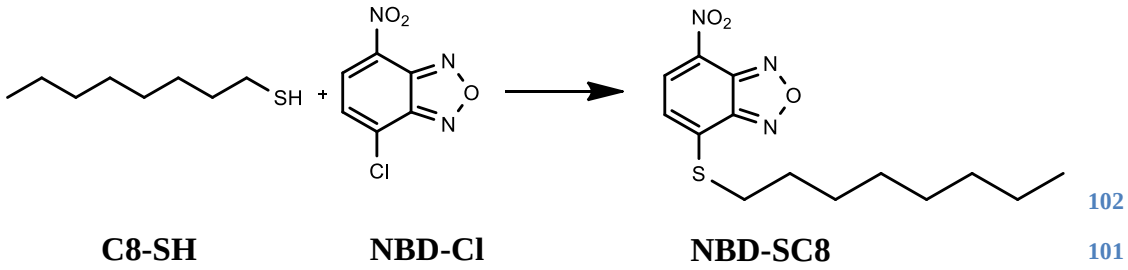

Scheme 4.1: The aromatic nucleophilic substitution reaction between C8-SH, **11** and NBD-Cl, **12** to give NBD-SC8, **13**.

Due to their hydroph **11** ature, **11** and **12** **12** ubilised in the apolar bilayer of t **13** DV **2**.[71] We wanted to explore whether reagents solubilised in the bilayer could move in and out of the bilayer. If so, it could be speculated that aggregation would result in exchange of reactants and consequently to an increase in product formation.

The reagents **11** and **12** (4 μM) were embedded separately in β-CDV **2** and **9** was added to either batch. The respective reagent (**11** or **12** at 40 μM) was added to the β-CDV **2** stock solution (100 μM) in chloroform during the preparation of the thin film cast. These solutions were then diluted ten times in order to obtain the desired concentration. The reaction between the reagents embedded in β-CDV **2●9** was compared to that of the free reagents in aqueous buffer. Analysis of product formation by UPLC confirmed reports in literature that the reaction between **11** and **12** in aqueous buffer is very slow (0.055 μM = 1.25% after 200 minutes) (Figure 5.17).[22] Even less product was formed between **11** and **12** when these were embedded

in β-CDV 2●**9**. This suggests that the reagents are well-confined in β-CDV **2●9** which prevents their reaction.

Addition of Au NP **1** brings the β-CDV **2●9** in close proximity. In principle, this could induce product formation if this process would induce exchange of reagents between the vesicles. However, this was not observed and product formation was still low in the presence of Au NP **1**. This result is interesting because it suggests that aggregation by β-CDV **2●9** does not result in fusion of the vesicles. It also shows that encapsulation of the reagents in the β-CDV **2●9** limits their movement and so that there is little, if any, exchange of reagents between the β-CDV 2●**9**.

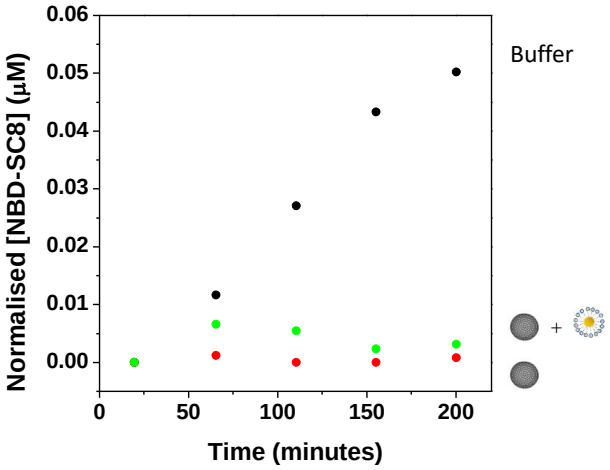

Figure 5.17: Increase in the concentration of **13** upon mixing **11** and **12** in buffer, β-CDV **2●9** containing embedded reagents, and upon addition of Au NP **1** to β-CDV **2** embedded with reagents. [**11**] = [**12**] = 4 μM, [β-CDV **2**] = 20 μM, [**9**] = 10 μM, [Au NP **1**] = 30 μM, [HEPES] = 10 mM, pH 7.0.

We attempted a different strategy and investigated whether the β-CDV **2●9** could take the reagents up from a solution of aqueous buffer. It would be expected that such uptake would favour their reaction on account of the more hydrophobic environment in the β-CDV **2●9**. Similar results were previously obtained for ATP-templated vesicles in the Prins' group.[22] This was indeed found to be the case since the reaction between **11** and **12** occurred in better yield when carried out in the presence of β-CDV **2●9** than in aqueous buffer (Figure 5.18).

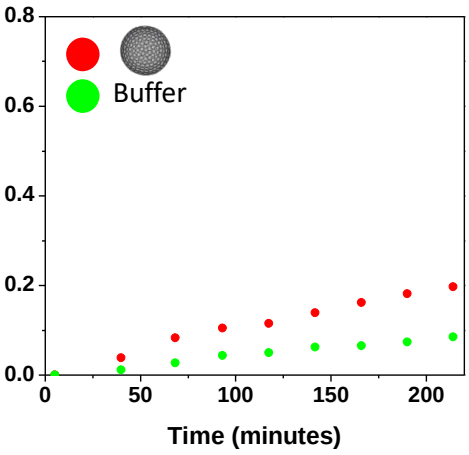

Figure 5.18: Increase in the concentration of **13** upon mixing the reagents in buffer and in β-CDV **2•9**. [**11**] = [**12**] = 4 μM, [β-CDV **2**] = 20 μM, [**9**] = 10 μM, [Au NP **1**] = 30 μM, [HEPES] = 10 mM, pH 7.0.

A further experiment was carried out whereby the reactants were added sequentially (Figure 5.19a). The reaction barely occurred in buffer. Addition of β-CDV **2•9** to the reagents in buffer slightly improved the reaction. Au NP **1** were then added to the solution. This resulted in a sudden increase in the amount of product, after which product formation reached saturation. A control experiment in which Au NP **1** was added to the reactants in buffer in the absence of β-CDV **2•9** suggested that the Au NP **1** were capable of enhancing the reaction to some extent by themselves, but this effect was minimal when compared to the increase in reaction observed for the addition of Au NP **1** in the presence of β-CDV **2•9** (Figure 5.19b).

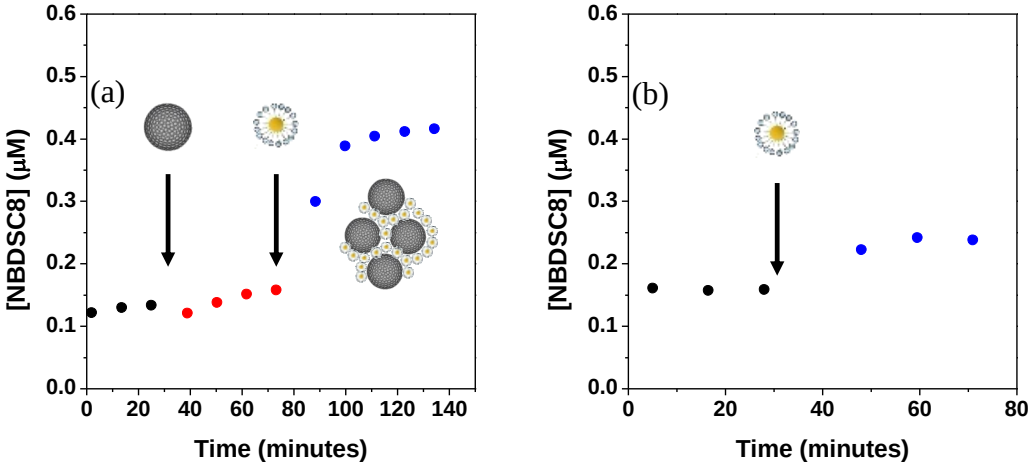

Figure 5.19: (a). A graph showing the concentration of **13** when the reaction is carried out in buffer followed by the addition of β-CDV **2•9** and subsequent addition of Au NP **1**. (b). Concentration of **13** upon carrying out the reaction in buffer followed by subsequent addition of Au NP **1**. [**11**] = [**12**] = 4 μM, [β-CDV **2**] = 20 μM, [**9**] = 10 μM, [Au NP **1**] = 30 μM, [HEPES] = 10 mM, pH 7.0.

Trapping of reagents in confined spaces has previously been reported to alter the chemical reactivity of the species.[1] A possible explanation for the improved reactivity upon addition of Au NP **1** could be that aggregation entraps the reagents and brings them in close proximity to the aggregated vesicles over a short period of time. This enables them to be taken up by β-CDV **2•9** at a rate which is faster than normal diffusion. Another potential explanation for the improved reactivity could be a change in the microenvironment. When the Au NP **1** bind the β-CDV **2•9**, the resulting electrostatic interactions could possibly dehydrate the contact area, rendering the environment more conducive to reaction.

The fact that product formation was induced by aggregation was further confirmed by covering the Au NP **1** with ATP. Au NP **1** were pre-mixed with ATP and added to the reactants in the presence of β-CDV **2•9**. As expected, product formation increased only slighty, since the β-CDV **2•9** remained unaggregated in this case (Figure 5.20).

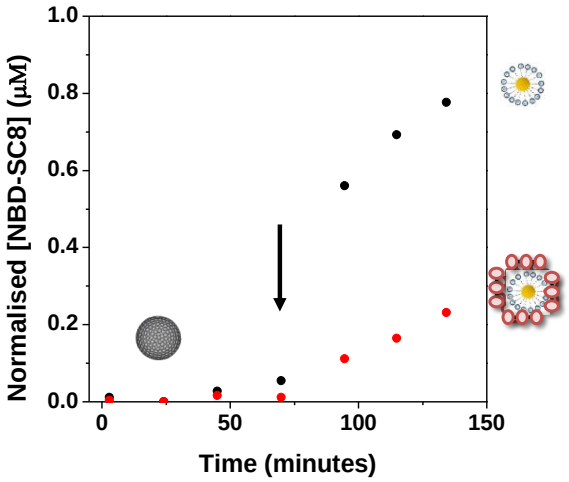

Figure 5.20: A figure showing the increase in the concentration of **13** upon addition of Au NP **1** (i) uncovered (control) and (ii) covered (pre-mixed) with ATP. [β-CDV **2**] = 20 μM, [**9**] = 10 μM, [Au NP **1**] = 30 μM, [ATP] = 20 μM, [HEPES] = 10 mM, pH 7.0.

We then wanted to study the same system under dissipative conditions. The reactants were mixed with β-CDV **2•9** in the presence of the enzyme potato apyrase. Au NP **1** pre-mixed with ATP as then added to the solution. The enzyme potato apyrase hydrolysed ATP and restored the attractive electrostatic interactions between the Au NP **1** and the β-CDV **2•9**. leading to aggregation. Indeed, it was observed that more product was obtained in this experiment when

compared to a control experiment carried out in the absence of the enzyme (Figure 5.21a). This suggests that the reaction between the **11** and **12** was promoted.

It was however noted that the amount of product formed in the presence of enzyme was less than the amount obtained in previous experiments in the absence of ATP. This can be attributed to the fact that the waste products affect the outcome of the reaction. In fact, adding Au NP **1** pre-mixed with the waste products (AMP and Pi mixed in a 1:2 ratio) to the reactants in β-CDV **2•9** resulted in the formation of a similar quantity of product (Figure 5.21b). However, the enzyme itself did not affect the outcome of the reaction, as emerged when the uncovered Au NP **1** were added to the reactants in β-CDV **2•9** in the presence of potato apyrase. In this case the enzyme did not influence the maximum amount of product formed. However, the system with the enzyme quickly destabilised and precipitated (Figure 5.21b).

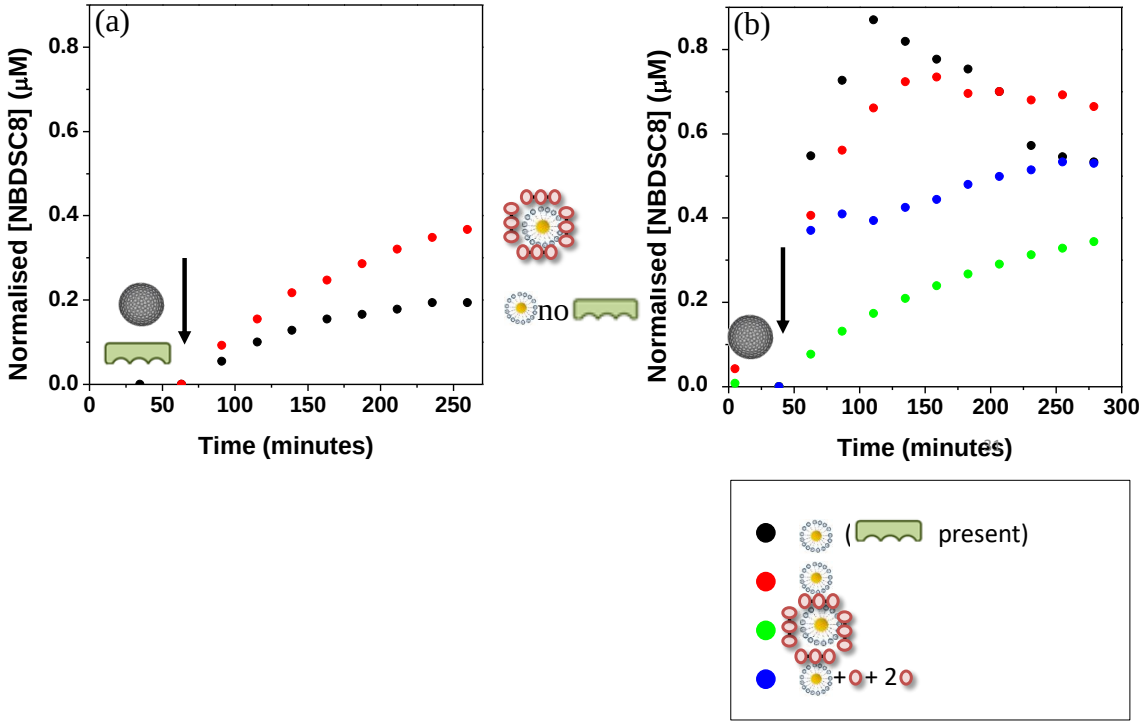

Figure 5.21: (a). Increase in **13** upon addition of 3.0 U potato apyrase. (b). Controls: (i) Addition of Au NP **1** to the reaction with β-CDV **2•9** in the presence of 5.0 U potato apyrase. (ii) Addition of Au NP **1** to the reaction in β-CDV **2•9**. (iii) Addition of Au NP **1** covered with 20 μM ATP to the reaction in β-CDV **2**. (iv) Addition of Au NP **1** pre-mixed with 20 μM AMP + 40 μM Pi. In both experiments, the values were normalised at the point of addition of nanoparticles, for better comparison of the graphs. [β-CDV **2**] = 20 μM, [**9**] = 10 μM, [Au NP **1**] = 30 μM [ATP] = 20 μM, [HEPES] = 10 mM, pH 7.0.

In this project we have developed a self-assembled system which aggregated and disaggregated in an organised fashion and demonstrated a level of molecular complexity which further led to the control of chemical reactivity. The trapped reagents reacted with faster kinetics than in the bulk solution. The reaction outcome was affected by factors which limited or enhanced the aggregation process. We envisage that the system can find further applications as chemical nanoreactors on a larger scale.

5.3 Aggregation-dispersion cycles induced by the interaction between gold nanoparticles and a light-responsive arylpyrazole

The principles formulated in the previous sections were used to design another system where the aggregation and disaggregation processes could be controlled by light. We make use of the reversible isomerisation of the azo-group in an arylazopyrazole, AAP, from *trans* to *cis* by irradiation with UV-Vis light at 365 nm and from *cis*- to *trans*- by irradiation with green light at 520 nm.[59]

An AAP with a carboxylate group (**14**) was chosen as the host for the β-CDV **2** (Figure 5.22a). When **14** binds the β-CDV **2**, it acquires a negative charge, which enables the electrostatic interaction with positively charged Au NP **1**. The *trans*- and *cis*- isomers of **14** differ in their affinity for β-CDVs. The *trans*- isomer is rod-like and apolar and is capable of forming stable inclusion complexes with β-CDVs ($K \sim 2000\ M^{-1}$).[60] On the other hand, the *cis*- isomer is polar and bent so that it is incapable of fitting inside the cyclodextrin cavities ($K \sim 500\ M^{-1}$).[60] The *trans*- isomer is therefore capable of imparting a negative charge to the β-CDV **2**, but the *cis*-isomer is much less effective at the same concentration of **14**. It is thus expected that much higher aggregation occurs when Au NP **1** is added to β-CDV **2** covered with the *trans*- **14** than when Au NP **1** is added to the β-CDV **2** covered with *cis*-**14** (Figure 5.22b). Moreover, if the aggregated β-CDV **2** coated with *trans*- **14** is irradiated at 365 nm, the *trans*-*cis* isomerization will lead to disaggregation. The process is expected to be reversible upon consecutive irradiation at 520 nm (green light) and 365 nm (UV-Vis light).

5.3.1 Cyclodextrin vesicles covered with carboxylate-containing arylazopyrazole

β-CDV **2** covered with **14** had a negative ξ-potential of -16.8 ± 4.7 mV, demonstrating that covering β-CDV **2** with **14** significantly increases the negative charge of β-CDV **2** (ξ-potential = -7.3 ± 0.9 mV). The ξ-potential is however slightly lower than that imparted by **9** (*vide supra*). This can probably be explained by the fact that each **9** has two binding sites while **14** has only one (Figure 5.23a). The host-guest interaction between β-CDV **2** and **14** was investigated using ITC assuming a 1:1 binding model, and the binding constant was determined to be in 2.2 × 10^3 M^{-1}, which compared well with literature values (Figure 5.23b) and which is indeed much lower than the binding affinity of **9**.[59]

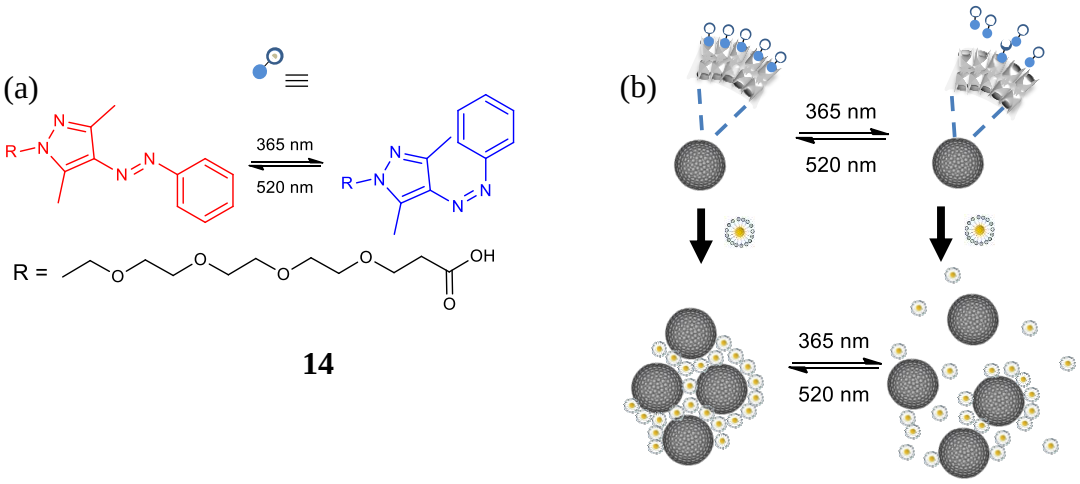

Figure 5.22: (a) Structure of *trans*- and *cis*- **14** used in this study. (b) Interconversion between *trans*- and *cis*- **14** by irradiation with light and interconversion between the aggregated and disaggregated states by irradiation with light.

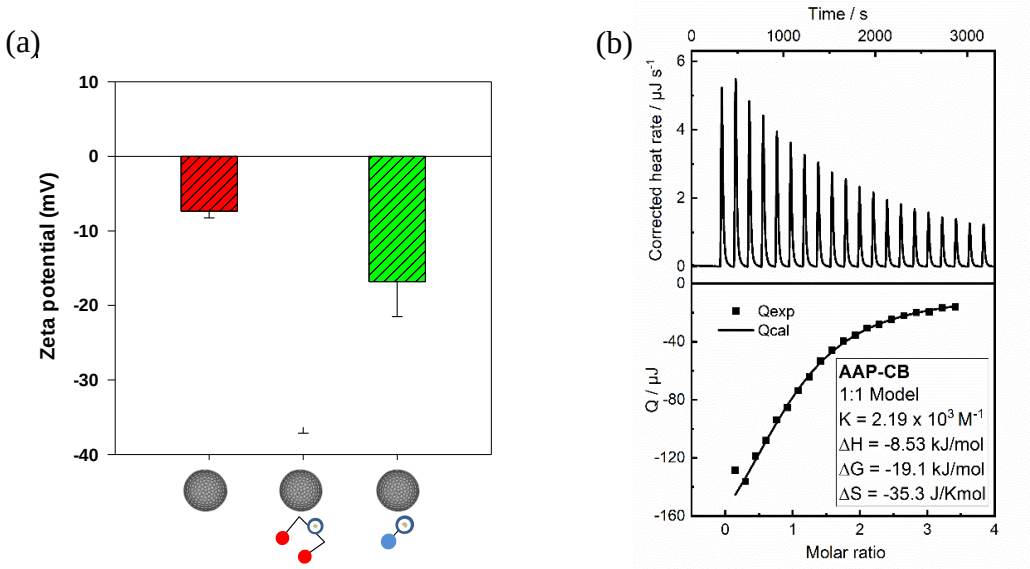

Figure 5.23: (a) Comparison of the zeta potential of the uncovered β-CDV **2**, the β-CDV **2** covered with **9** and the β-CDV **2** covered with ligand **14** at 100% decoration. (b) ITC titration curve and the corresponding fit to a 1:1 model of β-CDV **2** and **14** in water.

5.3.2 Aggregation and dispersion of cyclodextrin vesicles induced by UV-Vis and green light

β-CDV **2** does not spontaneously aggregate when **14** is added either as the *cis*- or the *trans*-isomer (Figure 5.24a). Addition of Au NP **1** to β-CDV **2** covered with *cis*- and *trans*-**14** causes aggregation in both cases, but the rate of aggregation is much higher for β-CDV **2** covered with *trans*-**14**, hereby defined as the aggregated state, compared to that covered with *cis*-**14**, hereby defined as the dispersed or disaggregated state. This is consistent with the fact that at the used concentration of 10 uM, *trans*-**14** binds β-CDV **2** while *cis*-**14** is mostly uncomplexed.

Addition of Au NP **1** to β-CDV **2** covered with *trans*-**14** leads to aggregation. Irradiation with UV-Vis light (365 nm) converts **14** to the *cis*- form (Figure 5.24b). This has a lower binding constant to the β-CDV **2** and the aggregate disperses. This was evident in an immediate lowering of the OD600, suggesting de-aggregation. The OD600 was restored again upon irradiation with visible light (520 nm), indicating full reversibility. It was possible to switch between the aggregated and dispersed state without decreasing the efficiency of the system by alternating UV-Vis irradiation at the respective wavelengths over a number of cycles.

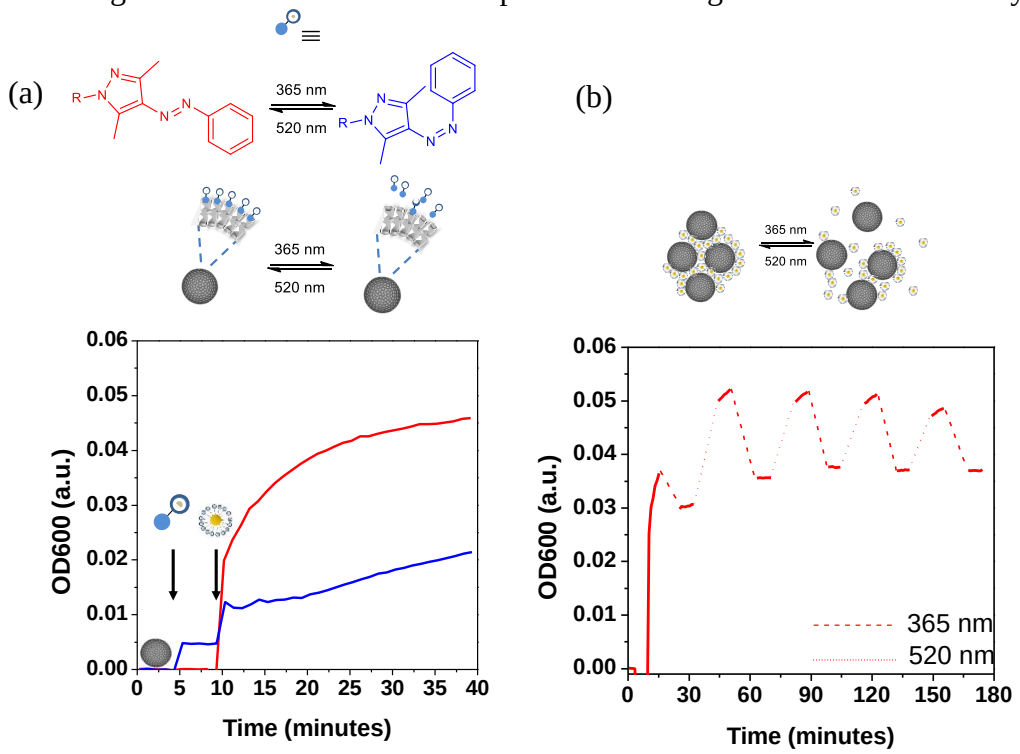

Figure 5.24: (a). OD600 nm upon addition of Au NP **1** to *trans*- (red) *and cis*- (blue) **14**. (b). Kinetic profile showing the OD600 for the cycling experiment where the aggregated state in the *trans* form was irradiated at 365 nm to the *cis* state resulting in disaggregation and cycling was repeated for a number of times. [β-CDV **2**] = 20 µM, [**14**] = 10 µM, [Au NP **1**] = 10 µM, [HEPES] = 10 mM, pH 7.0.

The aggregation and dispersion process could also be monitored by DLS (Figure 5.25). The β-CDV **2** covered with *trans*- **14** had an hydrodynamic radius of around 100 nm. Addition of Au NP **1** resulted in the formation of much larger structures with sizes of around 700 nm. Irradiation of the aggregate with UV-Vis light at 365 nm reduced the size of the aggregates to 150±10 nm, after which irradiation at 520 nm brought the sizes back to 700±100 nm. Alternate irradiation with UV-Vis and visible light shifted the size between approximately 150 nm and 700 nm with good reproducibility, affirming the reversibility of the process.

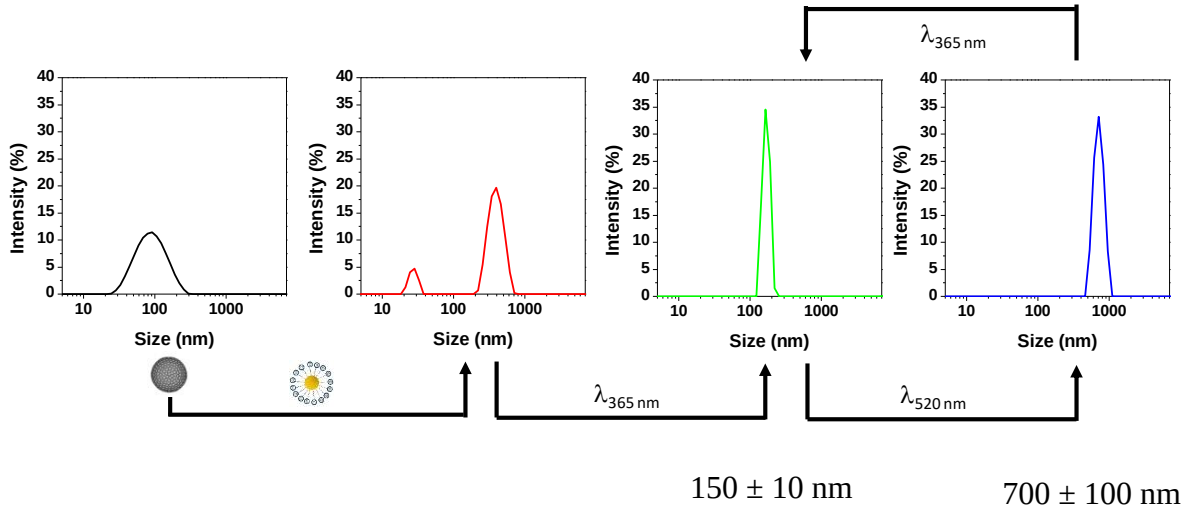

Figure 5.25: Monitoring of the aggregation/de-aggregation process using DLS showing the spectrum of (a) the vesicles covered with 100 % **14** (b) the vesicles upon addition of Au NP **1** (c) the β-CDV **2** with Au NP **1** upon irradiation with light at 365 nm (d) the β-CDV **2** with Au NP **1** upon irradiation with light at 520 nm.

The switching effect could be improved by doubling the concentration of **14** from 5 μM to 10 μM (Figure 5.26a). Under these conditions, the system could be cycled repeatedly but the efficiency of the system suffered with increasing cycles (Figure 5.21b). These results demonstrate the light-responsive character and the high reversibility of the supramolecular system based on Au NP **1** and β-CDV **2** covered with **14**.

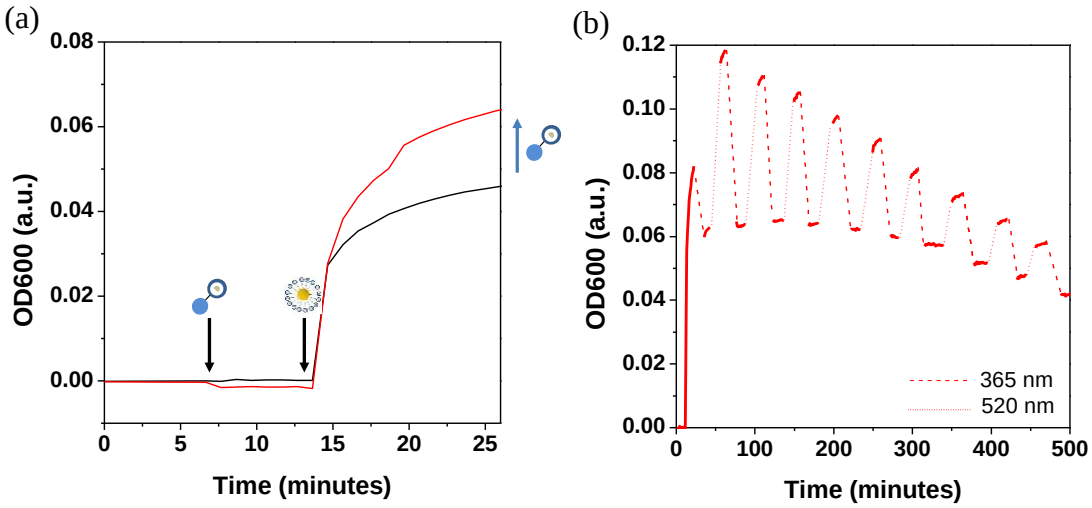

Figure 5.26: (a). Aggregation of the *trans*- (red) and *cis*- (black) isomers of **14** upon addition of Au NP **1** to the β-CDV **2**. (b). Switching cycles between aggregates containing the *trans*- and *cis*- isomers of **14**. [β-CDV **2**] = 20 µM, [**14**] = 20 µM, [Au NP **1**] = 30 µ M, [HEPES] = 10 mM, pH 7.0.

5.3.3 Exploiting aggregation and dispersion to displace a dye on the gold nanoparticles

The different capacity of *cis*- and *trans*- **14** to induce aggregation could be exploited to displace a dye from Au NP **1**. In previous work in the Prins group, fluorescence displacement assays were used, which exploit the ability of the positively charged Au NP **1** to quench the fluorescence of negatively-charged fluorophores which are directly bound on the surface of the nanoparticles.[72,73] Oligoanions have a strong affinity for the Au NP **1** surface and binding can occur under saturation conditions even at low micromolar concentrations in aqueous media. The surface saturation concentration (SSC) corresponds to the maximum concentration of fluorophore which can be accomodated on the nanoparticle surface. Au NP **1** quenches the fluorescence of fluorophores up to the SSC. However, in the presence of a competitor with a higher affinity for the nanoparticle surface the fluorescence probe is displaced, resulting in a "turn-on" of the fluorescence intensity (Figure 5.27). The trigger of fluorescence intensity is taken as an indication of the binding of the analyte to the Au NP surface and is thus proportional to the amount of fluorescent probe displaced. This enables a measurement of the quantity of analyte absorbed on the nanoparticle surface. In practice, displacement assays are usually carried out at concentrations which are slightly below the SSC to ensure a complete absence of fluorescence.[72,74]

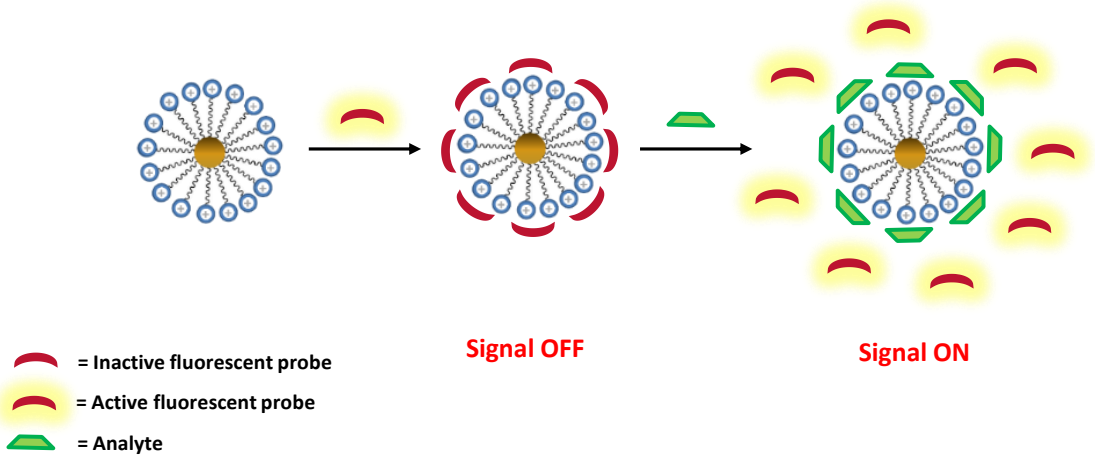

Figure 5.27: Schematic representation showing the binding of a fluorescent probe on the Au NP **1**. The signal is OFF when the fluorophore is added up to the SSC. Addition of a competitor with a higher affinity to the surface of Au NP **1** displaces the fluorescent probe and results in a turning ON of the fluorescence intensity.

The fluorescence displacement assay was carried out using a fluorogenic coumarin343 derivative which has been linked to a tripeptide (Gly-Asp-Asp), cGDDD, **15** (λ_{ex} = 450 nm, λ_{em} = 493 nm) (Figure 5.28a). This probe contains three carboxylate groups and is thus capable of interacting with the Au NP **1** surface on account of multiple electrostatic interactions.[69] The fluorophore **15** was added to 20 µM Au NP **1** at a concentration of 4.3 µM, which corresponds to 90% of the surface saturation concentration (SSC).[75] At this point the proximity of the dye to Au NP **1** causes a quenching of the fluorescence of **15**. β-CDV **2** covered with either *trans*- or *cis*- **14** was then titrated to the solution and the fluorescence intensity of **15** was monitored at 450 nm (Figure 5.28b). It was expected that aggregation would lead to a displacement of **15** from the surface of Au NP **1.** From the titration it emerged that β-CDV **2** covered with *trans*-**14** had a better capacity of displacing **15** compared to β-CDV **2** covered with *cis*-**14**. This is in line with the previous observation that *trans*-**14** has a better capacity to induce aggregation compared to β-CDV **2** covered with *cis*-**14**.

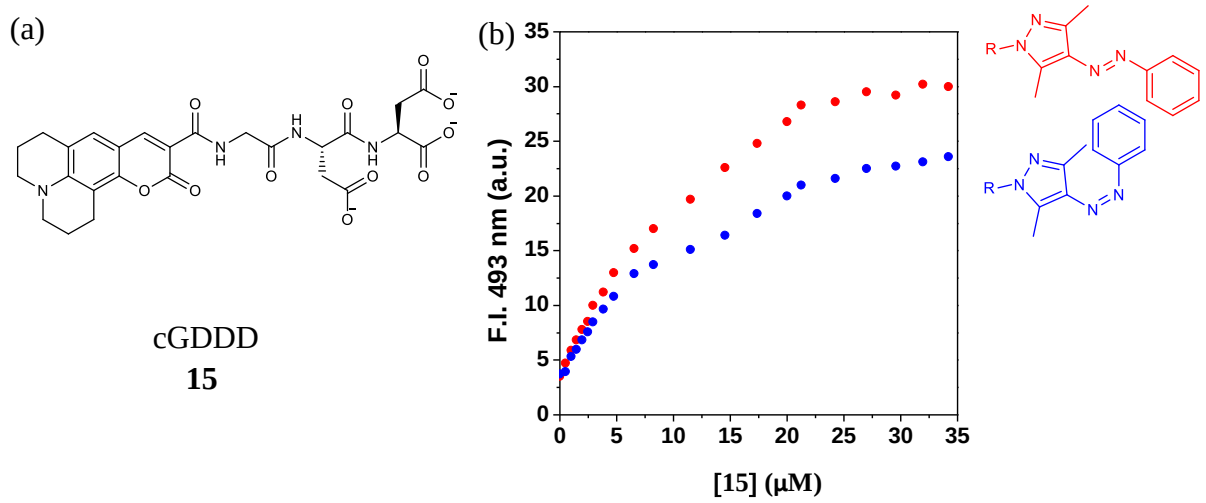

Figure 5.28: The fluorescence intensity at 450 nm upon titrating vesicles covered with *trans*- or *cis*-**14** to a solution containing Au NP **1** covered with a negatively charged coumarin derivative, **15**. [Au NP **1**] = 20 μM, [**15**] = 4 μM, [HEPES] = 10 mM, pH 7.0.

5.3.4 Aggregation/dispersion cycles in response to the input of multiple signals

The complexity of the system was then increased by combining the light-sensitive trigger with chemical triggers, *i.e.* the ATP/apyrase system used before. The system based on **14** was capable of responding to ATP and apyrase as well as to light (Figure 5.29). Au NP **1** was added to β-CDV **2** complexed with *trans*-**14** in the presence of the enzyme potato apyrase. An increase in the OD600 showed the occurrence of aggregation. Addition of ATP dispersed the system again, evidenced by a rapid decrease in the OD600. However, in time the enzyme hydrolysed ATP and the attractive electrostatic interactions between the β-CDV **2** covered with *trans*- **14** were restored leading to aggregation. The cycle was repeatable two more times by new additions of ATP. These experiments confirmed that the system containing **14** could also be transiently disaggregated using ATP as a chemical fuel. This prompted us to investigate how the system responded to a combination of triggers..

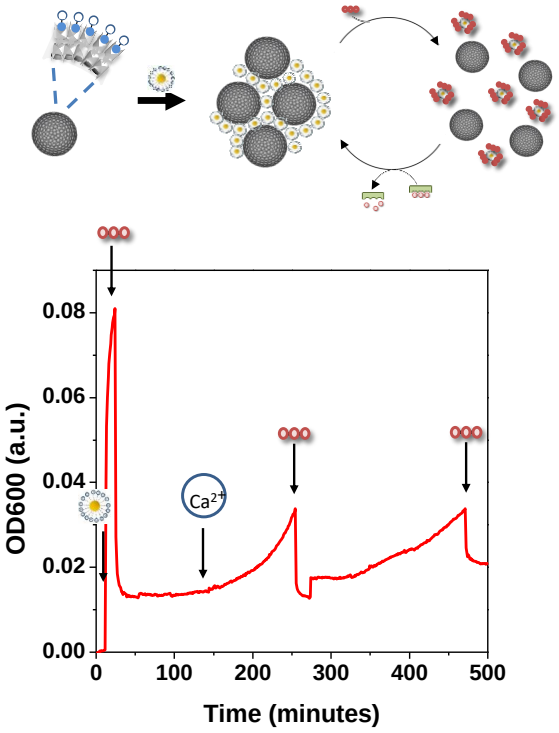

Figure 5.29: Figure showing the OD600 when Au NP **1** and ATP were added to β-CDV **2** covered with **14** in the *trans* state in the presence of the enzyme potato apyrase. (Ca^{2+} was added to the system at around 140 minutes to enhance the activity of the enzyme.) [β-CDV **2**] = 20 µM, [**14**] = 10 µM, [Au NP **1**] = 10 µM, [ATP] = 5 µM, [potato apyrase] = 0.8 U, [Ca^{2+}] = 0.25 mM, [HEPES] = 10 mM, pH 7.0.

In an initial scenario, a light-switching cycle was followed by an ATP/apyrase cycle (Figure 5.30). Au NP **1** was added to β-CDV **2** covered with *trans*-**14**, resulting in aggregation. Irradiation of the aggregates at 365 nm converts the *trans*- **14** to *cis*- **14**, leading to a drop in OD600. The aggregated state was then restored by irradiation at 365 nm. ATP was subsequently added to these aggregates of β-CDV **2** functionalised with *trans*- **14** resulting in a deaggregated state with the Au NP **1** covered with ATP. Potato apyrase and Ca^{2+} were added and the OD600 started to increase again suggesting that the ATP was being hydrolysed and causing the system to revert back to the aggregated state with **14** in the *trans*-form. To further investigate the dynamics of the system, the sample was illuminated at 365 nm, resulting in a decrease in the OD600 upon *trans* - *cis* isomerization. ATP was then added to this disaggregated vesicles with **14** in the *cis*- state and the OD600 decreased once again, as dispersion became the final predominant state.

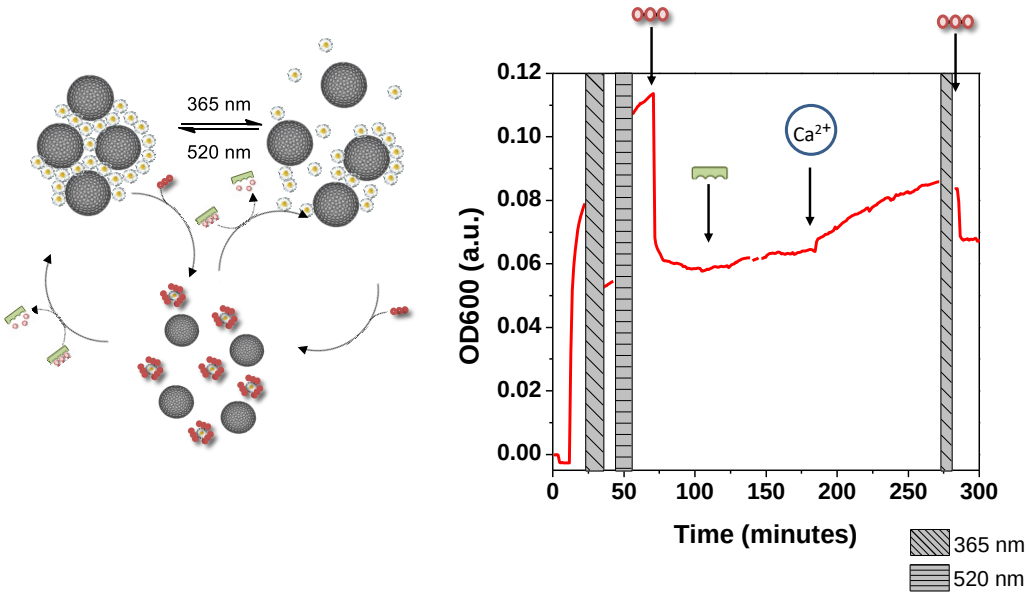

Figure 5.30: Cycles of aggregation/ disaggregation induced by a light-switching cycle followed by an ATP/apyrase cycle and later a mixed switching cyle. [β-CDV **2**] = 20 µM, [**14**] = 10 µM, [Au NP **1**] = 10 µM, [ATP] = 5 µM, [potato apyrase] = 0.8 U, [Ca^{2+}] = 0.25 mM, [HEPES] = 10 mM, pH 7.0.

In a second scenario, transient deaggregation was first induced by an ATP/apyrase cycle and then followed by a light-switching cycle (Figure 5.31). Au NP **1** was added to β-CDV **2** containing *trans*-**14** leading to aggregation. ATP was added causing deaggregation of the system. Potato apyrase and Ca^{2+} were subsequently added and the system started to aggregate once again as ATP was hydrolysed. This aggregated state in the *trans* form of **14** was irradiated with light at 365 nm to convert it to the deaggregated *cis*-state. Irradiation of the sample with green light restored the aggregation as *cis*- **14** was converted to *trans*- **14**. ATP was subsequently added again resulting in an immediate dispersion of the system, but the system spontaneously re-aggregated as the enzyme hydrolysed ATP.

In the third scenario, the transient deaggregation by ATP/apyrase was followed by two cycles of light irradation at 365 nm/560 nm (Figure 5.32a). It was observed that aggregation/deaggregation was more difficult in the second light-switching cycle. Addition of ATP to the aggregate irradiated at 520 nm (with **14** in the *trans*- form) resulted again in transient disaggregation. A final scenario was then devised where aggregation by the addition of Au NP **1** was followed by two irradiation cycles converting the aggregate from *trans* (aggregated) to *cis* (dispersed) to *trans* (aggregated) and to *cis* (dispersed) again before the addition of ATP (further dispersion) followed by apyrase (re-aggregation) (Figure 5.32b).

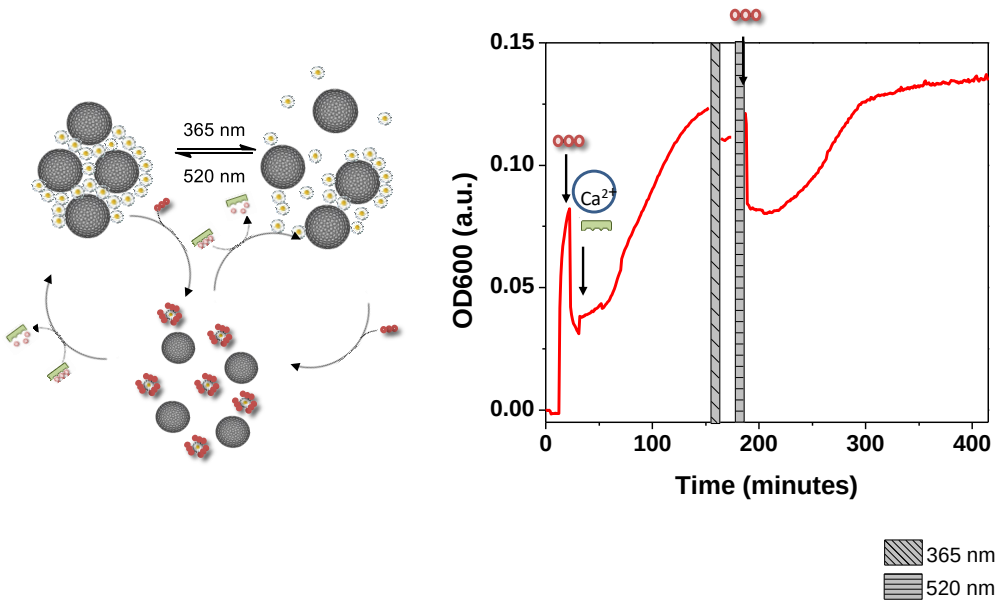

Figure 5.31: Cycles of aggregation/disaggregation induced by an ATP/apyrase cycle followed by a light/switching cycle. [β-CDV] = 20 μM, [**14**] = 10 μM, [Au NP•Zn^{2+}] = 10 μM, [ATP] = 5 μM, [potato apyrase] = 0.8 U, [Ca^{2+}] = 0.25 mM, [HEPES] = 10 mM, pH 7.0.

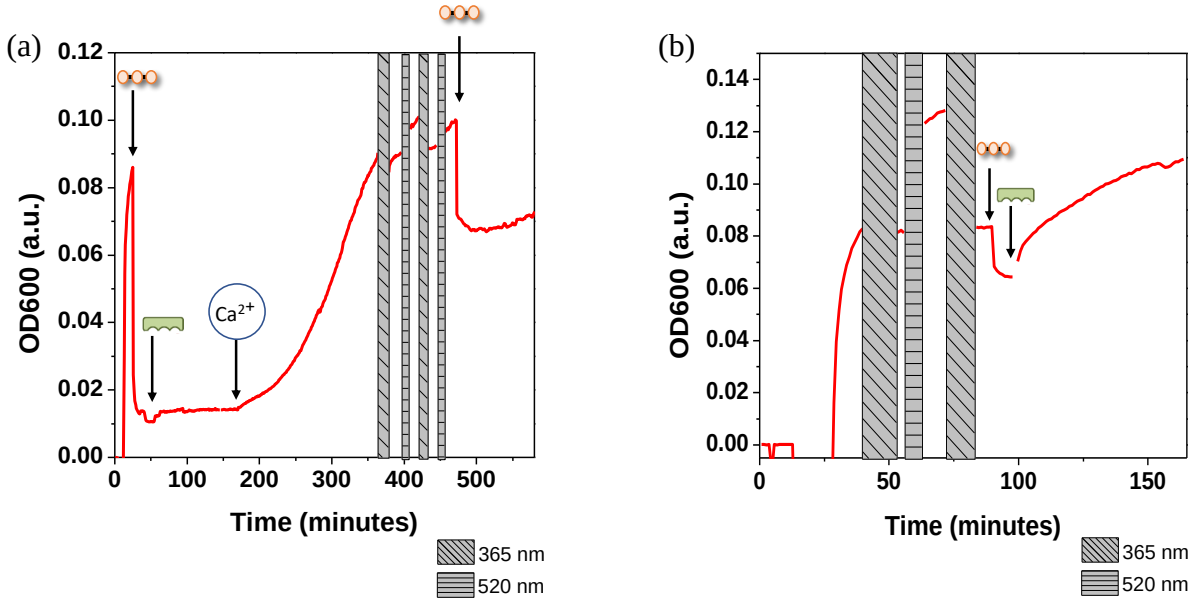

Figure 5.32: Further attempts at mixing the light switching with the ATP/apyrase cycles. (a). Aggregation/deaggregation induced by ATP/apyrase cycles followed by two light switching cyles and further addition of ATP. (b). Aggregation/deaggregation induced by light-switching cycles followed by an ATP/apyrase cycle. [β-CDV **2**] = 20 μM, [**14**] = 10 μM, [Au NP **1**] = 10 μM, [ATP] = 5 μM, [potato apyrase] = 0.8 U, [Ca^{2+}] = 0.25 mM, [HEPES] = 10 mM, pH 7.0.

In summary, in this second part we have developed a stimulus-responsive system based on Au NP **1** and β-CDV **2** and the light-sensitive regulatory element AAP **14**. Aggregation could be induced by the positively charged Au NP **1** when β-CDV **2** was complexed with *trans*-**14**, on account of the strong negative charge conferred by **14** to the surface of β-CDV **2**. However, the system disaggregated upon isomerisation of **14** into the *cis*-form, since this resulted in dissociation of **14** from β-CDV **2**. Aggregation and disaggregation could be reversibly induced by irradiation with visible and UV-Vis light. Further complexity was introduced by adding ATP as a trigger for transient disaggregation in the presence of enzyme. ATP binds Au NP **1** very strongly on account of multiple phosphate groups, which results in disruption of the binding between Au NP **1** and β-CDV **2**. ATP hydrolysis by potato apyrase restores the interactions between Au NP **1●14** and β-CDV **2** and consequently causes aggregation of the systems' components. The different stimuli could be used in the same system, thus showing the potential of the system for applications in stimulus-responsive materials.

5.4 Experimental

5.4.1 Instrumentation

UV/Vis Spectroscopy: UV-Vis measurements were carried out using a JASCO V-650 double-beam spectrophotometer (JASCO Labor- und Datentechnik GmbH, Gross-Umstradt) at 25 ^{o}C, using 1 mL low volume disposable poly(methyl methacrylate) (PMMA) cuvettes (Brand GmbH & CO, KG, Wertheim). The spectrometer was controlled using Spectra Manager version 2.08.04 program (Jasco Labor- und Daten-technik GmbH, Gross-Umstadt). The samples were measured in an appropriate solvent and measured against the same solvent. Generally, 1000 μL of 20 μM β-CDV **2** were placed in the cuvette. A volume of 10 μL of the appropriate additive prepared in a stock solution to give the required concentration was then added and the solution was mixed inside the cuvette. Readings were taken every minute. The Au NP **1** showed an absorbance at this wavelength and thus, unless otherwise specified, all measurements were corrected for this absorbance.

Irradiation experiments: Light irradiation was carried out using two different light sources. Irradiation with UV-Vis light was carried out using a Spectroline UV lamp, MODEL ENF-240C/FE 230 V, 50 Hz, 0.17 AMPS. Irradiation with green light was 520 nm was carried out using LED lights, RoHS Compliance Guirlade Electrique 80 Lampes 230 V, 50 Hz, 20 mA. An irradiation time of 10 minutes was used to interconvert the *trans*- to the *cis*-**14** and *vice versa*.

Transmission electron microscopy (TEM): In order to analyse the samples with TEM, samples were prepared on 200 mesh formvar-carbon-coated copper grids. A drop of the test solution was left on the grid for 2 minutes and then blotted gently with filter paper. Staining was then carried out using a drop of 2% (w/w) uranyl acetate, left to stand by for 5 minutes and blotted again. Samples were then analysed in a JEOL 2000 transmission electron microscope operating at 80 kV.

Fluorescence and light microscopy: Microscopic images were recorded with an Olympus inverted research microscope CKX41. The micrscope was equipped with a DX 20 L-FW camera (Kappa opto-electronics GmbH) controlled by the program Kappa Camera Control (version 2.7.5.7032). A mercury burner U-RFL-T was used to generate the excitation light.

Dynamic Light Scattering (DLS) and zeta potential measurements: DLS and zeta potential measurements were carried out on a Malvern Instruments Nano-ZS using 1 mL low volume disposable poly(methyl methacrylate) (PMMA) cuvettes (Brand GmbH & CO, KG, Wertheim).

Isothermal Titration Calorimetry (ITC): ITC was carried out using a TA Instruments Nano ITC Low Volume (Waters Forp. Milford, MA) with a cell volume of 170 µL using ITCRun version 2.1.7.0 Firmware version 1.31 (TA Instruments, WaterCorp., Milford, MA). All titrations were performed using a 50 µL syringe and 20 injections of 2.5 µL at a temperature of 25 ^{o}C with a stirring rate of 350 rpm while titrating the CD to the guest solution (**14** or **9**). All samples were prepared in ddwater and degassed for 10 minutes prior to use. Data analysis was carried out using NanoAnalyse Data Analysis version 2.36 (TA Instruments, Waters Corp., Milford, MA), Microsoft Excel version 14.07113.5005 as part of Microsoft Office Professional Plus 2010 (Microsoft Corp., Redmond, WA) and OriginPro 9.1.G (OriginLab Corp., Northhampton, MA). Prior to analysis, all data were corrected by subtracting a blank titration of the CD in the pure solvent.

UPLC experiments: UPLC experiments were carried out on an Agilent Technologies 1290 Infinity equipped with a DAD detector and a quadrupole LC/MS. A volume of 1 mL of sample was prepared in a vial at the appropriate concentration and the vial was sampled at regular intervals. The areas were quantified against a calibration curve of the product, **13**. Column: Zorbax SB-C3 Rapid Resolution HT 3.0 × 100 mm, 1.8 micron Conditions: Flow rate: 0.6 ml.min, Gradient: 50% B to 95% B (A: H_2O + 0.1% HCOOH, B: ACN+ 0.1% HCOOH) from 0.00 to 1.00 min; 95-100 % B in 1 to 1.1 min; 100 % B from 1.1 to 2.0 min; 100-50 % B in 2.0 to 3.0 min; and finally 50% B from 3.0 to 3.5 min.

Product formation between **11** and **12** was monitored by measuring the absorbance at 424 nm at R_t of 2.9 minutes, which originates from the product. A concentration of 4 µM reagents was used for the experiments. Upon mixing, a small amount of product formed instantaneously. In order to better compare the different samples, the initial value was subtracted from the final value. Thus, the normalised [NBD-SC8] corresponds to the relative increase in the concentration of **13** after subtracting the initial value.

5.4.2 Materials

All commercial reagents were used withour further purification. Stock solutions were prepared using deionised water filtered with a MilliQ-water-purifier (Millipore).

5.4.3 Synthesis and preparation

β-Cyclodextrin vesicles, β-CDV: The synthesis and characterisation of the β-CDV **2** has been described in literature.[27,38] Unilamellar vesicles were obtained by extrusion. Typically, several milligrams of the amphiphilic cyclodextrin were weighed in a 50 mL round-bottomed flask and dissolved in approxiamtely 1 mL chloroform. The solvent was evaporated while rotating the flask using nitrogen gas and heat resulting from the hand to yield a thin film on the glass of the round bottomed flask. Any residual solvent was removed under high vacuum. The appropriate volume of water or 10 mM HEPES buffer pH 7.0 was added to give a concentration of β-CD of 100 μM. The mixture was stirred overnight followed by sonication for 5 minutes or sonicated for 15 minutes. The solution was then extruded 15 times through a polycarbonate membrane with a 0.1 μm pore size filter in a LiposoFast extruder. DLS was used to check that the sample was homogenous with a vesicle approximate size of 100 nm.[38] The stock solution was stable in the fridge at 4 ^{o}C for several days after which precipitation occurred and the solution needed to be discarded. The stock solution was diluted to the appropriate concentration prior to use.

A β-CDV **2** concentration of 20 μM was used for the experiments. Only half of the cyclodextrin are exposed to the outer surface and thus only 10 μM of cyclodextrin spaces are available to host a guest. Each **9** guest molecule could occupy two cyclodextrin host spaces. This implies that in order to obtain 100% site occupation of the vesicles, it was necessary to use 5 μM of adamantane guest, assuming quantitative binding. The **14** forms a 1:1 complex with β-CDV **2** and thus a concentration of 10 μM **14** was used with a concentration of 20 μM β-CDV **2**.

Dye encapsulation: A 10 mM solution of the dye/reactant was prepared in the appropriate solvent. Several milligrams of the amphiphilic cylodextrin were weighed in a 50 mL round-bottomed flask and dissolved in approximately 1 mL chloroform. The appropriate amount of dye/reactant was added to give the required volume. The solvent was evaporated while rotating the flask using nitrogen gas and heat resulting from the hand to yield a thin film on the glass of the round bottomed flask. Preparation of the vesicles was continued as described above. The

dyes/reactants were entrapped in the bilayer of the β-CDV **2** on account of their hydrophobic character.

Reaction of 11 and 12 in the presence of β-CDV 2•9: UV-Vis studies suggested that the reagents (**11** and **12**) interfere with the aggregation (a lower OD600 value was observed when Au NP **1** were added to the CDV **2•9** in the presence of reagents than when the Au NP **1** were added to the CDV **2•9** in the absence of reagents). It is possible that the reagents compete with **9** as guests, reducing the negative charge on the CDV **2** and thus affecting the aggregation process. However this could be counteracted by increasing the amount of **9** used. Thus, the lost increase in OD600 was restored upon using a concentration of 10 μM **9** with a concentration of 20 μM β-CDV, which is twice the amount used in the previous studies.

Synthesis of 9: The synthesis and characterisation of **9** has been reported in literature.[59]

Synthesis of 14: The synthesis and characterisation of **14** has been reported in literature.[59,60]

Synthesis of nanoparticles: The synthesis and characterisation of Au NP **1** has been described in Chapter 4.

5.5 References

(1) Zhao, H.; Sen, S.; Udayabhaskararao, T.; Sawczyk, M.; Kučanda, K.; Manna, D.; Kundu, P. K.; Lee, J.-W.; Král, P.; Klajn, R. *Nat. Nanotech.* **2015**, *11*, 82.

(2) Hecht, S. *Nat. Nanotech.* **2015**, *11*, 6.

(3) Li, X.; Liu, D. R. *Angew. Chem., Int. Ed.* **2004**, *43*, 4848.

(4) Kanan, M. W.; Rozenman, M. M.; Sakurai, K.; Snyder, T. M.; Liu, D. R. *Nature* **2004**, *431*, 545.

(5) Yoshizawa, M.; Kusukawa, T.; Fujita, M.; Yamaguchi, K. *J. Am. Chem. Soc.* **2000**, *122*, 6311.

(6) Mal, P.; Breiner, B.; Rissanen, K.; Nitschke, J. R. *Science* **2009**, *324*, 1697.

(7) Yoshizawa, M.; Tamura, M.; Fujita, M. *Science* **2006**, *312*, 251.

(8) Sastre, G.; Corma, A. *J. Mol. Catal. A: Chem.* **2009**, *305*, 3.

(9) Chu, Y.; Han, B.; Zheng, A.; Deng, F. *J. Phys. Chem. C* **2012**, *116*, 12687.

(10) Kundu, P. K.; Olsen, G. L.; Kiss, V.; Klajn, R. *Nat. Commun.* **2014**, *5*, 3588.

(11) Wei, Y.-S.; Zhang, M.; Liao, P.-Q.; Lin, R.-B.; Li, T.-Y.; Shao, G.; Zhang, J.-P.; Chen, X.-M. *Nat. Commun.* **2015**, *6*, 8348.

(12) Yang, D.; Peng, S.; Hartman, M. R.; Gupton-Campolongo, T.; Rice, E. J.; Chang, A. K.; Gu, Z.; Lu, G. Q.; Luo, D. *Sci. Rep.* **2013**, *3*, 3165.

(13) Fallah-Araghi, A.; Meguellati, K.; Baret, J.-C.; Harrak, A. E.; Mangeat, T.; Karplus, M.; Ladame, S.; Marques, C. M.; Griffiths, A. D. *Phys. Rev. Lett.* **2014**, *112*, 028301.

(14) Komisarski, M.; Osornio, Y. M.; Siegel, J. S.; Landau, E. M. *Chem.–Eur. J.* **2013**, *19*, 1262.

(15) Crosby, J.; Treadwell, T.; Hammerton, M.; Vasilakis, K.; Crump, M. P.; Williams, D. S.; Mann, S. *Chem. Commun.* **2012**, *48*, 11832.

(16) Shevchenko, E. V.; Talapin, D. V.; Murray, C. B.; O'Brien, S. *J. Am. Chem. Soc.* **2006**, *128*, 3620.

(17) Macfarlane, R. J.; Lee, B.; Jones, M. R.; Harris, N.; Schatz, G. C.; Mirkin, C. A. *Science* **2011**, *334*, 204.

(18) Sánchez-Iglesias, A.; Grzelczak, M.; Altantzis, T.; Goris, B.; Pérez-Juste, J.; Bals, S.; Van Tendeloo, G.; Donaldson, S. H.; Chmelka, B. F.; Israelachvili, J. N.; Liz-Marzán, L. M. *ACS Nano* **2012**, *6*, 11059.

(19) Nykypanchuk, D.; Maye, M. M.; van der Lelie, D.; Gang, O. *Nature* **2008**, *451*, 549.

(20) Kalsin, A. M.; Fialkowski, M.; Paszewski, M.; Smoukov, S. K.; Bishop, K. J. M.; Grzybowski, B. A. *Science* **2006**, *312*, 420.

(21) Pezzato, C.; Prins, L. J. *Nat. Commun.* **2015**, *6*.

(22) Maiti, S.; Fortunati, I.; Ferrante, C.; Scrimin, P.; Prins, L. J. *Nat. Chem.* **2016**.

(23) Chen, J. L. Y.; Maiti, S.; Fortunati, I.; Ferrante, C.; Prins, L. J. *Chem.–Eur. J.* **2017**, *23*, 11549.

(24) Manea, F.; Bindoli, C.; Polizzi, S.; Lay, L.; Scrimin, P. *Langmuir* **2008**, *24*, 4120.

(25) Himmelein, S.; Lewe, V.; Stuart, M. C. A.; Ravoo, B. J. *Chem. Sci.* **2014**, *5*, 1054.

(26) Petter, R. C.; Salek, J. S.; Sikorski, C. T.; Kumaravel, G.; Lin, F. T. *J. Am. Chem. Soc.* **1990**, *112*, 3860.

(27) Jan, R. B.; Raphael, D. *Angew. Chem., Int. Ed.* **2000**, *39*, 4324.

(28) Nolan, D.; Darcy, R.; Ravoo, B. J. *Langmuir* **2003**, *19*, 4469.

(29) Jan, R. B.; Jean-Christophe, J.; Gerhard, W. *Angew. Chem., Int. Ed.* **2003**, *42*, 2066.

(30) Mazzaglia, A.; Forde, D.; Garozzo, D.; Malvagna, P.; Ravoo, B. J.; Darcy, R. *Org. Biomol. Chem.* **2004**, *2*, 957.

(31) Sukegawa, T.; Furuike, T.; Niikura, K.; Yamagishi, A.; Monde, K.; Nishimura, S.-I. *Chem. Commun.* **2002**, 430.

(32) Donohue, R.; Mazzaglia, A.; Ravoo, B. J.; Darcy, R. *Chem. Commun.* **2002**, 2864.

(33) In *Multivalency*.

(34) Kauscher, U.; Stuart, M. C. A.; Drücker, P.; Galla, H.-J.; Ravoo, B. J. *Langmuir* **2013**, *29*, 7377.

(35) Schibilla, F.; Stegemann, L.; Strassert, C. A.; Rizzo, F.; Ravoo, B. J. *Photochem. Photobiol. Sci.* **2016**, *15*, 235.

(36) Hendrik, S. J.; Avik, S.; Jan, R. B. *Adv. Mater.* **2014**, *26*, 1076.

(37) Kauscher, U.; Ravoo, B. J. *Beilstein J. Org. Chem.* **2012**, *8*, 1543.

(38) Patrick, F.; Woo, L. C.; Raphael, D.; Tobias, R.; Uwe, K.; Marcel, G.; M., M. A. T.; Adina, L.; W., C. A.; N., R. D.; Jan, R. B. *Chem.–Eur. J.* **2005**, *11*, 1171.

(39) Sasaki, D. Y.; Waggoner, T. A.; Last, J. A.; Alam, T. M. *Langmuir* **2002**, *18*, 3714.

(40) Doyle, E. L.; Hunter, C. A.; Phillips, H. C.; Webb, S. J.; Williams, N. H. *J. Am. Chem. Soc.* **2003**, *125*, 4593.

(41) Bondurant, B.; Last, J. A.; Waggoner, T. A.; Slade, A.; Sasaki, D. Y. *Langmuir* **2003**, *19*, 1829.

(42) Huskens, J.; Mulder, A.; Auletta, T.; Nijhuis, C. A.; Ludden, M. J. W.; Reinhoudt, D. N. *J. Am. Chem. Soc.* **2004**, *126*, 6784.

(43) Valérie, M. A.; Marie-Josephe, B.; Thaddée, G. K.; Jean-Claude, D.; Jean-Marie, L. *Chem.–Eur. J.* **2004**, *10*, 2342.

(44) Ma, X.; Zhao, Y. *Chem. Rev.* **2015**, *115*, 7794.

(45) Song, Q.; Li, F.; Tan, X.; Yang, L.; Wang, Z.; Zhang, X. *Polym. Chem.* **2014**, *5*, 5895.

(46) Gruber, B.; Kataev, E.; Aschenbrenner, J.; Stadlbauer, S.; König, B. *J. Am. Chem. Soc.* **2011**, *133*, 20704.

(47) Cromwell, W. C.; Bystrom, K.; Eftink, M. R. *J. Phys. Chem.* **1985**, *89*, 326.

(48) Meik, W.; Gerhard, W. *Macromol. Rapid Commun.* **1996**, *17*, 731.

(49) Voskuhl, J.; Stuart, M. C.; Ravoo, B. J. *Chem.–Eur. J.* **2010**, *16*, 2790.

(50) Versluis, F.; Voskuhl, J.; Stuart, M. C. A.; Bultema, J. B.; Kehr, S.; Ravoo, B. J.; Kros, A. *Soft Matter* **2012**, *8*, 8770.

(51) Versluis, F.; Tomatsu, I.; Kehr, S.; Fregonese, C.; Tepper, A. W. J. W.; Stuart, M. C. A.; Ravoo, B. J.; Koning, R. I.; Kros, A. *J. Am. Chem. Soc.* **2009**, *131*, 13186.

(52) Jens, V.; Tassilo, F.; A., S. M. C.; Birgit, W.; Carsten, S.; Jan, R. B. *Chem.–Eur. J.* **2010**, *16*, 8300.

(53) Lim, C. W.; Ravoo, B. J.; Reinhoudt, D. N. *Chem. Commun.* **2005**, 5627.

(54) Moratz, J.; Stricker, L.; Engel, S.; Ravoo, B. J. *Macromol. Rapid Commun.* **2018**, *39*, 1700256.

(55) Mohan, N. S. K.; Jan, R. B. *Angew. Chem., Int. Ed.* **2010**, *49*, 5371.

(56) Samanta, A.; Stuart, M. C. A.; Ravoo, B. J. *J. Am. Chem. Soc.* **2012**, *134*, 19909.

(57) Johanna, M.; Avik, S.; Jens, V.; Krishna, M. N. S.; Jan, R. B. *Chem.–Eur. J.* **2015**, *21*, 3271.

(58) Weston, C. E.; Richardson, R. D.; Haycock, P. R.; White, A. J. P.; Fuchter, M. J. *J. Am. Chem. Soc.* **2014**, *136*, 11878.
(59) Stricker, L.; Fritz, E.-C.; Peterlechner, M.; Doltsinis, N. L.; Ravoo, B. J. *J. Am. Chem. Soc.* **2016**, *138*, 4547.
(60) Stricker, L.; Böckmann, M.; Kirse, T. M.; Doltsinis, N. L.; Ravoo, B. J. *Chem.–Eur. J.* **2018**, *24*, 8639.
(61) Möller, N.; Hellwig, T.; Stricker, L.; Engel, S.; Fallnich, C.; Ravoo, B. J. *Chem. Commun.* **2017**, *53*, 240.
(62) Sagebiel, S.; Stricker, L.; Engel, S.; Ravoo, B. J. *Chem. Commun.* **2017**, *53*, 9296.
(63) Chu, C.-W.; Ravoo, B. J. *Chem. Commun.* **2017**, *53*, 12450.
(64) Adam, V.; Prusty, D. K.; Centola, M.; Škugor, M.; Hannam, J. S.; Valero, J.; Klöckner, B.; Famulok, M. *Chem.–Eur. J.* **2018**, *24*, 1062.
(65) Engel, S.; Möller, N.; Stricker, L.; Peterlechner, M.; Ravoo, B. J. *Small* **2018**, *14*, 1704287.
(66) Wiemann, M.; Niebuhr, R.; Juan, A.; Cavatorta, E.; Ravoo, B. J.; Jonkheijm, P. *Chem.–Eur. J.* **2018**, *24*, 813.
(67) Schnurbus, M.; Stricker, L.; Ravoo, B. J.; Braunschweig, B. *Langmuir* **2018**, *34*, 6028.
(68) Galstyan, A.; Kauscher, U.; Block, D.; Ravoo, B. J.; Strassert, C. A. *ACS Appl Mater Interfaces* **2016**, *8*, 12631.
(69) Pezzato, C.; Scrimin, P.; Prins, L. J. *Angew. Chem.* **2014**, *126*, 2136.
(70) Roberts, N. J.; Morieri, G.; Kalsi, G.; Rose, A.; Stiller, J.; Edwards, A.; Xie, F.; Gresshoff, P. M.; Oldroyd, G. E. D.; Downie, J. A.; Etzler, M. E. *Plant. Physiol.* **2013**, *161*, 556.
(71) Galinier, F.; Bertorelle, F.; Fery-Forgues, S. *Comptes Rendus Acad. Sci.* **2001**, *4*, 941.
(72) Pezzato, C.; Lee, B.; Severin, K.; Prins, L. J. *Chem. Commun.* **2013**, *49*, 469.
(73) Neri, S.; Pinalli, R.; Dalcanale, E.; Prins, L. J. *ChemNanoMat* **2016**, *2*, 489.
(74) Maiti, S.; Pezzato, C.; Garcia Martin, S.; Prins, L. J. *J. Am. Chem. Soc.* **2014**, *136*, 11288.
(75) Neri, S. Doctorate, University of Padova, 2016.

5.6 Appendix

5.6.1 Additional light microscope images obtained when gold nanoparticles were added to cyclodextrin vesicles

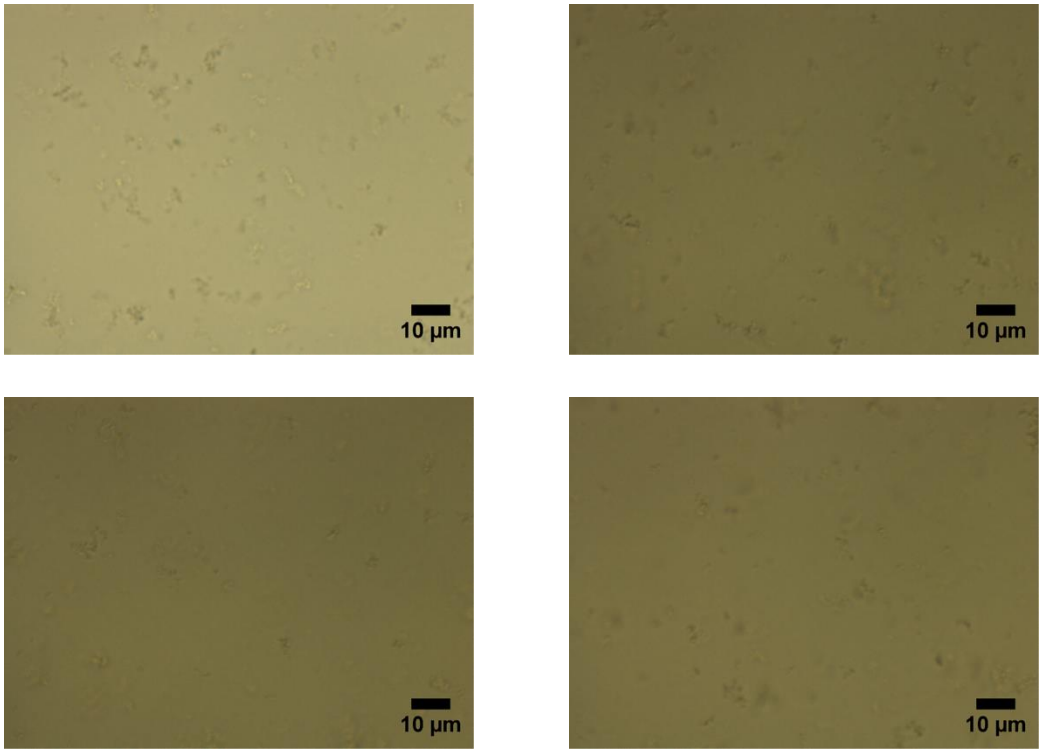

[β-CDV **2**] = 100 µM, [**9**] = 25 µM, [Au NP **1**] = 50 µM

5.6.2 Additional fluorescence microscope images obtained when gold nanoparticles were added to β-cyclodextrin vesicles

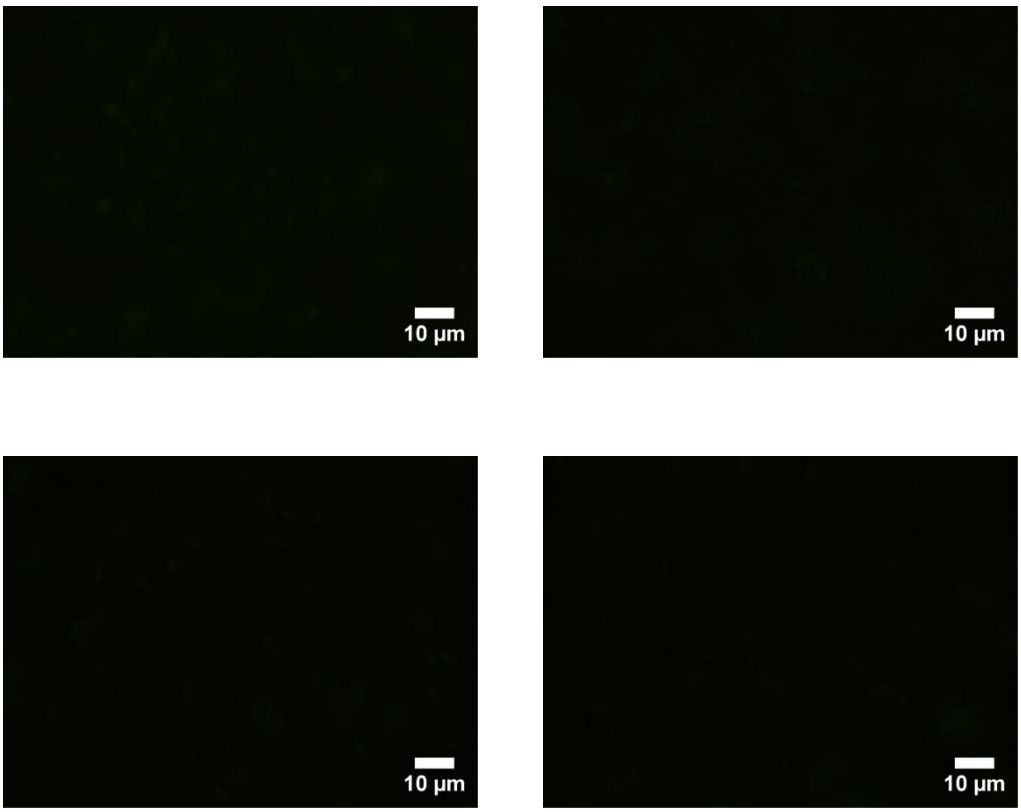

[β-CDV **2**] = 100 µM, [**9**] = 25 µM, [Au NP **1**] = 50 µM

5.6.3 Additional light microscope image obtained when ATP was added to the β-cyclodextrin vesicles aggregated with gold nanoparticles

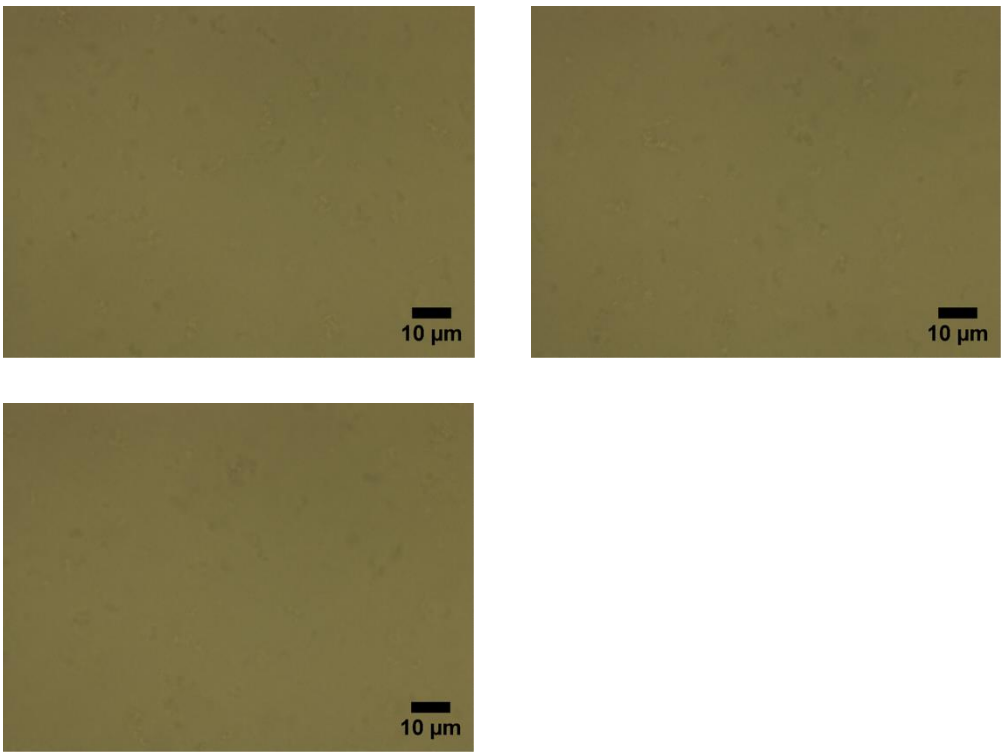

[β-CDV **2**] = 100 µM, [**9**] = 25 µM, [Au NP **1**] = 50 µM

5.6.4 Additional fluorescence microscope image obtained when ATP was added to the β-cyclodextrin vesicles aggregated with gold nanoparticles

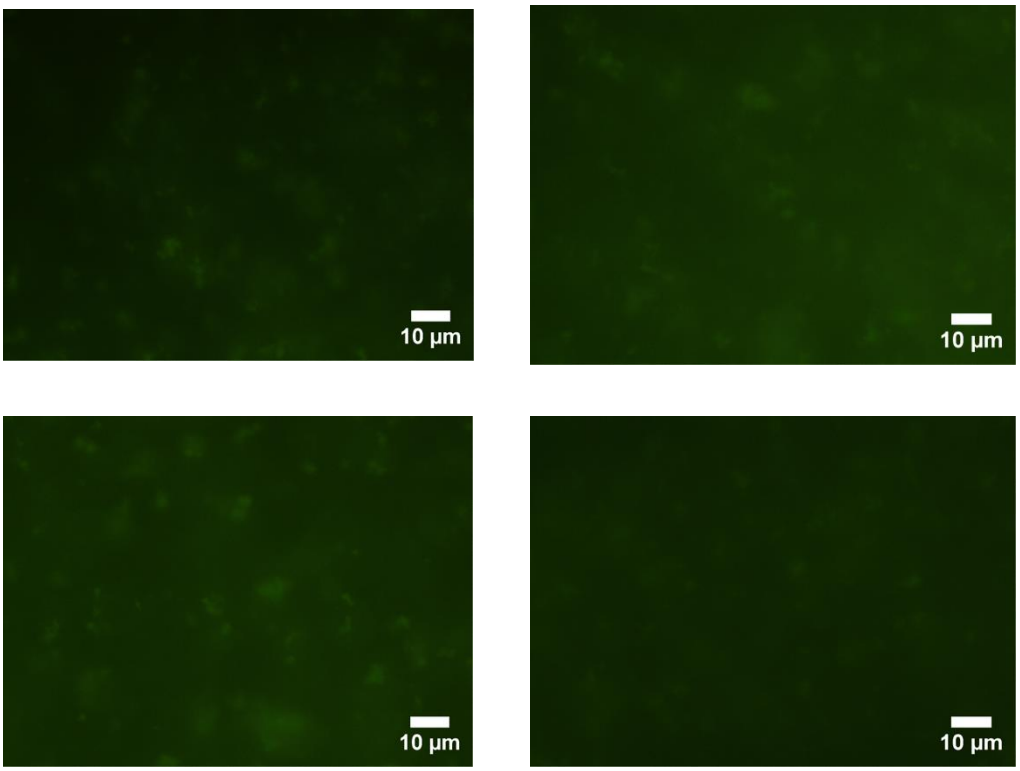

[β-CDV **2**] = 100 µM, [**9**] = 25 µM, [Au NP **1**] = 50 µM

5.6.5 Additional TEM images of gold nanoparticles

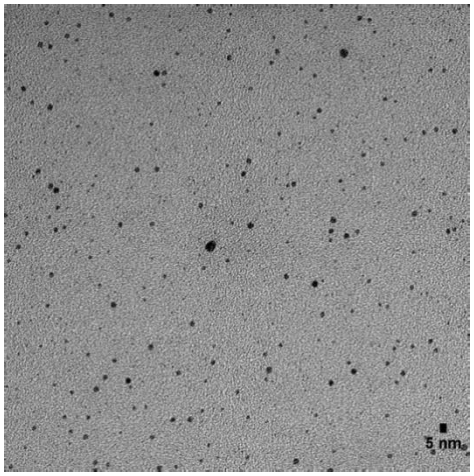

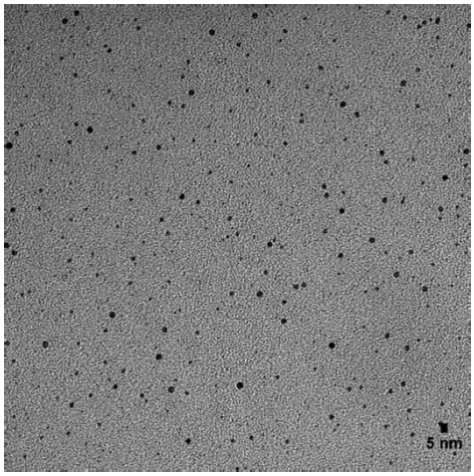

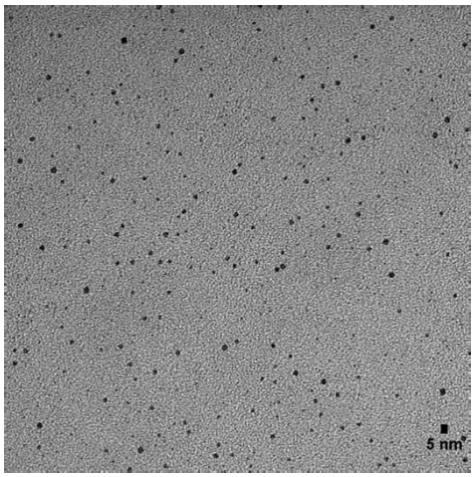

[Au NP **1**] = 50 µM

5.6.6 Additional TEM images of gold nanoparticles upon addition of β-cyclodextrin vesicles

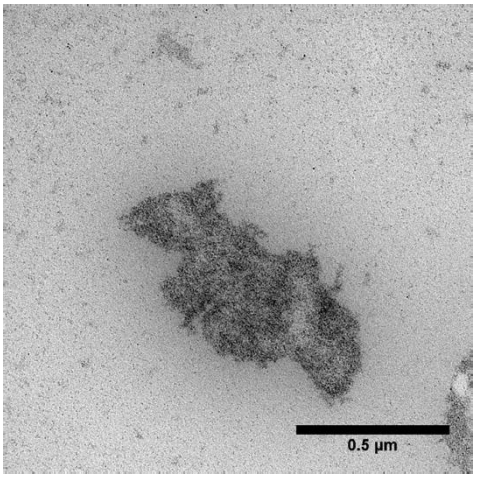

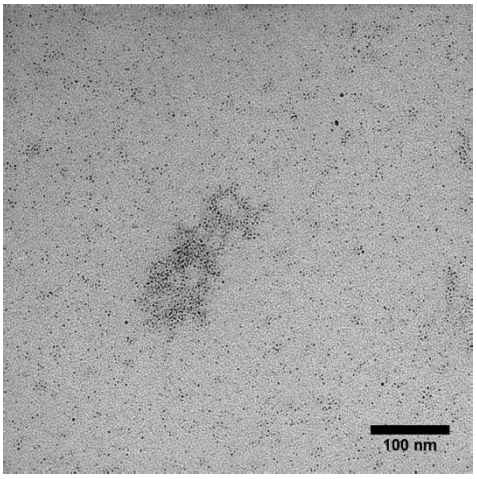

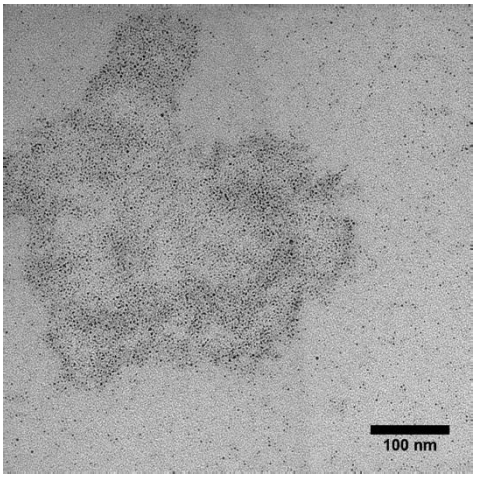

[β-CDV] = 100 µM, [**9**] = 25 µM, [Au NP **1**] = 50 µM

5.6.7 Calibration Curve of 13 in HEPES Buffer pH 7.0 by UPLC

The synthesis of **13** has been reported in literature.[1] The product **13** showed an absorption maximum at 424 nm by UV-Vis spectroscopy so this wavelength was used to quantify **13** by UPLC. A 10 mM solution of **13** was prepared by weighing 1.9 mg of solid in an appropriate vial and dissolving in 614 μL of acetonitrile. A 5 mM solution of **13** was subsequently prepared by serial dilution in acetonitrile. This was used to prepare a series of solutions of different concentrations in a volume of 1 mL. These were subsequently injected in the UPLC and the area at 424 nm was plotted against the concentration of **13**. Linear regression gave an equation of y = 25.8774x – 1.16034, which was used to convert the area at 424 nm into concentration of product.

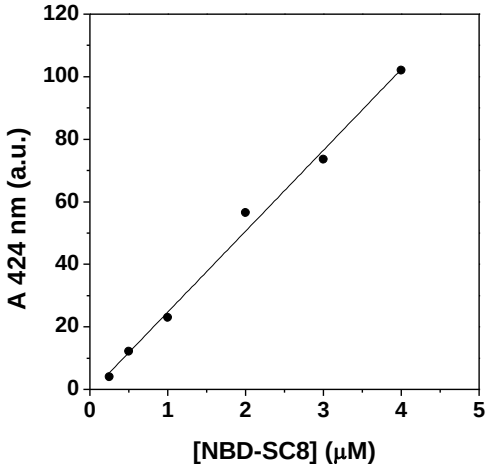

Equation	y = a + b*x		
Weight	No Weighting		
Residual Sum of Squares	48.87148		
Pearson's r	0.99671		
Adj. R-Square	0.9918		
		Value	Standard Error
B	Intercept	-1.16034	2.36326
	Slope	25.8774	1.05142

Figure 5.33: UPLC calibration curve of **13** in HEPES buffer pH 7.0.

5.6.8 References

(1) Maiti, S.; Fortunati, I.; Ferrante, C.; Scrimin, P.; Prins, L. J. *Nat. Chem.* **2016**.

Summary

Nature uses self-assembly to construct structures and to carry out a variety of functions which are essential to life. The cell membrane is an impressive example of a self-assembled structure, providing a confined space where chemical reactions take place in a microenvironment that is different from the outer aqueous environment. This has proven to be inspirational for chemists, who have harnessed the power of self-assembly processes to construct complex structures which are able to perform advanced functions such as catalysis and sensing. Traditionally, self-assembly processes have been carried out under thermodynamic or kinetic control. Yet, Nature uses dissipative self-assembly to activate functions for a limited period of time. In such systems, a continuous supply of energy is required in order to maintain a functional assembled state. For example, microtubule formation, an essential process for cell division is dependent on chemical energy from GTP to maintain an assembled state. This awareness has led to a recent shift in focus to synthetic self-assembly processes that operate far-from-equilibrium. In a similar way to what occurs in Nature, this provides temporal control over the functions associated to the self-assembled state. In this dissertation self-assembly under dissipative conditions is used as a control element to influence the outcome of chemical reactions.

In the first part, a self-assembled system which operates under dissipative conditions was developed. The surfactant $C_{12}TACN \bullet Zn^{2+}$ did not aggregate spontaneously up to mM concentrations, but self-assembled into vesicles at low micromolar concentrations in the presence of ATP, which acted as chemical fuel. Assembly formation required the presence of chemical fuel and the enzymatic hydrolysis of ATP by alkaline phosphatase led therefore to spontaneous deaggregation. The addition of ATP in the presence of enzyme therefore led to assembly formation, but only for a limited amount of time. The cycle could be repeated upon the addition of a fresh batch of ATP.

The assembled vesicles were then used as a chemical nanoreactor for the promotion of a hydrazone bond-formation reaction. The reaction between the hydrophobic reagents *trans*-cinnamaldehyde and 3-hydroxy-2-naphthoic hydrazide was very slow in aqueous buffer and in the unassembled $C_{12}TACN \bullet Zn^{2+}$ surfactant. However, a strong enhancement in the reaction was observed upon addition of ATP. The vesicles presented a more hydrophobic environment than the surrounding aqueous medium, and this was conducive to the otherwise unfavourable

reaction. The observation that rate enhancement is associated to the assembled state implies that temporal control over the assembly obtained by adding ATP can be used a tool to control chemical reactivity.

The responsive self-assembly of the surfactant $C_{12}TACN{\bullet}Zn^{2+}$ was then used for the selective formation of hydrazone-bonds. A small reaction mixture was created in which two aldehydes (2-pyridinecarboxylaldehyde and *trans*-cinnamaldehyde) competed to form a hydrazone with 3-hydroxy-2-naphthoic hydrazide. In the presence of just $C_{12}TACN{\bullet}Zn^{2+}$ it was observed that the reaction involving 2-pyridinecarboxylaldehyde proceeded at a higher rate. However, the addition of ATP resulted in vesicle formation, which led to a significant enhancement of the reaction between *trans*-cinnamaldehyde and 3-hydroxy-2-naphthoic hydrazide. Over time, the product composition changed so that the latter hydrazone was present in greater quantities compared to the first one. Because of time limitations, the reactivity response could not be studied under dissipative conditions yet. However, it is expected that the addition of a temporal dimension to the self-assembly process will lead to unprecedented kinetic profiles.

In a separate study - using monolayer protected gold nanoparticles as a model system - it was investigated whether the $TACN{\bullet}Zn^{2+}$ complexes played a role in the activation of ATP for enzymatic cleavage. Participation of the building blocks in the fuel-to-waste conversion process is of key importance for designing dissipative self-assembly schemes. Using ^{31}P NMR studies it was shown that the $TACN{\bullet}Zn^{2+}$ complexes in the monolayer, but not isolated ones, accelerated the hydrolysis of ATP by potato apyrase. This implied that the Au NPs played an important role in the dissipation of energy, which brings the system closer to natural ones.

The principles of self-assembly under dissipative conditions were then used to construct another system based on Au NPs containing $TACN{\bullet}Zn^{2+}$ head groups and negatively charged cyclodextrin vesicles bearing carboxylate groups. Mixing the systems together led to aggregation as a result of electrostatic interactions. Addition of ATP bearing phosphate groups, however, led to deaggregation, caused by the preferential binding of ATP to the nanoparticles. A transient aggregation process could be installed by adding ATP in the presence of the enzyme potato apyrase. The cycle could be repeated upon the addition of a new batch of ATP. This transient aggregate was then used to obtain temporal control over the nucleophilic aromatic substitution reaction between NBD-chloride and octane-thiol.

The same system could also be made responsive to light by introducing a light-sensitive co-factor. A carboxylate-substituted arylpyrazole was used as guest with a higher affinity in the *trans*-form compared to the *cis*-form. This enabled light-controlled switching between the aggregated and de-aggregated state. Further control over the aggregation process could be obtained by including ATP and apyrase in the same system. This allowed the development of a system which was responsive to multiple stimuli.

In this work, we have developed various self-assembled systems that can respond to external stimuli, such as chemical molecules or light. It was shown that this permits switching of the systems between an inactive and active state and, moreover, a transient activation in case the stimulus is spontaneously eliminated. It is shown that assembled states can act as accelerators for a chemical reaction, which does not take place in the unaggregated state. Thus, the stimulus-induced self-assembly process provides a means to control chemical reactivity. This study provides the basis for further developments related to the study of adaptation and the generation of smart and intelligent materials.

Acknowledgements

I would like to thank my supervisor, Professor Leonard J. Prins, for his guidance and help throughout these three years. Thanks for being a source of inspiration about how to do great science and for the opportunities you offered me throughout these three years. Special thanks also goes to Dr. Subhabrata Maiti, whose help was essential in the initial stages of the project.

Thanks also go to Professor Bart Jan Ravoo and Dr. Chih-Wei Chu from the University of Münster and to Professor Jurriaan Huskens from the University of Twente, for welcoming me in their labs to carry out collaborative projects. Both were very positive experiences where I had the opportunity to meet brilliant people and produce some very nice science.

Special gratitude also goes to the colleagues and staff at the Department of Chemical Sciences for all the help whenever needed. Thanks also goes to the technical staff, especially Stefano and Giulio for their much appreciated work. I will never forget our philosophical discussions Stefano!

I would also like to acknowledge the Professors and colleagues in the Marie-Curie Network. It was an honour to discuss my work with people from around the world. I hope that we might have the oportunity to meet again in the future.

Special thanks also goes to my friends, near or far, who have supported me, listened to me, laughed with me and shared with me important moments throughout this journey which has taught me a lot. I am today a much better, wiser person thanks to them. Thanks especially to Cheryl, Albana, Claire-Marie, Marco, Nadia, Carolina, Malcolm, Domenico, Giulia, Sun. Thanks to the people at the Centro Universitario, where I have found like-minded people with whom I could share interesting and meaningful discussions about life.

Last, but not least I would like to thank my parents, who have given me the opportunity to be who I am today. Thanks also to my siblings for being there.